Faculty of Pharmacy
University of Helsinki
Helsinki

RAMAN SPECTROSCOPY AND SURFACE PLASMON RESONANCE AS PHOTONIC TOOLS FOR BIOPHARMACEUTICAL APPLICATIONS

Tatu Rojalin

ACADEMIC DISSERTATION

To be presented, with the permission of the Faculty of Pharmacy of the University of Helsinki, for public examination in lecture room 3, Infokeskus Viikki building, on 9th of December 2016, at 12 am.

Helsinki 2016

Supervisors:

Professor Marjo Yliperttula
Division of Pharmaceutical Biosciences
Faculty of Pharmacy
University of Helsinki
Finland

Dr. Tapani Viitala
Division of Pharmaceutical Biosciences
Faculty of Pharmacy
University of Helsinki
Finland

Associate Professor Timo Laaksonen
Department of Chemistry and Bioengineering
Faculty of Natural Sciences
Tampere University of Technology
Finland

Professor Sebastian Wachsmann-Hogiu
Department of Pathology and Laboratory Medicine,
and Center for Biophotonics & Global Good
University of California Davis, CA & Intellectual Ventures, Bellevue, WA
The United States

Reviewers:

Professor Antonella Badia
Département de Chimie
Université de Montréal
Canada

Dr. Inger Vikholm-Lundin
BioMediTech
University of Tampere
Finland

Opponent:

Professor Emeritus Dennis L. Matthews
Department of Neurological Surgery, School of Medicine
Chair of International Science Committee, Center for Nanoscale Biophotonics, Australia
Chief Scientist, Tahoe Institute for Rural Healthcare Research, Truckee CA, The United States

ISBN (pbk.) 978-951-51-2732-7
ISBN (PDF) 978-951-51-2733-4

Printed at Unigrafia Oy
Helsinki 2016

ABSTRACT

Biophotonics is an emerging area of scientific research that uses light of photons to probe biological specimens, such as tissues, cells and molecules. The field of biophotonics is broad and considerably multidisciplinary. Therefore the prerequisite for understanding biophotonics is the capability to integrate the fundamental knowledge of the physics of light with perspectives of engineering of devices and instruments used to generate, modify, and manipulate light. Also, the fundamentals of biology and medicine are essential – particularly comprehension of the biochemical and cellular phenomena that occur in living systems, and how such phenomena can be scaled up to concern the physiology of organisms, for example humans. Biological pathways and processes differ in the healthy and diseased state, and that is why it is essential to develop understanding of pathophysiology and various states of disease such as cancer, neurodegenerative disease or infectious states. Consequently, solid insights into the functions of medical treatments, including biopharmaceutics, are needed. Raman and surface plasmon resonance (SPR) are both light-based technologies enabling label-free measurements with high sensitivity. The primary aim of this Thesis was to tackle the emerging hardships encountered in the fundamental biopharmaceutical research, clinical settings, or in the pharmaceutical industry by introducing applications and data analysis methods based on the cutting edge Raman and SPR technologies. These techniques represent the *biophotonic* cornerstones as tools for biopharmaceutical applications throughout this Thesis.

The scope of this Thesis was essentially broad. First, small drug molecules were investigated with state-of-the-art time-gated Raman technology, showing that the interfering photoluminescent backgrounds can be effectively suppressed thus improving the acquired Raman data significantly. Additionally, EVs were studied with laser tweezers Raman spectroscopy (LTRS) as larger scale analytes and representatives of a highly interesting topic in the current nanomedical field. When Raman data from several different types of *single EVs* was examined using sophisticated data analysis, distinct subpopulations were observed, and the differences could be related to the biochemical compositions of the vesicle membranes. For the first time, the study showed the importance of measuring single EVs instead of a pool of vesicles.

Multi-parametric SPR (MP-SPR) technology was harnessed to develop applications and data analysis methods for small and larger scale analytes. Hence, a new small drug molecule, spin-labeled fluorene (SLF), was investigated in the context of Alzheimer's disease (AD) – particularly its potential to interfere with the detrimental amyloid peptide aggregation processes. The developed *bio-functional*

in vitro platform in combination with rigorous data analysis and computational simulations demonstrated the capabilities of SLF when it was employed in various biomimetic aggregation schemes. Moreover, liposomes were examined with the MP-SPR as larger scale nanomedical particles for the purposes of safe and effective nanocarrier development. The administration of a liposomal nanocarrier into the blood circulation was mimicked in the designed *bionanophotonic in vitro* schemes. Undiluted serum was made to interact with immobilized model liposomes in dynamic flow conditions. The findings revealed that the variation in surface chemistries of the liposomes plays a role when serum – essentially immune system – components are interacting with the liposomes. In particular, distinct "soft" and "hard" protein coronas were observed and characterized during the interactions.

Collectively, the results and findings in this Thesis underline the broad potential of biophotonics for biopharmaceutical applications. The technical improvements in instrumentation, and creativity in the application and data analysis development make the future of biophotonics bright.

ACKNOWLEDGMENTS

This work was carried out at the Center for Drug Research and in the Division of Pharmaceutical Biosciences, Faculty of Pharmacy, University of Helsinki, and at the Center for Biophotonics, Department of Biochemistry and Molecular Medicine, University of California Davis, Sacramento, California, USA. For the past 2 years, from 2014 to 2016, I have been privileged to work in teams consisting of talented individuals whom I would like to thank respectfully.

With all my appreciation, I am grateful to my supervisors, Professor Marjo Yliperttula, Dr. Tapani Viitala, Associate Professor Timo Laaksonen, and Professor Sebastian Wachsmann-Hogiu. They have greatly supported and encouraged me throughout this work. Their exceptional ways of thinking and work as scientists has been an invaluable example for me to become one. Professor Yliperttula challenges herself and the others to exceed expectations every day – still being sympathetic and understanding. Dr. Viitala is a remarkably skilled and knowledgeable scientist, his enthusiasm spreads all around the work community – and he is a nice person to work with. Associate Professor Laaksonen has the merit of his interdisciplinary work in the demanding fields of biomaterials, nanoparticles, and drug release – his sharp observations have been very important throughout this work. I show a lot of respect to Professor Wachsmann-Hogiu who gave me the opportunity to work at the Center for Biophotonics for one year. He is very passionate about science, his endless curiosity is amazing, and he leads his teams with his agile and broad insights. The period in the USA shaped the overall framework for my doctoral studies with irreplaceable support from the people in Finland.

Professor Antonella Badia from the Université de Montréal and Dr. Inger Vikholm-Lundin from the University of Tampere are warmly acknowledged for their time and contribution to the review process of this Thesis. I am honored that Professor Dennis L. Matthews from the University of California, Davis was willing to share his time and take the long trip from California to Finland to be the opponent of my dissertation.

I want to thank all my co-authors for their efforts and commitment. They have worked really hard, and occasionally set aside their other duties in order to perform experiments, comment on manuscript drafts, and write their contributions: Lauri Kurki, Juha Kostamovaara, Keith Gordon, Leonardo Galvis, Clare Strachan, Silvia Hilt, Artturi Koivuniemi, Alex Bunker, John Voss, Zachary Smith, Changwon Lee, Randy Carney, Sidhartha Hazari, Alisha Knudson, Kit Lam, Heikki Saari, Elisa Lazaro Ibañez, Otto Kari, Stefano Salmaso, Michaela Barattin, Hanna Jarva, Seppo Meri, and Arto Urtti. Thank you. In addition, I want to thank all my other co-workers in the Division of Pharmaceutical Biosciences, and at the Center for Biophotonics.

Especially I want to thank Liisa Kanninen, Tuuli Salmi, James Chan, Ruby Gill, Chris Robertson, and Maria Navas Moreno for fruitful discussions. I also want to acknowledge my closest friends, Juke, Beni, Katja, Jukka, and Eero, for your truly important friendship. The doctoral programme in Materials Research and Nanosciences (MATRENA) is acknowledged for having me as their PhD Candidate. Special thanks to my teacher Anne Vaara long before my university studies, for encouraging me to learn mathematics, physics, and chemistry.

I would like to acknowledge all the funding agencies involved in the research included in this work. Tekes – the Finnish funding agency for technology and innovation, the Academy of Finland, MATRENA for travel grants, the Finnish Pharmacists' Association, and the University of Helsinki grants.

Finally, my deepest appreciation to my wife Kati, for staying always with me, sharing the moments of victory and loss, for never giving up, and most importantly, for your eternal love and support. I do not have enough words to acknowledge and thank my parents, Pirkko and Pekka, for their love and support. They have always encouraged me to study, showed me the most important things in life and the meaning of persistence, and made an endless amount of right decisions. Thank you so much.

CONTENTS

LIST OF ORIGINAL PUBLICATIONS

This Thesis is based on the following original journal publications:

I Rojalin T, Kurki L, Laaksonen T, Viitala T, Kostamovaara J, Gordon KC, Galvis L, Wachsmann-Hogiu S, Strachan CJ, Yliperttula M. Fluorescence-Suppressed Time-Resolved Raman Spectroscopy of Pharmaceuticals Using Complementary Metal-Oxide Semiconductor (CMOS) Single-Photon Avalanche Diode (SPAD) Detector. Analytical and Bioanalytical Chemistry 408: 761-774, 2016.

II Rojalin T‡, Hilt S‡, Viitala T, Koivuniemi A, Bunker A, Wachsmann-Hogiu S, Yliperttula M, Voss JC. Amyloid Beta Oligomerization Alters its Affinity for a Modulator of Peptide Aggregation and Toxicity. Submitted manuscript.
‡ Equal contribution

III Smith ZJ, Rojalin T‡, Lee C‡, Carney RP‡, Hazari S, Knudson A, Lam K, Saari H, Lazaro Ibanez E, Viitala T, Laaksonen T, Yliperttula M, Wachsmann-Hogiu S. Single Exosome Study Reveals Subpopulations Distributed Among Cell Lines with Variability Related to Membrane Content. Journal of Extracellular Vesicles 4: 28533-28547, 2015.
‡ Equal contribution

IV Rojalin T‡, Kari OK‡, Salmaso S, Barattin M, Jarva H, Meri S, Yliperttula M, Viitala T, Urtti A. Multi-Parametric Surface Plasmon Resonance Platform for Studying Liposome-Serum Interactions and Protein Corona Formation. Drug Delivery and Translational Research 1-13, 2016.
‡ Equal contribution

The publications are referred to in the text by their Roman numerals.

AUTHOR'S CONTRIBUTION

Publication I: Fluorescence-Suppressed Time-Resolved Raman Spectroscopy of Pharmaceuticals Using Complementary Metal-Oxide Semiconductor (CMOS) Single-Photon Avalanche Diode (SPAD) Detector

The author designed the experiments with the supervisors and co-authors. The author performed the experiments and analyzed the results. The author wrote the first draft of the manuscript, and actively participated to complete the final paper.

Publication II: Amyloid Beta Oligomerization Alters its Affinity for a Modulator of Peptide Aggregation and Toxicity

The author designed the experiments with the supervisors and co-authors. The author invented and developed the concept of demonstrating the capabilities of SLF to hamper the Aβ peptide aggregation in a biologically relevant *in vitro* environment. The experiments were carried out by the author and S. Hilt. The author performed the biophysical modeling and calculations for all the MP-SPR experiments, and analyzed the results. The author wrote major parts of the manuscript, and actively participated to complete the final form.

Publication III: Single Exosome Study Reveals Subpopulations Distributed Among Cell Lines with Variability Related to Membrane Content

The author established a collaboration between the research units in the Division of Pharmaceutical Biosciences, Finland, and the Center for Biophotonics, USA. The author designed and performed the LNCap EV experiments with the LTRS system at the Center for Biophotonics. EV characterization and LTRS measurements for the other EV types were performed by the author and co-authors. The author actively participated in the multivariate data analysis and writing the manuscript to finalize the article.

Publication IV: Multi-Parametric Surface Plasmon Resonance Platform for Studying Liposome-Serum Interactions and Protein Corona Formation

The author designed the experiments with the supervisors and co-authors. The experiments were carried out by the author and O. Kari. The author performed all the biophysical modeling and calculations, and analyzed the results. The author wrote the first draft of the manuscript, and actively participated to complete the final paper.

LIST OF ABBREVIATIONS

2D	Two-dimensional
3D	3-dimensional
AD	Alzheimer's disease
ADME	Administration, distribution, metabolism and excretion (ADME)
ADPPKD	Autosomal dominant polycystic kidney disease
AFM	Atomic force microscopy
AsLS	Asymmetric least-squares
ATR	Attenuated total reflection
ATR-FTIR	Attenuated total reflection Fourier transform infra-red spectroscopy
Au	Gold
BD	Bechet's disease
BCA	Bicinchoninic acid
BioMEMS	Biological micro electro mechanical systems
Biotin-PEG-SH	Biotinylated hexa(ethylene glycol) undecane thiol
CARS	Coherent anti-Stokes Raman spectroscopy
CCD	Charge coupled device
CD	Circular dichroism
CHAPS	3-[(3-Cholamidopropyl)dimethylammonio]-1-propanesulfonate
CM	Conditioned medium
CMD	Carboxymethyl dextran
CMOS	Complementary metal oxide semiconductor
CNS	Central nervous system
CSF	Cerebrospinal fluid
CW	Continuous wave
DDC	Drug delivery carrier
DFT	Density function theory
DLS	Dynamic light scattering
DMSO	Dimethyl sulfoxide
DNA	Deoxyribonucleic acid
DPBS	Dulbecco's phosphate buffered saline
DPI	Dual polarization interferometry
DSC	Differential scanning calorimetry
DTT	Dithiothreitol
EDTA	Ethylenediaminetetraacetic acid

EMA	European Medicines Agency
EV	Extracellular vesicle
FBS	Fetal bovine serum
FDA	U.S. Food and Drug Administration
FLIM	Fluorescence-lifetime imaging microscopy
FLIP	Fluorescence loss in photobleaching
FLIR	Forward looking infrared
FRAP	Fluorescence recovery after photobleaching
FRET	Fluorescence resonance energy transfer
FT	Fourier transform
GUI	Graphical user interface
HES	Hydroxyethyl starch
HF	Hartree-Fock
HFIP	Hexafluoro-2-propanol
HILIC	Hydrophilic interaction liquid chromatograph
HIV	Human immunodeficiency virus
HRP	Horseradish peroxide
HSP	Heat shock protein
HTS	High-throughput screening
ICCD	Intensified charge-coupled device
IR	Infra-red
ISEV	International Society for Extracellular Vesicles
ITC	Isothermal titration calorimetry
IUPAC	International Union of Pure and Applied Chemistry
LAL	Limulus amoebocyte lysate
LAMP	Lysosome-associated membrane glycoprotein
LASIK	Laser-assisted *in situ* keratomileusis
LB	Langmuir-Blodgett deposition
LC-MS	Liquid chromatography with tandem mass spectrometry
LDS	Liposomal drug delivery system
LIDAR	Light detection and ranging
LITT	Laser induced thermal therapy
LLLT	Low level laser therapy
LNP	Lipid-based nanoparticle
LTRS	Laser tweezers Raman spectroscopy
LUV	Large unilamellar vesicle
MAGE3	Melanoma-associated antigen 3
MATLAB	Matrix laboratory (software)
Mie	Mie scattering
MHC	Major histocompatibility complex
MOPS buffer	(3-morpholinopropane-1-sulfonic acid) buffer

MPS	Mononuclear phagocyte system
MP-SPR	Multi-parametric surface plasmon resonance
mRNA	Messenger ribonucleic acid
miRNA	Micro ribonucleic acid
MuOH	11-mercapto-1-undecanol
MV	Microvesicle
MVB	Multivesicular body
MVE	Multivesiclular endosome
NME	New molecular entity
NMR	Nuclear magnetic resonance
NIR	Near infra-red
NSOM	Near-field scanning optical microscopy
NTA	Nanoparticle tracking analysis
OGD	Oligo-guanidyl lipid derivative
PALM	Photo-activated localization microscopy
PAT	Process analytical technology
PBS	Phosphate-buffered saline
PC	Principal component
PCA	Principal component analysis
PCB	Poly(carboxybetaine)
PDT	Photodynamic therapy
PEG	Polyethylene glycol
PG	Poly(glycerol)
PGA	Polyglutamic acid
pHPMA	Poly(N-hydroxypropyl)methacrylamide
PLGA	(poly (lactic-*co*-glycolic acid)
PMDA	Pharmaceuticals and Medical Devices Agency
POC	Point-of-care
p(PEGMA)	Poly(poly(ethyleneglycol)
PSA	Polysialic acid
PVC	Polyvinyl chloride
PVP	Poly(vinylpyrrolidone)
QCC	Quantum chemical calculation
QCM	Quartz-crystal microbalance
RES	Reticular endothelial system
RIPA	Radioimmunoprecipitation assay buffer
RNA	Ribonucleic acid
RT	Room temperature
SAM	Self-assembled monolayer
SD	Standard deviation
SDS-PAGE	Sodium dodecyl sulfate polyacrylamide gel electrophoresis

SEM	Scanning electron microscopy
SERS	Surface-enhanced Raman spectroscopy
SFG	Sum-frequency generation spectroscopy
siRNA	Small interfering ribonucleic acid
SLF	Spin labeled fluorene
SPAD	Single-photon avalanche diode
SPR	Surface plasmon resonance
SRM	Super resolution microscopy
SRS	Stimulated Raman scattering
STED	Stimulated emission depletion
STORM	Stochastic optical reconstruction microscopy
SUV	Small unilamellar vesicle
TACSTD2	Tumor-associated calcium signal transducer 2
TBST	Tris-Buffered Saline with Tween™
TERS	Tip-enhanced Raman spectroscopy
TfR	Transferrin receptor
TGFB1	Transforming growth factor beta 1
TMV	Trypsinized microvesicle
TEIR	Total isolation reagent
TIR	Total internal reflection
TRIS	Tris(hydroxymethyl)aminomethane
UV-Vis	Absorbance spectroscopy using ultra-violet to visible light range

LITERATURE REVIEW

1 INTRODUCTION

Light is a convenient tool for studying and resolving various questions in life sciences and biopharmaceutical research. In essence, *photonics* as a field encompasses the technologies and applications whereby light interactions with matter are exploited to find out the chemical structures of compounds or to initiate light-sensitive reactions. *Biophotonics* concerns light interactions with biological matter – which can be expanded to cover biopharmaceutical compounds and different types of formulations, like small drug molecules, liposomes, and extracellular vesicles (EVs), respectively. Photonics and essentially biophotonics offer a wide variety of opportunities to tackle the emerging hardships encountered in life sciences. The evolution of lasers and sensitive detectors has paved the way for affordable, effective and compact instrumentation to counter these challenges. Regardless these technical advancements, the tedious and costly drug discovery process, further optimization tasks to improve drug formulations already in market, and the need for new in vitro testing methods continuously trouble researchers in the multidisciplinary field of biopharmaceutical research. Furthermore, the advent of *nanomedicine* has brought us to a new era. In the context of nanomedicine, there is a growing need for sensitive and robust preclinical platforms to detect various nano-sized cell organelles, extracellular vesicles (EVs), in order to better understand their complex biochemical pathways in the biological environment – particularly in cancer pathogenesis. Also, recent findings indicate that EVs could act as biomimetic targeted drug delivery carriers (DDCs) against tumor cells. A plethora of problems exist in the EV research; they cannot be observed by conventional diffraction-limited microscopy, the EV isolation and purification steps are labor intensive, their cumbersome biochemical composition plagues researchers worldwide, and there is a multitude of biological functions the EVs can perform in the body. Another important aspect relates to nanomedicine as well; namely, in the event of administering e.g. liposomal drug nanocarriers into the blood circulation, various biophysical phenomena occur at the *nano-bio interfaces* [1]. The rational design of such nanocarriers is in need of methods to fulfil the demanding requirements in different phases of the process and to better understand the functions of these interfaces. Such phenomena must be rigorously scrutinized to accomplish rational nanocarrier development, and to increase the *in vivo* relevance of *in vitro* studies.

From a diagnostic standpoint, biophotonics encompasses developing new technologies and applications for detecting and diagnosing biological states of health and disease, and observing for changes in these states. Early stage disease detection is seen as one of the important aims in diagnostic biophotonics since the probabilities of successfully treating and curing the disease are highest at its earliest

phase. New optical technologies are constantly needed to monitor and analyze these interactions and thus the development of such techniques is one of the key areas in biophotonics. The use of light and optics provides a number of advantages because the obtained and analyzed data is typically multi-dimensional, imaging and sensing performed at the scale of individual cells or molecules. Therefore in order to effectively implement these technical advantages in biophotonics, the applications and data analysis methods must be aligned to formulate biologically relevant assays. The therapeutic perspective of biophotonics covers the application of light for treating disease or altering biological processes. It can involve exploiting the higher energies of optical radiation that can alter the chemical or mechanical properties of cells and tissues, for instance resulting in the ablation of a tumor. Additionally, light can be utilized to change cellular and molecular functions via photochemical treatment, or photothermally or photomechanically manipulate tissues. Importantly, in therapeutic biophotonics an essential goal is to predict felicitously how the drug formulations interact with the living surroundings when administered into the body. All of the above taken into consideration, this is how new biophotonic technology is created and new biophotonic science – including applications and innovative data analysis methods – are discovered. Although advancement happens constantly, the current situation can be improved by harnessing the potential of biophotonics in previously unseen ways. Three distinct aspects can be emphasized in order to elucidate the main shortcomings of the present state – essentially why biophotonic methods in biopharmaceutics are in demand of novel approaches.

Firstly, the biophotonic *technologies* themselves are in need of innovative solutions; Raman spectroscopy is a scattering-based technique that provides a highly specific chemical fingerprint of the molecule of interest. However, thus far the major obstacle for its broader use outside the laboratory settings has been the strong photoluminescent background signals swamping the weak Raman responses, non-user-friendly equipment and data analysis, and high prized instrumentation. The aforementioned drawbacks can be overcome by the compact time-gated Raman system that utilizes the time difference between Raman scattering and photoluminescence phenomena. Additionally, Raman tweezers is a somewhat underused spectroscopic technique for acquiring Raman data from single particles trapped in the force field of a firmly focused laser. Such tweezers are particularly useful to investigate small drug molecules and nano-carriers with biochemical contents like EVs. Furthermore, surface plasmon resonance (SPR) is a well-established label-free technique for studying molecular interactions in real time. The multi-parametric SPR (MP-SPR) has been recently introduced as a next-generation SPR technique that essentially preserves the benefits of traditional SPR concurrently adding the possibility for thorough molecular surface characterization.

Secondly, there is a lack of innovative *methodologies and applications* based on biophotonics. For instance, the technical advantages of MP-SPR allow for the

development of creative *in vitro* biophotonic platforms for a diverse set of problems; in its traditional sense, it can be utilized for detecting interaction kinetics as with any other SPR system. However, the features of MP-SPR also yield valuable information on the properties of the surface after the analytes of interest have been adsorbed onto the sensor surface. Such pertinent properties include the layer thickness (d) and refractive index (n). In addition, by harnessing the benefits of Raman spectroscopy – such as its capability to give detailed structural information on the molecules and insensitivity to aqueous background signals of biological samples – it can be used in a considerably broader array of applications than it is used today. Hence, by developing new *in vitro* applications, prospective small drugs can be characterized and monitored from multiple standpoints; their kinetic properties can be evaluated while their functions can be demonstrated in biomimetic environments. In this Thesis, these assays are exploited as *bio-functional assays*. Moreover, larger scale analytes, such as liposomes and extracellular vesicles can be studied in biologically relevant *in vitro* environments that resemble the natural milieu they encounter when either administered in blood circulation as drug delivery carriers or when found as partners of intracellular communication.

Thirdly, in addition to novel technologies and applications, the *statistical analysis* of the raw data must be designed and refined in a way that it yields interpretable and explicit results. For example the surface characterization is based on the modeling and fitting of the measured MP-SPR spectral data with sophisticated algorithms. Multivariate analysis, on the other hand, are needed to interpret Raman data for which the visual inspection is not an option to distinguish the nuances between different spectra. From the standpoint of biopharmaceutics, the introduced innovations can be used to study small drugs as well as larger scale analytes and nanocarriers without *a priori* labeling. It is to be noted that – instead of replacing the existing well established methods, for instance fluorescence-based assays – biophotonic methods can provide valuable complementary information. Thus, the new viewpoints enable better understanding of the mechanisms underlying the phenomena of interest. In conclusion, revolutionary approaches are needed in the field of biopharmaceutics to resolve existing tenacious challenges as well as completely new ones. Biophotonic methods can offer feasible solutions for those demands.

2 BIOPHOTONICS

Biophotonics is an established term to cover the broad range of light-based technologies applied to the life sciences, for example pharmaceutical research and development, medicine, and biochemistry. Even though existing for decades, biophotonics has emerged during the 21st century as a very rapidly evolving field, primarily owing to the significantly improved laser technology; semi-conductor lasers allowing for developing compact-sized equipment with remarkably reduced cost of manufacturing while maintain the required power for given applications. Furthermore, the overall knowledge on the light-matter and -materials interactions, and increased computing capacity have been important advancements. In general, "photonics" is a technology-based term to encompass all the methods and techniques using light over the whole spectrum, and its interaction with any matter. In this context, biophotonics represents a novel extension to photonics. The roots of the word "biophotonics" extend back to the Greek language – "bios" being the expression for life and "phos" for light. Thus, biophotonics is a fusion of photonics and biology, dealing with the interactions between light and biological matter, and seeking answers to the mechanisms of fundamental life processes from micro to macro level, as well as the early detection, prevention, and therapy of diseases. In some cases "biomedical optics" is understood to cover the clinical applications of light in diagnostics and therapy while biophotonics represents a complementary term to biomedical optics [2]. In that context, biophotonics mostly deals with the fundamental research aspects, for example the investigation of cellular processes. However, being an all-encompassing, coherent and beautiful term, biophotonics is used throughout this Thesis to cover all the interactions between biological matter, biopharmaceutical compounds and structures, and light, from the very fundamental research level all the way to the highly sophisticated technologies used for clinical purposes and diagnostics.

Biophotonics is an excessively cross-disciplinary field of science that integrates four major technologies: lasers, photonics, nanotechnology and biotechnology. These technologies have been estimated to collectively generate several billions of dollars in the global marketplace [3]. Biophotonics has impact on a wide range of industries from biotechnology companies and health care organizations through medical instrument suppliers to pharmaceutical manufacturers, information technology and optical telecommunication. **Table 1** summarizes some of the many ongoing and future prospects dealing with biophotonics.

Table 1. Biophotonics is a pervasive field that integrates multidisciplinary expertise. Sorted by discipline, the table displays areas of development in biotechnology, biomedicine, and fundamental research where biophotonics is employed.

Discipline	Area of development and reference
Chemists	Development of fluorescent tags [4] Development and identification of chemical probes for analyte detection and high-throughput (HTS) assays [5, 6] Nanoscale chemistry for designing probe materials [7] Fundamental knowledge on the optical activation phenomena [8]
Physicists	Understanding the photochemical processes in biomolecules and bioassemblies [9, 10] Discerning the physical principles for imaging and biosensing [11, 12] Single molecule biophysics [13, 14] Nonlinear optical processes for research, therapy and diagnostics [15]
Engineers	Integration of new generation lasers, delivery systems and detectors [16] Device miniaturization, automation and robotics [17] Noninvasive or minimally invasive light activation [18] Development of in vivo optical spectroscopic techniques [19, 20] Optical micro-electro-mechanical systems (BioMEMS) and their nanoscale analogues [21]
Biomedical researchers	Early detection of infectious diseases and cancers [22, 23] Dynamic imaging of physiological responses to therapy and drug delivery [24, 25] Cellular mechanisms of drug activation [26] Toxicity of light-activated nanomaterials [27] Biocompatibility of biomaterials and implants [28]
Clinicians	In vivo human patient imaging [29-32] Tissue welding, contouring and regeneration [33] Laboratory tests (e.g. analysis of body fluids) and point of care (POC) diagnostics [34, 35]
Biopharmacists	Drug discovery and drug development [36-40] Pharmacokinetics and pharmacodynamics [41-45] High-throughput screening (HTS) and process analytical technologies (PAT) [46, 47]

An intuitive question would be, what is so special about light that makes it an ideal tool for life sciences? There exists a wealth of favorable features that make light an excellent probe to work with. Firstly, light offers a spatial scale of six orders of magnitude. Observations and object manipulation can be performed on a scale from several nanometers up to centimeters. This allows for detection and manipulation of macromolecules to subcellular manipulation and macroscopic diagnosis and tissue surgery. For instance, findings and applications on a single cell level can be adapted to the inspection of cellular networks and tissues. Another advantage in light-based research and development is the vast time scale for monitoring of events; from femtoseconds (10^{-15} s) to even days (10^{5} s). Extremely fast processes can be monitored or manipulated using pulsed femtosecond lasers. On the other hand, the stability of light sources enables long-term monitoring of structures and bioprocesses. In essence, photonics is the only available technology offering this formidable time scale. Moreover, optical technologies make it possible to

determine the different features of molecules, cells and tissue [48]. Examples include morphological features (e.g. measuring reflection, transmission/absorption, scattering), chemical features and their changes (e.g. utilizing Raman spectroscopy or fluorescence), mechanical features (e.g. using optical trapping) or movement (e.g. using dynamic light scattering measurements). The wide compatibility of light-based methods is beneficial in life sciences where cross-disciplinary work is always needed; optical methods can be combined easily with one another and measurements can be performed in the spatial and temporal domain. Furthermore, optical methods can also be combined with non-optical methods, and with other advanced technologies such as nanotechnology (nanoparticles, optically triggered nanocapsules, and optical nanostructures) and microsystems (microfluidics, lab-on-a-chip applications). Lastly, optical technologies are practical – which, in turn, is important especially when moving from bench to bedside, i.e. when transforming the technologies and applications achieved in fundamental research towards real life science methodologies. Contactless, non-invasive application, easy transmission of energy and signals, and minimal side effects to patient are some of the benefits facilitating this transformation. Additionally, opto-electric components have become compact and inexpensive, for example laser diodes, which allows the development of affordable systems [48]. In summary, the properties and advantages of photonics over the other biomedical tools, for example ultrasound, X-ray, or magnetic and nuclear medical technologies, are undisputable and offer cross-sectional methods to overcome a broad array of challenges in modern life sciences. In order to demonstrate the vast field of biophotonics, **Table 2** summarizes some important methods and technologies.

Table 2. Summary of essential methods and technologies in biophotonics.

Technology	Examples	Reference
Spectroscopy	Absorption (THz, microwaves, IR, UV-Vis) Emission (fluorescence methods in general; one-photon/ multi-photon fluorescence, FRET, FRAP, FLIM, FLIP) Elastic and inelastic light scattering (for example Rayleigh, Raman, CARS, SRS, SERS, TERS, Mie, LIDAR) Surface-sensitive technologies (SPR, label-enhanced SPR, MP-SPR)	[49-52]
Light microscopy	Fluorescence microscopy (autofluorescence or fluorescence labels, e.g. proteins), sub-diffraction techniques (optical nanoscopy, e.g. STED, NSOM, PALM/STORM, structured illumination) and 3D imaging techniques (e.g. confocal and multi-photon excitation microscopy) Raman microscopy (CARS, SRS, TERS) Contrast methods (e.g. phase contrast microscopy, digital holographic microscopy (DHM))	[53-56]
Chip-based analysis	Biochips and biosensors for POC diagnostics ("lab-on-a-chip")	[57]
Therapeutic methods	Photodynamic therapy (PDT), controlled release of bioactive agents, Laser-in-situ Keratomileusis (LASIK), low-level laser therapy (LLLT), laser-induced thermotherapy (LITT)	[58-60]
Optical micromanipulation	Optical tweezers, optical stretcher, laser catapulting, cell sorting and cell positioning	[61, 62]
Optical components	Light sources, detectors, and other optical components, e.g. ultrafast lasers, adaptive optics, fiber endoscopes	[63, 64]
Other technologies	Micro- and nanofluidics, biochemistry (evaluation of targets, development of marker molecules), data modeling (image analysis, chemometrics), data management (user-oriented GUI, Big Data handling, bioinformatics), system integration and automation	[65-68]

2.1 SPECTROSCOPY AND SURFACE-SENSITIVE TECHNIQUES IN BIOPHOTONICS

Today, the wide range of sophisticated spectroscopic methods enable detailed examination of (bio) chemical structures as well as physiological and biological processes. The evolution of spectroscopy has paved the way for molecular research in chemistry, biophysics, physical chemistry and biopharmaceutics. Prominent measurement technologies are label-free, and non- or minimally invasive, and observations can be performed in real time. The applicability of these technologies in life sciences is extremely broad. For instance, during the drug discovery process the chemical structures and solid state behavior of the potential drug molecules have to be evaluated, and their safety and efficacy tested *in vitro* according to the guidelines of the regulatory agencies in Europe, USA and Japan (FDA, EMA, and PMDA, respectively). Furthermore, an immense amount of various interactions can be

observed by spectroscopic methods – especially using surface-sensitive techniques that utilize photonics and biosensor technologies. Examples of interactions that can be detected on or at the close proximity of functionalized sensor surfaces include drug-protein affinities [69], protein-protein interactions [36], liposome interactions with various analytes [70], or various interaction schemes of biomimetic structures resembling cell lipid bilayers [71]. In general, interaction of light with (bulk) matter such as molecular aggregates having a size equal to or larger than the wavelength can result to reflection, refraction, scattering and absorption processes. These processes are depicted in **Figure 1**. In essence, the refractive index n at frequencies corresponding to the gap between the two different states of a medium (near the resonance, e.g. air and metal) is defined as a complex quantity given as , where the real part, describes the refraction and scattering, the imaginary part, , describes the absorption of light in a medium. Moreover, the dielectric properties of materials and evanescent field phenomena construct the bedrock for surface-sensitive techniques [72]. Particularly, scattering-based Raman spectroscopy and surface-sensitive surface plasmon resonance (SPR) as biophotonic methods, their current state and modern applications for the biopharmaceutical field are represented in detail throughout this Thesis.

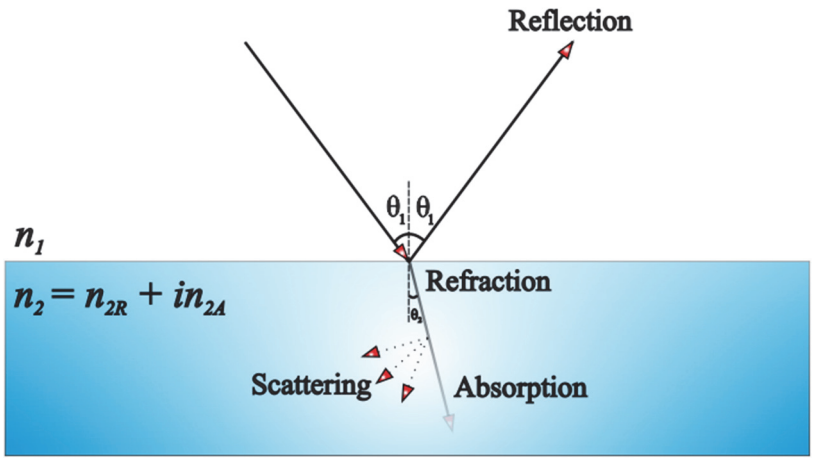

Figure 1. A beam of light is propagating from medium 1 (air) to a medium 2 (e.g. biological tissue or metal).

2.2 BIOSENSORS AND OPTICAL BIOSENSORS

Biosensor, by the definition of the International Union of Pure and Applied Chemistry (IUPAC), is *"a self-contained integrated device which is capable of providing specific quantitative or semi-quantitative information using a biological recognition element which is in direct spatial contact with a transducer element"* [73]. This definition has been challenged as unnecessarily stringent [74] but nevertheless the basic concept is in the use of a device that can measure biologically-derived signals. Originally biosensors were used to describe enzymatic interactions. The first biosensor was a glucose sensor. Soon it turned out that the possibilities offered by the biosensor technology could be utilized to investigate biological systems, receptors, nucleic acids, lipids, and a wide range of small molecule and bigger particle interactions with various ligands. Despite the signals are occasionally hardly recognizable, the biosensor technologies have established a strong position in the field of life sciences [75-82].

Optical biosensors, for one, are components that are used with optical techniques to detect and identify chemical or biological species. There are numerous advantages in using optical biosensing such as remote sensing with high selectivity and specificity and the opportunity to use highly modifiable biorecognition schemes. In addition, electromagnetic interference can typically be isolated during the measurements, which essentially means that the instrument-related noise can be minimized with minor effort. It is also useful that multiple channels and multi-parameter approaches can be used for detection, and the instruments are compact and affordable. Furthermore, detailed chemical information on analytes is provided by optical biosensors. The main aspects related to optical biosensing are (i) a choice of appropriate bio-recognition scheme and parameters to detect chemical or biological species, (ii) a transduction mechanism to convert the physical or chemical response of bio-recognition into a measurable signal, and (iii) selection of correct data analysis techniques to process and interpret reliably the acquired data. Being a part of biophotonic methods, optical biosensors can be found very useful in a vast number of applications, for instance, clinical diagnostics, drug development, environmental monitoring (air, water, soil) and food quality control. These features make optical biosensors an intriguing option for multiple purposes in life sciences, for example in biopharmaceutics.

An overview, examples and a chronological insight into the evolution of biosensors are provided for example in references [50, 83-88]. Ideally a biosensor-based assay is label-free and the measurements can be performed in real time. This, in turn, offers many advantages over the other techniques and methods in which complex sample preparation, sophisticated laboratory equipment or trained personnel may be needed. Additionally, instead of measuring solely the start and end phase of the phenomenon of interest in static conditions, biosensor assays enable monitoring

events constantly over the time and dynamic conditions are easily implemented e.g. by the use of microfluidics [38]. The aforementioned features serve as good starting points for various *in vitro* analysis and biomimetic assays in biopharmaceutics where fast, cost-effective, robust and highly modifiable methodology is needed in order to discover novel venues for studying pharmacodynamics and pharmacokinetic phenomena in biologically relevant environments.

2.2.1 Biosensor development

The main components of an optical biosensor system are (i) a light source, (ii) an optical transmission medium (e.g. fiber, waveguide), (iii) immobilized biological recognition element (e.g. enzymes, peptides, antibodies, lipid bilayers, liposomes, or cells), (iv) optical probes (e.g. fluorescent marker in labeled settings or surface plasmon propagation in label-free settings) for transduction, and (v) an optical detection system. In the case of evanescent wave sensing, such as surface plasmon resonance, a metal acts as a solid support for the bio-recognition elements. The bio-recognition elements are typically immobilized on the surface, either by physical (for example adsorption) or by chemical attachment. Since the first reports of enzyme-based biosensors for glucose by Clark et al. in 1962 [89], there has been an extensive evolution in the biosensor development [69]. Unless otherwise stated, throughout this Thesis, the bio-recognition material attached to the sensor surface is referred to as the *receptor ligand* or simply *ligand*. The detected material, for one, is called the *analyte*. Below, various immobilization techniques are briefly discussed.

Physical adsorption. Relatively straight-forward physical methods include bio-recognition containment within semipermeable membranes or adsorption on a solid support. Ionic, hydrophobic, or Van der Waals forces can be used for selective adsorption. The advantage of physical adsorption is simplicity, but it may suffer from the non-specific nature of the method or variation in the density of attachments, orientation and desorption of bio-recognition elements. A bio-recognition element can be immobilized on a solid support by electrostatic interactions between them. The polarity or charge of the bio-recognition element can be adjusted with varying pH conditions, and thus, by selecting suitable polymer (e.g. containing negatively charged sulfonic groups $-SO_3^-$, or positively charged ammonium groups $-NH_4^+$) carrying opposite charge, the bio-recognition element can be adsorbed onto the surface.

Physical entrapment. In this method the bio-recognition element is entrapped within a polymer of biomimetic matrices, for example polyacrylamide, polyvinyl alcohol, polyvinyl chloride, sol-gel processed glass or Langmuir-Blodgett film. The advantage is that the leaching (desorption) of the bio-recognition element and bio-fouling effect (adherence of non-specific biologics) can be minimized. However, the immobilized biomolecule has to retain its affinity, activity and stability in the

entrapped form, and it also has to be accessible to the analyte. In addition, the entrapment matrix has to be optically transparent.

Chemical immobilization. A formation of a covalent bond between the solid support or the sensor surface and the bio-recognition element is the basis of chemical immobilization techniques. Control of the surface density of bio-recognition element is crucial for achieving high efficiency. Of importance, the support surface is typically modified in order to introduce coupling groups such as –OH, $–NH_2$, –COOH, and –SH. Another covalent attachment scheme involves a –COOH reaction with an amine group to form an amide linkage. Furthermore, a frequently used covalent bio-recognition element association method is the immobilization on a gold surface – this is a common method especially in the case of SPR sensors. For this purpose, a self-assembling phenomenon of a molecular monolayer composing of long-chain molecules with an –SH group at one end and another functional group such as $–NH_2$ or –COOH at the other end is used. In principle, the –SH group binds to the gold surface whereas the $–NH_2$ or –COOH group at the other end is used to couple e.g. to an enzyme or an antibody at multiple sites. Moreover, cellulose, polyacrylamide, carboxymethyl-modified dextran (CMD), carboxylic-acid-modified polyvinyl chloride (PVC) or polystyrenes can be used as functionalized surfaces for binding with proteins. An important method for the chemical immobilization of biotinylated ligands/analytes is the avidin-biotin coupling technique [90]. The avidin-biotin coupling is illustrated in **Figure 2**.

In general, covalent attachment protocols yield more stable and reproducible activities than the physical methods, but the downside can be occasional complexity in the immobilization procedure. It is noteworthy that the covalent chemical immobilization techniques are most commonly used when preparing SPR sensors; glass slides are typically coated with a thin noble metal layer with good plasmonic properties such as gold, platinum or silver. Gold as the coating material is favored since it is relatively inert and affordable, and its plasmonic behavior with different excitation wavelengths is well established [91].

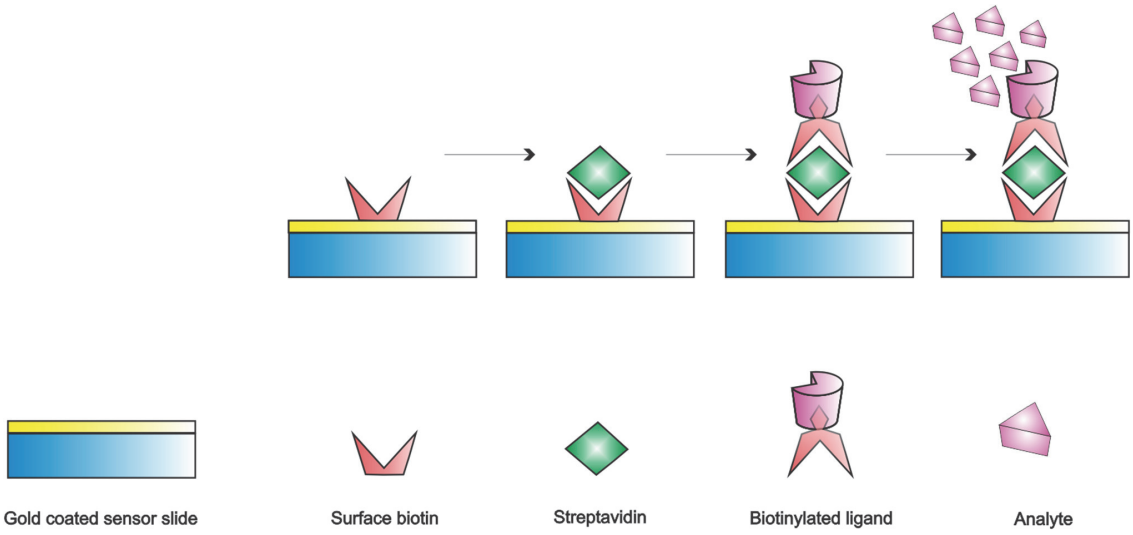

Figure 2. An artistic impression of the biotin-avidin coupling events.

2.2.2 Label-free detection

The cornerstones of life sciences research, pharmaceutical industry and medical diagnostics are the capabilities to investigate interactions among biomolecules, to observe activity and response of cells in the presence of different stimuli (e.g. drug molecules), and to detect analytes from bodily fluids, cell supernatants or at various stages of manufacturing processes. These tasks are enabled by the ability to perform biopharmaceutical, biochemical and cell-based assays in order to find out whether an analyte interacts with another, and if so, how strong the binding affinity is between the bio-molecular species. Furthermore, relevant questions are, for instance, what is the concentration of a biomarker for cancer within a patient's blood sample, what the chemical fingerprint of a certain biomarker is or how the physicochemical properties of the biomimetic or living environment are affected when drug molecules or drug carrier vehicles are introduced to the system. During the drug discovery and development process in the pharmaceutical industry, it is important to perform rigorous chemical characterization of the drug candidates in solid state as well as in dissolved state.

The development of technologies to meet the requirements mentioned above is ever-challenging, because the analytes in question can include small molecular drug compounds with molecular weights below 500 Da, DNA oligomers, peptides, enzymes, antibodies, and viral particles – in other words, the analytes can be exceedingly small and the measured concentrations in the range of fg/ml to pg/ml [90, 92]. Simultaneously, the samples can contain thousands of other molecules

at concentrations orders of magnitude greater or there are other distracting signals that hamper the detection of analytes, for example strong fluorescence background or non-specific binding events. Larger biochemical analytes such as bacteria, spores, cells, EVs or nano-sized drug carrier molecules are less difficult to observe – especially if they can be fluorescently labeled.

Overall, due to the difficulty in detecting biological and biopharmaceutical analytes using their intrinsic properties (e.g. mass, size, electrical impedance, dielectric permittivity), the methodology has relied upon attachment of a label to one or more of the molecules/viruses/cells/nanoparticles being studied. In general, the label is detected by its color or its ability to generate photons at a particular excitation wavelength and act as an indirect marker to indicate the presence of the analyte to which it has been attached. However, such treatments generally result in the death of the specimen or significant biological or chemical changes in the structures of the analytes [93]. In essence, label-based assays require a high degree of development to assure that the label itself does not block an important active site on the tagged molecule or modify the physicochemical properties of the molecules or particles. Particularly for sandwich-type assays, the washing conditions, blocking conditions, and exposure protocols for a range of reagents are needed. Moreover, labware for fluorescent assays must be constructed from non-auto-fluorescent materials, as unintentional background fluorescence can swamp the signals being measured.

Another challenge included in the use of labeling arises from the need to perform several thousands of individual measurements as in the biopharmaceutical discovery, for example, there is a need to perform a great number of assays in parallel in order to understand how molecular permutations affect the efficacy or safety of the potential drug candidate [94]. Thus, the cost of performing such assays regarding disposable labware, reagents, and personnel time must be considered with particular care. Lastly, the measured data must be translated into biologically relevant information efficiently, and thus the selection of a particular assay technology plays a significant role. Even though the range of technologies available is immense, it also brings about complexities; the choice of suitable reagents and instruments may require fundamental knowledge of the analytes beforehand. Hence, multiple trial-and-error efforts might be needed before the assay even starts functioning in an expected manner. Taking into account all the considerations above, there exists a notable need for the continuous research and development of label-free techniques and methods in the field of life sciences, for instance, biopharmaceutics and pharmaceutical industry. In particular, biophotonic methods allow for reducing the assay costs and complexity while providing more quantitative information with moderate high throughput capabilities [92].

2.2.3 Biophotonic label-free techniques in biomedicine

As the biosensor technology in general, biophotonic label-free detection generally involves a transducer capable of directly measuring certain physical property of the chemical compound, DNA, molecule, peptide, protein, virus, EV, cell, or drug carrier particle. For example, all biochemical molecules and cells have finite mass, volume, viscoelasticity, dielectric permittivity, and conductivity; these can be utilized to indicate their presence or absence using an appropriate technique and sensor. The sensor acts as a transducer that is capable of converting one or more of these physical properties into a quantifiable signal that can be collected by an appropriate instrument (e.g. current of voltage proportional to the surface-deposited mass or a photon diode detector). However, the question is not all about biosensors; label-free detection can also be performed using biophotonic spectroscopy techniques that allow for detection of absorbed or scattered light. Examples of such label-free techniques are infrared (IR) and Raman spectroscopy. These techniques are particularly practical when the measurement must be carried out without sensors or the amount of analyte is very low.

Overall, the experimental uncertainty generated by the effects of the label on molecular conformation, blocking of active binding sites, steric hindrance or inaccessibility of the labeled site itself can be overcome with label-free detection [93, 94]. Additionally, the complexity related to finding appropriate labels that function equivalently for all the molecules in a given experiment, can also be omitted. The time and effort required for the development of a robust assay are reduced and simplified, and the amount of experimental artefacts are decreased. At present, there are considerably many methods that allow direct detection of biological structures and biopharmaceutical compounds without *a priori* labeling. However, there are still limitations and cavities related to the current methodology; the instrumentation is considered non-user-friendly and costly, and data analysis steps are occasionally seen complicated. Furthermore, "thinking outside the box" has been lacking, and thus relying on the traditional formulas in the development of assays has been hampering the evolution of the field. In this context, Raman and SPR as biophotonic methods offer a wide array of opportunities in both directions; in the development of new instrumentation and revolutionary assays. It is also noteworthy that in the field of biopharmaceutics, the focus of development has to reside simultaneously in small and large analytes since such compounds and structures are practically always present in living systems. Thus, in this Thesis, small molecular drugs act as a conventional example of small-scale analytes under investigation, and liposomes and EVs as large-scale analytes of interest.

2.2.4 General theoretical overview of label-free optical biosensing

A biopharmaceutical small drug or a biological EV as an analyte – which are referred to as *analyte* in this text unless otherwise stated – have certain mass, a natural intrinsic property for label-free detection. Additionally, all molecules have the capability to interact with electromagnetic fields that pass through them because there are atoms with nuclei and a variety of electrons in different orbital states. Light is known to consist of an oscillating magnetic and electric fields perpendicular to each other. In essence, the electrons within molecules experience a force when exposed to the oscillating electromagnetic field associated with the propagation of light. Consequently, light's electromagnetic field will result in the polarization of the molecules with abundance of free electrons. This means that one side of the molecule will become temporarily more positively charged than the opposite side, and thus an electric dipole is formed. The extent of polarization may differ depending on the molecule; the size, shape and orientation with respect to the electric field determine the magnitude of polarization. A constant, *electric susceptibility,* X_e, quantifies the magnitude of a molecule's polarizability. Molecules with larger X_e are readily polarizable. Of importance, the Raman scattering phenomenon is fundamentally based on the concept of molecule's polarizability, which is more profoundly described in chapter "5.1 Physical principles of Raman spectroscopy".

A polarizable molecule set in an external electric field undergoes the described polarization, and the resulting dipole produces a secondary field. Finally, the resulting electric field (= the sum of the originally applied field and the secondary field) is of lower magnitude than that of the applied field. Furthermore, as the electromagnetic field related to light is varying with respect to time, the electrons within the molecule placed in that particular field experience a force that varies with respect to time. Thus, the electrons will oscillate within the molecule. By definition, moving electrons produce an electrical current. Hence, the molecule experiences a polarization current because of this motion of electrons. Subsequently, light travels more slowly through the molecule than it would through free space. Free space has a permittivity defined by the constant $\varepsilon_0 = 8.85 \times 10^{-12}$ F/m, and the permittivity of a dielectric material containing molecules is specified as $\varepsilon = \varepsilon_r \varepsilon_0$, where ε_r is known as the relative permittivity of the dielectric constant of the molecule. ε_r is related to the polarizability of the molecule since it is defined as $\varepsilon_r = 1 + X_e$.

The term refractive index (n), for one, is a more common physical quantity to describe a dielectric material. Generally, in an ordinary dielectric material at optical wavelengths, n is defined as n = ; the refractive index is directly related to the polarizability of the molecules within a dielectric material. It is worth pointing out that the refractive index is a quantity defined for a bulk material whereas the electric susceptibility and dielectric permittivity generally refer to individual molecules such as those adsorbed to optical biosensor surfaces. All the biological analytes (proteins, lipids, carbohydrates, cells, nucleic acids etc.) possess dielectric permittivity that is

larger than the dielectric permittivity of air and water. Such analytes are capable of hindering the propagation velocity of electromagnetic fields passing through them. The development of optical label-free biosensors relies on that physical principle; the biosensor simply must translate the change in propagation speed of the applied electromagnetic field, i.e. light, into a signal that is quantifiable and proportional to the amount of analyte deposited onto the sensor surface.

Notably, a common erroneous interpretation prevails in terms of what is actually measured by optical biosensors. Namely, typically the biosensor surface is covered with water molecules, and in the case of biological analytes associating to surfaces, some of the water molecules are superseded and substituted by the surface-associating analyte molecules. The analyte molecules, for one, are often easily polarized by the oscillating electromagnetic field of light. Consequently, the biosensor development must aim to find a suitable transducer element that possesses a measurable property that is altered by transitions in dielectric permittivity of the sensor surface. Thus, stringently taken, optical biosensors do not directly measure the mass of surface-deposited analytes but the changes in dielectric permittivity – however, such change is typically converted to change in surface concentration (or mass) of the adsorbed analytes. The changes in refractive properties of analytes at the biosensor surface and at the vicinity of the biosensor surface constitute the physical cornerstones of SPR, covered in more detail in chapter “6.1 Physical principles of SPR”.

Whether the incident light source is a laser, light-emitting diode or an incandescent light bulb, all of the introduced physical principles can be exploited in different spectroscopic and optical biosensing techniques. The mutual principle is to detect reflection, refraction, transmission and scattering phenomena as the samples are irradiated with light. In general, optical biosensors are affordable in terms of production since they can be engineered on glass or plastic surface instead of using e.g. etching or lithographic techniques that are often more complex and expensive. In addition, the optical biosensors are regarded as passive optical components; the alterations in properties of reflected/transmitted light are measured and the incident excitation light is delivered from external sources. The benefit is that the sensor does not deplete power, and measurable responses are achieved using relatively low irradiation. Lastly, the detection can be performed without making direct physical contact with the sensor or without prerequisites for electrical contacts – these features are definitely favorable for optical label-free biosensing.

3 BIOPHARMACEUTICAL RESEARCH WITH ITS NEW CHALLENGES

As of today, a number of varying definitions for "biopharmaceutical" exist [95]. Within the scope of this Thesis, the term "biopharmaceutical" includes, but is not restricted to biologics; it also covers the chemically synthetized pharmaceuticals, i.e. small drug molecules. "Biopharmaceutics", in this respect, refers to the scientific discipline concerned with the physicochemical properties of pharmaceuticals in relation to their bioavailability and pharmacokinetics. Furthermore, in this regard the liposomes and EVs are prominent biopharmaceutical particles for drug administration and diagnostics – representing larger scale of analytes in comparison to the conventional small molecular drugs in the field of biopharmaceutical research.

The physical and chemical characterization, interaction studies [96-99], and for instance, monitoring the morphological changes of drug compounds during the manufacturing process i.e. PAT are some of the important phases of biopharmaceutical drug research. Moreover, the number of Food and Drug Administration (FDA) approved nanoparticle-based drug preparations is relatively low; liposome-based formulations of drugs (Doxil, Ortho Biotech, Bridgewater, NJ, USA; DaunoXome, Gilead, Foster City, CA, USA), albumin-bound nanoparticles of paclitaxel (Abraxane, Abraxis BioScience, Schaumburg IL, USA), and products using nanocrystal technology (sirolimus (Rapamune), Wyeth Pharmaceuticals, Collegeville, PA, USA; Emend, Merck, Whitehouse Station, NJ, USA) [100, 101] are some of the few approved preparations. Recently, the bioequivalence guideline for liposome drug products was approved. In addition, the European Medicines Agency (EMA) is on the verge of adopting updated regulations in regards of novel nanotechnology-based formulations [102]. Thus, for instance extracellular vesicles provoke great interest as prospective "natural" drug carriers or diagnostic tools in the early-stage cancer detection [103, 104]. Spectroscopic techniques relying on the foundations of biophotonics have shown great potential in the aforementioned stages of biopharmaceutical drug discovery, development, industry processes, and diagnostics. Even though many of these techniques and methods are well established, the current pharmaceutical space is lacking novel approaches by which those techniques are implemented. The biopharmaceutical research and development has essentially stuck into two elements; there has not been a substantial driving force to develop (i) novel technology nor (ii) methodology (i.e. protocols relying on biophotonic technology) or (iii) data analysis techniques in order to pioneer uncharted venues. For example, Raman spectroscopy is still seen as an unnecessarily complex technique for real-life applications, and the versatile surface

plasmon resonance technique [105], traditionally considered highly applicable for analyte-ligand interaction with occasional issues with sensitivity [106], is not seen to offer much outside the interaction studies. However, there is much more to the picture than meets the eye.

3.1 SMALL DRUGS IN BIOPHARMACEUTICAL RESEARCH

Rational and successful drug discovery, development and further optimization is an extremely demanding process initiating from the potential candidate molecule screening, and further proceeding through *in vitro* testing phase to clinical trials [107-109]. Moreover, the journey does not end when the final drug preparation is released for the markets; the industry processes for large-scale drug production are constantly in need of optimization and better understanding of control over the various process parameters [110]. From the pharmaceutical perspective, small molecular drugs are conventional, orally administered drugs, e.g. as tablets or capsules. Christopher Lipinski's "rule of five" is one of the most well-known definitions for small molecular drugs [111-113]. It describes pharmaceutically relevant features for evaluating the potential and suitability of a molecule to act as an orally administered, therapeutically active compound. In brief, the molecule has to adhere at least three of the following properties: (i) it should not have more than 5 hydrogen bond donors, (ii) no more than 10 hydrogen bond acceptors, (iii) the upper limit of molecular mass is 500 Da, (iv) octanol-water partition coefficient log P not greater than 5. In fact, the physicochemical features described by the Lipinski's rule of five cover ~90% of the orally administered drugs in the market [112]. There also exists certain additions and specifications to the rule of five in order to enhance the applicability of the rule [114]. Importantly, the rule does not prefigure whether the molecule is pharmacologically active, but instead, it focuses on the pharmacokinetic properties of the molecule. Such properties affect greatly on the administration, distribution, metabolism and excretion (ADME) characteristics of the drug.

The pharmaceutical industry is on the verge of new era as personalized medicament and biological medicinal products (e.g. protein drugs that are copies or optimized relatives of endogenous human proteins [115]) are seen as the state-of-the-art preparations and attract special interest from the viewpoints of both, fundamental research and high-tech industry. However, conventional small molecular drugs are still the cornerstones of the pharmaceutical market. Regardless the increased proportion of biologics, for instance in 2015 33 new molecular entity (NME) approvals out of total 45 NME approvals were granted to small-molecule therapeutics by the FDA [116]. It is worth emphasizing that the trend of the FDA approvals in 2015 followed the tendencies observed during previous years [117].

The opportunities of biophotonic instruments and methods, in particular Raman spectroscopy and SPR for investigating small drugs are introduced in chapters “5 Raman spectroscopy” and “6 Surface plasmon resonance”, respectively.

4 NANOMEDICINE AND BIOPHOTONICS

In addition to conventional small drugs, researchers have increasingly been interested in the applications of nanomedicine. Nanomedicine is essentially a part of biomedicine, sometimes referred to as medical biology that implements biology and other natural sciences to clinical practice. The first research publications to use the term nanomedicine date back to the year 2000 [100]. Nanomedicine has been defined as a technology that utilizes molecular tools and knowledge of the human body for the purposes of medical diagnosis and treatment [118]. Another distinct and scientifically subtle definition emphasizes the physical effects taking place at the interface between molecular and macroscopic scale whereby quantum mechanics are of importance occurring in objects of nanoscale [119]. However, within the scope of this Thesis, nanomedicine is defined as the use of nanoscale or nanostructured materials in biomedicine. Their physicochemical structures have unparalleled medical effects, and as such are different from conventional small-molecule drugs. They may, for instance, have capability to cross biological barriers or are specifically targeted to certain types of cells or tissues. In essence, such medical effects are not constrained to size scale under 100 nm; although the strict physical definition of nanotechnology suggests to restrict the observations to particles within the range of 1-100 nm in diameter, the scale can be stretched up to 1000 nm. The justification for the size scale of 1-1000 nm is convenient since the better understanding of medical effects occurring in nanoscales requires new approaches from the viewpoint of manufacturing techniques, chemistry and physics. If the scale was stringently defined, essential features could be missed in the research and development of nanomedicines. However, a clear difference to small-molecule drugs is made; they are not specifically developed on the nanoscale to accomplish therapeutic effects that are in relation to their nanosize dimensions.

Nanotechnology has become a prominent tool in various disciplines – including biomedical science. For instance, targeted drug delivery carriers (DDC), for example liposomes, are intensively studied in order to gain comprehensive understanding of their safety and efficacy in biological surroundings [120] or to optimize and enhance their performance [121]. Furthermore, the nature and behavior of EVs hold promise for them to act as DDCs or diagnostic tools in nanomedical applications [104]. However, a prerequisite is rigorous knowledge of the chemistry, physics and biology involved in the interactions at the interfaces of nanoparticles (artificial or inherent) and living systems [1, 122]. It is to be noted that one of the fundamental problems in nanomedicine and –medication arise from the requirement for controllability and reproducibility of chemical reactions and interactions in the nanometer scale. The challenging goals of rational DDC design and other nanomedical needs can be met

by the strongly evolving field at the crossroad of nanoscience, biomedical research and optical science. The combination is also referred to as *bionanophotonics* [123]. In bionanophotonics, one of the challenges is the complex interaction of light and biological media, typically introducing a cascade of events. The interactions can evoke physical, chemical, thermal, and mechanical effects – or combinations of them. The development of label-free versatile instruments, probes and sensors can augment their applicability, and minimize the unwanted interferences with the native state of the analytes during the measurement or manipulation. In the following two chapters, liposomes and EVs, respectively, are introduced as important species from the perspective of nanomedicine. Consequently, from the standpoint of bionanophotonics, their investigation with Raman and SPR is dealt with in chapters "5 Raman spectroscopy" and "6 Surface plasmon resonance".

4.1 LIPOSOMES IN THE BIOPHARMACEUTICAL FIELD

Biophysicochemical laws apply to drug delivery carriers (DDCs) as well as essentially every foreign particle entering into the body. The transitions, exchange and excretion of external materials is effectively controlled by distinct physiological barriers. For instance, the endothelial cells of blood vessels are capable of halting the migration of potentially harmful compounds and particles [124]. Systemically administered drugs and nanocarriers are instantly recognized by the efficient barrier mechanism in blood circulation; the foreign compounds are marked with proteins via an opsonisation process [125], and consequently excreted from the systemic circulation by the mononuclear phagocyte system (MPS) [126]. The foreign nanoparticles are treated by a specific process whereby bloodstream proteins attach onto the surface of the particle before the phagocytes of the MPS system can recognize the invaders. The process is appreciated as the complement activation [127] or opsonisation [128]. Thus, the requirements for effective and safe DDCs are somewhat rigorous; first, upon administration, they must pass the endothelial vascular barrier, then evade the clearance processes of the immune system, and lastly, accumulate at the desired tissue in quantities that are adequate for the expected pharmacological efficacy. Notably, to some extent, the nanocarriers for controlled drug administration mimic the biophysicochemical properties of pathogenic particles; such particles strive to resolve exactly the same barriers that the DDCs encounter upon administration. Moreover, as denoted previously, EVs can act as model structures for the biomimetic, synthetic DDCs since they are constantly migrating throughout the aforementioned barriers.

The wide array of various DDCs consists of liposomes [129], dendrimers [130], carbon nanotubes [131], inorganic nanoparticles [132, 133], and polymer-based nanoparticles [134], for instance. One of the most pertinent nanotechnological tools

used in nanomedicine are liposomes [135, 136]. In fact, more than ten approved liposome-based drug formulations exist currently, and the research, development and clinical trials are continuously ongoing for new preparations to be launched [129]. In short, liposomes are membrane-delimited vesicles that are typically produced on hydration of dried phospholipids above their transition temperature [129, 137]. Three categories for liposome classification exist based on their size and the amount and type of lipid bilayers. Hence, the multilamellar vesicles are comprised of multiple lipid bilayers separated from each other by aqueous space. The multilamellar vesicles are relatively heterogeneous in size, typically ranging from few hundreds to thousands of nanometers in diameter. Furthermore, small (< 100 nm) unilamellar vesicles (SUVs) and large (> 100 nm) unilamellar vesicles (LUVs) compose of a single lipid bilayer constraining the inner, aqueous compartment of the liposome. When acting as DDCs, the drug molecules can be entrapped into the aqueous inner compartment of the vesicles or included into the lipid bilayers; this depends on the chemical and physical properties of the drug. Both hydrophobic and hydrophilic molecules can be incorporated. Of importance, the surface of liposomes is highly modifiable with various ligands and polymers for different purposes, which will be elucidated in the next chapter.

4.1.1 Conventional methods for studying liposomes

Biophysicochemical characteristics of liposome-based DDC determine their success in achieving the desired effects in the biological environment – simultaneously the safety of the nanocarrier must be ensured. Thus, relevant features in the rational liposome development are size, shape, deformability, surface charge, stability, and chemical composition [138]. Such properties affect the nanocarrier's capability to evade phagocytosis, determine the interactions with vasculature and traverse through cell membranes, and survive from endosomes before the drug degradation. Therefore, various experimental and computational methods are often needed for prosperous liposome design. Three distinguishable aims prevail in liposome engineering; to create a stealth shield against the MPS system, enable liposome targeting (passive [139] or active [140]), and in some instances, strive to optimize their performance (e.g. stability [141] or surface charge [142]). In brief, the purpose of stealth sheath is, in an optimal situation, to prevent unspecific protein binding and to block the complement activation cascade that may alter the biodistribution, decrease cellular uptake, and result in unwanted and rapid nanocarrier clearance from the systemic circulation in the body. By camouflaging the nanocarrier's foreign nature, its circulation time in the bloodstream can be increased. The prolonged circulation time, for one, can enhance the overall bioavailability, decrease the dose and dosing frequency, resulting to fewer side and adverse effects. The current gold standard for shielding the nanocarriers is the usage of polyethylene glycol (PEG) for

nanoparticle PEGylation [143, 144]. However, drawbacks of PEGylation have been demonstrated as it may induce immunological responses [145]. Additionally, trials to bioconjugate PEGylated nanocarriers with targeting ligands have shown that the overall controllability and reproducibility of the process may be difficult [146]. Since the use of PEG is not always unproblematic, substituting approaches are being charted [147, 148]. By using PEG alternatives, amended pharmacokinetic properties, enhanced stability and degradability can be accomplished. Biodegradable choices include polysialic acid (PSA), hydroxyethyl starch (HES), and polyglutamic acid (PGA). Examples of non-biodegradable alternatives are poly(carboxybetaine) (PCB), poly(N-hydroxypropyl)methacrylamide (pHPMA), and poly(vinylpyrrolidone) (PVP). Branched and comb-like alternatives for PEG could be poly(glycerol) (PG) or poly(poly(ethyleneglycol) p(PEGMA).

Of importance, several physicochemical components can be modified in the liposome design process [70]. Namely, (i) the liposome size and lamellarity can be tuned via the extrusion process, (ii) the phospholipid or synthetic phospholipid components for the liposome membrane bilayer can be chosen for optimal performance, (iii) surfactants or amphiphilic molecules (for instance cholesterol or ethanol) can be included, (iv) to produce the stealth sheath a subset of head groups of molecules in the membrane of the liposome can be functionalized, and (v) ligands for targeting purposes can be used. It is to be remembered that, all of the depicted nanocarrier properties can also be applied to rational development of EV-based targeted drug delivery carriers as well. In fact, the ongoing research within the field of DDCs constantly widens our knowledge of the nano-bio interfaces, and pioneers towards novel DDS applications. **Table 3** highlights the currently used methods and techniques that are used in liposome characterization and analysis. It is worth noticing, however, that the present toolbox for nanocarrier, and in particular, liposome characterization and modification still lacks complementary methods. Since labeling can induce considerable alterations to the biophysicochemical structures of the liposomes, particularly their lipid membranes, the properties of liposomes of interest may undergo significant changes. Consequently, such changes may bias the *in vitro* results, which often leads to problems during *in vivo* phase. In order to better bridge the gap between the significant amounts of papers published, and on the other hand, quite few actual breakthroughs in the form of actual approved drug formulations, especially novel label-free biological assays are needed. In this Thesis, such assays are appreciated as *bio-functional assays* where for example a new small drug candidate is tested in a biologically relevant *in vitro* environment – or interactions of DDCs and drugs with the living cell surfaces are investigated. In addition, the bio-functional assays can be complemented with computational simulations.

Table 3. Currently used methods and techniques for liposome characterization and analysis.

Method or Technique	Measured quantity or property	Reference
Fluorescence recovery after photobleaching	Characterizing membranes	[149]
Fluorescence resonant energy transfer (FRET)	Characterizing membranes	[150]
Dynamic light scattering (DLS)	Size and aggregation	[151]
Nanoparticle tracking analysis (NTA)	Size	[152]
ζ-potential measurements	Net electrical charge at the boundary between the hydrodynamic surface of the liposome and the dispersion media	[153]
Cryo-transmission electron microscopy (cryo-TEM)	Size, shape, dispersity, surface morphology	[154]
Nuclear magnetic resonance (NMR)	The arrangement of hydrocarbon chains in the liposome lipid bilayer. Lamellarity of liposomes.	[155]
Differential scanning calorimetry (DSC)	Phase transitions, partitioning and interactions of drugs, biomolecules, polymers and surfactants with liposomes	[156]
Isothermal titration calorimetry (ITC)	Phase transitions, partitioning and interactions of drugs, biomolecules, polymers and surfactants with liposomes	[157]
Langmuir film balance (LB)	Phase behavior, surface potential, and viscoelastic properties of lipid layers on an air-water interface	[158]
Brewster angle microscopy & imaging ellipsometry	Phase transitions in lipid layers on an air-water interface	[159, 160]
Quartz-crystal microbalance (QCM)	Phospholipid membranes and membrane interactions	[161, 162]
Surface plasmon resonance (SPR)	Phospholipid membranes and membrane interactions	[163]
Dual polarization interferometry (DPI)	Phospholipid membranes and membrane interactions	[164]
Attenuated total reflection Fourier transform infra-red spectroscopy (ATR-FTIR)	Bond vibrations; observing the structures of surface-adsorbed lipid bilayers and biomolecules in the presence of liposomes	[165]
Sum-frequency generation spectroscopy (SFG)	Revealing structural correlations between liposome lipid layer constituents and molecular dynamics in lipid layers	[166, 167]
Synchrotron small-angle X-ray scattering	Structural transitions	[168, 169]
X-ray & neutron reflectometry	Distribution of perpendicularly oriented molecules in lipid layers	[170, 171]

4.2 EXTRACELLULAR VESICLES: TERMS AND STRUCTURES

EVs are a group of membrane-bound, cell-derived biological nanoparticles. Varying definitions and nomenclature are abundant in the literature concerning the size characterization of these vesicles [104]. A common consensus prevails that exosomes are in the range of ~ 30-100 nm and microvesicles ~ 0.1-1 μm in diameter [172]. A single cell type can release both, exosomes and microvesicles [173, 174], and the circulating vesicle populations are evidently composed of exosomes and microvesicles. Still, one of the fundamental difficulties in the field of EV research is that the current isolation and purification methods do not fully guarantee that the exosomes and microvesicles can be discriminated, and their analysis is relatively laborious [175]. For instance, differences in size, morphology, buoyant density, and protein composition remains insufficient for legitimate distinction [176]. Unless otherwise stated, the term EVs is used herein to cover both of those subtypes to avoid confusion. In this respect, the focus is in introducing the extracellular vesicles as potential nanotechnological, bi-functional particles for the (i) diagnostic purposes as disease biomarkers and (ii) therapeutic purposes as drug delivery carriers. Consequently, as for the nanotechnological applications in general, biophotonics offers prospective tools for research in both of the abovementioned areas. A wealth of novel tools can be developed to meet the demands of physicochemical characterization of EVs, and their various interaction events with the surroundings – which can be highly modifiable biomimetic *in vitro* schemes.

Microvesicles are considered to originate by direct shedding from the plasma membrane whereas the exosomes stem from the inner compartments of the cells, released from the cells by multivesicular endosome (MVE) excretion processes by fusion of the MVEs with the plasma membrane [177]. Practically every cell type secretes EVs and thus, they can be found in a range of human body fluids; saliva [178], breast milk [179], plasma [180], urine [181], bile [182], and in cerebrospinal fluid [183]. In essence, EVs consist of a membrane evidently separating the inner compartment of the vesicles from the surrounding media. The membrane of EVs is similar to plasma membrane to some extent, in particular that of MVs, which are produced by direct shedding. However, since an important pathway of the biogenesis of EVs passes via an endosomal secretion, their membrane contents can be rather different from the plasma membrane [184]. The protein contents of EVs originating from a range of different sources have been analyzed for example using SDS-PAGE in combination with protein staining, immunoblotting, or proteomic analysis. It is important to note that in an optimal situation the EV samples are devoid of pollutants distracting the analysis; such pollutants can be serum proteins and protein components of intracellular compartments (e.g. endoplasmic reticulum or mitochondria). Due to the endosomal pathway of genesis, they carry membrane and transmembrane proteins such as tetraspanins (CD63, CD81, CD9) [185], heat

shock proteins (Hsp70 and Hsp90), and membrane fusion proteins (Annexins and Rabs) [186]. In addition, they are enriched in proteins associated with lipid rafts, including glycosylphospatidylinositol-anchored proteins and flotillins [187]. Contrary to plasma membrane, membranes of EVs originating from a variety of cells are abundant in cholesterol, sphingomyelin, and hexosylceramides whereas the proportion of phosphatidylcholine and phosphatidylethanolamine is lower [188, 189]. A natural corona structure is also found in the membranes of EVs, mainly consisting of various proteins [190]. Different cell types generate various types of EVs, and the discrepancies in their biochemical membrane contents may be related to their biological functions [104]. The interior of the vesicles is known to carry at least nucleic acids (DNA, RNA, siRNA, miRNA, noncoding RNAs) [191, 192] as well as various peptides, proteins and uptake/fusion machineries [190]. **Figure 3** illustrates the main structural components of an EV.

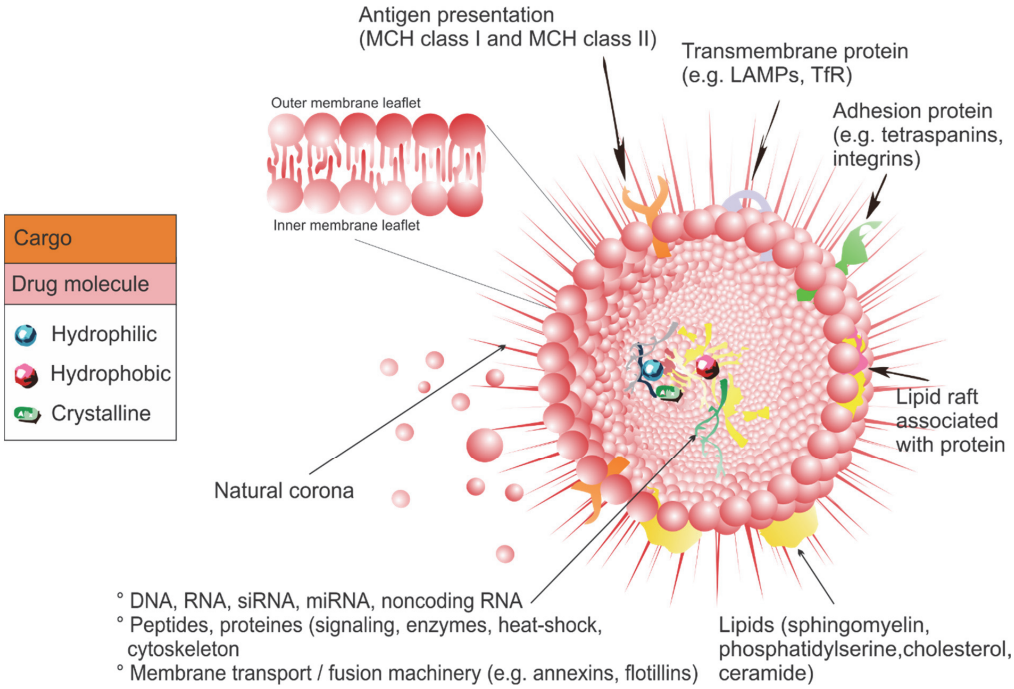

Figure 3. Visualization of an extracellular vesicle and the associated fundamental structures. The illustration also depicts a hypothesized role of the extracellular vesicles to act as targeted drug delivery vehicles when loaded with various drug molecules.

4.2.1 EV isolation and characterization techniques

The most common method for isolating EVs is to establish a cell line of interest in the cell culture, and recover the corresponding EVs from cell culture-conditioned media [175, 193, 194]. Witwer et al. introduced a detailed and rigorous overview on the isolation and characterization of EVs in 2013 [195]. In brief, the protocol for reticulocyte exosome purification from tissue culture-conditioned medium was developed by Johnstone et al. in 1987 [196], followed almost a decade later by the works of Raposo et al. and Zitvogel et al. [197, 198], and thoroughly described by Théry et al. in 2006 [175]. The protocol is based on differential centrifugation whereby the vesicles are sedimented by ultracentrifugation at 100 000 x g. It is noteworthy that the smallest vesicles – including exosomes, can be sedimented at this velocity. Instead of performing direct ultracentrifugation at 100 000 x g, larger vesicles are collected by consequently centrifuging at increasing velocities. There are also variants of this protocol that use e.g. higher speeds at 140 000 x g [199] or filtration steps in order to eliminate debris and larger vesicles [175]. Size-exclusion chromatography can be used to recover entities that are larger than 50 000 kDa, and thus discard soluble proteins [200]. Additionally, a number of protocols exist to isolate larger EVs, and are based on variants of centrifugation techniques, in general from lower speeds at 10 000 x g to 50 000 x g [201, 202]. However, caution is to be taken at any event since ultracentrifugation is not a "proper" purification; different EVs of similar size as well as protein aggregates can co-sediment at 100 000 x g. A method to separate membrane-enclosed vesicles from aggregated proteins is the exploitation of a sucrose gradient [197, 203]; the protein aggregates sediment through sucrose whereas the lipid-enriched EVs float upward to reach a position of equilibrium buoyant density. This method has also been tuned to purify EVs of clinical grade for therapeutic use [204]. The protocol defines a combination of filtration/concentration through a 500 kDa membrane and ultracentrifugation through a D_20/sucrose cushion in order to recover vesicles. Moreover, an immunoadsorption technique has been proposed and used for additional purification [187]. Recently, a variety of commercially available EV isolation kits have been introduced. The rationale for such kits is the opportunity to avoid somewhat arduous ultracentrifugation procedures, simultaneously providing easy and fast EV recovery. Heretofore the chemicals and reagents used in the kits are confidential but the presumed function lies on the foundations of polymer-based precipitation or immunocapture by antibody-coated beads. The use of polymers should precipitate a wider range of vesicles and the latter a more restricted scale of vesicles. However, the researchers working in the EV field are susceptive in relying on the isolation kits; first, up to this date, there are no thorough comparative studies addressing whether these novel tools are adequate or valid over the existing protocols and what types of vesicles they exactly precipitate. Secondly, such isolation approaches may fail to discriminate between EVs of different sizes and membrane-

free aggregates in the range of macromolecules. Thirdly, the reagents used in the isolation kits may contribute to the physicochemical nature of the vesicles, e.g. by coating the vesicles with synthetic chemical species of non-natural origin, and thus distorting the actual analysis. Overall, it is of utmost importance to take into account the described nuances between the different EV isolation methods in order to perform reproducible and rational EV assays. This minimizes the potential error sources arising from the isolation and purification steps.

Further characterization of EVs is typically performed using complementary biochemical methods, for example immunoblotting [205]. In addition, studies have been implemented to analyze the lipid [189, 206] and nucleic acid [191, 207] compositions of EVs. Mass spectrometry [208] and imaging techniques (e.g. confocal microscopy and electron microscopy (EM) [209]) are also widely applied techniques. In general, larger EVs are analyzed by conventional microscopy, and smaller sized EVs are deposited on electron microscopy grids as whole mount samples [197]. It is to be noted that the latter approach may result in EVs collapsing during drying, and consequently leading to cup-shaped vesicles. Thus, misinterpretations in terms of EV morphology are occasionally made. The cryo-electron microscopy performed for rapidly frozen and vitrified vesicles clearly shows the rounded shape of EVs [210]. Furthermore, atomic force microscopy (AFM) has been demonstrated as a feasible technique for EV size and morphology studies [211]. The advent of super resolution microscopy (SRM) has been introduced as a novel technique for imaging EVs beyond the diffraction limited threshold posed by conventional optical microscopes [212]. However, it has not yet been adopted as a standard EV characterization technique and more rigorous work is warranted for the widespread use of SRM. Up to this date, it remains to be demonstrated that single EVs can be detected by SRM.

The various microscopic techniques can be complemented with e.g. nanoparticle tracking analysis (NTA), which enables determination of the size distribution of EVs in the sample. NTA is based on the Brownian motion of EVs in suspension [213]. The drawback of NTA for determining the EV size distribution is that it is not capable of distinguishing a vesicle from a protein aggregate of similar size and the reproducibility of this technique is somewhat vague. A comprehensive guideline of using NTA instrument for EV analysis was published in 2013 by Gardiner et al. as an attempt to shape a framework for more reliable EV quantification and size-distribution analysis [214]. Flow cytometers can be used but the “resolution” (i.e. resolving between noise and vesicles) of the conventional setups is comparably low; EVs under the diameter of 300 nm cannot be distinguished. Therefore, a high-resolution method based on flow cytometry has been developed. In essence, the method can perform high-throughput analysis of single nanosized immunolabeled vesicles [215, 216]. However, the drawback is the use of fluorescent labeling of vesicles by lipid dyes; label-free methodology is in demand also for the EV characterization. Heretofore it is evident that EV analysis is not limited to a specific technique –

instead, multiple methods are typically needed. Raman [217, 218] and SPR [219] have been successfully implemented for EV characterization. However, they are still somewhat underused methods. Raman spectroscopy can offer fundamental information on the chemical contents of EVs, especially when used with rigorous spectral data analysis methods. SPR, for one, may provide opportunities to assess for example kinetic properties of given types of EVs, or to characterize the biolayers that are formed during EV adsorption onto a functionalized sensor surface. **Table 4** shows a summary of the abovementioned methods and techniques for studying and characterizing EVs.

Table 4. Currently used methods and techniques for studying and characterizing EVs.

Method or Technique	Measured quantity or property	Reference
Immunoblotting	Characterizing protein contents	[205]
Liquid chromatography with tandem mass spectrometry (LC-MS)	Proteomic analysis	[208, 209]
Confocal microscopy	Size and morphology, cellular uptake	[209]
Electron microscopy (e.g. TEM, cryo-TEM)	Size and morphology	[197, 210]
Atomic force microscopy (AFM)	Size and morphology	[211]
Nanoparticle tracking analysis (NTA)	Quantification and size distribution	[213, 214]
Flow cytometry, "high-resolution" cytometry	Quantification and size distribution	[215, 216]
Lipid analysis; hydrophilic interaction liquid chromatography (HILIC), mass spectrometry, reverse phase chromatography	Characterizing lipid contents	[189]
Sequencing techniques, e.g. PCR	Characterizing nucleic acid contents	[191, 207]
Raman spectroscopy	Analysis of the chemical composition	[217, 218]
Surface plasmon resonance	Immunoassay for protein profiling	[219]

Today, the EV research is still in urgent need of reliable and reproducible protocols in order to isolate and characterize EVs. In general, each new technique must be validated for any cell type or biological fluid of interest as a source of EVs to confirm the identity of purified EVs. Furthermore, several methods and often laborious steps are needed to resolve their physical, biochemical and morphological characteristics.

4.2.2 Extracellular vesicles in nanomedicine

EVs have an ever-increasing significance to act as potential diagnostic biomarkers, nano-sized drug delivery carriers (DDC), and mediators in intercellular communication [104]. In the broad sense the true biomedical relevance of EVs

has been unrevealed during the recent two decades. In general, almost every cell type – malignant and healthy, releases nanosized EVs in the extracellular space and thereafter to blood circulation. Migration of EVs between different compartments of the biological system is typically a continuous, dynamic movement affected by complex biochemical and biophysical pathways. Hence, EVs take part in various biological phenomena, for example intercellular communication related to the immune system, inflammation events and regeneration of tissues.

In addition to mediating targeted intercellular communication under physiological [220] conditions, EVs also play a significant role in pathophysiological circumstances; they have been observed to have functions in various types of cancers [221], asthma and allergic conditions [222], as well as neurodegenerative diseases [223]. It is worthwhile pointing out that although EVs are present in the bodily fluids of healthy and diseased individuals, e.g. the concentration and biomolecular compositions of EVs have been detected to undergone alterations in the state of disease [224]. Detection of such alterations with enhanced specificity, sensitivity and reproducibility warrants for development of novel techniques and data analysis methods. Furthermore, according to their biophysical characteristics, EVs hold potential to act as therapeutic agents in immune therapy, vaccines, drug-delivery carriers (DDCs) and regenerative medicine [172, 225]. Examples of EVs as disease biomarkers and therapeutic agents are provided within the next two chapters. Of importance, whichever of the two mentioned purposes is pursued, there is a clear need to better understand the complex structures and biological pathways of EVs in living systems since the already existing methodology has several limitations in terms of quantification accuracy, for instance [214].

4.2.3 EVs as disease biomarkers

The disease biomarkers represent an unmet clinical challenge, not only for different types of cancer but other human diseases as well. As EVs are found in every bodily fluid, they offer unequaled opportunities for early detection of cancers, neurodegenerative diseases, infectious diseases, autoimmune diseases, and other malignant states [104]. The cancerous tumor cells have been observed to produce EVs that carry a tumor-specific molecular fingerprint [103]. The EVs can carry a certain biomarker in their chemical composition, e.g. levels of plasmatic caveolin-1 and CD63-positive EVs were increased in the samples of melanoma patients [226] and glypican-1 –positive EVs were distinguishable in the serum of pancreatic cancer [227]. In general, even the elevated levels of EV concentration might have clinical relevance as indicating the status of the patient; as the gastro-intestinal stromal tumor was treated with imatinib, the concentration of EVs before the treatment was higher compared to the control [228]. Interestingly, EV-associated heat shock protein (HSP60) levels were decreased among colon cancer patients as the

tumor was surgically removed [229]. EVs have also acted as tumor biomarkers in glioblastoma (diagnosis; cancer biomarkers mRNA, miRNA, angiogenic proteins / early diagnosis; cancer biomarkers RNU6-1, miR-320, miR-574-3p) [230, 231], gastric cancer (prognosis; cancer biomarkers miR-21, miR1225-5p) [232], ovarian cancer (prognosis/therapy follow up; cancer biomarkers TGFB1 and MAGE3/6) [233], and bladder cancer (diagnosis; cancer biomarker TACSTD2) [234]. In addition to plasma and serum as sources for EVs, other body biofluids such as gastric juice, may be exploited for noninvasive (an example of liquid biopsy) and information-rich sources for cancer diagnosis or monitoring patient's status [232]. Furthermore, bronchoalveolar lavage, nasal lavage fluid and urinary EVs can be used as sources of biomarkers [235-237]. Notably, the EVs isolated from urine are considered as stable as the EVs from other body fluids, and the molecular composition of urinary EVs may reflect the pathophysiological status of the system – which extends the usability of urinary EVs to diagnosis of kidney injury or diabetic neuropathy [220].

Neurodegenerative diseases such as Alzheimer's disease (AD), Parkinson's, and amyotrophic lateral sclerosis have all been connected with various neurological diseases [238]. This is not particularly surprising since the central nervous system (CNS) neural and non-neural cells produce EVs, and consequently release them to biological fluids, blood and cerebrospinal fluid (CSF), among the others. Thereby the EVs originating from CNS hold extensive potential for carrying notable amount of biochemical information, and thus reporting of various disorders in the CNS. In particular, according to current knowledge, the complex pathogenesis of AD is characterized by the release and presence of neurotoxic protein species, amyloid peptides (Aβ) [239]. Aβ peptides are intrinsically disordered and have tendency to undergo a dynamic aggregation pattern [240]. Such pattern can ultimately result in deposited Aβ plaques in the brain. Interestingly, the researchers have observed that the Aβ peptides are released in association with EVs, and demonstrated that such EVs contain Aβ peptides. This, in turn, can facilitate the deposition of peptides into detrimental amyloid plaques or participate in the long-range transport of Aβ peptides [241]. However, the neuroprotective role of EVs has also been suggested in the form of clearance of amyloids [242, 243].

As the knowledge of EVs in parasitic diseases evolves, they can be used as biomarkers for infectious diseases [172]. Viruses, bacteria, fungi, protozoa, and helminths all generate EVs, and prions have been perceived in EVs [244, 245]. The roles of EVs in infectious diseases are many-faced; for instance HIV-1 and hepatitis C and A viruses can exploit EVs for altering the host cell or for transporting themselves into the host cells. Furthermore, infectious species may use EVs in order to spread infection by aiding the movement of infectious materials, and by escaping the host's immune system response [246]. Lastly, EVs have been recognized to contribute to several autoimmune diseases, for example Behcet's disease (BD),

a complex multiorgan inflammatory condition [247] and autosomal dominant polycystic kidney disease (ADPPKD) whereby the changes of surface glycosylation of urinary EVs were detected [248].

4.2.4 EVs as therapeutic agents

An intriguing question whether EVs could be used as therapeutic agents, has arisen. The answer is definitely affirmative; in fact, EVs have abundantly favorable physicochemical features to overcome the prevailing difficulties related to synthetic nanoparticles, e.g. unwanted provoking of the immune system [144]. In addition, EVs could be used as a biomimetic model system for the synthetic particles, i.e. their biochemical composition could be mimicked in order to achieve less adverse effects when administered to blood circulation as targeted drug delivery carriers, for instance [249-251]. However, further studies are warranted in order to show whether the "biomimetic synthetic EVs" could provide similar efficacy and safety as purified EVs from naturally secreted sources.

Initially the EVs isolated from B-cells were observed to convey MHC-peptide complexes on the surfaces of their membranes, thereby capable of exerting T-cell stimulatory functions [197]. Consequently, EVs originating from dendritic cells (DCs) were pulsed with tumor antigens, and they were seen to intercede antitumor responses [198]. Thus, EVs as vaccines for antitumor therapy have been introduced [252]. Furthermore, a similar approach has later been adopted to develop infectious disease vaccination by using EVs from DCs pulsed with infectious pathogens such as fungi, bacteria or parasitic protozoa [253]. EV therapies have also been considered as potential for treating various autoimmune, chronic, and acute inflammatory disorders, for example rheumatoid arthritis, inflammation of connective and vascular tissues, intestinal chronic inflammatory diseases, Crohn's disease, type I diabetes, and multiple sclerosis [225]. Moreover, regenerative therapies could benefit from the use of EV-mediated therapies; for instance myocardial infarction, ischemic stroke, acute and chronic kidney failure, drug-induced liver injury, and perinatal asphyxia.

EVs offer a potential alternative – or complement, to existing nanocarriers used in targeted delivery of drugs [254, 255]. Namely, the most used drug-delivery platforms to date are the liposomes or lipid-based nanoparticles (LNPs) [256]. Although effective, demonstrated to hold feasibility and safety, cavities in using LNPs still exist to a wide extent. For instance, their potential toxicity and immunogenicity can be troublesome. Their constrained ability to penetrate into organs and tissues may pose a problem in terms of their bioavailability. Therefore, there exists an undisputable need for new drug delivery carriers. EVs have been used for instance to dispense exogenous drugs (small molecules, miRNAs, and siRNAs) [257] and catalase, an exogenous protein to concede neuroprotection Parkinson's disease models [258].

A recently introduced approach dealt with the concept of developing biomimetic nanoparticles by functionalizing EV-sized PLGA (poly (lactic-*co*-glycolic acid) gold or silicon nanoparticles with cellular plasma membranes derived from cancer cell membranes. Profitable immune responses for vaccination [259], enhanced circulation times to avoid immune uptake, and increasing cancer cell specificity were observed [260]. In conclusion, the experts in the EV field are constantly searching for novel techniques and methods to reveal the multi-dimensional opportunities that EVs possess for the purposes of modern biomarker diagnostics and therapeutic use as DDCs. Creative development of biophotonic methods for the EV research can open up new venues to meet these demands.

Thus far small molecular drugs have been introduced as small-scale analytes whereas liposomes and EVs have been represented as larger, nanomedical analytes. Intriguing questions that merit for further studies are for example related to the development of *bio-functional* assays to improve the mechanistic understanding of small drug behavior in real biological environment, or to better predict the nanocarrier interactions with its surroundings in a living system. Biophotonics offers a wide variety of choices and technical advantages to counter the still unmet diagnostic and therapeutic challenges in the fields of small drug and nanocarrier research for biopharmaceutical applications. Thereby, biophotonic techniques and methods based on Raman and SPR are discussed next in more detail, and their current application to the analytes of small and larger scale is represented – as well as the cavities existing in present research. **Figure 4** summarizes the above discussed DDC and EV routes and interactions in biological environment. Of importance, the displayed events are also relevant from the viewpoint of bionanophotonics – and in particular, the illustrated phenomena are examples where biophotonic methods can be efficiently applied. The drug release from the DDC [261, 262] or EV interactions with living cells can be measured, for instance.

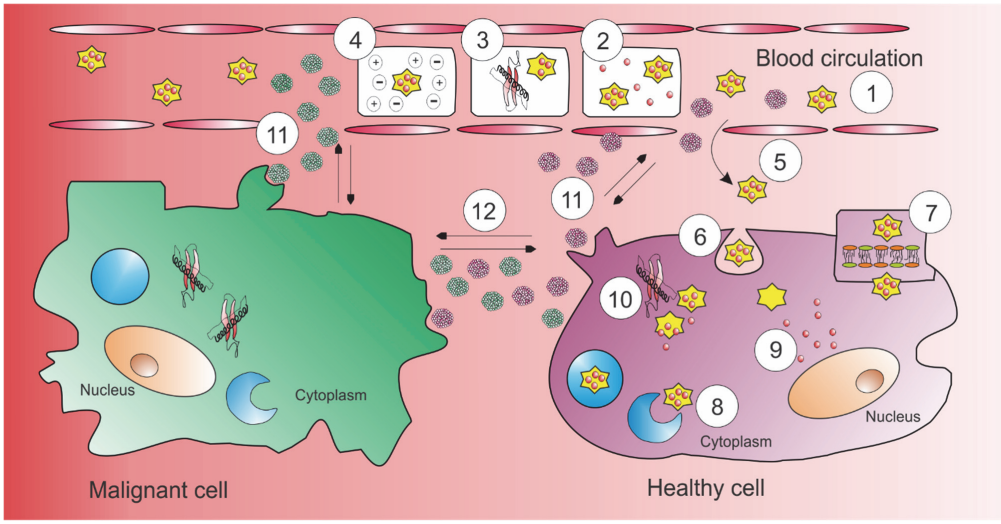

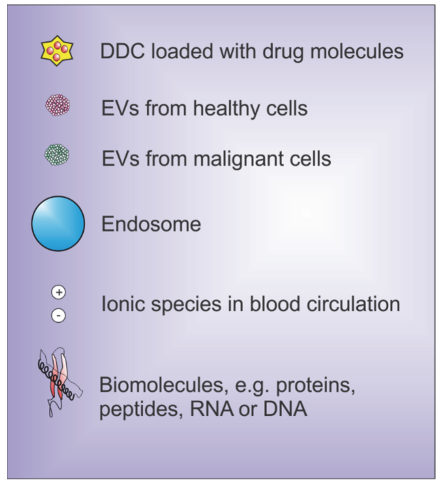

Figure 4. Events and pathways of DDCs and EVs in living system. (1) The DDC is administered into the blood circulation. (2) Vital phase in the DDC development is the stability of the drug-carrier system; if it is not stable, unwanted events, e.g. accidental drug release can occur before the DDC reaches its target. The possible interactions of DDC with (3) other biomolecules or (4) ions in blood circulation have to be investigated *in vitro* during the DDC development and optimization; in this regard the surface functionalization of DDC plays a major role. Another crucial step in the DDC surface modification concerns the DDC entrance into the extracellular space (5). Hence, the carrier has to be capable of penetrating between (or through) the capillary membranes at certain expedition simultaneously retaining the physicochemical stability of the carrier despite the changes of e.g. pH. The interactions at the interface of the target cell membrane and DDC determines whether the DDC can be taken up into the cell; two major pathways are (6) penetration through the cell lipid bilayer membrane via endocytosis or (7) directly through the plasma membrane. If the DDC internalizes via endocytosis, the nanocarrier has to be discharged from the endosome (8). In order to function in cytoplasm or nucleus, the active drug compound must be released from the nanocarrier (9); this can also be regulated by the biomolecules present in the intracellular space (10). (11) EVs are released from both; malignant and healthy cells. Dynamic migration of EVs from cells to blood circulation and vice versa is continually ongoing. It is noteworthy that the biochemical features in the membrane structures of EVs possess characteristics that form the basis of the relevance to act as disease biomarkers. (12) EV-mediated intercellular communication between the cells (healthy-healthy and malignant-healthy) have been observed as well.

5 RAMAN SPECTROSCOPY

All analytes, whether small molecular drugs or larger scale biological specimen, behave like any bulk medium in which light propagation induces absorption, scattering, refraction and reflection. These processes are depicted in **Figure 1**. However, probably the most emphasized effect is scattering. In biophotonics and spectroscopy the high scattering of samples of interest are exploited vastly. For instance, a biological sample typically consists of a turbid medium, and the solid-state samples have various solid-state forms, e.g. crystalline, amorphous, polymorphic forms. Therefore, the turbidity or apparent non-transparency of samples causes multiple scattering processes from excessively heterogeneous structures. Furthermore, the scattering results in spreading of a collimated light beam, e.g. laser beam, leading to a loss of its initial direction and defocusing of the light beam spot. **Figure 5** represents the important scattering processes; Mie, Rayleigh, Brillouin and Raman scattering.

Raman spectroscopy belongs to the group of vibrational spectroscopy techniques; other common techniques in the same group are mid-infrared (IR) and near-IR spectroscopy. Essentially, mid-IR and Raman are utilized to provide information of molecule's characteristic fundamental vibrations. Those vibrational states, for one, are highly specific for a given molecule and its chemical structures. Vibrational spectroscopy can be employed to investigate thin films and nanostructures as well as samples in bulk quantities. Furthermore, the types of measurable samples can vary over a wide array of possibilities, and assays can be carried out from fast and straightforward identification to rigorous full-spectrum analysis. In addition, Raman spectroscopy is easily applicable for both qualitative and quantitative studies. Raman and mid-IR are complementary techniques with one physically profound difference related to the way in which the incident photon energy changes the vibrational states of the analyzed molecule. Namely, in mid-IR spectroscopy radiation is absorbed into the sample changing the molecular vibrational energy states. Importantly, in IR spectroscopy one observes a resonance condition where an electric dipole moment mediated transition takes place between vibrational energy levels while Raman is a two-photon inelastic scattering phenomenon. Raman spectroscopy, in general, elucidates excellently symmetric vibrations of non-polar groups whereas IR is best at showing the asymmetric vibrations of polar groups.

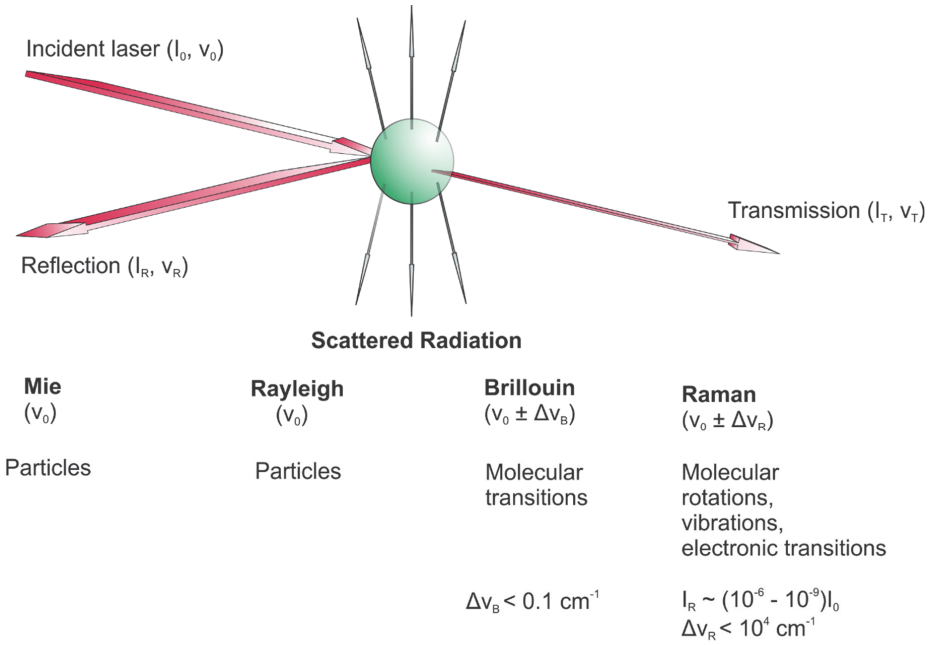

Figure 5. An illustration of the different scattering processes induced by the incident irradiation, for example laser light.

5.1 GENERAL THEORETICAL OVERVIEW OF RAMAN SPECTROSCOPY

Raman scattering was first hypothesized by Smekai in 1923. The first experimental observations were made in 1928 by Raman and Krishnan [263]. In essence, Raman scattering is seen as the change in frequency for a small percentage of the intensity in a monochromatic light beam as the result of coupling between the incident radiation and vibrational energy levels of molecules. A vibrational mode of the molecule will be Raman active only if the polarizability of the molecule undergoes a change.

When monochromatic radiation with a wavenumber $\overline{\nu}_0$ is incident on systems, most of it is transmitted without change. However, scattering of the radiation occurs as well. When the frequency content of the scattered radiation is analyzed, there will be the wavenumber $\overline{\nu}_0$ associated with the incident radiation. In addition, pairs of new wavenumbers of the type $\overline{\nu}_0' = \overline{\nu}_0' \pm \overline{\nu}_M$ are observed. Particularly the wavenumbers $\overline{\nu}_M$ are found in molecular systems to reside typically in the ranges associated with transitions between rotational, vibrational, and electronic levels; this scattering of radiation is the cornerstone of the Raman scattering phenomenon. Essentially, the normal modes of vibration can be explained by using vibrating mechanical models [264]. Today, Raman spectroscopy is a widely exploited

technique in order to investigate the vibrational structures of molecules of interest – and as such, highly applicable to biophotonics and biopharmaceutical studies. Infrared (IR) spectroscopy is occasionally used as a complementary technique for Raman [265].

The rigorous mathematical treatment of the theory of Raman scattering is profoundly described elsewhere [265-267]. In brief, the Raman scattering can be described using *classical theory* or *quantum mechanical* treatment. The origin of the modified frequencies found in Raman scattering is explained by the energy transfer, which occurs between the scattering system and the incident radiation (sometimes referred to as excitation radiation). When a system interacts with radiation of wavenumber $\overline{\nu_0}$ it makes an upward transition from a lower energy level E_1 to an upper energy level E_2. It must then acquire the necessary energy, $\Delta E = E_2 - E_1$, from the incident radiation. Hence, the energy ΔE can be expressed with regards to a wavenumber $\bar{\nu}_M$ connected with the two mentioned energy levels:

$$\Delta E = hc\bar{\nu}_M \quad (1)$$

The above stated energy consists of the absorption of one photon of the incident radiation energy $hc\bar{\nu}_0$ and the simultaneous emission of a photon of smaller energy $hc(\overline{\nu_0} - \bar{\nu}_M)$, thus the scattering of radiation of lower wavenumber, $\overline{\nu_0} - \bar{\nu}_M$, takes place. Alternatively, interaction of radiation with the molecule may cause a transition from higher energy level E_2 to a lower level E_1, in which case the emission of a photon of higher energy can be expressed as $hc(\overline{\nu_0} + \bar{\nu}_M)$, and the scattering at higher wavenumber $\overline{\nu_0} + \bar{\nu}_M$, occurs. Rayleigh scattering, for one, has no resultant change in the energy state of the system; a photon of the same energy as the incident one is simultaneously emitted. Therefore, in the Rayleigh scattering the unchanged wavenumber, $\overline{\nu_0}$, is observed.

On a conceptual level, a Raman band in the Raman spectrum is not characterized by its absolute wavenumber (i.e. $\overline{\nu_0}' = \overline{\nu_0}' \pm \bar{\nu}_M$). Instead, it is characterized by the magnitude of the shift of its wavenumber $\bar{\nu}_M$ from the incident wavenumber. The corresponding $\bar{\nu}_M$ are typically referred to as Raman wavenumbers. In general, $\bar{\nu}_M$ is positive for Stokes and negative for anti-Stokes scattering. The different scattering processes and infrared absorption phenomenon are displayed in **Figure 6**.

In the classical theory of electromagnetic radiation, electric and magnetic fields oscillating at a given frequency are capable of giving out electromagnetic radiation that is of the same frequency. The electromagnetic radiation theory can be utilized in order to explain the light scattering phenomena. In short, for the majority of systems of interest, only the induced electric dipole moment μ is taken into account. A power series can be used to express a dipole moment induced by an electric field E:

$$\mu = \mu^{(1)} + \mu^{(2)} + \mu^{(3)} + \ldots \quad (2)$$

where

$$\mu^{(1)} = \alpha * E \quad (3)$$

$$\mu^{(2)} = \frac{1}{2} \beta * EE \quad (4)$$

$$\mu^{(3)} = \frac{1}{6} \gamma * EEE \quad (5)$$

In essence, α is called the polarizability tensor; it is a second-rank tensor having all the components in the unit of $CV^{-1}m^2$. Typically, for components α, β, and γ the orders of magnitude are $\alpha \sim 10^{-40}$ $CV^{-1}m^2$, $\beta \sim 10^{-50}$ $CV^{-2}m^3$, and $\gamma \sim 10^{-61}$ $CV^{-3}m^4$. Thus, the contributions of $\mu^{(2)}$ and $\mu^{(3)}$ can be recognized as negligible unless the electric field is extremely high. Furthermore, since Rayleigh and Raman scattering are observed with very much lower electric field intensities, those can be explained in terms of $\mu^{(1)}$. When the interaction of a molecular system is considered to occur with the harmonically oscillating electric field in the frequency ω_o, and for simplicity, only the vibrational part is taken into account, the variation of components in polarizability tensor with vibrational coordinates can be expressed using Taylor series. The fundamental mathematical treatment is omitted as being out of the scope of this Thesis. The rigorous explanation is provided for example in [265-267]. However, the outcome of these mathematical calculations yield a very practical qualitative description for the Rayleigh and Raman scattering in terms of classical radiation theories. The Rayleigh scattering emerges from the dipole oscillating at ω_o induced by the electric field of the incident radiation at frequency ω_o. Raman scattering stems from the dipole moment oscillating at $\omega_o \pm \omega_k$, which is produced by the modulation of the dipole oscillating at ω_o with molecular vibration ω_k. In practice this means that the observed frequencies in Raman scattering are beat frequencies of the radiation frequency ω_o and the molecular vibration frequency ω_k.

The quantum mechanical approach for Raman scattering is based on the radiation, which is emitted or absorbed as a result of a system making an upward or downward transition between two discrete energy levels; the energy levels are considered quantized. Thus, a quantum mechanical treatment of spectroscopic processes treat the radiation and molecule together as an entity or system, and investigate how energy is transferred between the incident radiation and the molecule as a result of their interaction. A transition between energy levels of a molecular system occurs with the emission or absorption of radiation, given that, a transition moment associated with the initial and final molecular states is different from zero. The vibrational transition polarizability components used in the quantum mechanical treatment of Raman scattering establish better basis for

defining selection rules for vibrational transitions in Raman effect compared to the derived polarizability tensor components used in the classical treatment – which is considered as the overall benefit of relying on the quantum mechanical treatment, especially within the context of profound theoretical approaches.

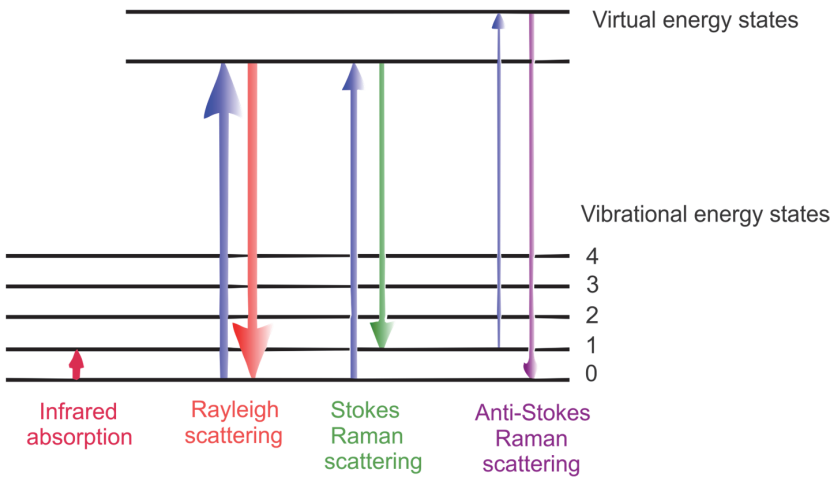

Figure 6. An energy level schematic for (i) Infrared absorption, (ii) Rayleigh scattering, (iii) Stokes Raman scattering, and (iv) Anti-Stokes Raman scattering.

5.1.1 Raman instrumentation

In Raman spectroscopy the emitted light from the sample is collected and focused onto a device capable of separating the light into distinct wavelengths. Two most commonly used such devices are monochromators in dispersive instruments and interferometers used in Fourier transform (FT) instruments [268]. Currently Raman instruments mainly consist of both grating-based systems using multi-channel detectors and interferometer-based (FT-Raman) spectrometers. A couple of decades passed after the first observations of Raman phenomenon before powerful enough excitation lasers and sensitive detectors (photo multipliers) were introduced. Still, hindrances were caused by bulky, non-practical instruments, and the range of analyzable samples was rather limited. A technique that was almost deemed inadequate, however, underwent a complete resurgence in the '90s. The most significant technical outreaches were multilayered dielectric filters that were manufactured using dichroic glass and extremely sensitive charge coupled device (CCD) detectors. Simultaneously affordable low-power irradiation lasers (~ 1-10 mW) became more common and also hardware speed and performance were increasing almost exponentially. Finally, the opportunity to couple for example

scanning electron microscopies (SEM) or confocal microscopies to Raman instruments accelerated the popularity of Raman systems.

Optical micromanipulation of biological specimens by laser light provides an intriguing concept for utilizing Raman spectroscopy. Such techniques are known as optical tweezers or optical traps [61]. Essentially, it means that an accurately focused continuous-wave (CW) laser beam is used to trap noninvasively single biological particles, and acquiring Raman spectra of the trapped particles. The working principle is based on the gradient force that is derived from the change in the momentum of light. Typically, the laser beam wavelength (usually 1064 nm from NdYaG) is chosen from the optical transparency region of the particle to avoid absorption of light. The trapped samples can vary from DNA molecules through subcellular organelles to whole cells. Another motives for laser micromanipulation may be for example to measure almost negligible forces present in biological systems [269] (i.e. in the order of piconewtons) or mechanically unzip DNA strands by trapping and stretching them [270].

5.1.2 Data analysis techniques in Raman spectroscopy

The vibrational energy levels are unique to each molecule, and thus Raman (and mid-IR, if used as a complementary technique) spectrum provides a fingerprint of the molecule. In Raman spectrum the vibrational bands are discriminated and characterized by three main components; their (i) frequency (i.e. energy), (ii) intensity (polar character of the molecule or simply polarizability), and (iii) band shape (the physical environment of chemical bonds). Importantly, the frequencies of molecular vibrations depend on the masses of the atoms that form the molecule, geometric arrangement of the atoms, and strength of the chemical bonds. All in all, the spectra can be appreciated as a window to the molecular structure, dynamics, and molecule's environment. Typically two distinct approaches are used in the spectra interpretation and subsequently, determination of molecular structures. Group theory in combination with mathematical calculations is used to interpret the forms and frequencies of molecular vibrations whereas empirical characteristic frequencies are used for determining the presence (or sometimes absence) of chemical functional groups. It is worthwhile pointing out that many empirically found group frequencies have been explained and elaborated using the mathematical theoretical approach – thus, the two mentioned principles are often used together.

Another important part of Raman spectroscopy is the raw data processing. After the Raman spectra have been experimentally acquired, the collected spectral data has to be processed in a way that relevant Raman spectral signatures can be revealed. Sometimes simple means are enough but occasionally somewhat rigorous algorithms and effort are needed to carry out further analysis. Some of the commonly used methods are described next.

In order to compare different spectra, generally the first step in the data processing is the background subtraction and Raman signal normalization. The background can be due to photoluminescent phenomena occurring simultaneously with Raman scattering or noise in the measurement instrumentation. Often the photoluminescent background spectrum – which typically is generated by fluorescence, is laborious to measure separately since the fluorescent components in the sample can be very difficult to separate physically. Thus, a straightforward subtraction is out of the question. The background subtraction can be accomplished by assuming that the whole spectrum is a combination of Raman bands and a slowly varying background that can be represented by a 3^{rd} or 4^{th} order polynomial. Subsequently, the background shape for the subtraction can be defined by choosing e.g. 4-5 reproducible anchor points in the "valleys" of the whole spectrum where the Raman contribution is minimal and the background dominates. Lastly, the determined background is subtracted from the whole spectrum. However, variation and arbitrariness can be manifested by the described "manual" background subtraction, mainly due to the choice of anchor points. Therefore more robust and reproducible automated methods have been introduced [271]. The benefit of using such algorithms is not only the robustness but also the high modifiability by e.g. MATLAB programming language. Moreover, possibly a more accurate background subtraction method at the expense of increased experimental complexity is known as shifted Raman spectroscopy [272]. The method is based on the physical fact that the Raman spectra peaks are prone to shifting due to small changes in the excitation wavelength. On the other hand, the fluorescent background is left practically unchanged because fluorescence emission spectra generally consist of broad spectral features, and they are not sensitive to subtle changes in the incident wavelength.

Once the spectra have been background subtracted and normalized, a meaningful approach has to be employed for finding out spectral variation between the collected spectra, and thus identify the physical and chemical components that may contribute to those variations. In general it may be useful to determine first, how much spectral variation exists between the samples of the same type. Such an estimate can be performed by recording e.g. 10 spectra from one single sample (e.g. sample type I) and consequently measuring 10 spectra from that same sample type I by picking randomly the samples for the latter measurement. Next, the relative variation of both measurements can be calculated by dividing the standard deviation (SD) by the mean, and finally, determining the ratio of the relative variations. This approach will roughly outline whether the sample types (e.g. type I, type II, type III, type IV) are inherently homogeneous and it would thus be realistic to discriminate between different samples; essentially if the described ratio resides approximately between 1-1.5 throughout the spectrum. For clarity, the calculation is displayed below:

$$\frac{SD\ of\ n_{spectra\_type\_I\_single}}{Mean\ of\ n_{spectra\_type\_I\_single}} : \frac{SD\ of\ n_{spectra\_type\_I\_random}}{Mean\ of\ n_{spectra\_type\_I\_random}} \quad (6)$$

In order to compare different sample types against each other, a relatively straightforward method is to subtract the means of two sets of spectra (e.g. sample type I and type II), and subsequently calculate the SD for that difference (it should be noted that it is the SD for the difference of means, i.e. not the SD of different sample types). Regions where the differences in the means are considerably bigger than ± 1 SD are feasible to have real biochemical differences.

The measured spectra can also be analyzed by a method called component decomposition. Such approach is based on the assumption that the original recorded spectrum is a linear superposition of component spectra (or basis spectra). Hence, each component spectra represents a certain biochemical constituent of the analyzed sample (e.g. protein, lipid, carbohydrate, DNA/RNA). The mathematical treatment is carried out using least-squares optimization to determine the linear coefficients that multiply each component spectrum thus producing a match to the originally measured spectrum. The disadvantages of the component decomposition are that it can be difficult to obtain the component spectra and often the measured spectrum is not a simple superposition of the components. Furthermore, it can be occasionally difficult to differentiate subtle spectral signatures by visual inspection. Principal component analysis (PCA), is a multivariate analysis method developed for that purpose. In essence, the aim is to reduce the number of variables in complex data sets potentially consisting of thousands of variables, and enable intuitive, easily interpretable representation in two or three dimensions [273].

In short, the PCA is a transformation method in which the original multi-dimensional coordinate system is rotated in such a way that the resulting new coordinate system directions are essentially linear combinations of the original (multi-dimensional) directions. Initially, each spectrum from the original data set is depicted in multi-dimensional space as a single dot whereby each wavenumber represents one coordinate direction, and respectively, the recorded intensity represents the magnitude of contribution of that particular wavenumber to the spectrum (i.e. those are the coordinates of the dot in a multi-dimensional space). As a result of the coordinate system rotation, the dimensions are reduced significantly. That, in turn, means that only the dimensions that are responsible for the largest variation between spectra, are left. As the spectra are depicted as dots in the new coordinate system, much clearer differentiation and grouping is usually observed. With regard to Raman spectra, typically 2-4 coordinates can explain most of the variations in the data. Finally, the observed groups can be further sorted and analyzed e.g. using clustering analysis.

In general, the spectral peak and band assignments are performed by using published literature references or by the mathematical calculations, or as a combination of both. The mathematical assignment of vibrational Raman frequencies is usually executed by means of computational methods, essentially the quantum mechanical methods, Hartree-Fock (HF) or density function theories (DFT), described in more detail e.g. in references [274, 275]. Moreover, various chemometric methods have been developed and introduced for quantitative Raman spectral analysis [276].

5.2 RAMAN IN BIOMEDICAL APPLICATIONS

Raman spectroscopy as a biophotonic method is feasible for a wide scale of biomedical applications; the measurements can be performed label-free, vibrational spectra can be obtained in aqueous medium since water has weak Raman scattering, and does not interfere with the relevant Raman bands of interest. In addition, samples can be measured in their natural states (e.g. liquid, solid, gel), no excessive sample preparation is needed, and the measurements can also be performed through the container walls or e.g. blister packages in the case of pharmaceuticals. Furthermore, the visible wavelength laser excitation source can be focused to a micron-sized spot. This, in turn, allows for acquiring Raman spectra of micro-size dimensions such as single cells. A specific chemical segment or subcellular component can be probed by resonantly enhancing the Raman scattering. One of the disadvantages of Raman spectroscopy is the very weak Raman signal; approximately every 10^6 to 10^7 photon is Raman scattered. Probably the most utilized technique for enhancing the weak Raman scattering phenomenon is surface enhanced Raman scattering (SERS), where the signal enhancement is achieved by using nano-plasmonic properties of noble metals. Another hindrance for the effective utilization of Raman spectroscopy can be a strong photoluminescent background produced by the various chemical structures (for example conjugated double bonds) in the investigated compounds. Such a background can overwhelm the already weak Raman spectra features completely and it has prevailed as one of the fundamental drawbacks in exploiting Raman spectroscopy to its full potential. Thus, a demand for new approaches has arisen.

5.2.1 Raman spectroscopy for the analysis of small drugs

Raman spectroscopy is a useful tool for characterizing small drugs. It has been used in a wide range of various applications in life sciences where small drugs are concerned. From the viewpoint of pharmaceutical research and development and PAT, pivotal assays are dosage form manufacturing, storage,

and administration [277]. Furthermore, material characterization, incoming (raw) material identification, end product quality control, and polymorph recognition are of relevance in the pharmaceutical industry setting [278]. Despite the earlier described benefits of Raman spectroscopy, the major limitations are the weak Raman signal, photoluminescence masking the already weak Raman scattering signals, and inadequately sensitive detectors [279]. Some of these hindrances have been resolved by improved hardware [280] and various spectral manipulation methods [281, 282]. However, drawbacks still exist; the instrumentations are often large, expensive and best suited only for laboratory setting, the analysis suffer from complexity, and the strong photoluminescent backgrounds can still perseveringly swamp important Raman spectral signatures leading to useless data. Essentially that poses a major problem in biopharmaceutical and several other life science settings where the overwhelming photoluminescent backgrounds are present due to the chemical nature of biological samples. An unmet need exists in order to develop affordable and user-friendly, label-free Raman spectroscopy technologies for characterizing highly fluorescent small drugs or for monitoring phase transitions, for instance [283].

5.2.2 Laser tweezers Raman spectroscopy for EV analysis

Initial proteomic studies have shown that EVs, in particular exosomes, contain a unique subset of cellular proteins. Some of the proteins are dependent on the cell type that secrets those exosomes, and on the other hand, some of the proteins can be found in most exosomes regardless the cell from which the exosomes are derived. Heretofore, relatively straightforward propositions have been made to explain these perceptions in exosome studies [284-288]. However, the overlap of protein expression between various subtypes of exosomes and existence of other biomolecules in the membranes and interior parts of exosomes has led to a junction of multiple paths. A common consensus prevails that cells actively control the packaging of various biochemical specimens, for example RNA, proteins and lipids, into exosomes. However, it remains ambiguous whether the biochemically distinct subpopulations emerge from varying packaging pathways during exosome biogenesis or alterations after the synthesis and release [289-291]. Thus, a clear need for complementary – and clarifying, methods and techniques exists in order to better understand the multiple roles of EVs in homeostasis as well as pathogenesis.

Raman spectroscopy, and particularly laser tweezers Raman spectroscopy (LTRS), allows for recording the unique biochemical Raman spectral fingerprint of samples. As a brief revision from chapter “5.1.1 Raman instruments”, it is based on a tightly focused laser beam that traps and holds small objects at the light’s focal point. The trapping laser simultaneously excites Raman scattering from the trapped particle, and the backscattered light can be collected through an objective. **Figure 7**

illustrates the working principle of a LTRS system. When equipped with a confocal photon collection and detection systems, the capabilities are further increased, and Raman scattering is acquired from a very precise focal volume. Therefore, cellular and sub-cellular particles, such as exosomes, can be studied on an individual basis. LTRS has already been successfully applied to study individual cancerous and non-cancerous cells [292, 293], activation responses of individual immune cells [294], bacteria [295] and spores [296]. Moreover, nano-sized particles such as lipid droplets in milk [297] and subcellular organelles [298] have been investigated. It is worth stressing that the prior studies show the capabilities of Raman spectroscopy to assess the biochemical fingerprints from individual nano- and micron sized particles. Such particles are conventionally below the limit of detection (LOD) for traditional methods whereby large amounts of starting material is typically required. Surprisingly, even though a relatively well-established technique, not until recently the potential of Raman tweezers for EV studies have raised common awareness [299]. A study in 2014 explored exosomes in clusters that were trapped in the laser tweezer focus [300]. However, the drawback was that the information gained was averaged over an exosome population in the focal spot rather than from single vesicles. To date, no studies have been performed to investigate single EVs from healthy and cancerous origins to potentially highlight their distinctive biochemical contents, and thus their functions in living systems.

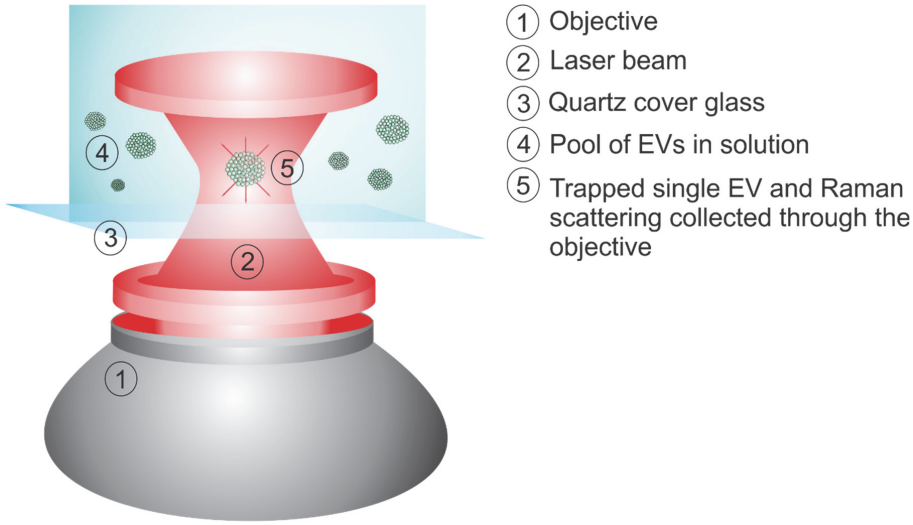

Figure 7. An EV measurement scheme for single EV using laser trap Raman spectroscopy. The force field created by tightly focused laser beam traps the EV and the scattered light is collected through the objective lens to the detector.

6 SURFACE PLASMON RESONANCE

Surface plasmon resonance (SPR) is an evanescent wave sensing technique and thus the SPR biosensors belong to the group of evanescent wave biosensors. Such sensors are based on total internal reflection (TIR) of light at the interface of the sensor surface and analyte solution. The TIR generates a surface-sensitive evanescent wave that extends a short distance into the solution. Already by 2003, over 3000 scientific papers had been published using optical biosensors based on surface plasmon resonance, planar waveguides and/or resonant mirrors [94], and the popularity of these techniques is constantly increasing. In SPR, a metal-dielectric interface is the pertinent milieu in terms of surface plasmon excitation and sensing events. Metals, in general, contain abundantly mobile free electrons, forming a "floating ocean of electrons" on the surface. Surface plasmons, in turn, are electromagnetic waves that are generated by external excitation energy, for instance light. Surface plasmons can propagate along the surface, and the most typical method to create them is attenuated total reflection (ATR). Further theoretical aspects of SPR are being discussed in the next chapter, below.

6.1 GENERAL OVERVIEW OF SPR

In the late 1960's Kretschmann, Raether and Ritchie made fundamental observations and experiments demonstrating that electrons at the interface of a dielectric and conductive metal surface can be excited by polarized light [301, 302]. The investigations gave rise to SPR, and since then the field has evolved significantly. In brief, plasmons are quasi-particles (and/or waves) connected with the collective oscillations of the free electron gas in a metal. A polarized light beam can excite plasmons via interacting with the metal surface at a physically defined incident angle at a certain wavelength, thus resulting in formation of surface plasmons. When the resonance condition is met, exact matching of photons and plasmons takes place [303]. However, optical excitation of plasmons by directly impinging light onto the metal surface is not possible. The phenomenon can be clearly seen in **Figure 8** that illustrates the situation when excitation light (I_i) is directed onto the metal surface at incident angle θ, and it reflects from the surface (I_r). The dielectric constants of air, metal, media on the other side of the metal are ε_0, ε_1, and ε_2, respectively. The wave vector of the incident light is given as k_{ph} and the wave vector of the surface plasmons as k_{sp}. Excitation of the surface plasmons is not possible due to the condition $|k_{ph,\,x}| < |k_{sp}|$; the resonance condition is not matched.

(7) $$k_{sp} = \frac{\omega}{c}\sqrt{\frac{\varepsilon_0 \times \varepsilon_2}{\varepsilon_0 + \varepsilon_2}} \quad and \quad k_{ph} = \frac{\omega}{c}\sqrt{\varepsilon_0} \quad and$$

$$|k_{ph,x}| < |k_{sp}| \quad for\ all\ \theta\ at\ air/metal$$

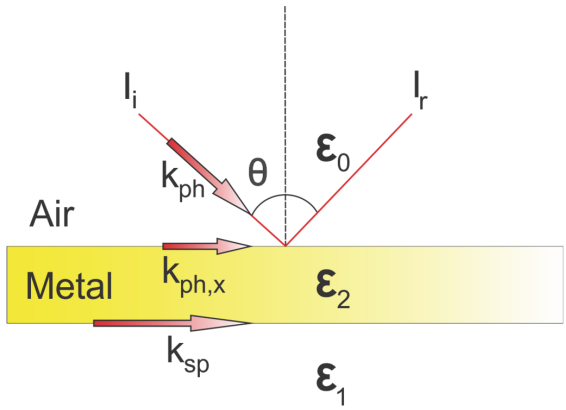

Figure 8. An illustration of the fundamentals of the surface plasmon resonance phenomenon.

Typically an optical arrangement called the Kretschmann-configuration is utilized to pass a parallel polarized (*p-polarized*) collimated light beam through a glass prism to the glass-metal-dielectric interface, ε_0, ε_1 and ε_2 being the dielectric constants of the prism (glass), the metal, and the medium in contact with it, respectively. **Figure 9** illustrates the effect of a prism coupling.

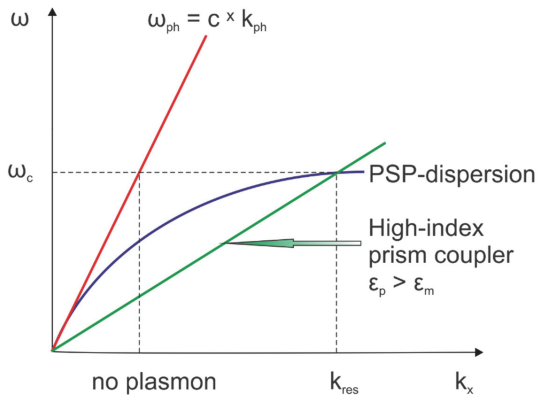

ω: Angular frequency
ω_c: Angular frequency at surface plasmon resonance
ω_{ph}: Angular frequency of photons
c: Velocity of light
k_{ph}: Wave vector of photons
PSP: Phonon surface polariton
ε_p: Dielectric constant of the prism
ε_m: Dielectric constant of the medium

Figure 9. The effect of a prism coupling to the surface plasmon excitation. No plasmon excitation is observed if the incident light is directed onto the metal surface without a coupler (red line). When a high-index prism coupler is used, the surface plasmon resonance can occur (green line and blue curve crossing at k_{res}).

Thus, energy is transferred from photons to plasmons, and the plasmon resonance condition is observable as a sharp minimum of the reflectance when the incident angle is varied. The fundamental mathematical depiction of surface plasmon resonance is derived from the Maxwell's equations, and has been described extensively elsewhere [72, 91, 303, 304]. In brief, when the wave vectors of the incident light photons (k_{ph}) and the plasmons (k_{sp}) match, the resonance condition is accomplished:

$$(8) \qquad k_{ph} = k_{sp} \qquad or \qquad \frac{\omega}{c}\sqrt{\varepsilon_0}\sin\theta_0 = \frac{\omega}{c}\left(\frac{\varepsilon_1\varepsilon_2}{\varepsilon_1+\varepsilon_2}\right)^{\frac{1}{2}}$$

where c is the speed of light in vacuum, ω is the light frequency, θ_0 is the angle of incidence of the light beam, and ε_0, ε_1, ε_2 are the dielectric constants of the prism, the metal, and the medium in contact with it, respectively. In general, the dielectric constant ε and refractive index n for a given material can be expressed in their complex forms as $\hat{n} = n + ik = \sqrt{\mu\hat{\varepsilon}}$, and $\hat{\varepsilon} = \varepsilon + i\varepsilon'$, where $\hat{n}$, n and k are the complex refractive index, real- and imaginary parts of the complex refractive index, respectively. The quantity μ denotes permeability, occurring in Maxwell's equations. Since the majority of materials are non-magnetic at optical frequencies, μ can be approximated very close to 1. Similarly, $\hat{\varepsilon}$, ε and ε' are the complex dielectric constant, real- and imaginary parts of the complex refractive index. As a sum of the definitions made here, the refractive index and dielectric constant are related as $\hat{n} = \sqrt{\hat{\varepsilon}}$. Furthermore, the detected reflectance (or transmittance), angle of incidence (θ), used laser wavelength (λ), layer thicknesses (d_i), refractive indices (n_i) and k_i-values (attenuation index of i^{th} layer) are physically related. They form the mathematical background for converting the measured SPR-signals to meaningful qualitative and quantitative observations in a broad range of different life and materials science applications [50]. SPR offers a robust and sensitive tool for label-free real-time interaction analysis, biosensing and thin film characterization [91].

6.1.1 Instrumentation and biosensors in SPR

A typical SPR system consists of a light source, prism, detector, flow channel and the sensor surface. Based on the previously discussed physical facts, the sensor surface comprises a conducting metal surface such as gold or silver in order to enable plasmon coupling. After immobilizing one of the interacting partners (ligand) onto the surface of the sensor, the other partner (analyte) is injected over the surface at a given flow rate through a microfluidic channel system. It is worth emphasizing, however, that halted state analysis can also be performed. In comparison to other surface-sensitive – and complementary techniques, for instance quartz crystal microbalance (QCM), SPR reveals the "dry mass" of the surface-deposited analyte,

even though measured in liquid environment [305], because SPR detects only the events occurring at the close proximity of the surface via refractive index and thickness changes. The most widely used SPR technology for biochemical interaction and drug interaction studies is the Biacore platform. It uses a fixed-angle, focused beam light-emitting diode (LED) to simultaneously excite a narrow range of incident angles (typically a few degrees), including the angular position of SPR peak minimum (θ_{SPR}), at which the resonance condition is met and minimal reflection is observed [306]. There is no scanning of incident angles involved.

From the viewpoint of biosensor design, the key of SPR is the *traveling evanescent field* that extends from the sensor surface into the test sample. The evanescent field is dependent on the used excitation wavelength and the refractive indices of the prevalent conditions and the field intensity decays exponentially with respect to distance from the sensor surface [307]. The penetration depth d_p is defined in terms of the used wavelength (λ), incident angle (θ), and dielectric constants of the prism (ε_p) and dielectric substrate in contact with the prism ($\widehat{\varepsilon_D}$) (Eq. 9).

$$d_p = \frac{\lambda}{2\pi\left(\varepsilon_p sin^2\theta - Re[\widehat{\varepsilon_D}]\right)^{1/2}} \quad (9)$$

Typically the wavelength range for optical biosensors used in SPR is in the range of 600-900 nm, and thus the evanescent field can be considered to extend ~ 100-150 nm into the test sample. Such a short distance allows for analyte detection at the very close proximity of the sensor surface while the unbound material in the solution does not affect the measurement. On the other hand, to circumvent this limitation, the characteristics of the evanescent field can be modified so that it can extend deeper or is constrained tightly to the sensor surface; the crucial aim in designing a high sensitivity SPR sensor is to match the highest chemical binding region to the regions with the highest evanescent field intensity.

However, the short reach of the evanescent field still poses a constraint in the SPR experiments [90], and the traditional instruments are capable of measuring the analyte-ligand interactions and acquiring kinetic data but not much else. In order to overcome these limitations, a next-generation SPR system has been developed [308, 309]. The multi-parametric SPR (MP-SPR) expands on the conventional SPR allowing for recording the full SPR angular spectrum over a wide angular range (~40 degrees) instead of monitoring only the narrow angular area near the θ_{SPR}. The angular position of the TIR is also recorded. In addition, the MP-SPR measurements can be performed using multiple excitation wavelengths. These technical features widen the applicability of SPR from kinetic assays also to optical characterization of surface-associated molecular layers in terms of their refractive index and thickness up to micrometer scale. The full SPR angular spectra recorded at two or more

independent wavelengths contain all the needed physical information to solve for the thin film thickness and refractive index [309, 310].

With the traditional SPR techniques it can be arduous to determine the proportion of *bulk effec*t in the change of θ_{SPR} [90]. If the refractive indices between the running bulk liquid and the injected sample liquid are different – which is often the case – the θ_{SPR} is a combined signal stemming from real binding events at the surface and from changes in the running bulk flow during the sample injection. With the traditional SPR instruments that bulk effect cannot be subtracted from the signal without using a reference channel and bulk correction calibration methods. However, by scanning over the wide angular range in MP-SPR, the bulk effect can be subtracted directly without the need to use reference channel and bulk correction calibrations. Since the main contribution of the bulk effect can be observed as a shift in the position of TIR, that information can be used to deduct the bulk effect contribution. In practice, a weighted subtraction algorithm is implemented using the recorded angular position of TIR. The bulk effect correction for the obtained *raw data* facilitates the subsequent *data analysis* steps, and enhances the accuracy of the analysis. In comparison with the traditional SPR techniques where the interaction kinetics have been in the focal point, the MP-SPR has shown potential for utilizing SPR in previously unseen ways in various applications of life and materials sciences.

Three essential data analysis methods used in SPR are introduced within the next "Data analysis" sections; the first chapter dealing with interaction kinetics calculations, the second covering the thin film thickness and refractive index evaluations, and the third describing the mathematical principles of relating the recorded change of θ_{SPR} with the change of mass on the sensor surface. Notably, the described methods are based on both the features of traditional SPR instruments, and the new capabilities of the MP-SPR.

6.1.2 Data analysis: Interaction kinetics

In the SPR data analysis phase, information from two distinct graphs is typically used. The non-scanning and scanning instruments record sensorgrams where the relative shift of the angular position of θ_{SPR} is shown as a function of time (**Figure 10**). Thus, the analyte injections can typically be seen as shifts in the position of θ_{SPR}. When the injected analyte concentrations are known, the affinities and kinetic parameters (association and dissociation rate constants) can be calculated using mathematical formulae as described later in this section. The SPR curve is another essential graph. It demonstrates the angular position of the incident light on the x-axis, and the intensity of reflected light or reflectivity on the y-axis (**Figure 11**). Notably, the scanning property is needed.in the instrumentation in order to acquire the reflectivity data as a function of incident angle.

The recorded sensorgrams can be pre-processed using baseline correction algorithms. The interaction kinetics are evaluated using established mathematical models [91, 311]. **Figure 10** illustrates an idealized sensorgram of the interaction between pre-immobilized ligand and analyte. Experimental sensorgrams are fitted to the chosen model, and typically the residuals are calculated in order to estimate, how the measured sensorgrams agree with the model. Parameters such as rate constants (k_a, k_d, KD) and maximum binding capacity (for instance B_{max}) can be derived from the fits using numerical integration. Two frequently utilized models are described and shown in **Table 5.** It is noteworthy to mention that there exists a plethora of more complex models for various interaction schemes. In short, the one-to-one binding system is a common curve fitting algorithm based on 1:1 analyte-to-ligand binding. Despite its simplicity, in most cases it generates reasonably good fittings. The algorithm and the yielded quantities are shown in **Table 5**. Respectively, the one-to-two binding model is suitable for interactions where the analyte in solution binds to two independent targets (i.e. ligand binding sites) on a solid support. The algorithm and the resulting quantities for one-to-two model are also shown in **Table 5**.

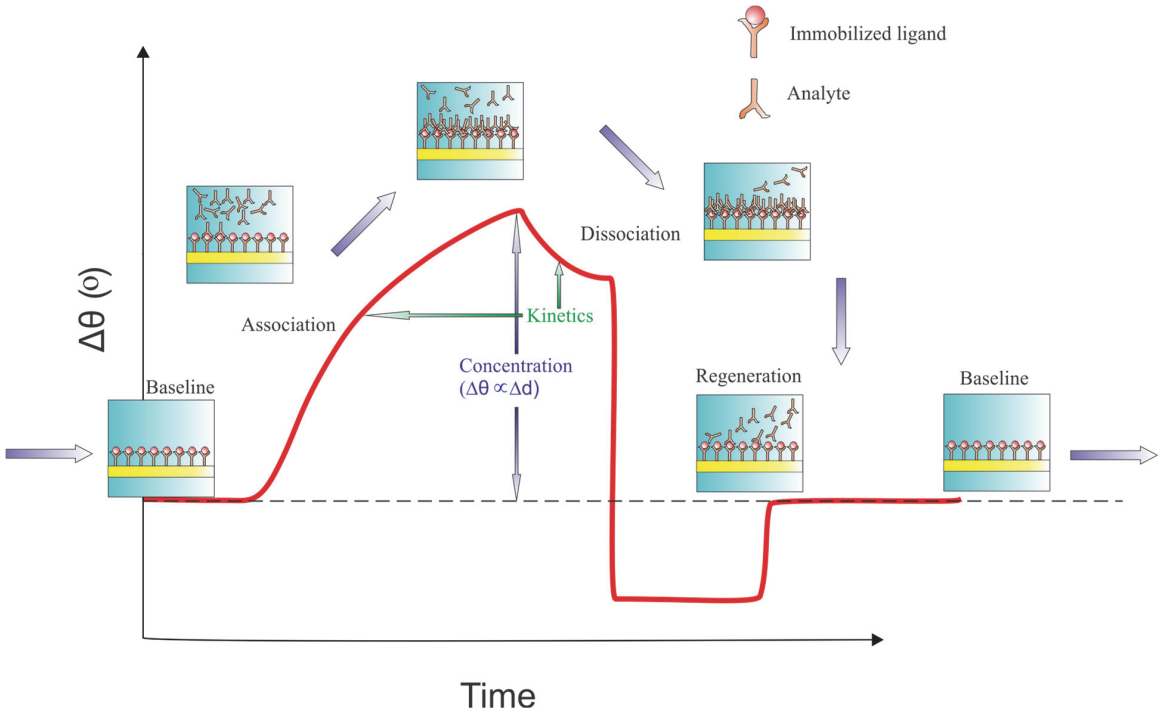

Figure 10. A typical sensorgram depicting the interaction events between the pre-immobilized ligand and analyte. After a stable baseline is observed at the beginning, the analyte is injected over the sensor surface. In the association phase the θ_{SPR} undergoes a shift that can be perceived as a relative shift in the sensorgram. In the dissociation phase the adsorbed analytes detach from the surface. Depending on the ligand-analyte interaction, the dissociation can take place partially, completely or it can be chemically forced with various regeneration methods. At the end, a stable baseline is observed.

Table 5. Two commonly used interaction models; One-to-One and One-to-Two binding kinetics.

Model	Equations	Conditions	Result
One-to-One	ka A + B ⇌ AB = Y kd $\frac{dY}{dt}$ = ka × cA × (Ymax – Y) – kd × Y	Y, t=0 = 0 A: Analyte B: Ligand Y: Concentration of the formed molecular complex (AB) Ymax: Total concentration of the immobilized ligand ka: Association rate constant kd: Dissociation rate constant cA: Concentration of the (injected) analyte A	Bmax [Signal units]: Maximum signal obtained (dependent e.g. on the number of receptors) ka = $[\frac{1}{(M*s)}]$ kd = $[\frac{1}{s}]$ BI [Signal units]: Bulk effect (if present)
One-to-Two	ka1 A + B ⇌ AB = Y1 kd1 ka2 A + C ⇌ AC = Y2 kd2 $\frac{dY1}{dt}$ = ka1 × cA × (Ymax – Y1 – Y2) – kd1 × Y1 – ka2 × Y1 + kd2 × Y2 $\frac{dY2}{dt}$ = ka2 × Y1 – kd2 × Y2	Y1, t=0 = 0 Y2, t=0 = 0 A: Analyte B: Ligand/binding site 1 C: Ligand/binding site 2 Y1: Concentration of the formed molecular complex (AB) Y2: Concentration of the formed molecular complex (AC) ka1: Association rate constant 1 kd1: Dissociation rate constant 1 cA: Concentration of the (injected) analyte A ka2: Association rate constant 2 kd2: Dissociation rate constant 2	Bmax1 [Signal units]: Maximum signal from target 1 (dependent e.g. on the number of receptors) ka1 = $[\frac{1}{(M*s)}]$ kd1 = $[\frac{1}{s}]$ Bmax2 [Signal units]: Maximum signal from target 2 (dependent e.g. on the number of receptors) ka2 = $[\frac{1}{(M*s)}]$ kd2 = $[\frac{1}{s}]$ BI [Signal units]: Bulk effect (if present)

6.1.3 Data analysis: Modeling for layer thickness and refractive index

For the layer thickness and refractive index modeling, the shape and quantities (θ_{SPR}, depth of minimum, width of minimum) associated with the SPR curve are utilized [307]. The Fresnel equations can be used to calculate the fraction of light wave reflected and transmitted by a flat interface between two media with different refractive indices. The Fresnel equations for *p-polarized* light can be expressed as:

$$r_{\parallel} = \frac{E_{0r}}{E_{0i}} = \frac{[n_i \times \cos(\theta_t) - n_t \times \cos(\theta_i)]}{[n_i \times \cos(\theta_t) + n_t \times \cos(\theta_i)]} \quad (10)$$

$$t_{\parallel} = \frac{E_{0t}}{E_{0i}} = \frac{2 \times n_i \times \cos(\theta_i)}{[n_i \times \cos(\theta_t) + n_t \times \cos(\theta_i)]} \quad (11)$$

where (Eq. 10) denotes the reflection coefficient, $r_{\parallel}$, E_{0r} and E_{0i} are the electric fields for reflected and incident light, respectively. The refractive indices for incident medium and transmitting medium are n_i and n_t, respectively. And θ_i is the angle of incidence for the light, θ_t is the angle of the transmitted light. Analogously, (Eq. 11) describes the transmission coefficient, $t_{\parallel}$ for the incident light; E_{0t} is the electric field for transmitted light. It is noteworthy that under ATR conditions, the transmittance coefficient $t_{\parallel}$ equals zero. Moreover, $R = |r_{\parallel}|^2$ for calculating the theoretical full SPR curve as a function of the incident light angle.

More exactly, the SPR curve can be described with Fresnel's equations as the reflectivity of a multilayered system for *p-polarized* light [307]. In principle, the layers are assumed linear, homogenous, and isotropic. The calculation is based on a 2 × 2 scattering matrix derived from Fresnel's complex-amplitude reflection and transmission coefficients; the matrix representing the summarized optical properties and expressed as a product of the interface and layer matrices of the entire structure. The intermediate zones between different layers are introduced into Fresnel's equations as new layers. Thus, the thickness of the intermediate layer describes the average roughness of the surface, its complex refractive index, for one, corresponds to the light losses via scattering and plasmon decoupling into radiative modes (especially the imaginary part). The overall benefit of this approach is that only Fresnel equations can be used in the model with no need to apply scattering theories. **Figure 11** depicts an example of this multilayer scheme. The whole procedure can be modeled step-wise by performing the curve fitting in each phase. However, the downside of this fitting procedure using data recorded with single incident wavelength is that at least either the d or n of the new layer should be known from the existing literature or otherwise estimated accurately.

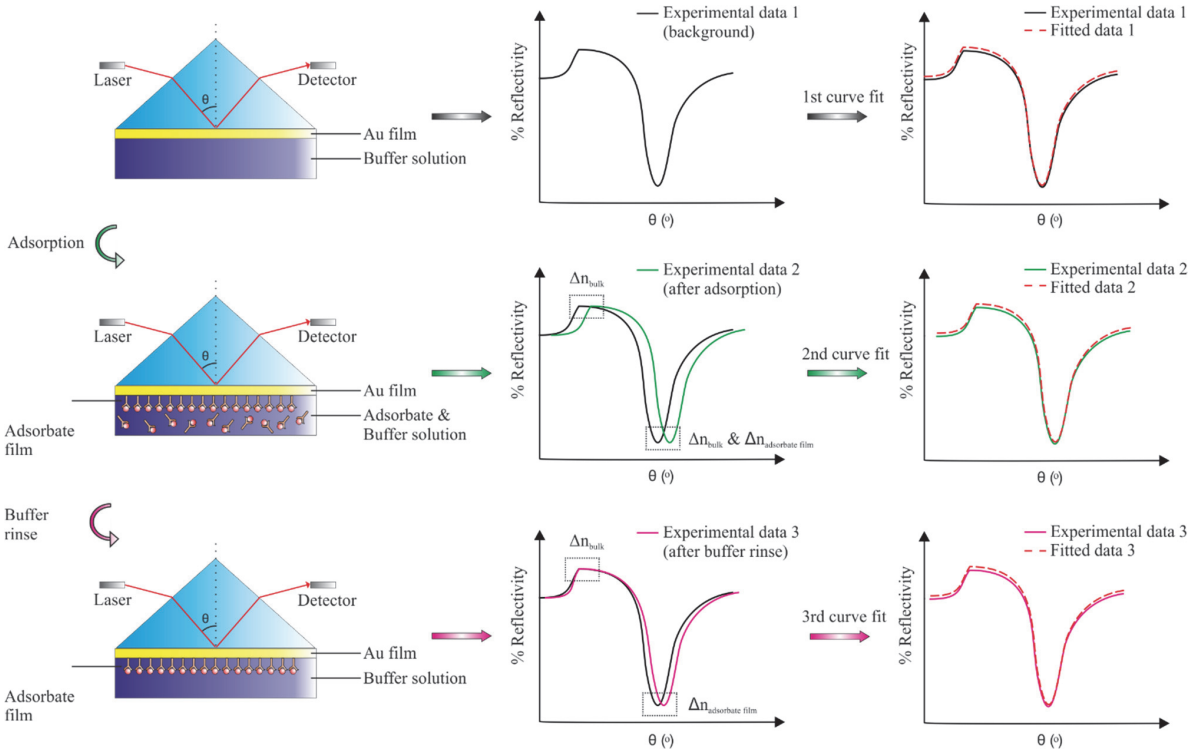

Figure 11. An example of the multilayer approach typically used for evaluating thicknesses and refractive indices of various layers. First, the gold sensor surface is measured in buffer solution (uppermost row). Second, the adsorbates in buffer solution are associating onto the surface (middle row). In this phase, the measured SPR curve undergoes a shift from the background (black) to the situation after the adsorption (green). Notably, the effect of adsorbate solution can be seen as a shift in the TIR angle (i.e. Δn_{bulk}). The angular position of θ_{SPR} is affected by the adsorbate solution and the adsorbing film (i.e. Δn_{bulk} & $\Delta n_{adsorbate\ film}$). Lastly, the surface is rinsed with the buffer solution (bottom row). The SPR curve (purple) can shift back slightly, the shift in TIR angle recovers, and the position of θ_{SPR} corresponds to the contribution of adsorbate film on the surface ($\Delta n_{adsorbate\ film}$).

Information produced by multiple independent incident wavelengths can be used to resolve for the layers more explicitly. The general solution for a multilayered, optically active system connected with measurable and controllable quantities, can be derived using the transfer matrix formalism of 2 × 2 matrices. In the complex refractive index $\hat{n} = n + ik$, the real part n corresponds to the refraction of light, and the complex coefficient k to the extinction or absorption of light by the material. Furthermore, the relationship $\hat{n} = \sqrt{\hat{\varepsilon}}$ connects the refractive index and dielectric constant. Finally, the surface plasmon wave vector (k_{sp}) is considered to contain all the information and constants that affect the measured SPR spectra, and lead to differences in SPR spectra measured at multiple wavelengths. Therefore, the continuum solution for the surface plasmon wave vector (k_{sp}) in one set of conditions

can be described by the mathematical relationship between (k_{sp}), the material layer thickness d, and the refractive index n:

$$k_{sp} \propto n * d \tag{12}$$

However, the definition above describes only the continuum solution for the (k_{sp}). The unique solution for the apparently interconnected thickness d and refractive index n of the layer can be found from the intersection of two continuum solutions from two different measurements in two different media or multiple wavelengths [308, 309]. In the mathematical treatment with the two-wavelengths, the refractive index n has a wavelength dependency, dn/dλ. Noteworthy, if a third wavelength is used, the dispersion coefficient dn/dλ can be accurately quantified [309]. For relatively similar materials and molecules this dependency can be assumed as linear, resulting in good approximations. Furthermore, by using the established dispersion coefficient values in combination with the two-wavelength technique results to significant improvement in accuracy compared to modeling where the value for either n or d is estimated or adopted from the literature for bulk materials [309]. The unique solution for layer thickness d and refractive index n can be found by solving for the equations:

$$k_{sp1} = n_{\lambda 1} * d \tag{13}$$

$$k_{sp2} = n_{\lambda 2} * d \tag{14}$$

where k_{sp1} denotes the surface plasmon vector for wavelength 1, $n_{\lambda 1}$ the refractive index for wavelength 1, k_{sp2} the surface plasmon vector for wavelength 2, and $n_{\lambda 2}$ the refractive index for wavelength 2, and:

$$n_{\lambda 2} = n_{\lambda 1} + \frac{dn}{d\lambda} * (\lambda_2 - \lambda_1) \tag{15}$$

and:

$$k_{sp1} = n_{\lambda 1} * d \tag{16}$$

$$k_{sp2} = (n_{\lambda 1} + \frac{dn}{d\lambda} * (\lambda_2 - \lambda_1)) * d \tag{17}$$

The statements above hold true for sample layers that do not absorb light at the wavelengths used in the SPR spectrum measurement. In practice, it means that the imaginary component k for the refractive index = 0, which is the case for the majority of organic sample layers. However, if the layer absorbs light, $k \neq 0$, then there is a unique solution for the sample layer in the $k_{sp} = (n + ik) * d$ space.

For instance, one can utilize laser wavelengths 670 nm and 785 nm that are aligned to irradiate simultaneously the same spot on the measured surface. Hence, the layer thickness can expected to be the same for both wavelengths. The complex refractive index can be input as an independent variable for the background (pure metal layer) modeling, or as a linearly dependent variable between the two used wavelengths for reasons described above. Overall, the two-wavelength method combined with the angular scanning has been demonstrated efficient for characterizing adsorbed (organic) thin and thick layers on surfaces [71, 310, 312, 313].

6.1.4 Data analysis: Surface mass density calculations

The θ_{SPR} has a correlation with the mass that adsorbs onto the SPR sensor surface [91, 314]. The surface mass densities can be calculated by using the de Feijter equation [305] derived from the definition of refractive index increment of adsorbed biomolecules $^{dn}/_{dc}$:

$$\frac{dn}{dc} = \frac{n_p - n_m}{C_p} \tag{18}$$

where n_p is the refractive index of a solution of biomolecule p with concentration C_p, n_m is the refractive index of medium and $^{dn}/_{dc}$ represents the concentration (mass) dependency of refractive index. Thus the surface density (Γ) is defined as the Gibbs surface excess:

$$\Gamma_p = C_p d_p \tag{19}$$

where d_p is the thickness of the adsorbed layer. By combining the two equations above, and eliminating C_p, the de Feijter equation relating the surface density to the refractive index increment and the layer thickness becomes:

$$\Gamma_p = \frac{(n_p - n_m) d_p}{^{dn}/_{dc}} \tag{20}$$

Since the instrument signal is an important factor to take into account, the latter equation is derived further to include the instrument signal:

$$n_p - n_m = \Delta n = \Delta\Theta \times k \tag{21}$$

and thus:

$$\Gamma_p = \frac{\Delta\Theta \times k \times d_p}{dn/dc} \quad (22)$$

where the constant k is the instrument (sensor, wavelength) dependent coefficient for sensitivity, and Θ is the θ_{SPR} shift obtained from the sensorgram where the θ_{SPR} is observed as a function of time. For thin layers the $k \times d_p$ can be approximated as a constant. The value can be experimentally defined, or by theoretical modeling of SPR peaks. In order to gain the conversion coefficient for calculating the surface mass densities, comparably good approximations can be achieved using a value of dn/dc = 0.182 cm³/g. As an example, for the SPR Navi 200 instrument (BioNavis Ltd., Tampere, Finland) it means that for 670 nm wavelength Γ_p = ΔΘ (mDeg) * 550 *n*g/cm² and for 785 nm wavelength Γ_p = ΔΘ (mDeg) * 1050 *n* g/cm². However, the aforementioned relationship holds true best for certain types of proteins. Some of the limitations and possible caveats of these approximations are discussed in the literature [314].

6.2 SPR IN BIOMEDICAL APPLICATIONS

As an optical technique, SPR is very sensitive and assays are generally performed without the use of labels. The real-time nature of SPR allows for time-resolved monitoring of events from rapid interaction phenomena in the order of few milliseconds to long-term monitoring of several hours. In addition, the prerequisite for the amount of starting materials is low. Thorough reviews on the subject and its applications can be found for example in the following references [50, 83, 315, 316]. In brief, SPR has been extensively used in life and materials sciences for monitoring a plethora of interactions and surface properties; for instance glucose and urea detection, immunoassays, DNA binding assays, real-time kinetics of drugs binding to various targets, graphene layers characterization [317] and living cell interactions with drugs [318].

6.2.1 SPR as a biophotonic tool for studying small drugs

Initially SPR started as an immunosensing tool [315], and soon after it was found a potential technique for a number of applications in the analysis of small molecules, for instance drugs. Meticulous overviews and examples of various assays have been provided e.g. by Rich et al. [319] and Shankaran et al. [320]. Essentially the cornerstone for small drug assays using SPR is to establish a well-defined and stable biosensor surface onto which the ligand is immobilized and the consequent steps with

the small drug analyte are performed. Hydrogel surfaces, particularly hydrophilic carboxymethyl-modified dextran (CMD) hydrogels, offer many advantages when used as an SPR sensor surface [321]. In general, a highly branched 3D CMD hydrogel surface is best applied for small molecular weight analyte detection whereas a 2D CMD surface performs better in the presence of large analytes, for instance liposomes and EVs.

Intriguingly, a pivotal perception can be made when the timeline of SPR is scrutinized with caution; a vast majority of the studies have focused on traditional interaction kinetics – which are obviously valuable as such but an evident need exists for fresh approaches in SPR-based small drug studies. The advent of novel SPR instrumentation allows for re-thinking the opportunities. For instance by utilizing the MP-SPR, SPR assays can be designed from a new standpoint. Because multiple parameters are acquired in the measurement, simultaneous characterization of interaction events and surface properties is enabled. When combined with rigorous analysis of experimental data, and computational modeling approaches, new *bio-functional assays* can be constituted. Essentially, in such assays the experimental *in vitro* environment is built to mimic the natural biological milieu, and the computational methods of choice complement the obtained experimental data. This, in turn, can open up unexpected venues in the discovery and development of small drugs. For example, a major hindrance in the development of therapeutic agents [322, 323] against Alzheimer's disease (AD) is the inadequate mechanistic insight of small molecule binding coordination and/or lack of tools to demonstrate their potential to disrupt the detrimental oligomerization of Aβ peptides [324, 325]. SPR-based bio-functional assays can provide real-time, label-free methods to overcome such barriers in the development of novel compounds.

6.2.2 Bionanophotonics: SPR for studying liposomes

To date the primary aim in nanomedicine is the development of safe and effective DDCs. One of the crucial aspects is to design drug preparations that fulfil the requirements during the multiple and complex interactions at the nano-bio interfaces [1]. Essentially, the nano-bio interface includes three important components that affect the overall performance of the DDC. The first component is the physicochemical characteristics of the nanocarrier surface. Secondly, the events occurring at the solid-liquid interface phenomena while the carrier interacts with the surrounding medium. Thirdly, the events occurring at the solid-liquid interface between the nanocarrier and biological structures (e.g. cell membranes). In particular, the lack of knowledge of the overall mechanistic behavior of the DDC at the solid-liquid interfaces is one of the major contributors in troublesome DDC development. As previously touched on, *bionanophotonics* can offer tools for

mechanistic understanding to facilitate the somewhat rocky steps of nanocarrier engineering.

Importantly, liposomes represent a group of DDCs that have been approved for therapeutic use. Liposomal drug delivery systems (LDSs) have been investigated with SPR in various instances. Examples include drug-liposome interactions [326], rapid monitoring of solute leakage from liposomes [327], and liposome interactions with model receptor surfaces [328]. When liposomes are administered into the blood circulation in the body, they encounter a highly dynamic environment. Complex interactions with different biomolecular specimens affect the circulation time and bioavailability of the LDS [256, 329]. Essentially a dynamic layer consisting of proteins and various plasma components is adsorbed onto the surfaces of LDSs; the layer is typically called the "protein corona" and it can be furthermore divided into "hard corona" and "soft corona" according to the physicochemical characteristics of the layer [330]. Such layer can direct the macrophages of reticular endothelial system (RES) to recognize and eliminate the LDSs from the circulation as foreign particles. The PEGylation and other hydrophilic shielding methods have been widely used to prevent the premature clearance of LDSs [145, 331]. However, such coatings can provoke increased immunogenicity and drastic hypersensitivity responses against the existing LDSs have been observed [143, 332]. The effects of PEGylation coatings – and other surface modifications of LDSs have been studied to an extent but significant cavities exist among the current methodologies [329, 333]. Firstly, the studies have been carried out investigating diluted serum which is not an adequate model system for thorough understanding of the liposome-serum interactions. The diluted serum is far from its native state and thus the results can be ambiguous. Secondly, liposomes interacting with *individual* serum proteins have been studied with SPR but the downside of those studies is that more than 200 corona proteins have been identified. It is an uphill battle to screen through such an amount of proteins on an individual basis. Due to the undisputable biological significance of the liposome-serum interactions and particularly the protein corona formation, novel label-free bio-functional *in vitro* assays are needed to probe these interactions at early stages of LDS development. Furthermore, such assays would offer considerable *in vivo* relevance for the purposes of LDS design processes.

6.2.3 Bionanophotonics: SPR for studying EVs

The EVs represent a typical group of complex biological nanostructures whereby carbohydrates, lipids, proteins and nucleic acids are present. In general, SPR devices have been successfully utilized in the EV research for example in molecular profiling [334] and determining the concentration of EVs – which, however, still remains a puzzle without a universally adopted method in the EV research [335].

Since the EVs are a group of large scale analytes which have low diffusion rates in SPR measurements, an important point to be taken into account is whether the binding phenomena are being observed under mass-transport-limited conditions [311]. In general, mass-transport-limited binding can occur when the binding of the analyte to the surface-immobilized ligand is faster than the diffusion of the analyte from the bulk solution to the sensor surface. The same phenomenon applies reversibly when the analytes are leaving the surface in the dissociation phase; in mass-transport-limited conditions the analyte can re-bind to free ligand before diffusing back into the bulk solution. In essence, large analytes which have low diffusion rates (e.g. EVs), and analytes having fast association rates (in relation to the diffusion rate) are prone to this effect. In order to minimize the bias in analysis, i.e. to strive for operating in the kinetics-driven conditions, very low surface concentrations of ligands and high flow rates must be used – which occasionally requires optimization of the experimental setting. During the data analysis phase it is also possible to use kinetic fitting algorithms that take into account the conditions with a "mass transport" rate constant [336].

The antibody (for example anti-CD9 and anti-CD63) immobilization onto the SPR biosensor surface has been used to profile the protein content of EVs [219]. **Figure 12** illustrates the protocol exploiting immobilized anti-CD63 antibodies that are targeted against the CD63 tetraspanin protein found in the membrane structures of most EVs. However, the tetraspanin proteins such as CD9 and CD63 are abundantly expressed in the membranes of several EV types, and these assays lack the specificity for the purposes of cancer diagnostics, for example. The tumor-associated EVs could act as biomarkers for cancer diagnostics [104, 337], or models for biomimetic DDCs [250, 251]. However, the application of tumor-originating EVs as biomarkers is still difficult. The most pertinent problem appears the lack of compounds or other means that could provide *specific* targeting to EVs. The vigorous efforts to address this problem have also led to humane misinterpretations of the obtained data [338]. In order to acquire valid and accurate data on the structures and interactions of EVs, multiple measurement methods are often needed. A demand for a specific EV detection platform tenaciously exists as the highly selective EV recognition is considered as one of the "holy grails" in the EV research. Furthermore, even though the EV characterization methods have evolved, surprisingly many fundamental physicochemical characteristics of EVs are laborious to determine. For example, determining the mass of a single EV, the biological binding kinetics of different EV types, or defining the overall biochemical composition of EVs lack tools. And should be preferably done with label-free and reliable assays.

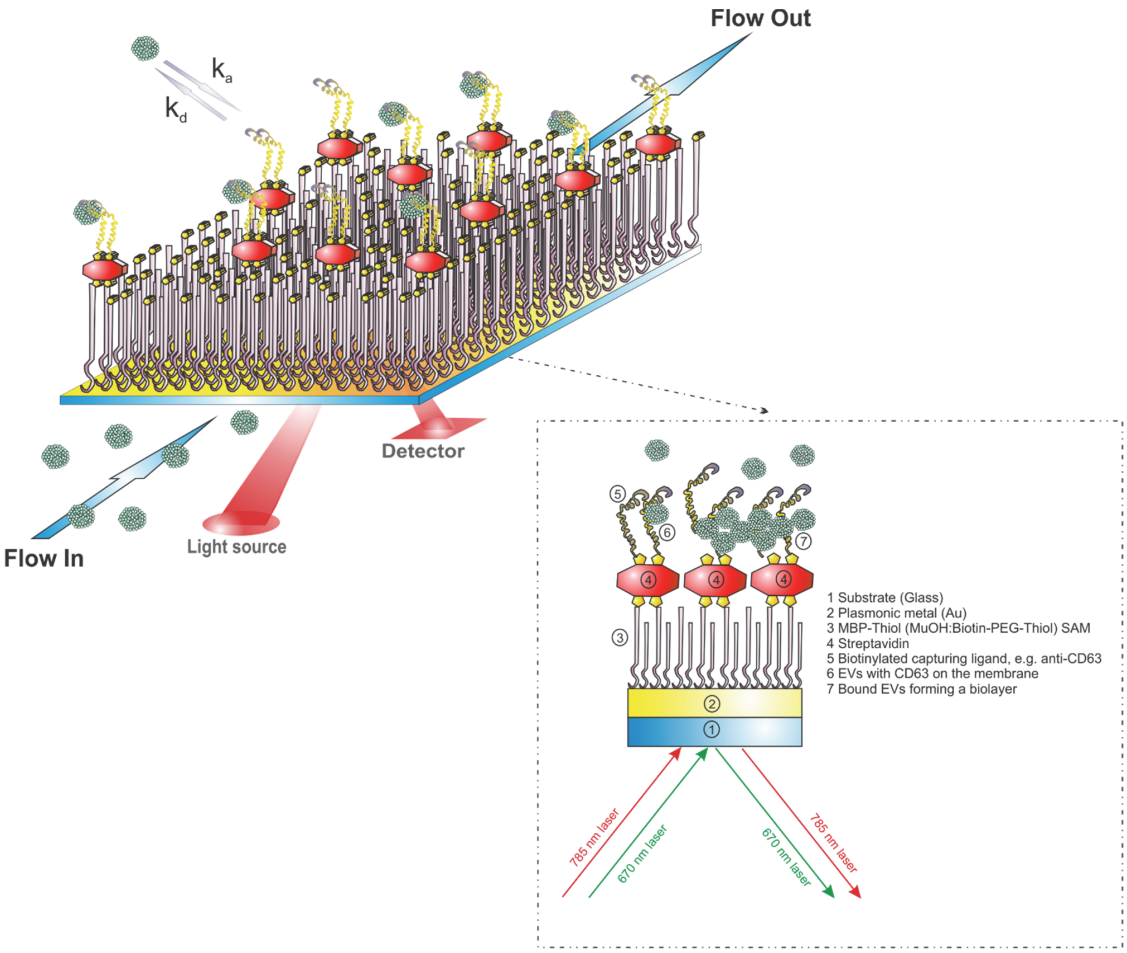

Figure 12. A schematic representation of an MP-SPR measurement using two excitation wavelengths (670 nm and 785 nm) to detect EVs. A self-assembled monolayer (SAM) can be constructed *ex situ* onto the gold sensor surface for example with MuOH (11-mercapto-1-undecanol) + Biotin-PEG-Thiol (biotinylated hexa(ethylene glycol)) undecane thiol (85:15 mol %). Consequently, streptavidin is immobilized *in situ* on the SAM having biotin counterpart available. Lastly, the EVs that have tetraspanin protein CD63 on their membranes can be captured using immobilized (biotinylated) capturing ligand, anti-CD63.

7 CONCLUSIONS OF THE LITERATURE

Biophotonics can provide complementary information to answer the unsolved questions in the field of biopharmaceutical research. Such issues are for instance the perpetual need for new *in vitro* methodology for the purposes of small drug development and the necessity to better understand the pit holes and opportunities in the nanocarrier development. However, caution should be exercised to avoid oversimplification by claiming that biophotonics can replace the existing methods like label-based imaging techniques, proteomics or various chromatographic analysis. Instead, the most informed decisions can be made when the existing methodologies are complemented with new approaches.

The current state of biopharmaceutical research has some prominent gaps that can be bridged by developing biophotonic technology, methods and data analysis techniques. Namely, the resilient photoluminescence problems in Raman spectroscopy hinders its widespread use in many applications – for instance solid state analysis of small molecular weight drugs. There is a need to develop novel technology in order to overcome those drawbacks. Furthermore, techniques and methods for rigorous biochemical characterization of extracellular vesicles on a *single vesicle* level are highly warranted in the field. Such studies could highlight and clarify the diverse functions of extracellular vesicles in living systems, and elucidate their potential to act as nano-medical drug delivery carriers. Advanced Raman spectroscopy techniques, for instance Raman tweezers, enable measurements of biological samples, and they provide high specificity to various chemical structures. Hence, such techniques may bring new insights into the prevailing difficulties confronted in extracellular vesicle research.

In addition, the SPR-based *in vitro* methodologies today are somewhat delimited to monitor merely the interaction kinetics of analytes – regardless the size scale of analytes; small or large. The MP-SPR technology holds a wealth of opportunities for designing *in vitro* protocols whereby the analysis of interaction kinetics can be combined with sophisticated surface characterization. That, in turn, allows for developing *bio-functional assays* whereby the experimental *in vitro* platforms have increased *in vivo* relevance. The biopharmaceutical industry is constantly seeking methods to either accelerate the slow and arduous drug design process or to reduce the astronomical expenditures related to drug development – or both. To facilitate such hardships, MP-SPR platforms could be utilized for testing prospective small drugs in biomimetic environments or for investigating the various phenomena at the *nano-bio interface* that e.g. liposomal drug delivery carriers encounter when administered into the blood circulation. On the other hand, an MP-SPR platform

could act as a diagnostic tool for specifically detecting and characterizing cancerous extracellular vesicles.

It is worth pointing out that it would be favorable to perform the abovementioned analysis in real time without the need of any labels that may alter or bias the measured quantities. In the optimal sequence of events computational simulations and well-refined data analysis methods in combination with complementary experimental methodologies can be used to yield valuable qualitative and quantitative information.

8 AIMS OF THE STUDY

The overall aim of this Thesis was to develop biophotonic technologies, methods and data analysis approaches for modern biopharmaceutical research. The specific aims can be distinguished as follows:

I Demonstrate the effectiveness of the new time-gated Raman spectroscopy system in small drug studies where robust *fluorescence suppression* is utterly needed to acquire interpretable Raman spectral data.

II Develop a biologically relevant experimental *in vitro bio-functional* MP-SPR platform combined with computational simulations to study, how small drugs can interfere the aggregation of Aβ peptides that are known to contribute to the neurodegenerative progression of Alzheimer's Disease. Demonstrate the feasibility of the developed platform using a novel molecule, spin-labeled fluorene (SLF).

III Utilize Raman tweezers technology and multivariate spectral data analysis to investigate and characterize *single extracellular vesicles* isolated from several different cell lines. Demonstrate that the obtained spectral data can be used to interpret the biochemical variation between different types of vesicles.

IV Design an *in vitro bionanophotonic* MP-SPR platform for advanced liposome-based drug delivery carrier (DDC) engineering. To better understand the interactions at the *bio-nano interface*, dynamic flow conditions, undiluted (100%) serum, and novel data analysis methods are employed.

9 SYNOPSIS OF THE MAIN RESULTS

The main results of the studies (I-IV) are illustrated in **Figures 13** and **14**. In **Figure 13** are represented the studies where Raman spectroscopy was used to investigate small drug molecules (I) and EVs as larger scale analytes (III). Correspondingly, **Figure 14** represents the studies where SPR was used to characterize SLF as a potential small drug molecule (II) against AD. Liposome-serum interactions were scrutinized in (IV) to demonstrate the feasibility of SPR for larger scale analytes.

Small drug molecules having varying levels of photoluminescence, more specifically fluorescence, were measured with the time-gated Raman and conventional CW Raman systems (I). The technical advances of the time-gated Raman instrumentation showed significant improvement in fluorescence suppression over the conventional CW Raman systems. The applicability of the LTRS system for EV characterization on a single-vesicle basis was demonstrated in (III). Meticulous Raman spectra analysis revealed differences in the biochemical contents on the membranes of the investigated EV populations originating from healthy and cancerous cells.

An SPR-based study of using a small drug candidate, SLF, in hampering the Aβ peptide aggregation was introduced in (II). The approach was unprecedented; biomimetic environments of various Aβ aggregation schemes were built on a SPR sensor surface. Interaction kinetics between the SLF and the different Aβ forms were determined. Concurrently, it was possible to address that the SLF is capable of acting as a decelerating agent in the Aβ aggregation. In the last stage of SPR studies, the attention was paid to elucidate the role of surface modification of the model liposomes to serum complement system activation (IV). Four different types of surface-immobilized liposomes were let to interact in dynamic flow conditions with undiluted (100%) serum. This novel approach demonstrated that the physicochemical content of the liposomes played a role in the formation of soft and hard protein corona.

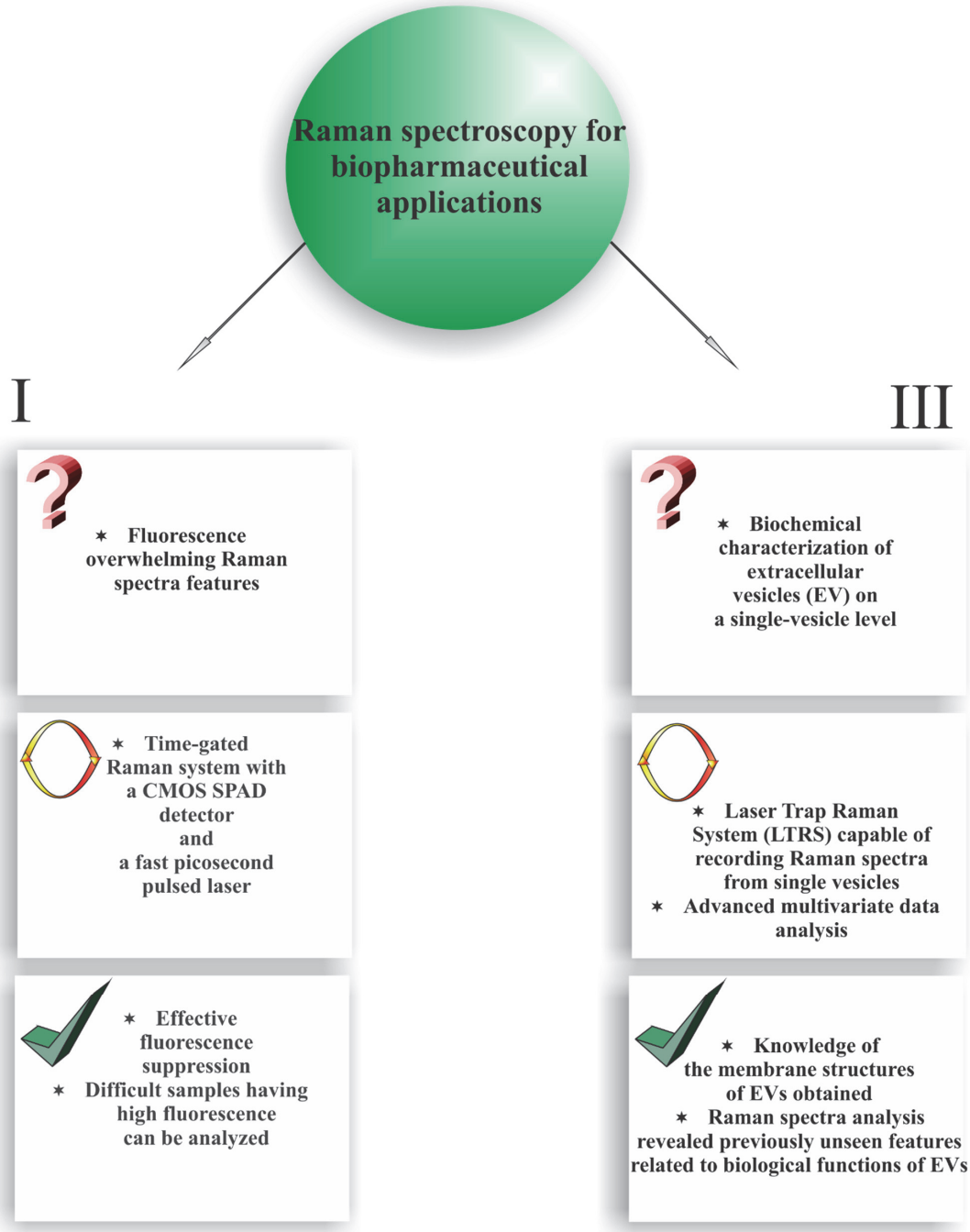

Figure 13. A summary of the main results of Raman spectroscopy studies. The entities are numbered with Roman numerals according to the order of appearance in this Thesis; **(I)** Time-gated Raman system development and optimization for solid state pharmaceuticals, **(III)** LTRS system for single EV studies.

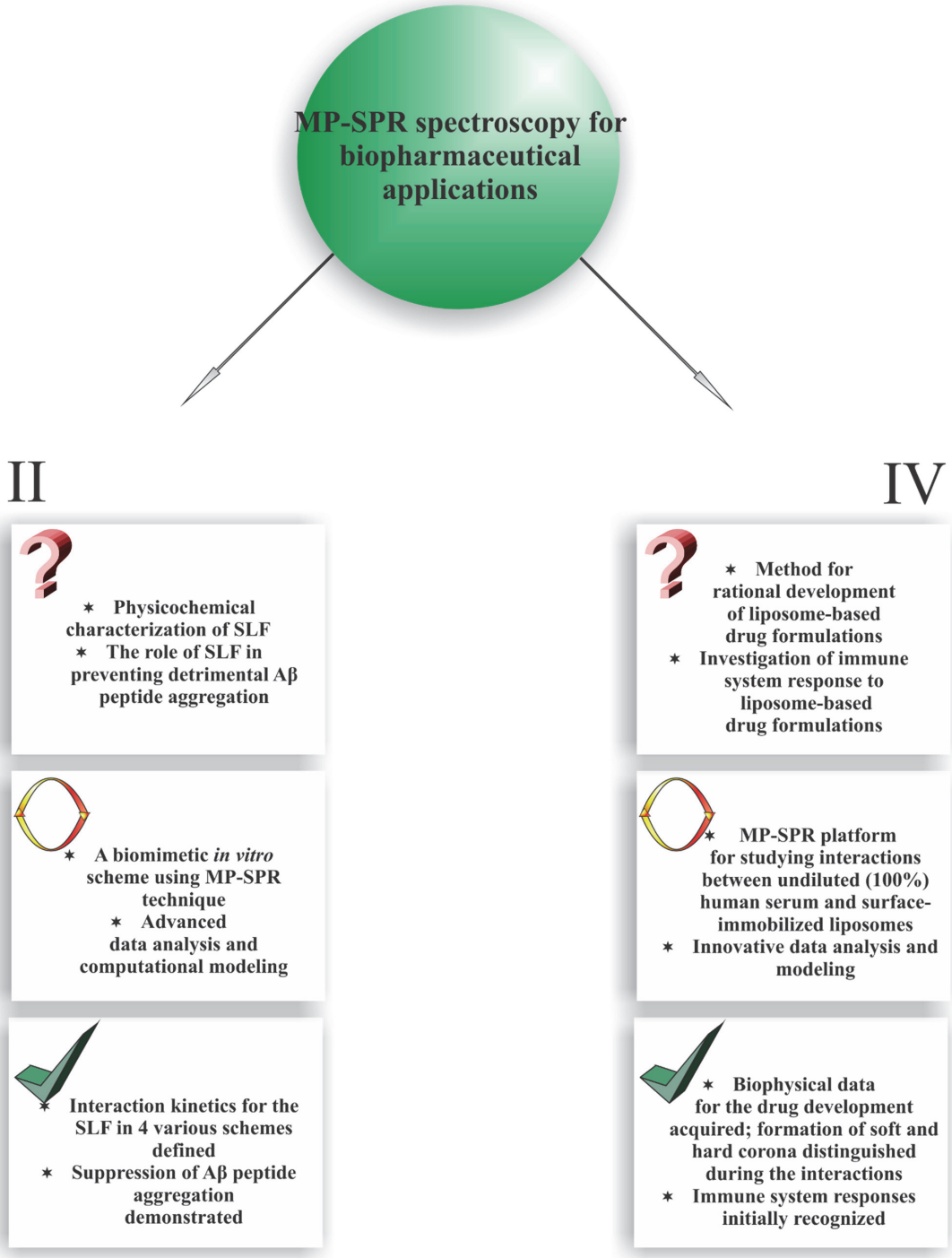

Figure 14. A summary of the main results of MP-SPR studies. The entities are numbered with Roman numerals according to the order of appearance in this Thesis; **(II)** MP-SPR assay platform for studying SLF and amyloid-β aggregation, **(IV)** MP-SPR platform for studying liposome interactions with undiluted serum.

10 OVERVIEW OF THE MATERIALS AND METHODS

The **Table 6** summarizes the essential materials and methods used in the studies.

Table 6. The materials and methods and their purpose used in publications I-IV.

Publication	Material / Method / Technique	Purpose
I	• Caffeine anhydrate • Ranitidine hydrochloride (polymorphic form II) • Indomethacin (crystalline γ-form) • Indomethacin (amorphous) • Continuous wave (CW) Raman instrument at 785 nm excitation wavelength • CW Raman instrument at 532 nm excitation wavelength • Time-gated picosecond Raman instrument at 532 pulsed excitation wavelength & CMOS SPAD detector • MATLAB® software • OriginPro 8.6 software • Gaussian 09 software • GaussSum 2.2 software • GaussView 5.0 software	• Non-fluorescent model compound • Fluorescent model compound • Fluorescent model compound • Fluorescent model compound • Reference system • Reference system • Novel Raman system • Data analysis • Data analysis • Quantum chemical calculations (QCC) • QCC • Visualization of QCC results
II	• Hexafluoro-2-propanol (HFIP) • Dimethyl sulfoxide (DMSO) • Biotin-PEG-SH • 11-Mercapto-1-undecanol • Streptavidin • Biotin • β-amyloid peptide (1-40) • Biotin labeled β-amyloid peptide (1-40) • Low ionic strength buffer (25 mM TRIS, 1 mM EDTA, pH 8.0) • High ionic strength buffer (25 mM TRIS, 150 mM NaCl, pH 7.0) • Dynamic Light Scattering (DLS) • Gold sensor slides (Thickness of Au layer 50 nm) • MP-SPR 200TM instrument with 670 nm and 785 nm excitation wavelengths • SPR NaviTM Data Viewer 4.0 software • TraceDrawer 1.6 software • SPR Navi LayerSolver 1.0.2 software • OriginPro 8.6 software • Autodock Vina 1.1.2 software • GROMACS 5.0.4 software • Automated Topology Builder server v. 2.2 • VMD software	• Solvent • Solvent • Self-assembled monolayer component • Self-assembled monolayer component • Biosensor development • Reference compound • Investigation of Aβ aggregation • Investigation of Aβ aggregation • Monomer peptide preparation • Oligomer peptide preparation • Particle size analysis • Biosensor development • Next-generation SPR system • Data analysis • Data analysis; kinetics evaluation • Data analysis; layer characterization • Data analysis • Molecular docking simulations • Molecular dynamics simulations • Molecular dynamics simulations • Visualization of simulation results

III	• Laser Tweezers Raman Spectroscopy system (home-built) at 785 nm excitation wavelength • Cell culturing using cell lines; Human lung carcinoma (A549), Human hepatocarcinoma (Hu-7), Mouse embryonic fibroblast (3T3), Human lung normal fibroblast (IMR90), Human ovarian carcinoma (SKOV3), Human acute T-cell leukaemia (Jurkat), Human acute myeloblastic leukaemia (Kasumi-1), Human prostate cancer (LNCaP) • Total Exosome Isolation Reagent • Differential centrifugation • Trypsin treatment • Size-exclusion chromatography • Transmission electron microscopy (TEM) • Immunoblot analysis • Nanoparticle tracking analysis (NTA) • Zetasizer Nano Z • MATLAB® software	• Laser trap system for Raman spectroscopy • Sources for extracellular vesicles (total 8 different types) • Exosome isolation; commercial precipitation reagent as a chemical method • Exosome isolation; physical method • Cleavage of EV surface membrane proteins • Purification of trypsin-treated EVs • EV characterization; shape • Confirm EV isolation and digestion of EV surface proteins by trypsin • EV characterization; size distribution and confirmation of nanoparticle contamination • Zeta potential measurements for EVs • Data analysis
IV	• Undiluted (100%) serum; 7 healthy and fasted donors • FLIR TG165 imaging IR thermometer • Liposome samples; Replicas of the Doxil© formulation with and without PEG (DOX+PEG and DOX), Positively charged liposomes with oligo-guanidyl lipid derivative (OGD), In situ PEG-coated OGD liposomes (OGD+PEG) • Human native complement component C3b • Limulus Amoebocyte Lysate (LAL) assays • Zetasizer APS DLS • Zetasizer Nano ZS • MP-SPR 200TM instrument with 670 nm and 785 nm excitation wavelengths • Gold sensor slides (Thickness of Au layer 50 nm) with 6 kDa thin carboxymethyl dextran hydrogel layer functionalized with dodecyl lipid anchors • SPR Navi LayerSolver 1.2.1 software • SPR NaviTM Data Viewer 4.0 software • TraceDrawer 1.6 software • Origin Pro 8.6 software	• Interaction studies with surface-immobilized model liposomes • Heat homogeneity monitoring of serum samples • Model liposomes for surface immobilization and investigation of the nano-bio interface using undiluted serum in flow conditions (i.e. biomimetic environment • For studying kinetic behavior with model liposomes • Endotoxin detection • Physicochemical characterization of liposomes; hydrodynamic diameter • Physicochemical characterization of liposomes; surface charge • Next-generation SPR system • Biosensor development; for immobilizing model liposomes • Data analysis; layer characterization • Data analysis • Data analysis; interaction kinetics • Data analysis

11 (I) Fluorescence-Suppressed Time-Resolved Raman Spectroscopy of Pharmaceuticals Using Complementary Metal-Oxide Semiconductor (CMOS) Single-Photon Avalanche Diode (SPAD) Detector

Adapted from (License CC BY-NC 4.0): Rojalin T, Kurki L, Laaksonen T, Viitala T, Kostamovaara J, Gordon KC, Galvis L, Wachsmann-Hogiu S, Strachan CJ, Yliperttula M. Fluorescence-Suppressed Time-Resolved Raman Spectroscopy of Pharmaceuticals Using Complementary Metal-Oxide Semiconductor (CMOS) Single-Photon Avalanche Diode (SPAD) Detector. Analytical and Bioanalytical Chemistry 408: 761-774, 2016. http://dx.doi.org/10.1007/s00216-015-9156-6

Anal Bioanal Chem
DOI 10.1007/s00216-015-9156-6

RESEARCH PAPER

Fluorescence-suppressed time-resolved Raman spectroscopy of pharmaceuticals using complementary metal-oxide semiconductor (CMOS) single-photon avalanche diode (SPAD) detector

Tatu Rojalin[1,2] · Lauri Kurki[3] · Timo Laaksonen[1] · Tapani Viitala[1] · Juha Kostamovaara[3] · Keith C. Gordon[4] · Leonardo Galvis[6] · Sebastian Wachsmann-Hogiu[2] · Clare J. Strachan[5] · Marjo Yliperttula[1]

Received: 9 September 2015 / Revised: 22 October 2015 / Accepted: 27 October 2015

Abstract In this work, we utilize a short-wavelength, 532-nm picosecond pulsed laser coupled with a time-gated complementary metal-oxide semiconductor (CMOS) single-photon avalanche diode (SPAD) detector to acquire Raman spectra of several drugs of interest. With this approach, we are able to reveal previously unseen Raman features and suppress the fluorescence background of these drugs. Compared to traditional Raman setups, the present time-resolved technique has two major improvements. First, it is possible to overcome the strong fluorescence background that usually interferes with the much weaker Raman spectra. Second, using the high photon energy excitation light source, we are able to generate a stronger Raman signal compared to traditional instruments. In addition, observations in the time domain can be performed, thus enabling new capabilities in the field of Raman and fluorescence spectroscopy. With this system, we demonstrate for the first time the possibility of recording fluorescence-suppressed Raman spectra of solid, amorphous and crystalline, and non-photoluminescent and photoluminescent drugs such as caffeine, ranitidine hydrochloride, and indomethacin (amorphous and crystalline forms). The raw data acquired by utilizing only the picosecond pulsed laser and a CMOS SPAD detector could be used for identifying the compounds directly without any data processing. Moreover, to validate the accuracy of this time-resolved technique, we present density functional theory (DFT) calculations for a widely used gastric acid inhibitor, ranitidine hydrochloride. The obtained time-resolved Raman peaks were identified based on the calculations and existing literature. Raman spectra using non-time-resolved setups with continuous-wave 785- and 532-nm

Published in the topical collection *Nanospectroscopy* with guest editor Mustafa Culha.

Electronic supplementary material The online version of this article (doi:10.1007/s00216-015-9156-6) contains supplementary material, which is available to authorized users.

✉ Tatu Rojalin
tatu.rojalin@helsinki.fi

✉ Clare J. Strachan
clare.strachan@helsinki.fi

[1] Division of Pharmaceutical Biosciences, Centre for Drug Research, University of Helsinki, P.O. Box 56, 00014 Helsinki, Finland

[2] Department of Pathology and Laboratory Medicine, and Center for Biophotonics, University of California Davis, 2700 Stockton Blvd, Sacramento, CA 95817, USA

[3] Faculty of Information Technology and Electrical Engineering, Department of Electrical Engineering, University of Oulu, P.O. Box 4500, 90014 Oulu, Finland

[4] Department of Chemistry, MacDiarmid Institute for Advanced Materials and Nanotechnology, University of Otago, Union Place West, Dunedin 9054, New Zealand

[5] Division of Pharmaceutical Chemistry and Technology, University of Helsinki, Viikinkaari 9, 00014 Helsinki, Finland

[6] School of Chemical Technology, Department of Forest Products Technology, Aalto University, P.O. Box 16300, 00076 Helsinki, Finland

Published online: 09 November 2015

excitation lasers were used as reference data. Overall, this demonstration of time-resolved Raman and fluorescence measurements with a CMOS SPAD detector shows promise in diverse areas, including fundamental chemical research, the pharmaceutical setting, process analytical technology (PAT), and the life sciences.

Keywords Raman · Time resolved · CMOS SPAD · Pharmaceuticals · Fluorescence suppression · Process analytical technology (PAT)

Introduction

Raman spectroscopy is beneficial for diverse types of quantitative and qualitative analyses in fundamental chemical research [1], life sciences [2, 3], and pharmaceutical research and development, for example during dosage form manufacturing, storage, and administration [4, 5]. Other disciplines include material analysis and mineralogy. However, major limitations to its use have included photoluminescence frequently masking the Raman signal [6], weak Raman scattering, and insufficiently sensitive detectors. Some of these problems have been resolved with improvements in hardware, such as the development of efficient, low-noise, silicon-based array detectors, stable high-power diode lasers, and high-resolution spectrometers [7]. Thus, Raman has become widely applied in both basic and applied chemistry. Despite the significant technical advances, the weak signal and simultaneously strongly interfering background from photoluminescence are still hindrances in Raman spectroscopy. This is particularly problematic in the biomedical, life science, and pharmaceutical settings where the analysis of biological samples and drug molecules typically suffers from strong photoluminescence backgrounds. At the same time, there is an unquestionable need for label-free technologies with sufficient temporal resolution for the detection of in situ real-time phenomena. Such measurements include, for example, phase transformation analysis of various drugs and experiments with living cells [8].

The photoluminescence (PL) phenomena can be divided into various types according to the specific molecular relaxation sequences that take place after the absorption of an incident photon [9]. However, fluorescence is usually the main component of photoluminescence and also the one that overlaps spectrally with the Raman spectrum, making it very difficult to remove from Raman measurements. Strong fluorescence is typically created in conjugated double bonds and polycyclic aromatic rings, which are common structures in many drugs and biological molecules. This fluorescence frequently occurs on the same wavelength range as the Raman fingerprint in a given experiment, and as fluorescence is usually a much stronger phenomenon, it can completely overwhelm the Raman signal. The means to alleviate this fluorescence problem in Raman spectrometry can be essentially divided into continuous-wave (CW) and time-resolved approaches. In addition, various algorithm-based methods relying on the spectral post-processing have been introduced. In order to clarify why these methods are typically used, several statements related to photochemical and physical mechanisms of photoluminescence phenomena are needed. Herein, we assume that a laser with the center wavelength λ_L is used as the excitation source. Firstly, the Raman phenomenon is an inelastic scattering process present at all excitation wavelengths, whereas fluorescence requires a nonzero electronic molecular absorption coefficient at λ_L. The intensity of Raman scattering is approximately proportional to $\frac{1}{\lambda_L^4}$. Thus, as a rule of thumb, shorter wavelength lasers give rise to stronger Raman signal intensities. Secondly, the spectral shape of fluorescence from a collection of identical fluorophores is independent of λ_L while the Raman spectrum as a whole is moved to shorter or longer wavelengths along with the excitation. Thirdly, the temporary storage of energy within the molecule after the absorption and relaxation processes entails a characteristic statistical average delay (having an exponential distribution with a certain expectation value) before the emission of a fluorescence photon. This is manifested as the fluorescence "tail" after a short excitation pulse. Theoretically, Raman scattering is an instantaneous process, and it does not involve such delays. However, significant temporal broadening can be observed, which occurs in thick scattering samples; it could be so that the analyte molecules deeper in the sample will interact with the excitation photons even hundreds of picoseconds later than the molecules on the surface [10, 11]. Methods to determine the decay rate of Raman scattering have also been introduced [12]. It turns out that the time dimension provides, in a sense, the most general way to deal with fluorescence in Raman spectrometry. In the following, the CW and time-resolved approaches are briefly described.

In 1976, Funfschilling and Williams resolved the fluorescence-related problems for the first time [13]. They exploited the previously known method of phase sensitive detection that had been effectively applied in nuclear magnetic resonance (NMR), electron paramagnetic resonance (EPR), and photoelectron spectroscopy. The common basis for those methods was to shift the signals of interest away from the interfering background. Thus, by modulating the Raman excitation wavelength, the Raman signal could be recovered from the overlapping fluorescence signal. Later on, a wavelength differential technique was developed and became known as shifted excitation Raman difference spectroscopy (SERDS) [14]. To some extent, differential techniques are applicable to separate fluorescence and Raman signals [15]. Noteworthy approaches include frequency and polarization modulations. The advantage of these differential methods lies in the possibility to separate the non-shifted continuous-

wavelength (CW) fluorescence and Raman signals in a quantitative way. However, in general, these techniques have their limitations, for example acquiring two separate spectra for post-processing in order to resolve the Raman signals.

Since the Raman intensity is proportional to the fourth power of the excitation laser's frequency, the shorter wavelength (i.e., higher frequency) lasers give rise to a stronger Raman signal intensity. However, increasing the excitation photon energy increases also the likelihood of a sample to contain electronically excitable chromophores, each one of which may contribute to fluorescence. Conversely, decreasing photon energy decreases the number of such chromophores. Using λ_L in the NIR range (typically 785–1064 nm) often makes the fluorescence-to-Raman signal ratio decrease markedly or even vanish. FTIR-Raman may be considered the gold standard here. The downsides include the required detector technology (e.g., InGaAs) having a high dark current, which, combined with low Raman efficiency, leads to a reduced signal-to-noise ratio (SNR) [16]. The required high laser powers can also lead to sample damage and destruction by heating. Using λ_L in the UV range (<400 nm) has two advantages: Raman efficiency is high and while fluorescence might be present, it resides in the longer (VIS) wavelengths and thus does not overlap with the Raman spectrum. However, the phenomenon that UV excited Raman does not suffer from fluorescence since it occurs in a different wavelength range is only true for excitation wavelengths in the deep UV below 260 nm. The downsides include the generally increased difficulty in making optics, lasers, detectors, and high-resolution spectrographs for UV, along with the sample degradation due to high photon energy compared to the VIS range [7]. Using algorithms solely without any instrument-based means to subtract the fluorescence background also has drawbacks. For instance, even though the fluorescence profile of the measured sample is relatively recognizable and smooth, a subtraction algorithm produces only an estimate on fluorescence; relevant spectra features may be subtracted, thus biasing the result. Moreover, an additional problem with subtracting fluorescence is that the shot noise will remain. Finally, using photobleaching as a means to exterminate the fluorescence-generating chromophore groups of the molecules can be slow and cause physical changes like burning to the samples. In addition, photobleaching is not a suitable technique for living organism- and cell-based assays.

Next, we consider the time-resolved approach to Raman spectrometry. Several different types of time-gated Raman systems has been demonstrated, among others those based on an intensified charge-coupled device (ICCD) [17], a streak camera, and an optical Kerr gate [18]. The ICCD can reach <100 ps time gate width, and the full optical Kerr gate, combined with a suitable laser, can reach time resolution of a few picoseconds or better. The main drawbacks of these systems compared to the current system based on a complementary metal-oxide semiconductor (CMOS) single-photon avalanche diode (SPAD) matrix and microchip laser are related to the inherent complexity, bulkiness, and/or cost. Instead, the technology at hand in principle enables the development of robust, compact, and affordable time-gated Raman spectrometers with <100 ps time resolution. This follows from the facts that the CMOS SPAD detector does not require extreme cooling unlike scientific CCDs, and the laser technology is also potentially compact. Therefore, this technology offers great promise as practical instrumentation and replacement of CW Raman systems not only in the field of pharmaceuticals but also in general.

A schematic temporal shape of a Raman band with a PL background is shown in Fig. 1. The curves represent schematically the time evolution of the Raman, PL, and total emission intensity following an incident excitation pulse. The elastic part (Rayleigh scattering and Fresnel reflection) has not been depicted. As mentioned before, the Raman process differs from the luminescence mechanisms with respect to the nature and magnitude of the associated delays between photon incidence and emission. The typical time scales for Raman are in the sub-picosecond to picosecond range [12, 19], whereas those of fluorescence (the fastest spontaneous PL process) are in the 10-ps to 100-ns range [9]. Thus, if we take the laser pulse width Δt=150 ps, the shape of the depicted Raman pulse is very close to that of the excitation pulse apart from a scaling factor. Using a fast photodetector such as a SPAD, one can choose to record only the part of the emission pulse containing the Raman pulse, in other words rejecting the PL tail. Essentially, the associated photon noise is also rejected—and this is the one fundamental advantage of a time-resolved Raman measurement over any possible CW Raman measurement, including differential techniques [20]. However, careful inspection of Fig. 1 and the actual measurement data shows that with our 150-ps excitation pulse, some luminescence is emitted already during the pulse. This part of the PL we henceforth call residual fluorescence (RFL). These issues will be discussed in more detail later in this article.

In the present study, we demonstrate for the first time the use of a novel detector system based on CMOS SPAD technology for the study of several pharmaceutical compounds. Here, we utilize the power of combining a picosecond pulsed laser with the time-resolved detection system to efficiently reject the fluorescence and record detailed Raman spectra for those compounds. Using a fast CMOS SPAD detector, we are able to choose and to record only the part of the emission pulse containing the Raman scattering by rejecting the fluorescence tail. The drug molecule response is recorded during the short laser pulses, and the CMOS SPAD detector is synchronized with the laser pulse. However, typically, a part of fluorescence, RFL, temporally overlaps the Raman signal and cannot be rejected by time gating. To overcome the RFL, we present a convenient algorithm to enhance the accuracy of acquired

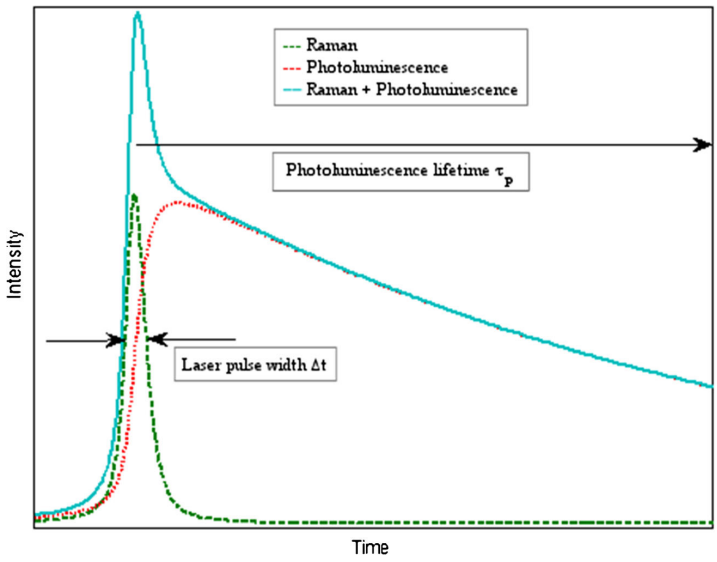

Fig. 1 Schematic representation of the laser excitation, Raman, and photoluminescence signals

Raman spectra. We use a time-gated Raman to measure the Raman spectra of four pharmaceutical compounds. These were selected to include caffeine, as an easy reference compound; ranitidine HCl as a previously less studied and difficult compound; and indomethacin in both amorphous and crystalline forms, as particularly difficult ones suffering from strong fluorescence issues. The capabilities of the new setup were explored and compared to a conventional CW Raman instrument.

Materials and methods

Materials The studied drugs were caffeine anhydrate (Orion Pharma, Helsinki, Finland), ranitidine hydrochloride polymorphic form II (Hawkins Pharmaceutical Group, Minnesota, USA), and indomethacin (crystalline γ-form, Hangzhou Dayangchem, China). The molecular structures of the studied compounds are presented in Table 1. Amorphous indomethacin was prepared by heating the crystalline powder in an aluminum dish for ~15 min. All the other chemicals were measured as received. In conventional Raman measurements, the compounds were measured in sample holders with the powdered drug layer height of approximately 2 cm. In the time-resolved Raman measurements, a smaller amount of drug (approximately 100–200 mg) was placed onto a sample holder. The laser beam was directed onto the samples from above with both setups.

Raman measurements at 785 nm The Raman measurements at 785 nm were performed using a CW Raman RXN1-PhAT-785-D-laser Invictus 785 nm (Kaiser Aerospace & Electronics Company, USA). The probe was PhAT System Probehead (Kaiser Optical Systems, Inc., USA), with collimated incident radiation and a sampling diameter of approximately 6 mm. The average laser power on the sample was ~20 mW. The detector was a charge-coupled device (CCD), 1024×256 EEC MPP Type (Kaiser Optical Systems, Inc., MI, USA) cooled to −70 °C. The measurements were performed at ambient temperature and humidity, with dark background subtraction. Raman shift calibration was performed using cyclohexane. The CW 785-nm Raman spectra presented in this paper are an average of ten scans, each with an acquisition time of 3 s and a spectral resolution of approximately 4 cm^{-1}.

Raman measurements at 532 nm A continuous excitation laser beam was focused down to a micrometer-sized spot on standard substances through a confocal Raman microscope. A frequency doubled Nd:YAG, 532 nm linear polarized excitation laser (~20 mW) was used in combination with ×20 (Nikon, NA 0.40) and ×10 (Nikon, NA 0.25) microscope objectives. The spectra were acquired using a CCD camera (Andor Newton DU970-BV, Andor Technology plc, Belfast, UK) behind a grating (600 g mm^{-1}) spectrograph with a spectral resolution of 2–3 cm^{-1}. Integration times of the signal were 0.5, 1, 2, and 5 s.

Time-gated picosecond Raman The time-resolved measurements were performed using a laboratory setup with the following specifications: The excitation source was a custom-made 532-nm Nd:YVO microchip pulsed laser. The average power used was 14 mW, repetition rate 40 kHz, pulse width 150 ps, focus diameter 50 μm, pulse energy 0.35 μJ, peak power 2 kW, and maximum irradiance 28 MW cm^{-2}. To

Table 1 The chemical structures and physical characteristics of the studied compounds

Drug	Molecular structure, color and appearance
Caffeine	White powder 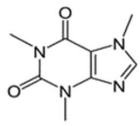
Ranitidine hydrochloride	Pale yellow powder 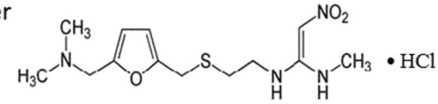
Indomethacin (crystalline)	White powder 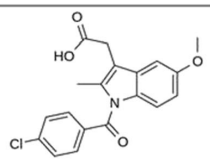
Indomethacin (amorphous)	Yellow, glassy flakes 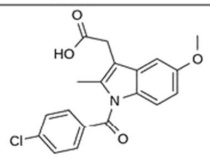

alleviate photobleaching effects, the focal point was periodically moved over an area of about 1 mm^2 by utilizing a custom-made galvo-mirror arrangement. The spectrograph slit was 50 μm, with ×1.7 magnification, 3.4 nm mm^{-1} dispersion, and about 13 cm^{-1} spectral resolution. The detector was the 128×8 CMOS SPAD matrix detector developed by Kostamovaara's group in the University of Oulu. The detector accumulates single-photon events in an internal time histogram consisting of four bins. Only one of these bins was used as the "time gate" in the data analysis presented below. The instrument response function (IRF) is dominated by the laser pulse shape, SPAD response shape, and time gate width of the electronic width generator. The FWHM of the IRF, which is a measure of the system's time resolution, was approximately 250 ps. This approximation has been demonstrated earlier in the literature [16]. The time-resolved spectral datasets were collected by sequentially moving the gate in 50-ps steps using the electronic delay generator. The data acquisition and setup control was maintained by a digital microchip, field-programmable gate array (FPGA). Data acquisition software and setup control were carried out by in-house programs, which were coded using LabVIEW (National Instruments Corporation, TX, USA) language. The data was processed and 3D graphics were plotted using Matlab (MathWorks, MA, USA). The measurements were performed at ambient temperature and humidity, and spectra were the sum of 1.2×10^8–1.7×10^9 pulses corresponding to overall measurement times in the range of 1–12 h. The signal level (counts/laser pulses/pixel) was kept at the suitably low level of a few percent at maximum to avoid signal distortion by photon counting pile-up effects. It is to be noted that the acquisition of a time-gated Raman spectrum alone, without the need to collect the whole temporal shape using a 50-ps step size, can be done in a fraction of the time mentioned above, for instance in the order of minutes or seconds. In future versions of the hardware, larger detectors and adjustable laser repetition rates enable bringing the measurement times to a level that is practical in even field and industrial process applications. The schematic illustration of the Raman and fluorescence events is presented in Fig. 1.

Residual fluorescence background subtraction The RFL subtraction was performed by assuming that the fluorescence is the only contributing factor in the "valleys" of the time-resolved Raman spectra. That signal can then be used to estimate the contribution of fluorescence to the signal intensity in the same time range as the Raman scattering (i.e., where the Raman peaks occur). Unfortunately, the acquired Raman data can be difficult to use for this, as the valleys are at varying heights due to baseline shift and no simple control value can be chosen. In order to get data to be internally comparable, the whole Raman spectrum was first baseline corrected at each

time step using a built-in function (msbackadj) of Matlab. Next, a control value was chosen as the control valley area where it was assumed that the signal is pure fluorescence with no Raman scattering. For better representation of fluorescence, an average signal from three adjacent wavenumber bins was used. The pure Raman spectra were obtained by eliminating the amount of fluorescence by subtracting the control valley from the overall time-resolved response signal.

Fluorescence decay estimations The fluorescence decay estimations were performed assuming that the tested compounds do not have multiple fluorescent components. Thus, a single-exponential decay model, which fits well for gross estimations performed herein, was chosen for the fluorescence decay estimations. Furthermore, the fluorescence decay estimations were based on the assumption that there is only negligible delay between photon absorption and the molecule's relaxation to the lowest vibrational level in the first excited electronic state before transitioning to the electronic ground state by emitting a photon (fluorescence) and non-radiatively (internal conversion) with the rate constants k_F and k_{nr}, respectively. We used a single-exponential decay model based on Eqs. (1) and (2):

$$N(t) = N_0 e^{-(k_F + k_{nr})t}, \quad (1)$$

in which N_0 is the population of excited molecules immediately after a very short (delta function) laser pulse.

$$\Phi_F(t) = k_F N(t), \quad (2)$$

in which Φ_F is the instantaneous fluorescence intensity (photons per unit time) at time t. The overall response function of the instrument is essentially a convolution of the shape of the laser pulse, the IRF, and the exponential decay shape that is described by the characteristic photoluminescence behavior of the sample. To perform the fluorescence decay time estimations for the samples, single-exponential fitting was done to the tail part of the collected data using Eqs. (1) and (2), where applicable. Ideally, the influence of the laser pulse and IRF would be differentiated from the exponential part. However, instead of attempting a de-convolution process to separate the exponential part from the effect of the laser pulse and IRF, estimates of the prospective error were performed with approximate simulations that are described in the "Discussion" section.

Quantum chemical calculations Density functional theory calculations were performed for vibrational mode assignment of the ranitidine HCl spectra (modeled as ranitidineH^+). Molecular optimization and vibrational frequency calculations were performed with Gaussian 09 [21] software using density functional theory (DFT), and the B3-LYP functional with the 6-31G(d) basis set. The predicted vibrational modes were scaled with the recommended factor of 0.9614 [22] using GaussSum 2.2 [23] software and visualized using GaussView (v. 5.0, Gaussian, Inc. Wallingford, CT, USA).

Results

CW Raman measurements at 785 and 532 nm The conventional CW Raman spectra of the model drugs were measured in the region 800–1800 cm^{-1}. This spectral range encompasses the informative Raman features in both the fingerprint and group frequency regions. The CW Raman spectra are shown in Fig. 2A–H. In the Electronic Supplementary Material (ESM) Tables S1–S4, the Raman peaks for every drug are assigned between 800 and 1800 cm^{-1}, based on the quantum chemical calculations published previously or performed in this study. In the tables, selected peaks are assigned for CW non-time-resolved measurements and time-resolved measurements. The spectra have been normalized from 0 to 1, and in order to represent raw spectra, they have not been smoothed.

Panels A and B of Fig. 2 show the Raman spectra of caffeine for CW 785-nm excitation source and CW 532-nm excitation source, respectively. Very low fluorescence intensity can be observed, and the Raman peaks can be easily recognized. Panels C and D of Fig. 2 show the acquired CW 785- and 532-nm Raman spectra for ranitidine hydrochloride. A relatively large fluorescence background hampers the interpretation of both, and only a handful of weak Raman peaks really stand out. In Fig. 2E, F, for the crystalline form of indomethacin, a fluorescence background is present, but observable Raman peaks can be separated with both setups. Using the CW 785-nm excitation source for amorphous indomethacin, Fig. 2G, does not show any spectral details as fluorescence dominates the whole spectrum. As observed in Fig. 2H, the experiment with the CW 532-nm setup reveals more interpretable spectral features.

On the basis of these CW measurements, all the samples had undefined background increase, indicating photoluminescence, except for caffeine. Using the CW 785-nm setup, the most fluorescent sample appears to be amorphous indomethacin, followed by ranitidine hydrochloride and gamma crystalline indomethacin. However, with the CW 532-nm instrument, the most fluorescent drug is

Fig. 2 The Raman spectra obtained using the CW 785-nm Raman spectrometer for caffeine (**A**), the CW 532-nm Raman spectrometer for caffeine (**B**), the CW 785-nm Raman spectrometer for ranitidine hydrochloride (**C**), the CW 532-nm Raman spectrometer for ranitidine hydrochloride (**D**), the CW 785-nm Raman spectrometer for crystalline indomethacin (**E**), the CW 532-nm Raman spectrometer for crystalline indomethacin (**F**), the CW 785-nm Raman spectrometer for amorphous indomethacin (**G**), and the CW 532-nm Raman spectrometer for amorphous indomethacin (**H**). All spectra are normalized from 0 to 1 ▶

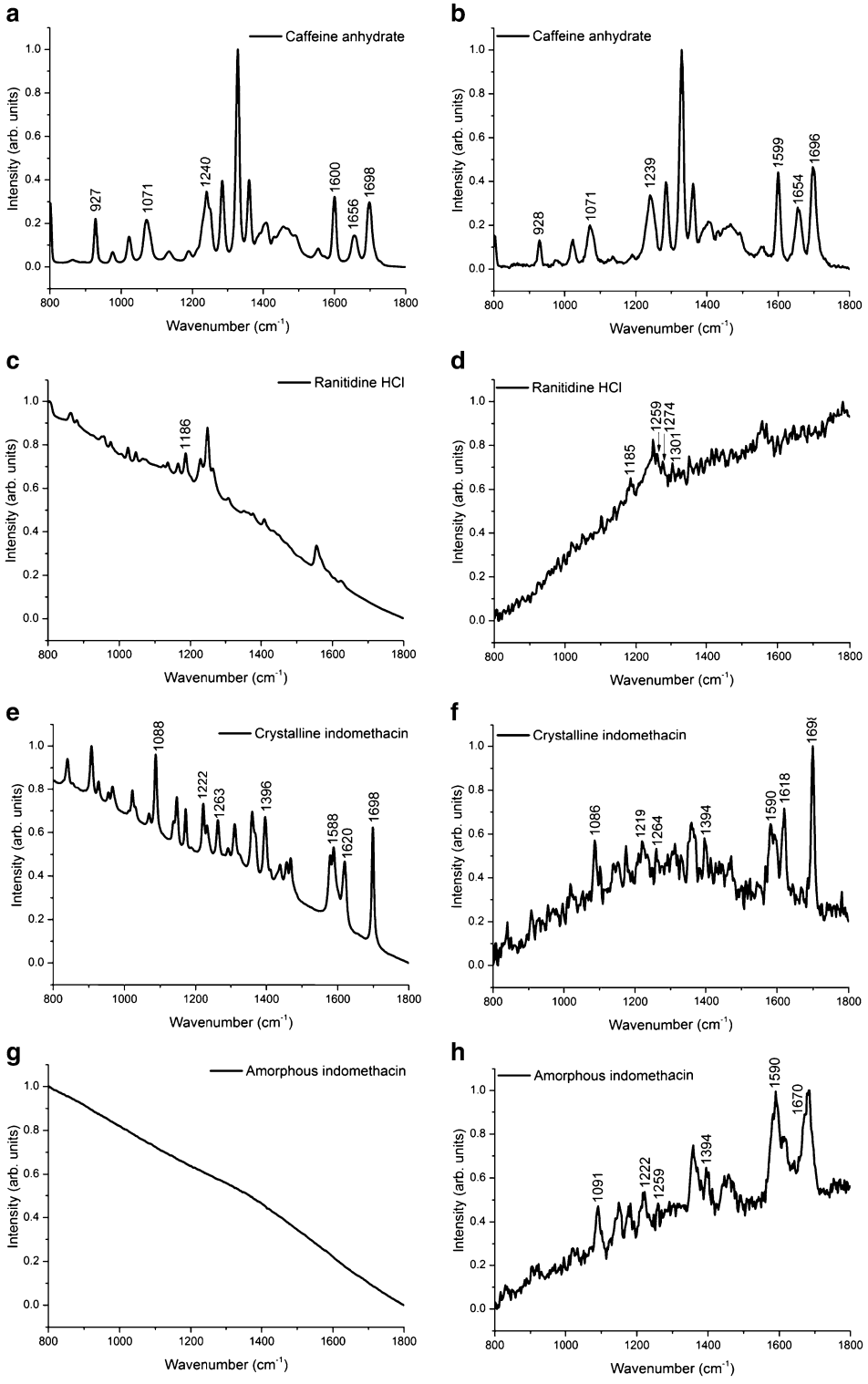
a
Caffeine anhydrate
927
1071
1240
1600
1656
1698
b
Caffeine anhydrate
928
1071
1239
1599
1654
1696
c
Ranitidine HCl
1186
d
Ranitidine HCl
1185
1259
1274
1301
e
Crystalline indomethacin
1088
1222
1263
1396
1588
1620
1698
f
Crystalline indomethacin
1086
1219
1264
1394
1590
1618
g
Amorphous indomethacin
h
Amorphous indomethacin
1091
1222
1259
1394
1590
1670
Intensity (arb. units)
Wavenumber (cm-1)

ranitidine hydrochloride, followed by amorphous indomethacin and then gamma crystalline indomethacin.

Time-resolved Raman measurements The time-resolved spectra for the model drugs are represented in Fig. 3A–D. In the panels, black lines correspond to acquired raw data, blue spectra represent the baseline- and photoluminescence-corrected data, and the 3D representations show the evolution of the measured signal in time dimension. The measurement region was 800–1800 cm^{-1}. The time-resolved spectra (Fig. 3A–D) were recorded separately for the regions 800–1300 and 1300–1800 cm^{-1}. The reason for this is related to the length difference between the detector array and the spectrum produced by the spectrograph in the current setup. The spectra have not been smoothed.

Figure 3A illustrates the time-resolved Raman spectrum for caffeine. Very little fluorescence is observed. However, for ranitidine HCl and both forms of indomethacin (Fig. 3B–D), the fluorescence background is substantially reduced, and more Raman details in the spectra can be seen. As described earlier in this text, the residual fluorescence (RFL) can be subtracted with simple data manipulation. This is demonstrated below for amorphous indomethacin as an example. Figure 4A, B illustrates the acquired raw data. In the next step, the baseline correction is performed, as shown in Fig. 4C, D. A control valley at 1056 cm^{-1} was chosen as the control area where it is assumed that the signal is pure fluorescence with little or no Raman photons. As the shape of the fluorescence does not change much in time, the contribution of this control valley was subtracted from the overall response signal, Fig. 4E, F. The method was able to isolate the Raman peaks, as the 3D spectrum is now homogenously flattened everywhere except the Raman peak areas. In particular, the region between 950 and 1250 cm^{-1} becomes clear with this treatment and four strong and sharp Raman peaks can be easily seen. The estimated decay time for the control valley was the same as the decay time estimated for the raw data. Therefore, the spectral treatment was able to preserve the shape of the fluorescence signal and to isolate the fluorescence free time-resolved Raman response. In summary, this straightforward data processing enhances the interpretation possibilities even further, as the blue spectra show in Fig. 3A–D.

With the present CMOS SPAD detector, three different factors are simultaneously defined: the time distribution of detected photons (Fig. 3A–D: the 3D panel representations; time axis), the photon intensity (Fig. 3A–D: the 3D panel representations; intensity axis), and the energies of photons that arrive at the detector (Fig. 3A–D: the 3D panel representations; wavenumber axis). Thus, an informative representation of photon distribution is obtained as represented in the panels. The 3D representations show the exact starting point of the increase in Raman signal immediately after the laser pulse, as well as the fluorescence rise and decay. For example, in Fig. 3D for amorphous indomethacin, in the time domain, the maximum signal from Raman scattering occurs shortly after the laser shot (yellow- and red-colored peak regions). Moreover, the fluorescence appears to start dominating the response signal at ca. 2.5 ns (blue, decaying slope). It is worth stressing that in the case of relatively thick scattering samples, temporal broadening of Raman signals may have contribution to the time at which the fluorescence starts dominating the response signal [10, 11]. Importantly, this is a sample-specific phenomenon and depends on the sample's fluorescence. The time-domain analysis can be utilized to estimate the fluorescence decay times, which we introduce in the "Discussion" section. Another observation that can be made in the spectra of Figs. 2 and 3 is that the shape of the fluorescence background is negative for the measurements recorded with CW 785-nm excitation, changing to a positive slope in the time-resolved measurements. This effect can be attributed to the different excitation wavelength and to the fact that the NIR experiment is performed at the edge of the sensitivity curve of the CCD detector.

Discussion

Fluorescence rejection with the pulsed picosecond laser and the CMOS SPAD detector

The time-resolved setup used in this study has a 532-nm pulsed laser, and it is combined with the CMOS SPAD detector having relatively fast electronic gating possibility to temporally resolve the Raman spectrum from the fluorescence background. An example can be seen with the amorphous form of indomethacin, which is yellow in color. With the non-time-resolved CW 785-nm setup, it was not possible to detect any Raman peaks due to the fluorescence, and another CW 532-nm instrument had to be used to acquire interpretable Raman spectrum. With the time-resolved CMOS SPAD system, the analysis could be conveniently done at once for all the model

Fig. 3 Time-resolved Raman spectra. *Panels* represent the 2D, traditional Raman spectra (*left*) and the 3D spectra (*right*). The 2D plots are reconstructed from two separate measurements after normalization of the data. The *vertical line* separates the two measurements. The acquired, unprocessed raw data is shown in the 3D plots to give a clear view of the events in the time domain after the laser pulse; the initial rise of signal after the laser pulse consists mainly of Raman scattering, and the settling of the signal consists of the decaying fluorescence signal. The drugs shown in the *panels* are **A** caffeine, **B** ranitidine hydrochloride, **C** indomethacin (crystalline), and **D** indomethacin (amorphous)

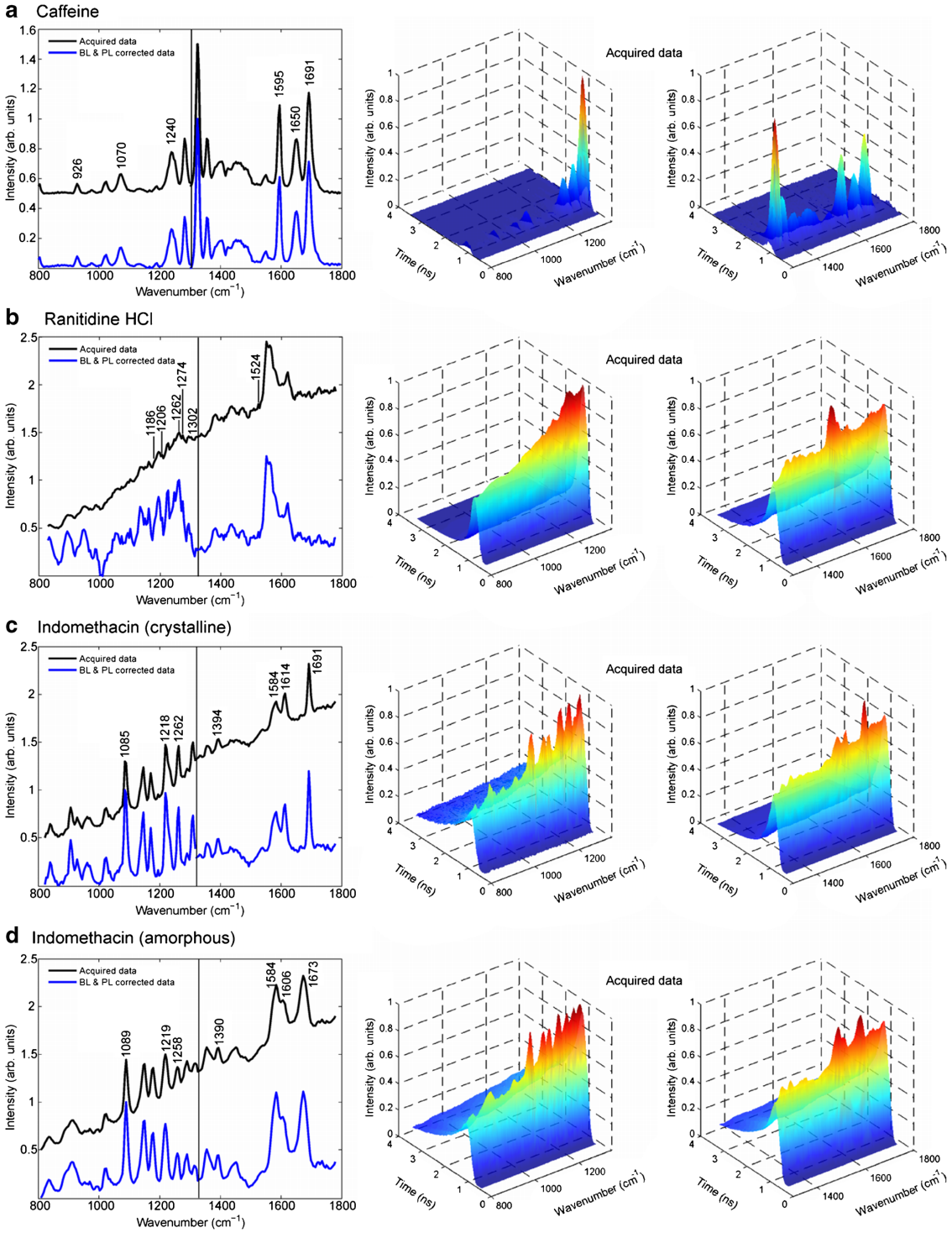
a Caffeine
Acquired data
BL & PL corrected data
926
1070
1240
1595
1650
1691
Intensity (arb. units)
Wavenumber (cm^{-1})
Acquired data
Time (ns)
Wavenumber (cm^{-1})
b Ranitidine HCl
1186
1206
1262
1274
1302
1524
c Indomethacin (crystalline)
1085
1218
1262
1394
1584
1614
1691
d Indomethacin (amorphous)
1089
1219
1258
1390
1584
1606
1673

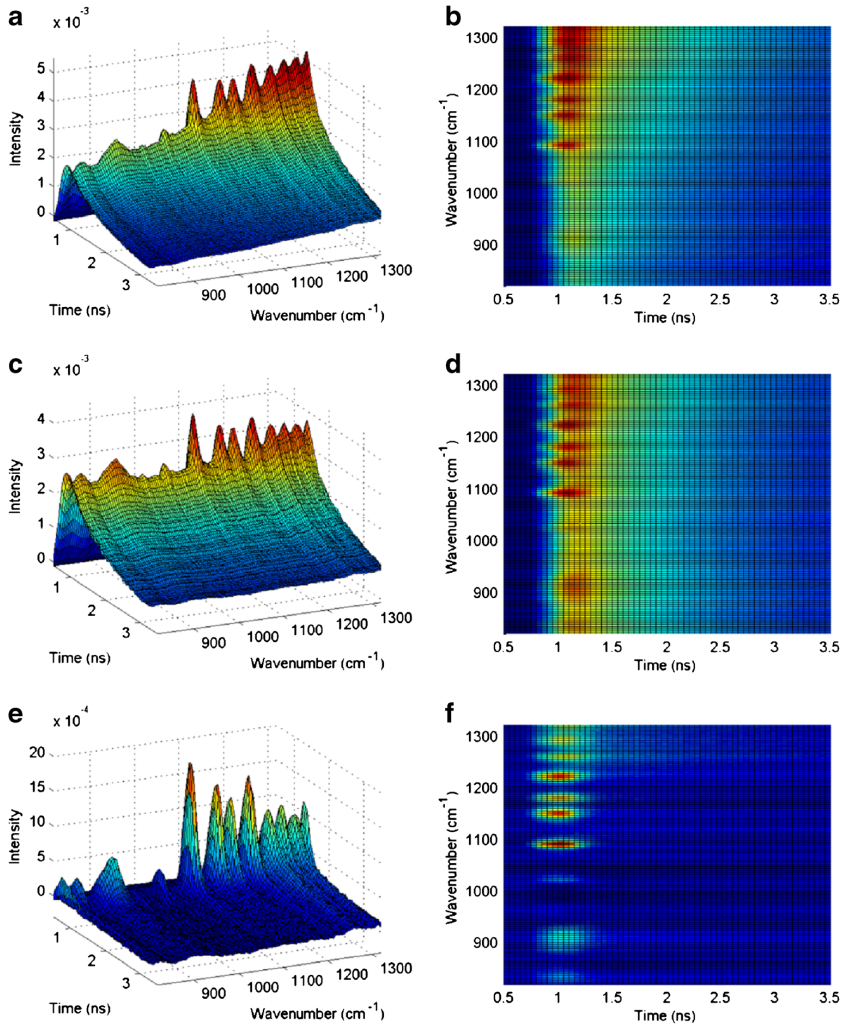

Fig. 4 Acquired Raman data from amorphous indomethacin (**A**, **B**), baseline-corrected data (**C**, **D**), and fluorescence-subtracted data (**E**, **F**). *Panels* on the *left* illustrate the intensity vs. time measurements for each wavenumber shown as a 3D stack. *Panels* on the *right* are also the *top views*

compounds. Furthermore, the other benefits of Raman spectroscopy, such as minimal sample preparation, significant amount of chemical information, and lack of sensitivity to sample water content, are preserved. Combined with the fluorescence-suppressed Raman spectra, the time-domain studies could be a useful tool in Raman spectroscopy to evaluate various changes in a system such as phase transitions or changes in the chemical content of the medium in cell cultures. At the end of this discussion, we preliminarily address the potential of exploiting the time-dimension analysis parallel to the fluorescence-suppressed Raman data. The effect of time resolution is shown in Fig. 3; the spectra are shown as 2D and 3D representations. The 2D spectra represent the spectrum with the highest Raman scattering intensity collected after the laser shot, i.e., it corresponds to one specific time point in the 3D spectrum. This is close to the CW Raman spectra in appearance (Fig. 2), and in terms of signal-to-noise ratio, it is clearly better. On the other hand, if one is interested in the Raman and fluorescence signals' time evolution, the 3D data show the stack of spectra from moments before the emission pulse, the rise of Raman and fluorescence signals, and the decay of fluorescence. Further spectral treatments with simple algorithms can be used to fully eliminate the contribution of residual fluorescence (Fig. 3: BL- and PL-corrected data, Fig. 4) from the time-resolved spectra. It is noteworthy that the time-resolved raw spectra alone are able to show Raman details on all the tested compounds. This makes the instrument potentially able to, for example, identify

compounds or different solid-state forms. However, in accurate quantitative analysis, the algorithm-treated data can be more useful.

Analysis of the measured drugs—new possibilities with the time-resolved Raman

The Raman shifts for selected peaks from the CW 785-nm, CW 532-nm, and the time-resolved spectra are shown in ESM Tables S1–S4. For all crystalline samples, the band positions are in close agreement. Raman band assignments have been previously published using DFT calculations for caffeine and crystalline and amorphous indomethacin, and these are also included in ESM Tables S1, S3, and S4. Computational chemistry-based band assignments have not previously been published for ranitidine hydrochloride, and thus, density functional theory calculations have been included in this study (modeled as ranitidineH^+) and prominent bands assigned in ESM Table S2, together with their corresponding eigenvector diagrams in ESM Fig. S2.

Although the thermodynamically stable crystalline forms of drugs are most commonly used in solid dosage forms, disordered amorphous forms of poorly soluble drugs, such as indomethacin, are of much interest to the pharmaceutical industry as a means to increase their apparent solubilities and associated dissolution rates. The time-resolved setup is capable of revealing the fine structure of both forms, whereas with the CW non-time-resolved instruments, obtaining Raman spectra for both forms was more arduous. This is of utmost importance in the pharmaceutical setting where discrimination between crystalline and amorphous forms of substances is required in order to determine phase transitions or ratios of the two forms in a mixture. Moreover, as the time-resolved setup was able to reveal even subtle Raman spectral features, differentiation between solid-state forms of compounds can be made with this novel Raman system. In the following section, we discuss in more detail the band assignments for the model drugs and describe in conceptual level some benefits that the detailed Raman spectra can offer in pharmaceutical formulation and processing contexts, as well as the novelty value of these Raman measurements compared to traditional methods and instruments.

Caffeine (1,3,7-trimethylpurine-2,6-dione) Caffeine is a well-known central nervous system stimulant, found in many dietary products and occasionally used to stimulate the cardiac and bronchial systems. Caffeine is sensitive to polymorphism—and, from a pharmaceutical point of view, is an interesting compound for closer examination due to the fact that different polymorphs have potentially varying physicochemical properties as well as pharmacological activities [24]. For caffeine, both experimental and computational Raman data are well established; Fig. 2A, B; Fig. 3A; and ESM Table S1 show the measured Raman spectra and band assignments for caffeine, respectively. In the present study, caffeine was chosen to act as an easily measured reference drug. As expected, spectra acquired by CW and time-resolved setups clearly show the bands, and the peaks are in accordance between the instruments and with the DFT-based calculated values that can be found in the literature [24, 25]. The contributions from C–C, C–N, C=N, and C=O bonds can be easily used in, e.g., chemometric analysis.

Ranitidine HCl (*N*-[2-[[[5-[(dimethylamino)methyl]-2-furanyl]methyl]thio]ethyl]-*N*-methyl-2-nitro-1,1-ethenediamine hydrochloride) Ranitidine HCl is a widely used gastric acid inhibitor, acting as an H2 receptor antagonist. Ranitidine HCl has two major polymorphs, form I and form II [26]. Different solid-state forms or polymorphs of the same compound exhibit different pharmaceutically important physical properties such as crystal habit (morphology), melting point, and aqueous solubility. Therefore, identification and characterization of the solid-state forms is important. In the case of ranitidine HCl, form II exhibits favorable filtration and drying characteristics over form I due to morphological differences, and this practical advantage was the basis for its much disputed patent upon its serendipitous discovery by Glaxo Group Ltd in 1981. Part of the patent disputes focused on difficulties in analysis of the solid-state forms. Raman spectroscopy has since been shown to be a convenient technique for this purpose [27]. Here, we present for the first time the quantum chemical calculations to determine Raman peaks for ranitidine HCl. On the basis of computational chemistry we performed, the furan ring and CH_2 (1170 cm^{-1}), the CH_2 groups (asymmetric rock at 1254 cm^{-1} and wag 1301 cm^{-1}), furan (symmetric stretch at 1533 cm^{-1}), and the CH_2SCH_2 group (symmetric wag at 1276 cm^{-1}) contribute to the Raman spectrum of ranitidine HCl. According to Fig. 2C, D; Fig. 3B; and ESM Table S2, the CW 785-nm Raman system has very limited capability to resolve interpretable peaks, whereas the CW 532-nm and the time-resolved CMOS SPAD instruments accomplish better to provide peaks that are relatively well in line with the DFT calculated values. However, these observations begin to show the limitations of conventional CW Raman setups; one has to rely on multiple-wavelength systems to measure various samples, which is not often feasible or even possible. Interestingly, the Raman peak at 1185 cm^{-1} has been evaluated to be characteristic of ranitidine HCl polymorphic form II whereas the peak at 1208 cm^{-1} would describe the existence of form I [28]. In Fig. 3B, 1186 and 1206 cm^{-1} exhibit shoulders of other peaks, suggesting the existence of both polymorphic forms in the sample. Furthermore, if the time-resolved representation of the 2D spectrum, in Fig. 3B (black line showing the acquired raw data), was chosen to be constructed from a slightly different time point, the feature at 1186 cm^{-1} appeared more

dominant (data not shown), and the signal was not swamped by the otherwise strong fluorescent background, leading to the hypothesis that form II was dominant in the sample. This observation shows an important feature which is available with the time-resolved CMOS SPAD technique. Namely, by varying the time point (sampling point), from which the 2D Raman spectrum is constructed, it is possible to utilize the acquired raw data without further processing. A CW system at 532 nm performed better over the CW 785-nm system in the case of ranitidine HCl, but in general, the apparent fluorescence rejection factor is very low, even with the time-resolved Raman setup. It is worth stressing that the relatively low fluorescence rejection factor might be due to a short lifetime fluorescent impurity contribution that is difficult to sort out regardless of the system used. Nonetheless, compared to the conventional CW systems, which have no possibility to examine the spectra in the time dimension and at different time points after the laser shot, the potential of this time-resolved technique becomes clearer.

Indomethacin (crystalline) (2-[1-(4-chlorobenzoyl)-5-methoxy-2-methylindol-3-yl] acetic acid) Indomethacin is a non-steroidal anti-inflammatory drug. The crystalline γ-form is the most stable form of indomethacin at room temperature, and it exists as dimers in this solid-state form [29]. In the present study, Fig. 2E, F; Fig. 3C; and ESM Table S3 show the experimental and calculated data for crystalline indomethacin. Variations between the measured and calculated values exist for some peaks; however, the same trend can be observed in an earlier study [30]. Nonetheless, the measured positions for the peaks with the CW Raman systems and the time-resolved setup match up relatively well, and the characteristic chlorobenzene and indole ring contributions as well as oxygen and nitrogen containing stretching vibrations are clearly observed in the spectra.

Indomethacin (amorphous) For poorly water-soluble drugs, the amorphous form has a significant advantage over the crystalline form, with a higher dissolution rate and apparent solubility, but the downside is reduced stability during processing and storage [31]. Thus, e.g., the manufacturing process involving amorphous forms can be hard to control. Raman spectroscopy has proven to be the most sensitive method for the investigation of various amorphous forms of indomethacin when the forms have been studied with different techniques and multivariate analysis [32]. However, a 1064-nm FT-Raman accessory has been a prerequisite to acquire an interpretable Raman spectrum without prior bleaching for amorphous indomethacin. Figure 2G, H; Fig. 3D; and ESM Table S4 show the experimental and calculated data for amorphous indomethacin. Herein, with the 785-nm CW Raman system, a useful Raman spectrum was practically impossible to acquire. The CW experiment at 532-nm excitation gave quite visible Raman peaks; however, the sample was not chemically stable with 5-s integration times, leading to a dramatically raised baseline and subsequent saturation of the detector due to photoluminescent degradation products. Thus, the integration time of 2 s was chosen to be used with the CW 532-nm setup.

When using the 532-nm excitation laser and time-resolved detection, we are able to acquire a detailed Raman spectrum for amorphous indomethacin. In an attempt to avoid the laser-induced sample degradation, the galvo-mirror arrangement was used to move the laser beam spot on the sample constantly. Thus, we get the advantage of the short-wavelength excitation source giving rise to higher Raman scattering intensities while fluorescence is simultaneously efficiently suppressed by the time-resolved technique. A similar inconsistency between DFT calculated peak values and measured peak values is seen as in the case of the crystalline form of indomethacin. However, the spectra in Fig. 3C, D reveal detailed features that can be conveniently utilized to investigate crystalline and amorphous forms of indomethacin. For instance, the region between wavenumbers 1080–1450 cm^{-1} shows clear shifts in peak intensities, shapes, and positions. Similar differences are also seen in the range of 1500–1700 cm^{-1}.

The acquisition of accurate Raman spectra of both forms can be performed with effective fluorescence suppression without the need to switch between systems or perform excessive data processing. Therefore, the time-resolved technique presented here could open up new possibilities, e.g., in analyzing the phase transition processes in pharmaceutical settings and investigating compounds that are known to be laborious to measure with Raman instruments due to weak signals and interfering fluorescence backgrounds.

Preliminary perspectives on the capabilities of the time-dimension analysis The current time-gated measurement system has two main capabilities: first, rejection of sufficiently long-lived fluorescence or other background radiation from a Raman signal, and on the other hand, measuring the spectrally resolved fluorescence decay shape. We applied the previously described single-exponential tail fitting to the studied samples. Now, since caffeine does not have a fluorescence background to speak of, and ranitidine HCl has very short fluorescence lifetime, the only meaningful results are found in indomethacin. However, in the case of ranitidine HCl, even with the time-resolving capacity in the present study being restricted by the compound's short fluorescence lifetime and thus the setup's time resolution, we were still able to make an estimate of the fluorescence lifetime of ranitidine HCl. Namely, we could tell whether the fluorescence lifetime was short or long—a feature not available on conventional Raman setups. The fitted, uncorrected lifetimes for indomethacin are about 2.1 ns for crystalline indomethacin and 2.3 ns for amorphous indomethacin. According to a rough simulation model we

performed, the actual, de-convolved lifetimes are approximately 100–200 ps shorter (data not shown). The exponential fittings on the measured data are shown in ESM Fig. S1. The capabilities of the system to measure general fluorescence decay shapes (e.g., find parameters of multi-exponential decays) will be expanded in the future. This involves determination of the instrument response function (IRF) in the sense that its effects can be de-convolved. For measuring the actual vibrational dynamics associated with the Raman processes [12, 19], neither the time nor the wavelength resolution of our system is sufficient. Nevertheless, in our current data, one can detect certain ambiguities concerning the temporal shapes of certain Raman peaks; these observations merit a further study with higher temporal resolution in order to ascertain their origin and significance.

Conclusion

We have shown the potential of fast, picosecond pulsed 532-nm laser excitation coupled with a fast and sensitive CMOS SPAD detector to overcome the known Achilles heel, fluorescence, in Raman spectroscopy. In addition, compared to the conventional methods, we are potentially able to have more detailed structural information on our sample molecules with Raman spectroscopy by utilizing the efficiently fluorescence-suppressed and accurate Raman spectra, and the time-domain detection capability. The technical advantages of this CMOS SPAD detector have been previously discussed elsewhere [16]. Now, we demonstrate for the first time a step towards applications with this time-resolved Raman system. We record fluorescence-suppressed Raman spectra of solid, amorphous and crystalline, and non-photoluminescent and photoluminescent drugs such as caffeine, ranitidine hydrochloride, and indomethacin (amorphous and crystalline forms). The raw data acquired by utilizing only the picosecond pulsed laser and a CMOS SPAD detector proved useful for identifying the compounds directly without any data processing. Relatively straightforward algorithms can further diminish the fluorescence contribution in the acquired spectra, showing potential for accurate quantitative analysis. In summary, our major findings were as follows. Firstly, by utilizing the high photon energy 532-nm pulsed excitation source, we are able to observe accurate Raman spectra features. The quantum mechanical calculations for one of our model drugs, ranitidine hydrochloride, the comparison to existing literature, and experiments performed with CW 785- and 532-nm Raman setups verified this. Secondly, we are able to diminish the strong fluorescence backgrounds, especially on amorphous indomethacin. The findings with our model drugs indicate the applicability of this time-resolved Raman technique to overcome the ever-present problems of weak signal and fluorescence in Raman spectroscopy—not only in pharmaceutical settings but also in many other fields that would benefit from the accurate chemical information Raman spectroscopy offers. Several applications in the field of pharmaceutical industry and bio- and life sciences would benefit from the time-domain assays with Raman spectroscopy. For example, phase transition processes, cellular uptake studies, and cell culture studies regarding changes of the chemical concentrations in the culture medium or nanoparticle uptake studies would be potential areas for future research. Another potential option for further studies would be an investigation of several drug molecules in amorphous and crystalline solid-state forms. The setup described is potentially a powerful and convenient tool to overcome current fluorescence-related limitations of Raman spectroscopy for laboratory and off-laboratory use, while simultaneously providing complementary information for Raman measurements in the form of time-domain analysis. The advantages of using this CMOS SPAD technique over the existing instruments (for example [17, 18]) are practical and robust operation of the system, compact size, and affordable cost. In the case of varying samples in terms of fluorescence interference, the CMOS SPAD setup can be feasibly used for a range of samples without the need to change from one instrument to another. Thus, it offers a very potential choice of instrument for the field of Raman spectroscopy. Having showed that this new Raman technique effectively suppresses fluorescence, we envisage that it has also widespread application in different pharmaceutical and biopharmaceutical contexts that have previously suffered from fluorescence phenomena.

Acknowledgments Timo Laaksonen, Tapani Viitala, and Marjo Yliperttula acknowledge funding from the Academy of Finland grants no. 258114, 137053, and 292253, respectively. Clare Strachan and Tatu Rojalin acknowledge funding from the University of Helsinki for a 3-year research project (2014–2016).

Conflict of interest Lauri Kurki is affiliated with the company that commercialized the introduced CMOS SPAD detector technology. The other authors have no conflict of interest.

References

1. Kudin KN, Ozbas B, Schniepp HC, Prud'Homme RK, Aksay IA, Car R (2008) Raman spectra of graphite oxide and functionalized graphene sheets. Nano Lett 8(1):36–41

2. Cao YC, Jin R, Nam J-M, Thaxton CS, Mirkin CA (2003) Raman dye-labeled nanoparticle probes for proteins. J Am Chem Soc 125(48):14676–14677
3. Bell SE, Sirimuthu NM (2006) Surface-enhanced Raman spectroscopy (SERS) for sub-micromolar detection of DNA/RNA mononucleotides. J Am Chem Soc 128(49):15580–15581
4. Wartewig S, Neubert RH (2005) Pharmaceutical applications of Mid-IR and Raman spectroscopy. Adv Drug Deliv Rev 57(8): 1144–1170
5. Vankeirsbilck T, Vercauteren A, Baeyens W, Van der Weken G, Verpoort F, Vergote G, Remon JP (2002) Applications of Raman spectroscopy in pharmaceutical analysis. TrAC Trends Anal Chem 21(12):869–877
6. Cialla D, März A, Böhme R, Theil F, Weber K, Schmitt M, Popp J (2012) Surface-enhanced Raman spectroscopy (SERS): progress and trends. Anal Bioanal Chem 403(1):27–54
7. Denson SC, Pommier CJ, Denton MB (2007) The impact of array detectors on Raman spectroscopy. J Chem Educ 84(1):67
8. Kneipp K, Haka AS, Kneipp H, Badizadegan K, Yoshizawa N, Boone C, Shafer-Peltier KE, Motz JT, Dasari RR, Feld MS (2002) Surface-enhanced Raman spectroscopy in single living cells using gold nanoparticles. Appl Spectrosc 56(2):150–154
9. Lakowicz JR (2006) Introduction to fluorescence. In: Principles of fluorescence spectroscopy. 3rd edn. Springer Science+Business Media, LLC, New York, NY, pp 1-26
10. Hooijschuur J-H, Iping Petterson IE, Davies GR, Gooijer C, Ariese F (2013) Time resolved Raman spectroscopy for depth analysis of multi-layered mineral samples. J Raman Spectrosc 44(11):1540–1547. doi:10.1002/jrs.4369
11. Everall N, Hahn T, Matousek P, Parker AW, Towrie M (2001) Picosecond time-resolved Raman spectroscopy of solids: capabilities and limitations for fluorescence rejection and the influence of diffuse reflectance. Appl Spectrosc 55(12):1701–1708
12. Laubereau A, von der Linde D, Kaiser W (1972) Direct measurement of the vibrational lifetimes of molecules in liquids. Phys Rev Lett 28(18):1162–1165. doi:10.1103/PhysRevLett.28.1162
13. Funfschilling J, Williams DF (1976) CW laser wavelength modulation in Raman and site selection fluorescence spectroscopy. Appl Spectrosc 30(4):443–446
14. Shreve AP, Cherepy NJ, Mathies RA (1992) Effective rejection of fluorescence interference in Raman spectroscopy using a shifted excitation difference technique. Appl Spectrosc 46(4):707–711
15. Angel MKD SM, Hanck KW, Wertz DW (1984) Computer-controlled instrument for the recovery of a resonance Raman spectrum in the presence of strong luminescence. Anal Chem 56:3000–3001
16. Kostamovaara J, Tenhunen J, Kögler M, Nissinen I, Nissinen J, Keränen P (2013) Fluorescence suppression in Raman spectroscopy using a time-gated CMOS SPAD. Opt Express 21(25):31632–31645. doi:10.1364/OE.21.031632
17. Efremov EV, Buijs JB, Gooijer C, Ariese F (2007) Fluorescence rejection in resonance Raman spectroscopy using a picosecond-gated intensified charge-coupled device camera. Appl Spectrosc 61(6):571–578
18. Matousek P, Towrie M, Parker A (2002) Fluorescence background suppression in Raman spectroscopy using combined Kerr gated and shifted excitation Raman difference techniques. J Raman Spectrosc 33(4):238–242
19. Rothschild WG (1976) Motional characteristics of large molecules from their Raman and infrared band contours: vibrational dephasing. J Chem Phys 65(1):455. doi:10.1063/1.432789
20. Kabuss J, Werner S, Hoffmann A, Hildebrandt P, Knorr A, Richter M (2010) Theory of time-resolved Raman scattering and fluorescence emission from semiconductor quantum dots. Phys Rev B Condens Matter Mater Phys 81(7):075314
21. Frisch M, Trucks G, Schlegel H, Scuseria G, Robb M, Cheeseman J, Scalmani G, Barone V, Mennucci B, Petersson G (2009) Gaussian 09, revision A. 1. Gaussian Inc, Wallingford, CT
22. Scott A, Radom L (1996) Harmonic vibrational frequencies: an evaluation of Hartree-Fock, Moeller-Plesset, quadratic configuration interaction, density functional theory, and semiempirical scale factors. J Phys Chem 100(41):16502–16513
23. O'boyle NM, Tenderholt AL, Langner KM (2008) Cclib: a library for package-independent computational chemistry algorithms. J Comput Chem 29(5):839–845
24. Nolasco MM, Amado AM, Ribeiro-Claro PJ (2006) Computationally-assisted approach to the vibrational spectra of molecular crystals: study of hydrogen-bonding and pseudo-polymorphism. ChemPhysChem 7(10):2150–2161. doi:10.1002/cphc.200600308
25. Pavel I, Szeghalmi A, Moigno D, Cinta S, Kiefer W (2003) Theoretical and pH dependent surface enhanced Raman spectroscopy study on caffeine. Biopolymers 72(1):25–37. doi:10.1002/bip.10248
26. Pratiwi D, Fawcett JP, Gordon KC, Rades T (2002) Quantitative analysis of polymorphic mixtures of ranitidine hydrochloride by Raman spectroscopy and principal components analysis. Eur J Pharm Biopharm 54(3):337–341
27. Taylor LS, Langkilde FW (2000) Evaluation of solid-state forms present in tablets by Raman spectroscopy. J Pharm Sci 89(10): 1342–1353
28. Chieng N, Rades T, Aaltonen J (2011) An overview of recent studies on the analysis of pharmaceutical polymorphs. J Pharm Biomed Anal 55(4):618–644. doi:10.1016/j.jpba.2010.12.020
29. Kistenmacher TJ, Marsh RE (1972) Crystal and molecular structure of an antiinflammatory agent, indomethacin, 1-(p-chlorobenzoyl)-5-methoxy-2-methylindole-3-acetic acid. J Am Chem Soc 94(4): 1340–1345. doi:10.1021/ja00759a047
30. Strachan CJ, Rades T, Gordon KC (2007) A theoretical and spectroscopic study of gamma-crystalline and amorphous indomethacin. J Pharm Pharmacol 59(2):261–269. doi:10.1211/jpp.59.2.0012
31. Hancock BC, Parks M (2000) What is the true solubility advantage for amorphous pharmaceuticals? Pharm Res 17(4):397–404
32. Savolainen M, Heinz A, Strachan C, Gordon KC, Yliruusi J, Rades T, Sandler N (2007) Screening for differences in the amorphous state of indomethacin using multivariate visualization. Eur J Pharm Sci 30(2):113–123

Analytical and Bioanalytical Chemistry

Electronic Supplementary Material

Fluorescence-suppressed time-resolved Raman spectroscopy of pharmaceuticals using complementary metal-oxide semiconductor (CMOS) single-photon avalanche diode (SPAD) detector

Tatu Rojalin, Lauri Kurki, Timo Laaksonen, Tapani Viitala, Juha Kostamovaara, Keith C. Gordon, Leonardo Galvis, Sebastian Wachsmann-Hogiu, Clare J. Strachan, Marjo Yliperttula

Table S1 Selected peak assignments for caffeine

CW 785 nm (cm^{-1})	CW 532 nm (cm^{-1})	Time-resolved (cm^{-1})	DFT values (cm^{-1})	Predicted description
927	928	928	927	imidazole in-plane ring deformation [1]
1071	1071	1070	1073	C-C stretching + C-N stretching [1]
1240	1239	1240	1241	C-C stretching + C-N stretching [1]
1600	1599	1595	1599	C=N, C-N stretching + CH_3 symmetric bending [1]
1656	1654	1650	1654	C = C stretching [1]
1698	1696	1691	1698	C = O stretching [1]

Table S2 Selected peak assignments for ranitidine hydrochloride

CW 785 nm (cm^{-1})	CW 532 nm (cm^{-1})	Time-resolved (cm^{-1})	DFT values (cm^{-1})	Predicted description
1186	1185	1186	1170	Furan ring and CH_2
-	-	1206	1203	CH_2 symmetric rock with furan ring
-	1259	1262	1254	CH_2 asymmetric rock
-	1274	1274	1276	CH_2SCH_2 symmetric wag
-	1301	1302	1301	CH_2 wag
-	-	1524	1533	Furan symmetric stretch

Table S3 Selected peak assignments for indomethacin (crystalline)

CW 785 nm (cm^{-1})	CW 532 nm (cm^{-1})	Time-resolved (cm^{-1})	DFT value (cm^{-1})	Predicted description
1088	1086	1085	1074	C-C stretching, in-plane chlorobenzene ring breathing [2]
1222	1219	1218	1222	C-C stretching, out-of-phase C-O-C stretching, out-of-phase C-N-C stretching (mainly dimer) [2]
1263	1264	1262	1254	Out-of-phase C-N-C stretching (monomer) and out-of-phase N-C-C stretching (dimer), out-of-phase C-O-C stretching, in-plane indole and chlorobenzene ring deformations, C-O stretching (dimer) [2]
1396	1394	1394	1408	C-C stretching, in-phase C-H inversion [2]
1588	1590	1584	1595	Chlorobenzyl ring deformation, C-C stretching [2]
1620	1618	1614	1615	C-O stretching, indole ring deformation [2]
1698	1698	1691	1705	C=O stretching [2]

Table S4 Selected peak assignments for indomethacin (amorphous)

CW 785 nm (cm^{-1})	CW 532 nm (cm^{-1})	Time-resolved (cm^{-1})	DFT value (cm^{-1})	Predicted description
-	1091	1089	1074	C-C stretching, in-plane chlorobenzene ring breathing [2]
-	1222	1219	1222	C-C stretching, out-of-phase C-O-C stretching, out-of-phase C-N-C stretching (mainly dimer) [2]
-	1259	1258	1254	Out-of-phase C-N-C stretching (monomer) and out-of-phase N-C-C stretching (dimer), out-of-phase C-O-C stretching, in-plane indole and chlorobenzene ring deformations, C-O stretching (dimer) [2]
-	1394	1390	1408	C-C stretching, in-phase C-H inversion [2]
-	1590	1584	1570	In-plane indole ring deformation [2]
-	-	1606	1615	C-O stretching, indole ring deformation [2]
-	1670	1673	1705	C=O stretching [2]

Fig. S1 Single exponential fittings on the response functions for the fluorescence decay estimations. Panels: A) caffeine (wavenumber range 1800 cm^{-1}-1300 cm^{-1}), B) caffeine (1300 cm^{-1}-800 cm^{-1}), C) crystalline indomethacin (1800 cm^{-1}-1300 cm^{-1}), D) crystalline indomethacin (1300 cm^{-1}-800 cm^{-1}), E) amorphous indomethacin (1800 cm^{-1}-1300 cm^{-1}), F) amorphous indomethacin (1300 cm^{-1}-800 cm^{-1})

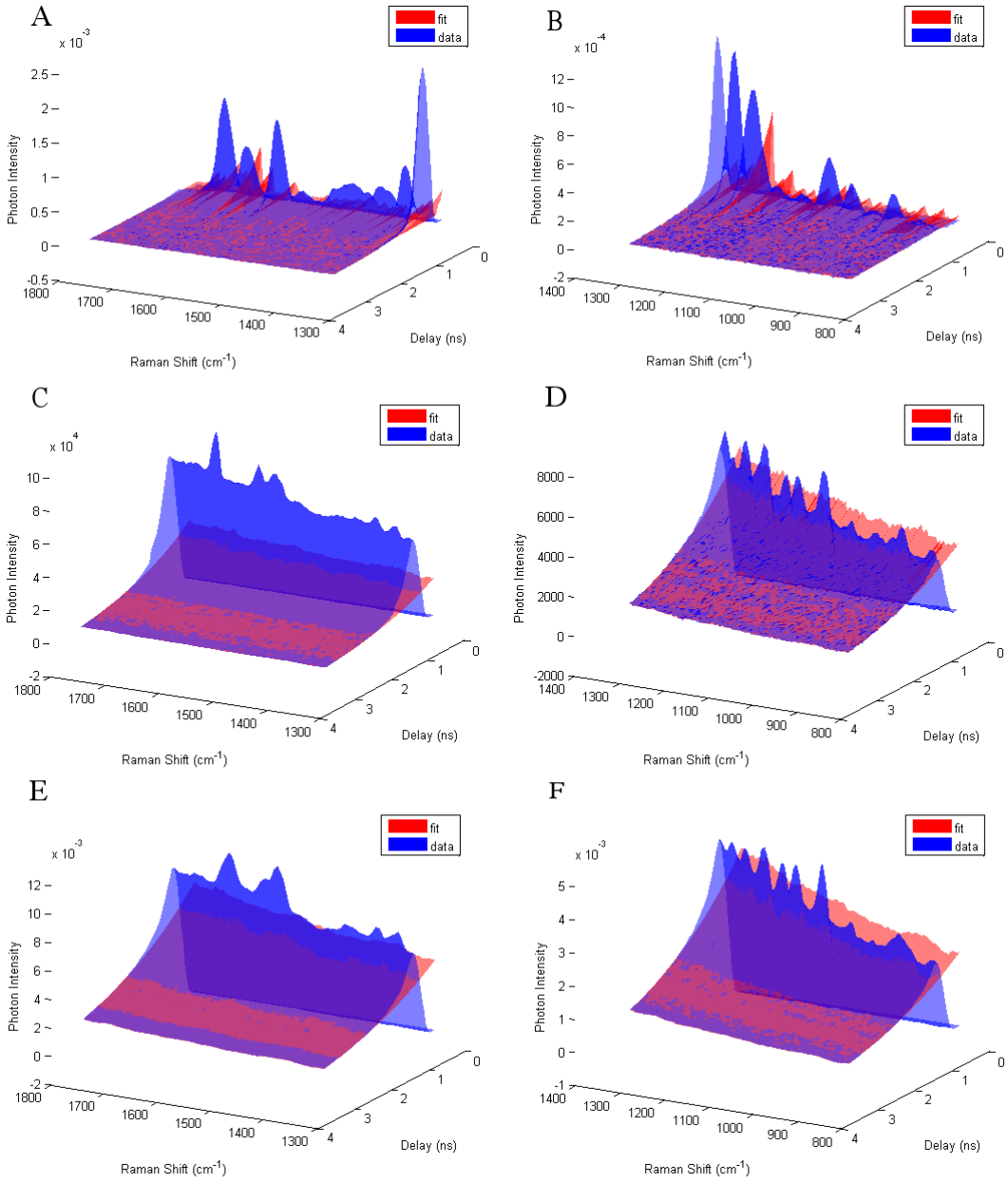

Fig. S2 Eigenvector diagrams for prominent modes of ranitidine HCl (modeled as ranitidineH^+). Values are calculated frequencies as presented in Table S2

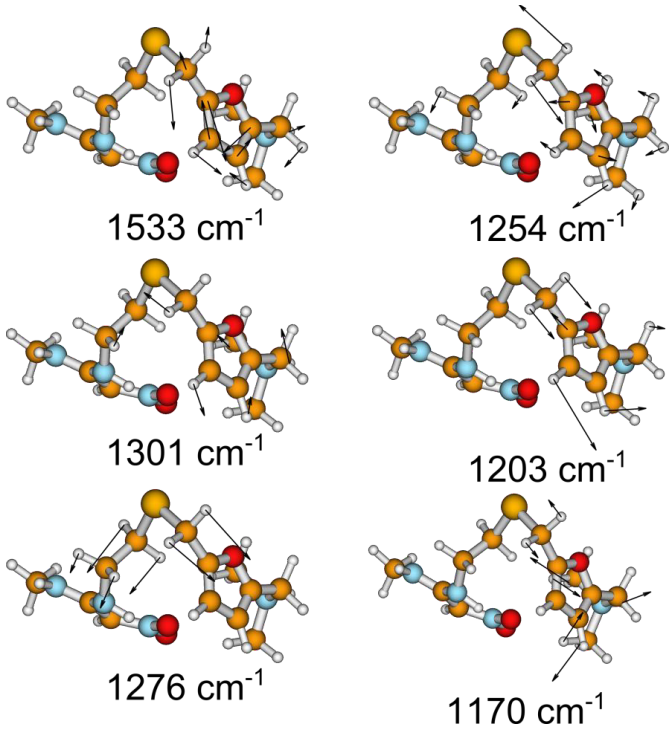

References

1. Nolasco MM, Amado AM, Ribeiro-Claro PJ (2006) Computationally-assisted approach to the vibrational spectra of molecular crystals: study of hydrogen-bonding and pseudo-polymorphism. ChemPhysChem 7 (10):2150-2161. doi:10.1002/cphc.200600308

2. Strachan CJ, Rades T, Gordon KC (2007) A theoretical and spectroscopic study of gamma-crystalline and amorphous indometacin. J Pharm Pharmacol 59 (2):261-269. doi:10.1211/jpp.59.2.0012

12 (II) Amyloid Beta Oligomerization Alters Its Affinity for a Modulator of Peptide Aggregation and Toxicity

Rojalin T‡, Hilt S‡, Viitala T, Koivuniemi A, Bunker A, Wachsmann-Hogiu S, Yliperttula M, Voss JC. Amyloid Beta Oligomerization Alters its Affinity for a Modulator of Peptide Aggregation and Toxicity. Submitted manuscript.
http://dx.doi.org/
‡ Equal contribution

AMYLOID BETA OLIGOMERIZATION ALTERS ITS AFFINITY FOR A MODULATOR OF PEPTIDE AGGREGATION AND TOXICITY

Silvia Hilt[1‡], Tatu Rojalin[2,3‡], Tapani Viitala[3], Artturi Koivuniemi[3], Alex Bunker[3], Sebastian Wachsmann-Hogiu[2,4], Marjo Yliperttula[3,5], and John C. Voss[1*]

[1] Department of Biochemistry & Molecular Medicine, University of California, Davis, CA 95616, USA

[2] Department of Pathology and Laboratory Medicine, and Center for Biophotonics, University of California Davis, USA

[3] Centre for Drug Research, Division of Pharmaceutical Biosciences, University of Helsinki, Finland

[4] Intellectual Ventures / Global Good, Bellevue, WA, USA

[5] Department of Pharmaceutical Sciences, University of Padova, Italy

[‡]S.H. and T.R. contributed equally to this work

*Email: jcvoss@ucdavis.edu.

Running Title: Aβ-SLF interaction: binding kinetics and peptide disassembly

Key words: Amyloid Beta, Alzheimer's disease, Spin-Labeled Fluorene, Aβ Oligomer, MP-SPR, surface plasmon resonance, molecular docking, molecular dynamics simulations, toxic oligomer

ABSTRACT

The soluble oligomeric form of the amyloid beta (Aβ) peptide is generally recognized as the major causative agent in the molecular pathogenesis of Alzheimer's disease (AD). We have previously developed a pyrroline-nitroxyl fluorene compound (SLF) that blocks the toxicity of Aβ. Here we introduce the multi-parametric surface plasmon resonance (MP-SPR) approach to quantify SLF binding and effect on the self-association of the peptide. MP-SPR provides a label-free, real-time approach for measuring the interaction of SLF with soluble Aβ. Kinetic analysis of SLF binding to oligomeric Aβ and measurements of layer thickness alterations inform on the mechanism underlying the ability of SLF to inhibit Aβ toxicity and its progression towards larger oligomeric assemblies. Remarkably, depending

on the oligomeric state of Aβ, distinct binding affinities for SLF are revealed by MP-SPR. The Aβ monomer and dimer uniquely possess sub-nanomolar affinity for SLF, as well as a weaker binding state of ~20 μM. Sub-nanomolar binding is not found in oligomeric Aβ, which displays an affinity for SLF on the order of 100 μM. To complement these experiments we carried out molecular docking simulations to explore how SLF interacts with the Aβ-peptide. Docking calculations predict Aβ-peptide folds around the SLF molecule shielding it from aqueous surroundings. The binding energy calculated for this interaction is on par with the lower affinity interaction measured by MP-SPR. The MP-SPR results together with *in silico* modeling provide essential affinity data on how small molecules interact with Aβ and allow us to develop a new general method for examining protein aggregation.

INTRODUCTION

Alzheimer's Disease (AD) is a progressive, devastating neurodegenerative disease that currently affects nearly five million people in US alone. The incidence of AD is expected to triple by 2050 (1). Although the etiology of AD is complex, multiple lines of genetic, histological and biochemical evidence suggests the amyloid peptide (Aβ) is the primary causative agent (2). The Aβ is constitutively released in the brain through proteolytic processing of the amyloid precursor protein (APP), which is, in turn, cleaved sequentially by β and γ secretases, two aspartyl proteases. Both the rate and site of APP cleavage, as well as the efficiency of Aβ clearance determine eventual neuropathology. Aβ is an intrinsically disordered peptide that undergoes a dynamic aggregation pattern that can ultimately lead to Aβ plaques deposited in the brain (3,4).

Importantly, numerous studies have established that the soluble oligomeric form of Aβ (AβO) represents the neurotoxic form of the peptide (5-7). Hence, there is significant interest in identifying compounds that inhibit Aβ oligomerization. To date diverse set of small molecules have been found to interfere with Aβ oligomerization and amyloid fibril formation, although the binding coordination and structural mechanism for inhibition remains unknown (8-12). A major obstacle to the development of such therapeutic agents is the dynamic structure of the soluble Aβ peptide; toxicity results from various oligomeric forms present throughout the aggregation pathway (13).

We have previously shown that a novel, bifunctional compound can block both Aβ toxicity and oligomer growth (14,15). This small molecule, named spin-labeled fluorene (SLF), contains a fluorene moiety for Aβ-targeting as well as a nitroxide spin label (**Fig. 1).** Biophysical studies indicate that SLF disrupts and inhibits oligomer growth (14,15). The protective effect of SLF against Aβ toxicity is augmented by the free radical scavenging property of the nitroxide spin label (14,16), which is efficient in addressing the strong oxidative element of AD pathogenesis (17-20).

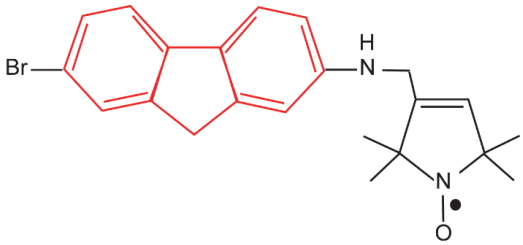

Fig. 1. The chemical structure of spin-labeled fluorene (SLF), a novel compound that disrupts the formation of amyloid plaques. The amyloid binding moiety is shown in red, and the nitroxide spin label in black.

Although the toxic state of Aβ is ill-defined, multiple lines of evidence correlate toxicity with oligomers on the order of 10-60 kDa that contain a high degree of conformational disorder distributed amongst oligomers in dynamic equilibrium (reviewed in (21)). Depending on the conditions, these oligomers progress to larger aggregates or transition into fibrillar-competent species. Obtaining a quantitative description of Aβ structure and toxicity remains a challenge, and the dynamic nature of oligomeric Aβ further complicates efforts to address the mechanism of small molecule modulators of Aβ toxicity. We have therefore employed a label-free approach using surface-immobilized Aβ to measure SLF binding affinity to different oligomeric states of the peptide. The method, multi-parametric surface plasmon resonance (MP-SPR), is additionally useful because it also detects changes in layer thickness (22), and thereby provides information on how small molecule binding can modulate Aβ self-association.

MP-SPR is a feasible technique for studying label-free biomolecular interaction measured in real-time, providing detailed analysis of affinity and kinetics of small molecule interactions as well as a unique method for measuring peptide and protein self-assembly (23). We use the MP-SPR to demonstrate, how the Aβ self-assembly and aggregation can be hampered with our novel SLF molecule. The measurements provide kinetic constants for distinct SLF-Aβ interaction modes, leading to a better understanding of the role SLF plays in modulating Aβ aggregation and toxicity. Furthermore, by calculating layer thickness, the molecular masses deposited onto the MP-SPR sensors are modeled in terms of oligomer size. We demonstrate that MP-SPR is an effective tool for observing Aβ self-assembly and evaluating agents that can modulate peptide aggregation. Finally, we carried out molecular dynamics simulations of the SLF-Aβ interaction, providing insights into possible conformational states that correlate to a lowered toxicity and aggregation propensity for the Aβ peptide. This work represents a continuation in our development of the synergistic combination of label-free analytics and molecular dynamics to obtain key mechanistic insights of pharmaceutical relevance (24). The developed in vitro methodology represents a *bio-functional assay platform* where the biological environment is mimicked in order to enhance the *in vivo* relevance of the study. The platform can also provide a potential multi-purpose tool for other resembling studies where the protein aggregation plays a role.

RESULTS

For all the MP-SPR measurements we used two separate wavelengths, 670 nm and 785 nm. However, the response for each of the lasers of both flow channels was grouped by wavelength and only the 670 nm laser signals for the sensorgrams and MP-SPR angular spectra are shown for easy reading. The mobile phase in experiments consisted of the buffer specific to

the form of Aβ applied in the MP-SPR analysis. Initially, the physicochemical characterization of SLF was performed in four schemes whereby different Aβ peptide compositions and oligomeric Aβ peptide compositions were mimicked and investigated. Thus the mobile phase for monomer analysis consisted of the low ionic strength buffer (25 mM Tris, 1 mM EDTA, pH 8.0) and for AβO consisted of high ionic strength buffer (25 mM Tris, 150 mM NaCl, pH 7.0). In order to demonstrate that the chosen approaches using low and high ionic strength buffers for monomer and oligomer analysis, respectively, yield the desired conditions, dynamic light scattering (DLS) measurements were performed. As determined by the DLS, monomeric Aβ displays a mean diameter 1.4 nm, in agreement with earlier measurements of the Aβ monomer (25). In contrast, the 4-hour AβO species have an average hydrodynamic radius of ~75 nm. The results are shown in **Table 2**.

SLF binds Aβ monomer with a very high affinity. We have shown in previous work that, the SLF small molecule binds to soluble Aβ oligomers and protects against Aβ-induced cell death (14,15). To characterize the binding of spin labeled fluorenes to Aβ, we employed real-time, label-free detection of SLF binding to biotinylated Aβ tethered to a SAM as shown schematically in **Fig. 2**.

We first measured the SLF binding kinetics to the immobilized monomeric Aβ alone. Affinity measurements were carried out by flowing increasing concentrations of SLF over the surface, which has been shown advantageous in the SPR study of high-affinity molecular interactions (26-28). Serial injections of increasing concentrations of SLF over the biotinylated Aβ (**Fig. 3**, blue trace) result in an increase in baseline maintained after the dissociation phase, indicative of SLF binding Aβ and retained as a binary Aβ/SLF complex. Similarly increasing concentrations of SLF injected over the control sensor surface (**Fig. 3**, green trace) show no increase in the baseline, indicative of lack of non-specific binding of SLF to the streptavidin functionalized SAM surface.

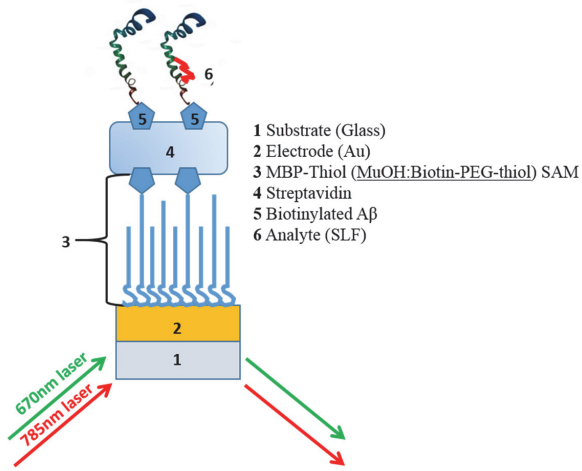

Fig. 2. Schematic diagram of the MP-SPR sensor surface construction (the MBP-Thiol SAM/streptavidin + biotinylated Aβ/analyte assembly). The sensor surface is coated with biotin-functionalized (for streptavidin binding) PEG derivative [MuOH: Biotin-PEG-thiol (85:15 mol %)]. The MBP-Thiol SAM surface is then coated with streptavidin, which immobilizes with high affinity and specificity to biotin. Injection of biotinylated Aβ results in the attachment of Aβ to the sensor surface biotin binding to the available sites of the immobilized streptavidin-biotin bond. The analytes (SLF and/or Aβ) are then flowed over the surface of immobilized Aβ, and SLF binding and/or Aβ self-association result in signal amplification. The volume of all injections is 300 µL and flow rate is 10 µL/mL for streptavidin, biotin, and Aβ, and 20 µL/mL for SLF.

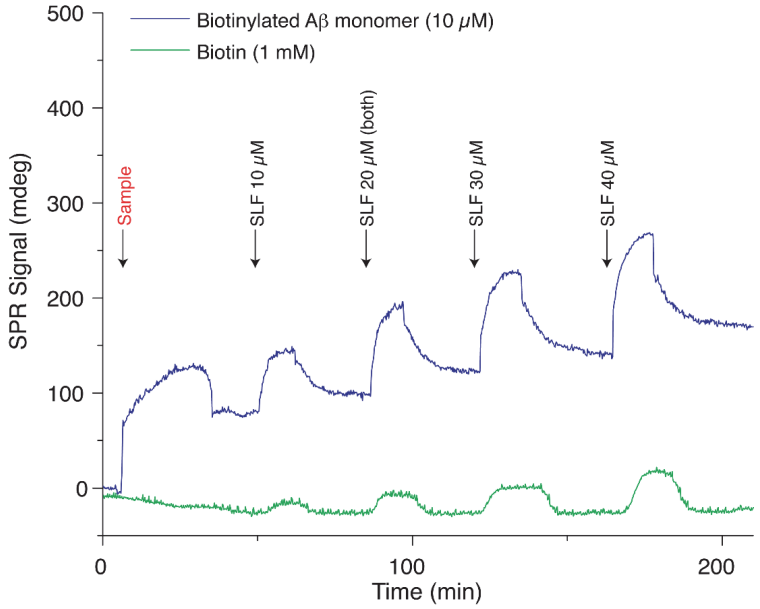

Fig. 3. SLF binds biotinylated Aβ with high affinity. MP-SPR signal response after injections of increasing concentrations of SLF in both flow channels (10, 20, 30, and 40 μM). The sensor surfaces were pre-coated with 10 μM biotinylated monomeric Aβ in the upper flow chamber (blue trace) and the control consisting of 1 mM biotin in the lower channel (green trace). The arrows indicate the time when the injections into both channels were made

SLF binding was best fit according to the 1:2 binding model, indicating that Aβ contains at least two distinct sites or modes for SLF binding (**Fig. 4A**). The presence of two binding sites or modes for SLF within Aβ is also consistent with molecular dynamics simulations (see below). As seen in **Table 1**, using the 1:2 fitting model, we acquire two affinity constants, K_{D1} and K_{D2}. Respectively, the B_{max1} and B_{max2} values are calculated (**Table 1**). In general, the B_{max1} and B_{max2} indicate the maximum signal obtained, which is dependent for example on the number of immobilized ligands or receptors on the surface. Hereby, the B_{max1} and $Bmax_2$ show the relative amount of SLF binding to corresponding binding sites. It is of note that the other parameters of the interaction kinetics analysis (k_{a1}, $k_{d1,}$ etc.) are shown in the *Supplemental Information* **Table S1**. The first value, K_{D1} (~ 1.5×10^{-5} M) tells about a relatively strong binding of SLF. On the other, the K_{D2} ($<1\times10^{-9}$ M) shows that a very strong binding of SLF also takes place to Aβ, indicating binding at some sites is effectively irreversible on the time scale of these measurements. Because the calculation for K_{D2} carries a high level of uncertainty as determined within the time domain of these experiments, its value cannot be accurately determined. However, we can conclude that K_{D2} corresponds to a binding affinity of 1 nM or less. The lack of SLF dissociation is also reflected in the time-resolved presentation of the MP-SPR signals where the baseline raises after each concentration. The significance of the high affinity binding of SLF to the Aβ monomer is discussed below. Overall, the 1:2 fitting model sufficiently accommodates the measured data, with a comparatively low χ^2 value = 34.39. The success of the fitting can also be estimated in the curves of **Fig. 4A**, where the bold red line is the measured data, and the dotted line represents the fitting.

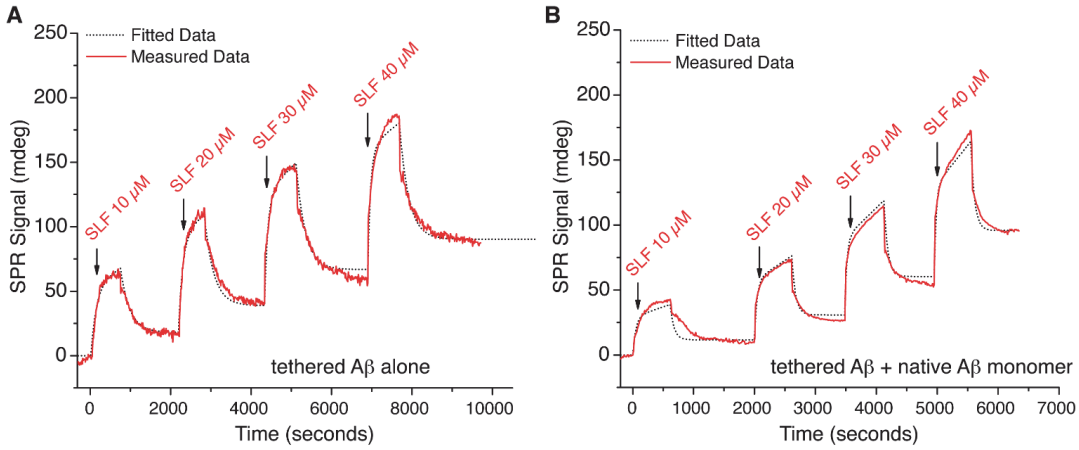

Fig. 4. Binding kinetics show Aβ presents two binding sites. The sensorgrams are extracted from binding of SLF to the tethered monomers of biotinylated Aβ alone (**A**), or a surface consisting of native Aβ monomers bound to the biotin-tethered Aβ monomers (**B**). The native Aβ monomer in (**B**) was injected at 10 μL/min. The flow rate SLF addition in both (**A**) and (**B**) was 20 μL/min. The sensorgrams are shown as a red line, and the fits are shown as a black dashed line. The kinetic parameters obtained from the fits are shown in **Table 1**.

Table 1. Calculated affinity values for different interaction scenarios of Aβ/SLF binary complexes. Data was processed and fitted using TraceDrawer™ for MP-SPR Navi™. Values in parenthesis represent the statistical uncertainty. *An upper limit for K_{D2} is given, as precision in fits cannot be obtained due to the limited dissociation of SLF binding in these samples.

	B_{max1} (Signal)	B_{max2} (Signal)	K_{D1} (M)	K_{D2} (M)	χ^2
SLF with biotinylated Aβ monomer	123.73 ($\pm$ 8.07×10^{-1})	119.58 ($\pm$ 4.28×10^{-1})	1.49×10^{-5} ($\pm$ 8.81×10^{-7})	<1×10^{-9}*	34.39
SLF with native Aβ bound to biotinylated Aβ monomer	137.69 ($\pm$ 1.05×10^{0})	947.24 ($\pm$6.40×10^{-1})	4.06×10^{-5} ($\pm$ 2.36×10^{-6})	<1×10^{-9}*	23.30
SLF with AβO	440.06 ($\pm$1.18×10^{0})	1530.53 ($\pm$8.49×10^{-1})	1.08×10^{-4} ($\pm$-1.48×10^{-5})	1.21×10^{-4} ($\pm$-1.80×10^{-7})	41.63
SLF with AβO pretreated with SLF	499.48 ($\pm$ 1.25×10^{0})	1169.44 ($\pm$ 1.09×10^{0})	1.15×10^{-4} ($\pm$ 1.06×10^{-5})	9.84×10^{-5} ($\pm$ 1.11×10^{-7})	44.63

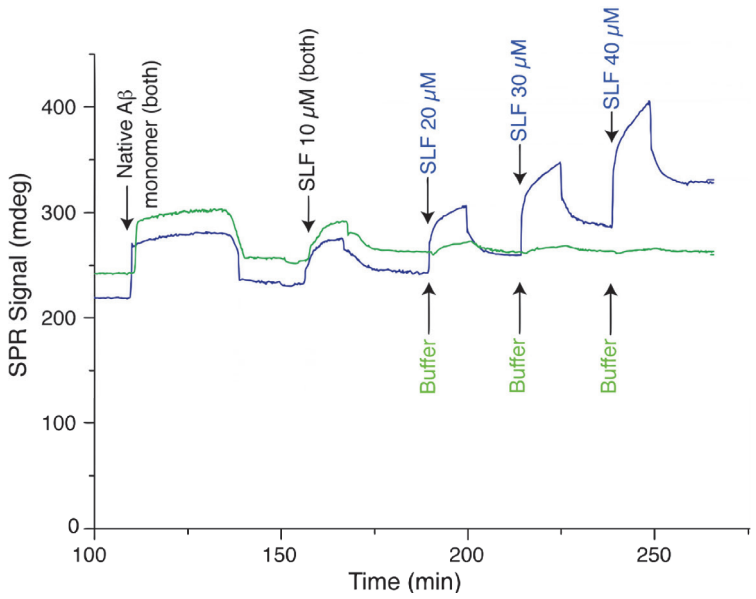

Fig. 5. High affinity SLF binding is also observed with native monomeric Aβ. In the first injection, both sensor surfaces containing biotin-tethered Aβ monomer were coated with 10 μM native monomeric Aβ. The MP-SPR signal response was then followed after injections of various concentrations of SLF, 10, 20, 30, and 40 μM in the upper flow channel (blue trace), and 10 μM SLF, followed by 3 injections of low ionic strength buffer in the lower channel (green trace). SLF and buffer were injected at 20 μL/min.

SLF binds to non-biotinylated Aβ similar to biotinylated Aβ. To compare the binding of SLF to non-biotinylated Aβ we ran another control set-up by flowing 10 μM non-biotinylated Aβ in low aggregation buffer twice over the biotinylated Aβ, at 10 μL/min for 30 min, in low aggregation buffer. Under these conditions, we predict a native monomer binding to the tethered Aβ, resulting in a *mostly dimeric species* on the surface. As shown in **Fig. 5**, injection of the monomer increases the baseline in both channels, consistent with the native Aβ monomer pairing with the tethered Aβ species. After the baseline was stabilized we injected the same series of increasing concentrations of SLF over the biotinylated Aβ, as shown in **Fig. 5**. As before, we kept the injection and flow buffer in low aggregation conditions to minimize Aβ self-association as much as possible. MP-SPR measurements show a similar binding pattern of SLF to non-biotinylated Aβ as the binding to biotinylated Aβ (**Fig. 4B**). The fitting model is again consistent with Aβ containing at least two binding sites or modes for SLF, K_D values of the same order as SLF binding to biotinylated Aβ (affinity parameters shown in **Table 1.**). This result suggests that dimeric Aβ also contains the capacity to bind SLF with a sub-nanomolar affinity.

Oligomeric Aβ lacks very high binding affinity. We next investigated SLF binding to complexes of oligomeric Aβ (AβO) associated with the surface-immobilized Aβ. AβO was prepared in an aggregation-promoting buffer as described in *Experimental Procedures*, and measured by MP-SPR (**Fig. 6,** green trace). Kinetic analysis of the AβO/SLF complexes was also performed using the 1:2 fitting model that takes into account the probability of AβO having at least two binding sites or modes

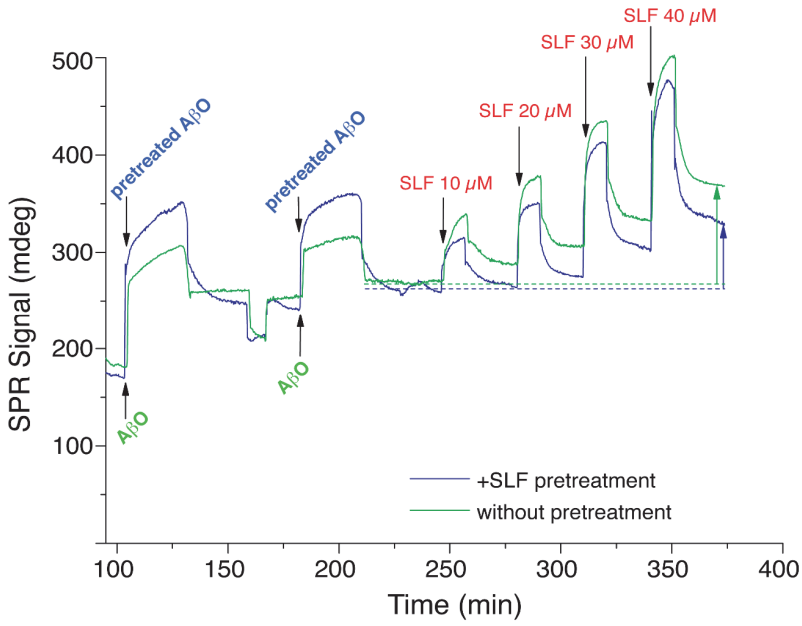

Fig. 6. SLF binding to oligomeric Aβ (AβO). MP-SPR signal response after two successive injections of 10 μM AβO, with (blue trace) or without (green trace) pretreatment of the AβO with 20 μM SLF. After baseline stabilized, increasing concentrations (10, 20, 30 and 40 μM) of SLF were applied through both flow channels. Mobile phase consisted of the high ionic strength, pH 7.0 buffer.

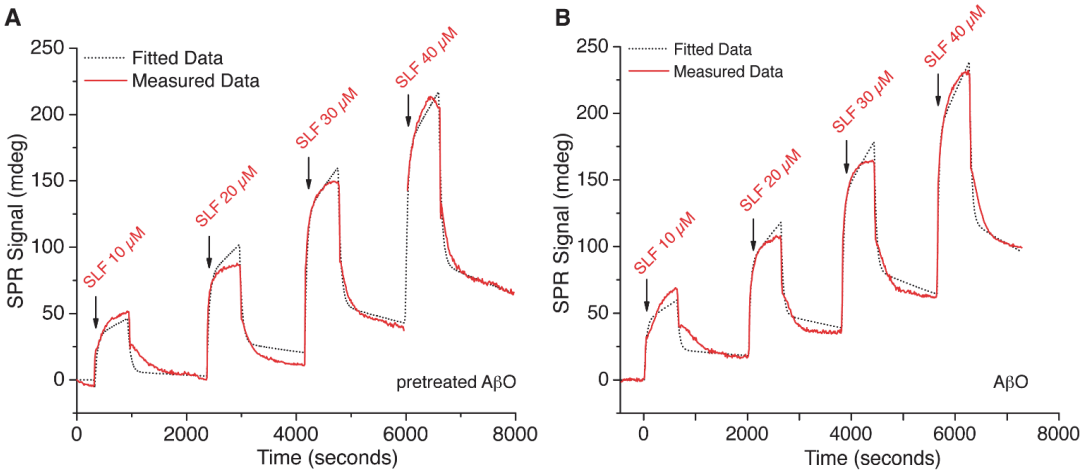

Fig. 7. Binding kinetics of SLF onto oligomeric Aβ. The sensorgrams are extracted from SLF binding to AβO associated with tethered monomers of biotinylated Aβ. The binding of SLF to AβO pretreated with 20 μM SLF is shown in Panel (**A**). The binding of SLF to AβO alone is shown in Panel (**B**). The AβO samples were injected at 10 μL/min, and the SLF solution's flow rate was 20 μL/min. The sensorgrams are shown as a red line, and the fits are shown as a black dashed line. The kinetic parameters obtained from the fits are shown in **Table 1**.

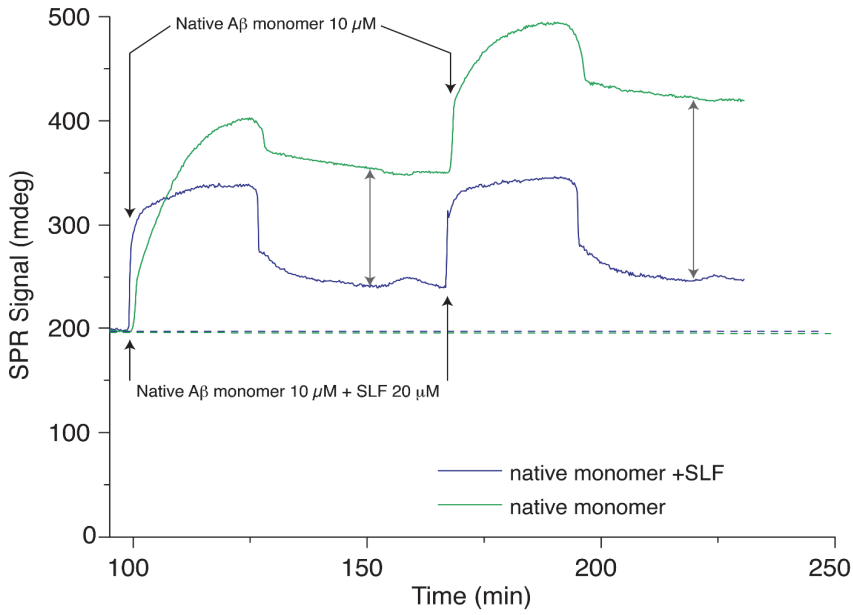

Fig. 8. SLF inhibits Aβ self-association. MP-SPR signal response after injections of native monomeric Aβ (10 μM) over a surface of tethered Ab monomers. Sample without SLF addition is shown by the green trace (lower channel). The same sample mixed with 20 μM SLF is given by the blue trace (upper channel). In both channels the mobile phase is the low ionic strength buffer, pH 8.0, with a flow rate of 10 μL/min.

for SLF (**Table 1; Fig. 7A**). A substantially higher error (i.e. higher χ^2 values) was observed when evaluated by the 1:1 model. Interestingly, in these oligomeric samples both K_D: s are of the same order of magnitude (~10^{-4}-10^{-5} M). Thus, the pre-assembled AβO lacks the very high affinity binding, displaying a comparable lower affinity for SLF in both K_{D1} and K_{D2}. This finding suggests that monomeric/dimeric Aβ displays a uniquely high affinity binding site for SLF, which may also serve to dock other amyloidophilic compounds as well.

In order to evaluate how SLF affects AβO binding, we compared the MP-SPR response of AβO applied over the surface of immobilized Aβ (**Fig. 6**, green trace) to AβO pre-incubated with a 2-fold molar ratio of SLF (**Fig. 6**, blue trace). As shown over the first two injections, AβO without SLF pretreatment binds and sharply returns to baseline, however AβO with SLF pretreatment displays a prominent dissociation phase, suggesting that AβO pretreated with SLF is a more optically-active entity than AβO without SLF pretreatment. Thus the initial interaction signals induced by the pretreated AβO are also stronger. In addition, the dissociation of loosely bound SLF can be clearly seen in the case of pretreated AβO, as it resembles the dissociation kinetics observed when the compound is consecutively injected over AβO. As with the previous SLF binding schemes, the SLF binding to pretreated AβO was performed using the 1:2 binding model (**Fig. 7B**), which yields K_D values similar to AβO without SLF pretreatment (**Table 1**). Noteworthy are the injections of SLF after adsorption of AβO or AβO pretreated with SLF on the surface. As indicated by the smaller increase in the baseline of the sample pretreated with SLF (pretreated AβO; blue trace), a smaller net SLF binding is

observed, consistent with this sample having a lower binding capacity for additional SLF.

SLF inhibits the self-association of Aβ. To investigate if SLF inhibits the self-association of Aβ, we compared the binding of Aβ pre-mixed with SLF (at 1:2 molar ratio based on our previous two binding sites or modes results) with the binding of Aβ alone. Both sample solutions and flow solvent were in low aggregation conditions, favoring monomeric Aβ. As shown in **Fig. 8**, we flowed monomeric Aβ+SLF (blue trace) and monomeric Aβ alone (green trace) over the non-biotinylated Aβ immobilized on the sensor surface. The Aβ without SLF was retained on the sensor surface in a much higher amount, as revealed by the increase in the baseline (green trace) and Aβ+SLF was retained in a much lesser quantity as shown by the lower baseline (blue trace). This result is consistent with previous spectroscopic studies showing that SLF inhibits Aβ self-association (14,15).

SLF mediated oligomerization of Aβ can also be detected by change in layer thickness. Since the theoretical findings (29-31), the multi-wavelength approach in MP-SPR for surface characterization has been successfully demonstrated in multiple applications (32-34). The unique solution for the apparently interconnected thickness (d) and refractive index (n) of the sample layer can be found from the intersection of two continuum solutions, thus the MP-SPR measurements performed at multiple wavelengths can provide a direct indication of the layer thickness, thereby quantification of the mass added to the surface (32,33).

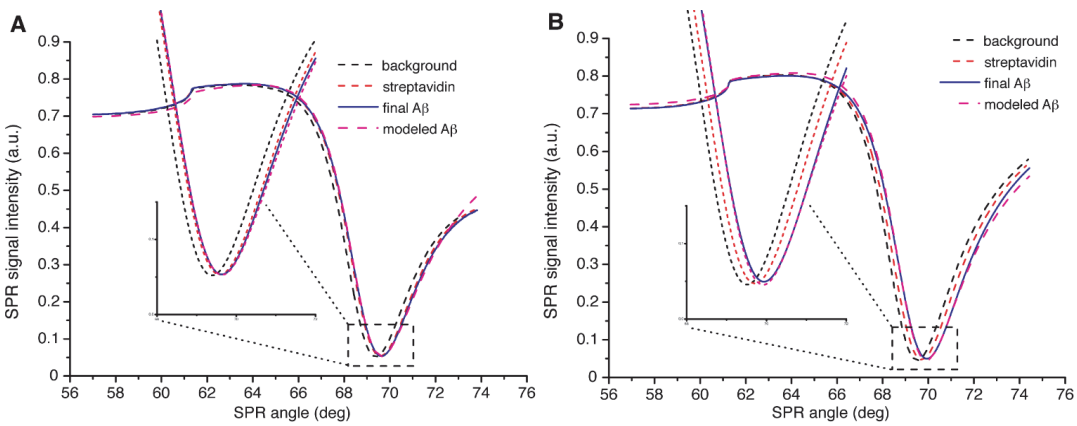

Fig. 9. Layer modeling results for different situations of Aβ layer build-up. Panel **A** represents the biomolecular layer formation from the measurements in **Fig. 8**, where the SLF hampers the self-assembly processes of Aβ. Panel **B** shows the layer construction from the measurement in **Fig. 8** where SLF was not present in the measurement, resulting in greater peptide aggregation (increased layer thickness).

The MP-SPR angular spectra in **Fig. 9** represent the whole layer modeling procedure with intermediate steps shown, based on the data in **Fig. 8**. We started the modeling by determining first the background for our measured layer system, i.e. the metal (gold) layer. It should be noted that this background modeling step was performed with the inclusion of the SAM layer into the background calculation for two reasons; firstly, the contribution of SAM layer was considered very small to the measured MP-SPR angular spectra, and secondly, previous observations support the estimate that the calculation does not suffer from inaccuracies within the context of this analysis (34). The layer after the streptavidin immobilization was measured next, and lastly the final situation after injection of the native Aβ monomer. For clarity, the 670 nm laser data is shown in **Fig. 9** panels (the 785 nm laser data not shown), and the measured MP-SPR angular spectrum is shown with dashed lines in part of the first two steps, and with solid line at the end of the experiment. A shift in the MP-SPR angular spectrum resonance angle to higher angles is observed as the peptide layer is building up in the lower sample channel (**Fig. 9B** and the inset displaying the SPR peak minimum (θ_{SPR}) shift; see also **Fig. 8A** green trace). The corresponding shift is distinctly smaller in the MP-SPR angular spectrum representing the upper channel where the SLF was disrupting the Aβ self-assembly and oligomerization (**Fig. 9A** and inset; see also **Fig. 8A** blue trace). The measured and modeled MP-SPR angular spectra at the final situation are in relatively good agreement for both sample channel layers. Thus we can consider the calculated layer thicknesses (31.89 nm and 1.33 nm) and refractive indices (1.34070 and 1.37139, respectively) being relatively good and descriptive in the context of this analysis.

The layer thickness is clearly increased when SLF was not present in comparison to the situation where SLF was disrupting the self-assembly of the Aβ (**Table 2**). Furthermore, an interesting physical phenomenon can be observed in the refractive indices (RIs); the thinner layer (1.33 nm) without Aβ aggregation has a higher RI than the thicker layer (31.89 nm). This is in agreement with previous observations where a thin molecule layer can possess a higher RI than a thicker layer. Since the molecules can be assembled in a thin layer much more densely than in a sparse, aggregated layer, the light is also refracted more in a denser (but virtually thinner) layer. Another possibility lies in the different swelling properties of the layers; the water-based buffer content of the denser bio-molecule layer is smaller than the buffer content in the sparse, aggregated layer, thus resulting to the observed difference in refractive indices. The hydrodynamic diameters determined by the DLS analysis are shown in the **Table 2**. When the SLF was present, the Aβ peptide layer thickness is close to the hydrodynamic diameter of monomeric Aβ. When the SLF was not present and the Aβ self-association was let to happen freely, the Aβ peptide thickness resembles the hydrodynamic diameter of oligomeric Aβs.

Table 2. Layer thickness and refractive index calculations from the data in **Fig. 9**. For comparison, the hydrodynamic diameters of Aβ monomers and Aβ oligomers determined by DLS are shown.

Flow channel	Layer Thickness (nm)	Refractive Index
Upper (SLF present)	1.33	1.37139
Lower (SLF not present)	31.89	1.34070

Hydrodynamic diameter (nm)	
Monomeric Aβ	1.4
Oligomeric Aβ	75

Signal-to-mass conversions for surface mass density (Γ) evaluations. The mass deposition calculations revealed features that may be related to the binding properties of SLF or its capability to reduce the Aβ aggregation – or both. In order to evaluate the utility of surface-deposited molecular mass measurement for determining the extent to which SLF can modulate Aβ self-assembly, we made two sets of surface mass density calculations; one set to determine the extent of SLF binding, and a second set to measure the effect of SLF on Aβ self-assembly. The latter case is discussed in more detail in the *Supplemental Information*. With respect to both sets, surface mass density calculations correlate the layer thickness measurements to kinetic analysis and are thereby complementary to the evaluation of binding sites identified by kinetic parameters.

As described in *Experimental Procedures*, the sensorgrams (i.e. the SPR peak minimum (θ_{SPR}) shift vs. time) used for the signal-to-mass conversions were generated from the full MP-SPR angular spectra, and TIR-corrected with regard to the possible bulk effect. Baseline correction and normalization were applied for the recorded sensorgrams in order to make the observed shifts comparable with each other and between different datasets. Surface mass densities were then calculated from the sensorgrams as described in *Experimental Procedures*. Measurements of surface mass density alterations resulting from SLF additions to monomeric and oligomeric Aβ are shown in **Fig. 10**, and the calculated values reported in **Table 3**. Injections of SLF over a range of 10 μM to 40 μM to the tethered Aβ monomer results in a surface mass density increase of ~120 ng/cm² (**Fig. 10A**). With the same SLF treatment to Aβ comprised of tethered monomers exposed to 2 injections of monomeric native peptide, we observe a surface mass density increase of ~66 ng/cm² (**Fig. 10B**). This result is similar to what is observed when the same range of SLF is injected over tethered Aβ monomer interacting with AβO pretreated with SLF, where a mass density increase of ~69 ng/cm² is calculated (**Fig. 10C**). A slightly higher increase in the surface mass density is obtained when SLF is added to AβO alone, ~84 ng/cm² (**Fig. 10D**). This result is consistent with the kinetic analysis above reflecting AβO has a lower capacity for additional SLF binding following SLF pretreatment.

Table 3. Surface mass density calculations for the different SLF interaction schemes.

SLF Interaction	Surface mass density (Γ) (ng/cm2)
Tethered Aβ monomer	120
Monomeric native Aβ	66
AβO pretreated with SLF	69
AβO only	84

Based on the results of kinetic analysis in **Fig. 5**, it is somewhat surprising that injections of native monomeric Aβ to the tethered monomeric Aβ resulted in a lower net surface mass density increase compared to the tethered peptide alone (~66 ng/cm² and ~120 ng/cm², respectively). However, these samples are not comparable as the measurements in **Fig. 10B** were carried out with two separate injections of monomeric Aβ. Thus, rather than being comprised primarily of dimeric species as in **Fig. 5**, it is likely the additional injection of Aβ in **Fig. 10B** results in the formation of small oligomers. This interpretation is consistent with our finding of weaker SLF binding to further progressed AβO species (**Table 1**).

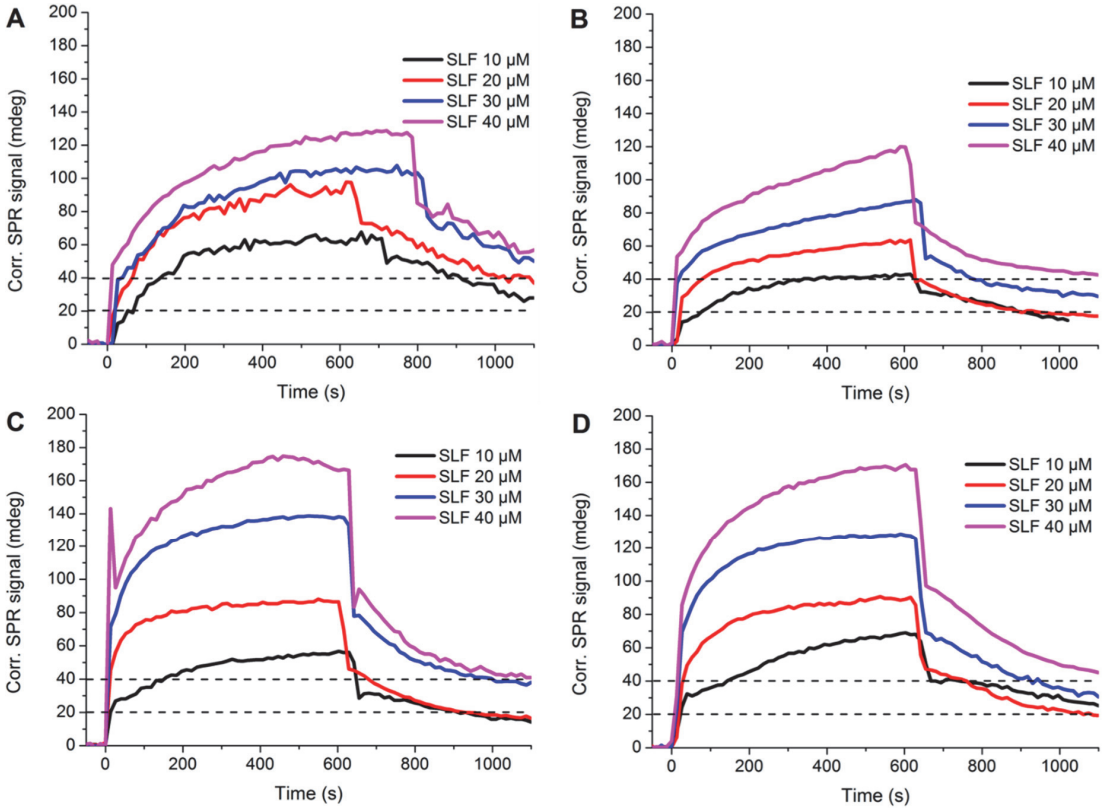

Fig. 10. Surface mass density calculations. Calculations for different SLF interaction schemes with tethered monomeric Aβ alone (**A**); native monomeric Aβ bound to tethered monomers (**B**); AβO pretreated with SLF at a 1:2 molar ratio bound to tethered monomers (**C**); AβO bound to tethered monomers (**D**). The traces have been normalized in order to calculate the approximate surface mass density that is generated by the SLF molecules when they are interacting and associating to investigated forms of Aβ.

Molecular docking and molecular dynamics simulations as a computational tool for modeling SLF interaction with Aβ-peptides. We carried out docking calculations to find out the most potent interaction sites for SLF at the surface of Aβ-peptide. Since the Aβ-peptide is a highly dynamic and disordered peptide when in solution, we carried out a single 20 ns long simulation (referred to as S1) in order to generate four structures for docking calculations (see **Table 4.**). In this fashion, it was possible to estimate the degree to which the binding sites and free-energies are affected by the possible secondary structure changes and amino acid side chain conformations. The RMSD of the Aβ-peptide backbone was stabilized after 3 ns (See **Fig. 11A**). In addition, the secondary structure of the Aβ-peptide did not deviate considerably from the starting conformation although some minor changes were expected, as it is known (35-38) that this structure is weakly ordered in aqueous solution (See **Fig. 11B**). We chose four structural snapshots starting from time point separated by 5 ns intervals for docking. The docking results are shown in (**Fig. 11**). The lowest binding free-energies are marked next to the peptide conformations in each case. The docking results generated using several Aβ-peptide conformations indicate that there is no specific binding site for SLF (See **Fig. 11C**). Nevertheless, the binding free-energies varied between -7.5 and -6.8 kcal/mol and this was in good agreement with the SPR derived binding free energies of -6.8 and -6.2 kcal/mol (K_{D1} with native biotinylated or non-biotinylated Aβ, respectively). Notably, these biding energies are on par with from simulations of Aβ and a bromo-fluorene containing a dimethyl-amino group in the position of our spin-label (39). We therefore have a reasonable thermodynamic basis for the low docking free energies that are observed experimentally; consistent with an interaction between the Aβ-peptide and SLF that does not involve a specific binding site. However, our simulations did not find a docking configuration on the order of -20 kcal/mol, which would account for the sub-nanomolar binding also observed within preparations of monomer/dimer samples.

Table 4. Simulated systems and the length of simulations.

	Simulation time	Molecules	Reason
S1	20 ns	Aβ-peptide+water	For docking purposes
S2	100 ns	Aβ-peptide+SLF+water (site 1)	For probing SLF and Aβ interactions
S3	100 ns	Aβ-peptide+SLF+water (site 2)	For probing SLF and Aβ interactions

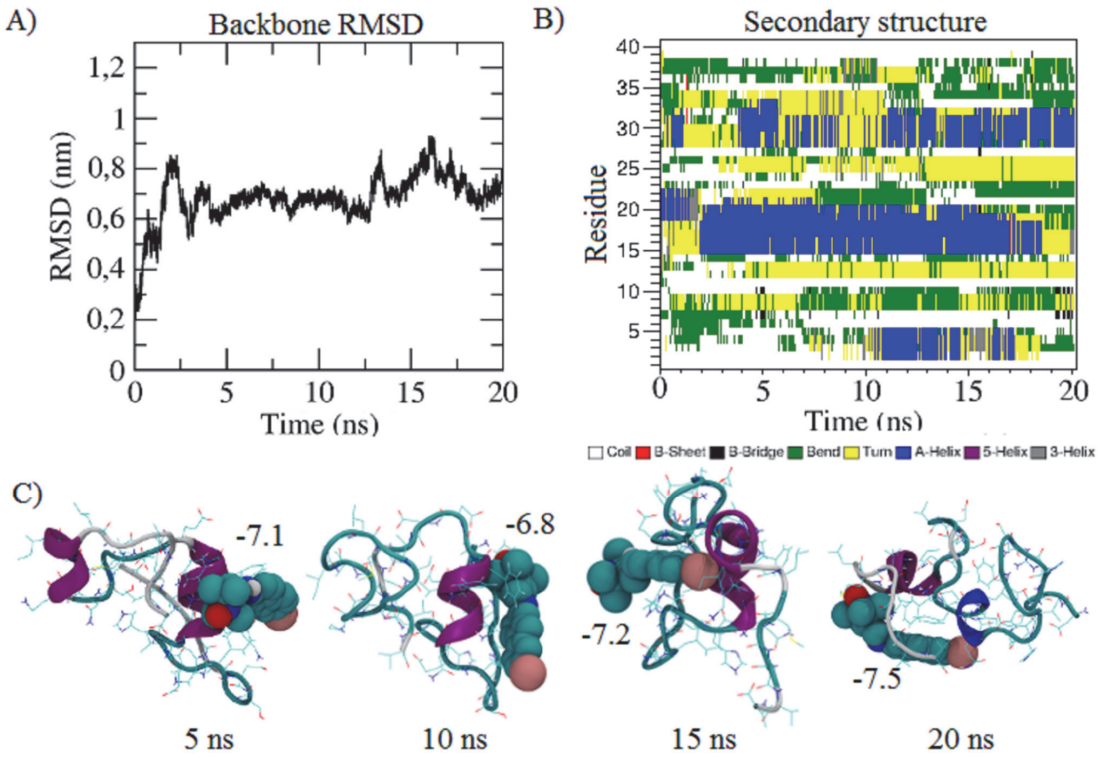

Fig. 11. Docking calculation results for four snapshots derived from S1 simulation. (**A**) The secondary structure of Aβ-peptide as a function of S1 simulation time. Aβ-peptide has been rendered using cartoon representation and colored according to the secondary structure. (**B**) The root mean square deviation of (RMSD) Aβ-peptide backbone as a function of time. (**C**) The binding free-energies of SLF generated by the Autodock Vina are shown next to SLF molecules in kcal/mol (van der Waals representation). Purple color indicates α-helix, white random coil, and cyan turn structure. The SLF molecule is rendered van der Waals spheres and colored according to atom types. White spheres are hydrogen atoms, cyan carbon, red oxygen, blue nitrogen, and pink bromine atoms.

Since the results of the docking calculations indicated that the interaction between the SLF with the Aβ-peptide were strong yet mostly non-specific, we carried out two 100 ns long molecular dynamics simulations that we refer to as simulations S2 and S3, to probe the behavior of the SLF molecule at the surface of the Aβ-peptide. MD simulations were started with the SLF either at the lowest free-energy binding site of the 15 ns or 20 ns snapshot. The snapshots and atomic contacts between the SLF molecules and the Aβ-peptide revealed that the SLF molecule stays at the surface of the Aβ-peptide (See **Fig. 12**). By careful inspection of the simulation trajectories and atomic contacts it was found that the Aβ-peptide can at least transiently fold around the SLF molecule during both simulations (See **Fig. 12**). To estimate the effect of a SLF induced binding pocket to its binding free-energy, we docked the molecule once again to the Aβ-peptide structure of simulation S2 after the 100 ns simulation. The docking calculation results showed that the refolding of the Aβ-peptide around the SLF molecule resulted in a small free-energy of binding increase up to -8.5 kcal/mol.

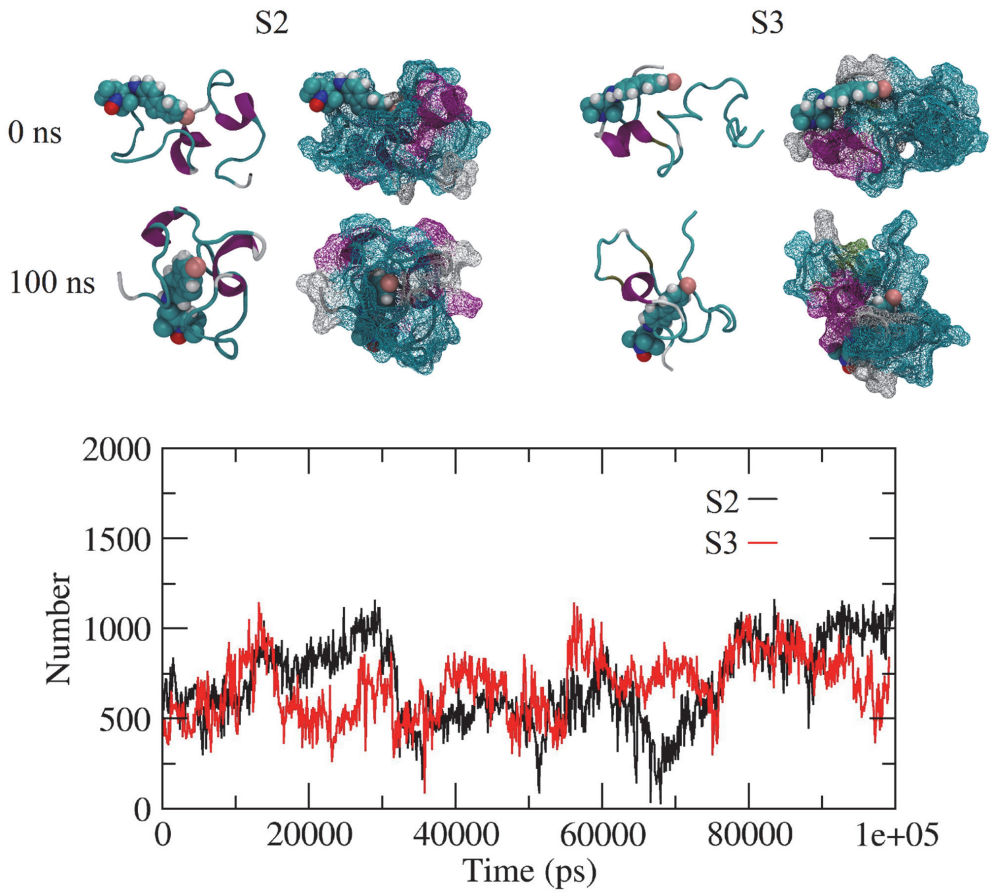

Fig. 12. Snapshots from the beginning and end of SLF simulations S2 and S3 (top). Number of contacts between SLF and Aβ-peptide as a function of simulation time (bottom). Aβ-peptide has been rendered using cartoon or wireframe representation and colored according to the secondary structure. Purple color indicates α-helix, white random coil, blue 3_{10}-helix, and cyan turn structure. SLF molecule is rendered van der Waals spheres and colored according to atom types. White spheres are hydrogen atoms, cyan carbon, red oxy

DISCUSSION

As there is ample evidence in the literature that the neuronal damage in AD is derived from the toxicity of soluble Aβ oligomers (6,40), there remains, however, much to be discovered regarding the toxicity of the Aβ oligomers due to the many faces of the complex aggregation pattern of Aβ. The relationship between function and structure is altered to a higher degree when a dynamic oligomerization/aggregation pattern yields oligomers with a large number of interchangeable, yet distinct conformational polymorphisms (41). It is thus very possible that Aβ toxicity is associated with the process of aggregation and its many resulting species rather than a specific oligomeric state (21,41,42).

The SLF interaction kinetics analysis was started using a relatively simple 1:1 modeling. However, it was not descriptive or consistent with the experimental data in any of the four

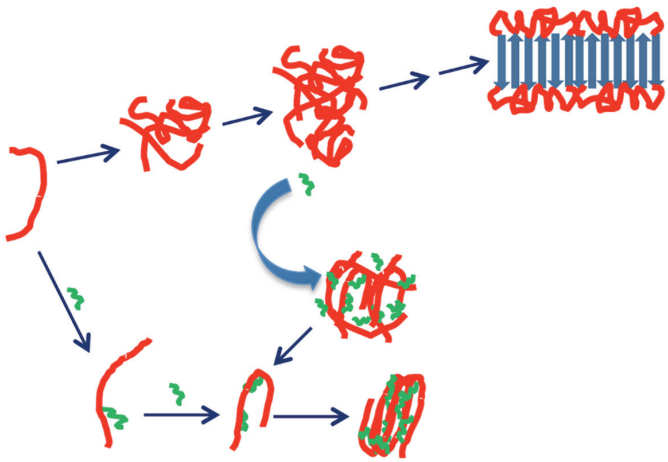

Fig. 13. Schematic for Aβ-SLF interactions. Experimental and *in silico* evidence suggests the central hydrophobic core encompassing residues 17-21 in the peptide as the target for small molecule and peptide-based inhibitors of Aβ aggregation and/or fibrillation (39,43-46). Our simulations, as well as those by Li et al. on a related fluorene compound (39), suggest a non-specific interaction of SLF around the hydrophobic core of Aβ (residues 17-21) with binding energies correlating to micromolar affinity. However, the basis for the high affinity SLF binding to the monomer is not clearly evident. One possibility is that high affinity binding requires tertiary pocket available in the monomer that is not present in the oligomer, which to favor a largely disordered antiparallel arrangement (47-49). For example, such a pocket could be formed by a β-hairpin fold of the monomer (50,51). Oligomers of Aβ in hairpin conformations have been observed in Aβ modified with a disulfide cross-link (52), however these species have increased neurotoxicity as opposed to the non-toxic SLF oligomers (14,15).

calculated scenarios – the Chi^2 values being in the order of ~500-700 (data not shown). On the basis of our previous studies (e.g. references 14-16) we had an initial hypothesis that the SLF may express multivalent binding. Thus a 1:2 binding model was employed yielding significantly more accurate fitting. The relatively small Chi^2 values for the four calculated scenarios are shown in **Table 1**, and the molecular docking simulations support these perceptions providing rationale for using the 1:2 binding model in the interaction kinetics calculations. For monomeric Aβ, K_{D1} of 15 μM and K_{D2} in the sub-nanomolar range were calculated. When SLF interacts with a surface comprised of native monomeric Aβ bound to a tethered Aβ monomer, K_{D1} (41 μM) and K_{D2} (sub-nanomolar) are on par with the tethered monomer. It is noteworthy that the lack of appreciable SLF dissociation within the high affinity (K_{D2}) binding mode produces relatively large uncertainty in its calculated value. Although the current methodology cannot precisely generate K_{D2} values for the monomer/dimer samples, we designate these affinities as "subnanomolar", which represents a conservative upper limit for the observed binding behavior. Nevertheless, these results indicate Aβ maintains a highly avid SLF binding in both the monomer or dimer states.

For oligomeric Aβ, the affinity of AβO for SLF is substantially lower, with both K_{D1} and K_{D2} in the 100 μM range (**Table 1.**). In addition, the B_{max1} and B_{max2} values (**Table 1.**) report about the relative amount of SLF binding to corresponding binding sites, i.e. in the 1:2 binding model those sites are represented by the affinity values K_{D1} and K_{D2}. As SLF

interactions are tested across the various Aβ configurations of tethered monomer, dimer, AβO and SLF-pretreated AβO, the relationships of B_{max1} and B_{max2} values shift from (~ 1:1 → 1:7 → 1:3 → 1:2.5), respectively, thus indicating that the secondary SLF binding site (K_{D2}) already becomes more occluded in the dimer configuration. This is consistent with the slightly weaker K_{D2} value obtained for the Aβ dimer (~ 10^{-13} M) vs. the tethered monomer (~ 10^{-15} M), although again these values should be viewed with caution due to the inherent uncertainty of calculating dissociation values in this regime. It is to be noted that the secondary binding site of SLF becomes slightly more crowded in the case of AβO vs. SLF-pretreated AβO in terms of the relationship of B_{max} values (1:3 vs. 1:2.5). This implies that the SLF binding capacity of AβO is slightly higher than that of the SLF-pretreated AβO. Furthermore, these results suggest that inter-peptide interactions preclude a high affinity binding conformation that is available to the monomer. A schematic summarizing SLF binding and its effect on the Aβ oligomer growth is shown in **Fig. 13**.

The very high binding affinity detected in the monomer could also arise from an induced fit within a local binding pocket requiring a backbone configuration that is not favored in the oligomer. For example, in X-ray structures of Orange G and a peptide of the central hydrophobic core two modes of small molecule binding were found (43). One mode being a highly specific binding to a beta zipper structure and the second being a non-specific interaction at an adjacent cavity. Other backbone conversions may also underlie a high affinity induced fit for SLF binding. For example, we have previously shown that SLF generates a circular dichroism spectral shape resembling the polypro (II) structure (15). Studies by Danielsson et al (53) suggest that in the peptide monomer, the backbone within the N-terminal portion of Aβ (including the central core of 17-21) readily converts between β and polypro(II)-like conformations, with the later state being less prone to aggregation. Thus, it is also possible that SLF binds and stabilizes a specific secondary structural state occupied by the monomer.

Although SLF inhibits oligomer growth and reduces the size of preassembled oligomers, previous FCS (fluorescence correlation spectroscopy) analyses indicate that these complexes assemble into a smaller, more stable form of AβO (15) (**Fig. 13**). Thus, regardless of the mode of high affinity SLF binding in the monomer, initial thermodynamic forces driving monomeric Aβ and SLF interaction are not available in the oligomer. In addition to the steric factors discussed above, other considerations can be a reduction of the hydrophobic effect on binding once the peptide-SLF is buried in the oligomer or, given that SLF has both H-bond acceptors and donors, the interference of coordinating H-bonds by groups involved in intermolecular H-bonds.

Layer thickness analysis provided additional support for the ability of SLF to slow the progression of Aβ oligomerization, by showing that there is significantly more Aβ deposited on the sensor surface in the absence of SLF than in the presence of SLF, in fact factor of 30 more (**Table 2**). The optical modeling performed on the basis of the measured full SPR angular spectra yielded consistent results with the DLS measurements. When the SLF was hampering the self-association of the Aβs, close to monomeric Aβs formed ~ 1.33 nm peptide layer onto the sensor surface in low aggregation buffer flow. On the other, the DLS demonstrated the mean hydrodynamic

diameter of ~ 1.4 nm when the Aβs were measured in the similar low aggregation buffer conditions. Furthermore, the modeled Aβ layer when SLF was not present can be interpreted as an early oligomerized Aβ layer, the optical modeling showing the thickness of 31.89 nm (as displayed in **Table 2**). To support this, the DLS measurements showed the mean hydrodynamic diameter of ~ 75 nm for the AβOs. It is worth emphasizing that both the MP-SPR measurements were carried out in low aggregation buffer whereas the DLS measurements for the AβOs were performed in high aggregation buffer, which may explain the difference in the latter thickness and mean hydrodynamic diameter (31.89 nm vs. 75 nm). Nevertheless, a clear trend – the Aβ layer thickness growing towards the measured mean hydrodynamic diameter of AβO – can already be seen if the SLF is not employed to prevent those processes. In addition, these perceptions also underline the fact that the four different experimental schemes for investigating the physicochemical properties and interactions of SLF can be considered to have successfully encompassed the monomeric or close-to-monomeric states of Aβs to oligomerized forms of Aβs (AβO).

The surface mass density analysis complemented the perceptions that the closer to the monomeric state the Aβ are, the more prone they are to avid SLF binding. However, some precautions should be included in the surface concentration analysis performed on the basis of the MP-SPR signals and the de Feijter equation. Firstly, even though the variations in the refractive index of the medium (n_m in Eq. (6)) are typically small, the differences in $^{dn}/_{dc}$ for biomolecules in different buffers may have distinct variations (54-56). In addition, the refractive index increment is dependent of the measurement wavelength. In general, lower refractive indices can be found with increasing wavelength. Another point to take into account is the degree of hydration that varies in the protein layers, thus inducing possible variation to the calculations. To sum the mentioned caveats, a uniform $^{dn}/_{dc}$ value for proteins can be challenging to define accurately, and its applicability depends on the desired level of accuracy in the analysis. For example, in biophysical studies focusing on protein interactions, the refractive index increment is utilized to measure the protein concentrations or surface layer thickness, and the small errors lie within a tolerable range (57). However, the value for increment $^{dn}/_{dc}$ = 0.182 cm^3/g can be considered to provide adequate accuracy within the context of this analysis since other experimental errors may contribute to a larger extent to these calculations than the value for increment alone. Hence, we can conclude that these calculations yielded satisfactory approximations on the masses of molecules deposited onto the sensor surface during the interactions, in addition to providing additional mechanistic insight into the molecular interactions of Aβ peptides and the role played by SLF.

Based on docking calculations and MD simulations we suggest that the binding of SLF to the surface of the Aβ-peptide is non-specific since the binding site and energies were seen to depend on the both the amino acid side chain conformations and secondary structure fluctuations. These results are verified by the experimental results that show binding energy is in rough agreement with our simulation results. Furthermore, the MD simulations indicated that the SLF remains at the surface of the Aβ-peptide and can be surrounded or shielded by the peptide. The docking

calculations produced binding free-energies that were comparable to the K_D-values produced by several of the experiments (-8.5 kcal/mol). We were, however, not able to produce binding free-energies comparable with the highest K_D reported by the experiments. (~-20 kcal/mol). As seen in our simulations, it is possible that the structure of the Aβ-peptide refolds when it interacts with SLF so that it can better shield the hydrophobic SLF molecule from its aqueous surroundings. Consequently, the shielding of SLF by the Aβ-peptide could increase the binding free-energy of SLF considerably as was shown by our subsequent docking calculations. Admittedly, since the Aβ-peptide is weakly structured, our simulations were clearly not able to sample the accessible phase space of this complex molecule completely, thus the specific highest K_D value conformations were probably missed for this reason. Our results are in broad agreement with the majority of the K_D measurements, however, indicate that the non-specific binding mechanism, involving alteration of the Aβ-peptide to shield the SLF is a probable mechanism. A further, more rigorous simulation study, involving several simulations of microsecond lengths and greater, could find the higher K_D binding conformation, however, it is beyond the scope of the current study. We hypothesize that the SLF molecule binds strongly to the surface of the Aβ-peptide and modify its conformational fluctuations in a way which could hinder the aggregation of the peptides. It is known that the Aβ-peptide is mostly unfolded in the aqueous solution although it possesses transient structural fluctuations depending on the physicochemical surroundings (58,59). Some of these transient structures such as β-sheets are more prone to the formation of initial Aβ-peptide aggregation nuclei (60) and thus, if the stochastic prevalence of these structures are minimized by novel drug agents such as SLF, it could possibly be a practical therapy to inhibit the aggregation of Aβ-peptides.

CONCLUSIONS

In summary, in this work we have presented a novel method for studying protein aggregation and small molecules interactions, while presenting valuable kinetic binding data. The new findings suggest that SLF not only prevents Aβ oligomerization, but that the effect is expected to be significantly greater at early stage of peptide aggregation. In fact, the rationale of targeting monomeric Aβ prior to neurotoxic oligomer formation has been previously postulated (61). To our knowledge, the findings present the first biomolecular layer thickness and refractive index evaluations to measure the accumulation and aggregation of Aβ, a process central to the elucidation of AD pathogenesis. We envisage that the demonstrated *biofunctional assay* methodology could offer a valuable tool to probe for various biophysical phenomena, therapeutic agents binding kinetics – not only in the context of AD, but possibly other diseases as well, where protein aggregation is the mechanism of interest, like plaque formation in cardiovascular disease, and other neurodegenerative diseases.

EXPERIMENTAL PROCEDURES

Materials. Hexafluoro-2-propanol (HFIP) was purchased from Sigma-Aldrich (catalog number 105228-25G, St. Louis, MO). Dimethyl sulfoxide (DMSO) was purchased from Fisher Scientific (catalog number D12345, Pittsburgh, PA). Biotin-PEG-SH was purchased from Nanocs Inc. (catalog number PG2-BNTH-5k, New York, NY). 11-Mercapto-1-undecanol ($HS(CH_2)_{11}OH$) was obtained from Sigma Aldrich, St. Louis, MO (catalog number 447528-1G). The thiols were used as received. Streptavidin was purchased from Thermo Scientific (catalog number 43-4301, Pittsburgh, PA). Biotin was purchased from Sigma Aldrich (catalog number B4501-500MG) St. Louis, MO). β-amyloid peptide (1-40) (**Seq:** DAEFRHDSGYEVHHQKLVFF AEDV GS NKGAIIGLMVGGVV) and Biotin labeled β-amyloid peptide (1-40) (**Seq:** Biotin-DAEFRHDSGY EVHHQKLVFFAEDVGSNKGAIIGLMVGGVV) were purchased from EZBiolab Inc., Carmel, IN. Spin-labeled fluorene HO-4160 (SLF) was synthesized as described in (16).

Preparation of amyloid beta (Aβ) peptide samples. To prepare monomers of biotinylated or native Aβ, the Aβ peptide was dissolved in HFIP and incubated at room temperature with gentle rocking for 48-72 hours. Vacuum evaporation was then used to remove the HFIP, resulting in a monomeric Aβ pellet. Immediately before the given experiment, the HFIP-treated pellet was warmed to room temperature and reconstituted in 10 μL of fresh DMSO. The Aβ in DMSO stock solution was then diluted in low ionic strength buffer (25 mM Tris, 1 mM EDTA, pH 8.0) to a 10 μM final concentration of the peptide monomer and the sample used immediately. For oligomeric Aβ (AβO), the DMSO Aβ stock was diluted into high ionic strength buffer (25 mM Tris, 150 mM NaCl, pH 7.0) to a final concentration of 40 μM and allowed to incubate at room temperature for 4 hours. Just prior to MP-SPR measurements the AβO solution was centrifuged at 15,000 x g for 5 minutes for amorphous aggregate removal. The supernatant contained the AβO used for MP-SPR measurements. As demonstrated previously (14,62) these oligomeric preparations are anti-amyloid (A11)-positive oligomers, with a 40 μM solution producing particles at 4-hours of ~10 nm in diameter by AFM imaging. The AβO 40 μM solutions were diluted to 10 μM in high aggregation buffer just prior to injection into MP-SPR fluidic channels.

To produce SLF labeled AβO, we treated the 4 hrs AβO incubations with either 80 μM SLF (1:2 Aβ/SLF molar ratio to saturate Aβ binding sites) or vehicle, and allowed these solutions to incubate at room temperature for 4 hrs. Just prior to MP-SPR measurements the AβO/SLF and AβO/vehicle solutions were centrifuged at 15,000 x g for 5 minutes, and the supernatant removed for MP-SPR measurements.

Characterization of monomer and oligomer preparations by dynamic light scattering. Particle size analysis of was carried out at using dynamic light scattering (DLS) with a Brookhaven 90Plus instrument that monitors scattered light at 90° to the excitation. For monomer samples, Aβ(1-40) was HFIP-treated and dried. Immediately before measurement, dried pellets were dissolved in DMSO and diluted into either low salt buffer, pH 8.0 (for monomeric preparations) or diluted into high salt buffer, pH 7.0 (for oligomeric preparations). Monomeric samples were measured for 20 minutes, immediately after solvation into aqueous buffer to a concentration of 10 μM. Oligomeric samples were first incubated for

4-hr incubation in high ionic strength buffer. All samples were filtered through 0.22 μm filter to remove dust particles and large amorphous aggregates just prior to measurement. The average hydrodynamic radius was calculated using the ZetaPlus Particle Sizing Software Version 3.57 (Brookhaven Instruments). The calculated hydrodynamic diameters of Aβ monomers was ~1.4 nm, while the AβO species have an average hydrodynamic radius of ~75 nm.

MP-SPR measurements. MP-SPR measurements were performed using SPR-Navi 200™ instrument (BioNavis Ltd., Tampere, Finland). The MP-SPR instrument allows for expanded SPR sensing, having the capability to record the full SPR angular spectra over a wide angular range (~ 40-78 degrees). The instrument was equipped with two different wavelength lasers (670 nm and 785 nm) for plasmon excitation in two independent fluidic channels, which are integral parts of a PDMS flow cell (volume of each flow cell 1 μL). The liquid flows were controlled via a peristaltic pump and a 12-port chromatography injector, the typical flow rates varying between 10-100 μL/min, and in this particular study, between 10-20 μL/min. The scanning angle feature and utilization of two or more wavelengths enables recording full SPR angular spectra (intensity of reflected light as a function of angle of incidence) in real time. These, in turn, can be used to model and calculate e.g. the layer thicknesses (d) and refractive indices (n) for the studied molecular layers as well as kinetic parameters for the interaction phenomena using well-established physical models. Additional technical details are given in *Supplemental Information*.

Preparation of the gold sensors for MP-SPR measurements. We used the SPR Navi™ gold sensor slides SPR102-AU-10 (Au as the plasmonic layer, d = 50 nm) provided by BioNavis for all of our MP-SPR measurements. To functionalize the gold sensor surface we followed the standard protocol, as described by (23) and adapted it to using biotinylated Aβ peptide as the ligand layer as shown in **Fig. 2**. We constructed a supramolecular assembly composed of a self-assembled monolayer (SAM) to which we attached the biotinylated Aβ peptide to form the functionalized gold sensors. Before surface assembly, the plain gold sensors were cleaned with absolute ethanol, and dried with nitrogen gas. First, we reconstituted the 11-Mercapto-1-undecanol and the biotin-PEG-SH in absolute ethanol to form a MuOH: Biotin-PEG-thiol (85:15 mol %, 5mM) (MBP-thiol) SAM solution. An adsorbed biotinylated, self-assembled monolayer (SAM) was generated directly on the gold sensor; the mixed, MBP/PEG thiols make a better self-assembly layer than PEG-thiol alone by resisting non-specific protein adsorption. The gold sensors were then immediately immersed in an MBP-thiol SAM solution, in a glass Petri dish, gold face up, and incubated for at least 16hrs, at room temperature, in the dark and the MBP-thiol was allowed to adsorb onto the gold sensor. The Petri dish was sealed with wax paper to prevent evaporation. Subsequently, the gold sensors were removed from the solution, washed in absolute ethanol and dried with nitrogen gas and loaded into the instrument. The second molecular layer was constructed by immobilization of streptavidin monitored *in situ* with the MP-SPR instrument, as 200 μg/ml of Streptavidin in DI water, was flown over the MBP-thiol SAM sensor surface at 10 μl/min. After a stable baseline was obtained we proceeded to build the third molecular layer by injecting 10μM biotinylated Aβ in low aggregation buffer (25 mM Tris, 1 mM EDTA, pH 8.0) at 10μL/min, followed by low

aggregation buffer until a stable baseline was noted. For the control channel (shown in **Fig. 3**, green trace) we followed the same procedure for the first and second layer, except that the third layer was built by flowing 300 μL of 1mM biotin, at 10 μl/min until a stable baseline was noted. Peptide/peptide and peptide/SLF interactions were detected by measuring the shift in the SPR peak minimum (θ_{SPR}) before and after each sample injection.

To investigate SLF/Aβ binding, various SLF dilutions (10 μM, 20 μM, 30 μM, 40 μM) in low ionic strength buffer, pH 8.0, were flowed over the biotinylated Aβ biosensor surface at the concentrations indicated in the figures. Non-specific binding was tested by application of the same SLF dilutions over the MBP-Thiol SAM/Streptavidin/biotin surface without Aβ. Similarly, to check for non-specific Aβ binding, 10 μM of non-biotinylated Aβ was flowed over the MBP-Thiol SAM/Streptavidin/biotin surface.

Physical principles of the interaction kinetics analysis. Kinetic analyses were performed using the SPR Navi™ Data Viewer 4.0 (BioNavis Ltd., Tampere, Finland) and the TraceDrawer 1.6 software (Ridgeview Instruments AB, Vänge, Sweden) - data shown in **Table 1**. Graphs in all figures were constructed using OriginPro 8.6 (Northampton, Massachusetts, USA). We started the kinetic analysis by selecting the desired interactions of each particular scheme. The kinetic fitting is based on the sensorgrams, which show the change in the SPR resonance angle (change in the SPR peak minimum (θ_{SPR})) as a function of time (**Fig. 4**). We performed the analysis of SLF interactions in 4 different schemes; (i) SLF interacting with biotinylated Aβ, (ii) with native (non-biotinylated) Aβ, (iii) with AβO, and (iv) with AβO pretreated with SLF at a molar ratio of 1:2. The sensorgrams were baseline corrected by using a baseline level correction algorithm. Consequently, the bulk- and baseline-corrected sensorgrams were processed in the fitting phase with two different binding models within the TraceDrawer 1.6 software. SLF-Aβ interaction schemes were best fit using the 1:2 model appropriate for binding to two independent targets on a solid support. The mathematical description of the two used models is extensively described elsewhere (e.g. (63,64)). As the refractive properties of DMSO can change the bulk conditions quite drastically, the fitting was performed by taking into account the possible bulk effect the DMSO may have had during the experiment. The injection of an analyte dissolved in the DMSO typically induces a clear shift in the total internal reflection (TIR) angle. Since the full SPR angular spectrum is recorded, the bulk correction can be performed by subtracting the contribution of the TIR shift from the overall change in the angular position of the SPR peak minimum.

Basic SPR theory and physical principles of layer thickness modeling. The fundamental mathematical depiction of SPR is derived from the Maxwell's equations, and has been described profoundly for example in (64-67). Briefly, when the matching of incident light photons and plasmons occurs, the resonance condition is met:

$$\frac{\omega}{c}\sqrt{\varepsilon_0}\sin\theta_0 = \frac{\omega}{c}\left(\frac{\varepsilon_1\varepsilon_2}{\varepsilon_1 + \varepsilon_2}\right)^{\frac{1}{2}} \qquad (1)$$

where c is the speed of light in vacuum, ω is the light frequency, θ_0 is the angle of incidence of the light beam, and ε_0, ε_1, ε_2 are the dielectric constants of the prism, the metal, and the medium in contact with it, respectively. In general, the dielectric constant ε and refractive index n for a given material can be expressed

in their complex forms as $\hat{n} = n + ik = \sqrt{\mu\hat{\varepsilon}}$, and $\hat{\varepsilon} = \varepsilon + i\varepsilon'$, where $\hat{n}$, n and k are the complex refractive index, real- and imaginary part of the complex refractive index, respectively. The quantity μ denotes permeability, occurring in Maxwell's equations. Since the majority of materials are non-magnetic at optical frequencies, μ can be approximated very close to 1. Similarly, $\hat{\varepsilon}$, ε and ε' are the complex dielectric constant, real- and imaginary part of the complex refractive index. As a sum of the definitions made here, the refractive index and dielectric constant are related as $\hat{n} = \sqrt{\hat{\varepsilon}}$.

For the layer thickness and refractive index modeling, the shape and quantities associated with the SPR spectra were utilized. The spectra can be described with Fresnel's equations as the reflectivity of a multilayered system for *p-polarized* light. In practice, the modeling and solving for the matrix formalism was performed by mathematical fitting tools, or dedicated software. The layer thicknesses and refractive indices of the thin bio-molecular layers were solved by the two-wavelength method with angular scanning in all our experiments (29-31). LayerSolver 1.0.2 (BioNavis Ltd., Tampere, Finland) software was used for modeling and solving for the layer properties.

The thicknesses of the modeled layers were linked as common variables in the modeling performed with the LayerSolver, i.e. the layer thickness was expected to be the same for both wavelengths since the MP-SPR angular spectra were measured from the same spot in the upper and lower sample channels. The complex refractive index was input as an independent variable for background (pure metal layer) modeling, or as a linearly dependent variable between the two used wavelengths.

Physical principles of the surface mass density calculations. The molecular mass that binds onto the SPR sensor surface has a well-defined correlation with the observed MP-SPR angular spectrum – in particular, the SPR resonance angular shift (57,64). Importantly, since water is very weakly optically active compound in SPR measurements, only the deposited dry mass is detected (68). In order to calculate the surface mass densities of biomolecules deposited onto the sensor surface, a surface mass density (Γ) conversion coefficient of $^{dn}/_{dc}$ = 0.182 cm³/g was used. Consequently, that yields a conversion factor Δ1 mdeg = Δ (Γ) ~ 0.6 ng/cm². This has been shown to serve as a good approximation for proteins, although limitations and caveats have been noted (57), and are discussed in the text.

Molecular docking, molecular dynamics simulations and analysis. Autodock Vina 1.1.2 (69) was utilized to find the most probable binding sites and free-energies for SLF at the surface of Aβ-peptide. We chose to carry out the initial docking calculations to the solution structure of Aβ (1-40) solved with NMR (70). The PDB code for the structure is 1IYT. The PDB structure consists of several different conformations for the Aβ-peptide, but we chose to use only the first one since our aim was also to carry out 20 ns MD simulation (referred as S1) for Aβ-peptide in water surroundings. The docking calculations were repeated for structures that were derived from S1 simulation (2 ns intervals). All non-polar hydrogens of Aβ-peptide and SLF were merged to the corresponding heavy atoms, which is a perquisite for Autodock docking calculations. In general, the docking parameters were kept to their default values. One rotatable dihedral present in the SLF molecules were set to flexible. The size of the docking grid was set

to 47 Å x 47 Å x 47 Å, which overlaid the entire Aβ-peptide.

All molecular dynamics simulations were carried out using the GROMACS 5.0.4 package (71) and the GROMOS54A7 force field (72). The GROMOS54A7 force field parameters for SLF were generated with Automated Topology Builder (ATB) server version 2.2 (73,74). The SPC model was used for water molecules (75). To maintain zero net charge in the simulated systems three Na^+ counter ions were added. All MD simulations were carried out under the isobaric–isothermal (NPT) ensemble with periodic boundary conditions. A time step of 2 fs was used for integrating the equations of motion. The v-rescale and Berendsen algorithms were employed to maintain physiological temperature at 310 K (0.1 ps^{-1}) and an isotropic pressure of 1 bar (1.0 ps^{-1}) (76). The cutoff for Lennard-Jones interactions were set to 1.4 nm. For long-range electrostatics the particle mesh Ewald (PME) method was employed with a real-space cutoff of 1.4 nm (77). The LINCS algorithm was applied to constrain all bonds (78). The simulated systems consisted of one Aβ-peptide, one SLF molecule (except one simulation where the SLF molecules was not present), three Na^+ counter ions and 4719 water molecules. Three different MD-simulations were carried out. The simulated system 1 (S1) consisted of only the Aβ-peptide, ions and water molecules. This simulation was performed up to 20 ns as previously described, solely to obtain four independent initial docking conformations. In the simulation systems 2 (S2) and 3 (S3) the SLF molecule was initially present in the docking sites 1 and 2 that were produced by the initial docking calculation. S2 and S3 systems were simulated up to 100 ns. The secondary structure of the Aβ-peptide was analyzed using the gmx do_dssp analysis tool included in the GROMACS simulation package (79). The root mean square deviation (RMSD) of the Aβ-peptide was analyzed with the gmx rms program. The number of contacts was calculated using the gmx mindist program, which is also included in the GROMACS simulation package. The maximum distance for contacts between SLF and Aβ-peptide atoms were set to 0.6 nm. VMD were used to visualize the docking and simulation results (80).

ACKNOWLEDGMENTS

Financial support by the Academy of Finland (grants: #263861 and #292253), Tekes – the Finnish Funding Agency for Innovation EV-Extra-Tox project and the Professor Pool – Orion Research Foundation are gratefully acknowledged. CSC – The IT Center for Science (Helsinki, Finland) is acknowledged for providing supercomputer facilities. The authors also acknowledge support from the UC Davis STAIR Program to JCV.

CONFLICT OF INTEREST

T.R. receives a stipend from BioNavis Ltd, the manufacturer of instrumentation used in this study.

AUTHOR CONTRIBUTIONS

SH and TR designed and conducted the MP-SPR experiments, and analyzed the results. SH designed and performed the dynamic light scattering experiment and analyzed the results. TR and TV designed all the biophysical modeling and fitting for the MP-SPR data, and

analyzed the results. AK and AB performed the molecular dynamics simulations and analyzed the results. SWH and MY analyzed data and wrote parts of the manuscript. JCV initiated the project, coordinated the experiments, and oversaw the manuscript preparation, with writing contributions from all authors.

REFERENCES

1. Hebert, L. E., Weuve, J., Scherr, P. A., and Evans, D. A. (2013) Alzheimer disease in the United States (2010-2050) estimated using the 2010 census. *Neurology* **80**, 1778-1783

2. Viola, K. L., and Klein, W. L. (2015) Amyloid beta oligomers in Alzheimer's disease pathogenesis, treatment, and diagnosis. *Acta Neuropathol* **129**, 183-206

3. Walsh, D. M., Klyubin, I., Fadeeva, J. V., Rowan, M. J., and Selkoe, D. J. (2002) Amyloid-β oligomers: their production, toxicity and therapeutic inhibition. *Biochemical Society Transactions* **30**, 552-557

4. De Simone, A., Kitchen, C., Kwan, A. H., Sunde, M., Dobson, C. M., and Frenkel, D. (2012) Intrinsic disorder modulates protein self-assembly and aggregation. *Proceedings of the National Academy of Sciences of the United States of America* **109**, 6951-6956

5. Kayed, R., Head, E., Thompson, J. L., McIntire, T. M., Milton, S. C., Cotman, C. W., and Glabe, C. G. (2003) Common structure of soluble amyloid oligomers implies common mechanism of pathogenesis. *Science* **300**, 486-489

6. Klein, W. L., Stine, W. B., Jr., and Teplow, D. B. (2004) Small assemblies of unmodified amyloid beta-protein are the proximate neurotoxin in Alzheimer's disease. *Neurobiology of aging* **25**, 569-580

7. Cheon, M., Chang, I., Mohanty, S., Luheshi, L. M., Dobson, C. M., Vendruscolo, M., and Favrin, G. (2007) Structural reorganisation and potential toxicity of oligomeric species formed during the assembly of amyloid fibrils. *PLoS Comput Biol* **3**, 1727-1738

8. Bartolini, M., Bertucci, C., Bolognesi, M. L., Cavalli, A., Melchiorre, C., and Andrisano, V. (2007) Insight into the kinetic of amyloid beta (1-42) peptide self-aggregation: elucidation of inhibitors' mechanism of action. *Chembiochem* **8**, 2152-2161

9. Sgarbossa, A. (2012) Natural biomolecules and protein aggregation: emerging strategies against amyloidogenesis. *Int J Mol Sci* **13**, 17121-17137

10. Aulic, S., Bolognesi, M. L., and Legname, G. (2013) Small-molecule theranostic probes: a promising future in neurodegenerative diseases. *Int J Cell Biol* **2013**, 150952

11. Jameson, L. P., Smith, N. W., and Dzyuba, S. V. (2012) Dye-binding assays for evaluation of the effects of small molecule inhibitors on amyloid (abeta) self-assembly. *ACS Chem Neurosci* **3**, 807-819

12. Wang, Q., Yu, X., Li, L., and Zheng, J. (2014) Inhibition of amyloid-beta aggregation in Alzheimer's disease. *Curr Pharm Des* **20**, 1223-1243

13. Oddo, S., Caccamo, A., Smith, I. F., Green, K. N., and LaFerla, F. M. (2006) A dynamic relationship between intracellular and extracellular pools of Abeta. *Am J Pathol* **168**, 184-194

14. Petrlova, J., Kalai, T., Maezawa, I., Altman, R., Harishchandra, G., Hong, H. S., Bricarello, D. A., Parikh, A. N., Lorigan, G. A., Jin, L. W., Hideg, K., and Voss, J. C. (2012) The influence of spin-labeled fluorene compounds on the assembly and toxicity of the abeta Peptide. *PLoS One* **7**, e35443

15. Altman, R., Ly, S., Hilt, S., Petrlova, J., Maezawa, I., Kalai, T., Hideg, K., Jin, L. W., Laurence, T. A., and Voss, J. C. (2015) Protective spin-labeled fluorenes maintain amyloid beta peptide in small oligomers and limit transitions in secondary structure. *Biochim Biophys Acta* **1854**, 1860-1870

16. Kalai, T., Petrlova, J., Balog, M., Aung, H. H., Voss, J. C., and Hideg, K. (2011) Synthesis and study of 2-amino-7-bromofluorenes modified with nitroxides and their precursors as dual anti-amyloid and antioxidant active compounds. *Eur J Med Chem* **46**, 1348-1355

17. Cai, Z., Zhao, B., and Ratka, A. (2011) Oxidative stress and beta-amyloid protein in Alzheimer's disease. *Neuromolecular Med* **13**, 223-250

18. Rosini, M., Simoni, E., Milelli, A., Minarini, A., and Melchiorre, C. (2014) Oxidative stress in Alzheimer's disease: are we connecting the dots? *Journal of medicinal chemistry* **57**, 2821-2831

19. Sultana, R., and Butterfield, D. A. (2010) Role of oxidative stress in the progression of Alzheimer's disease. *J Alzheimers Dis* **19**, 341-353

20. Rochet, J. C. (2007) Novel therapeutic strategies for the treatment of protein-misfolding diseases. *Expert Rev Mol Med* **9**, 1-34

21. Hubin, E., van Nuland, N. A., Broersen, K., and Pauwels, K. (2014) Transient dynamics of Abeta contribute to toxicity in Alzheimer's disease. *Cell Mol Life Sci* **71**, 3507-3521

22. Kubiak-Ossowska, K., Cwieka, M., Kaczynska, A., Jachimska, B., and Mulheran, P. A. (2015) Lysozyme adsorption at a silica surface using simulation and experiment: effects of pH on protein layer structure. *Phys Chem Chem Phys* **17**, 24070-24077

23. Ihalainen, P., Majumdar, H., Viitala, T., Törngren, B., Närjeoja, T., Määttänen, A., Sarfraz, J., Härmä, H., Yliperttula, M., Österbacka, R., and Peltonen, J. (2013) Application of Paper-Supported Printed Gold Electrodes for Impedimetric Immunosensor Development. *Biosensors* **3**, 1-17

24. Bunker, A., Magarkar, A., and Viitala, T. (2016) Rational design of liposomal drug delivery systems, a review: Combined experimental and computational studies of lipid membranes, liposomes and their PEGylation. *Biochim Biophys Acta*

25. Snyder, S. W., Ladror, U. S., Wade, W. S., Wang, G. T., Barrett, L. W., Matayoshi, E. D., Huffaker, H. J., Krafft, G. A., and Holzman, T. F. (1994) Amyloid-beta aggregation: selective inhibition of aggregation in mixtures of amyloid with different chain lengths. *Biophys J* **67**, 1216-1228

26. Karlsson, R., Katsamba, P. S., Nordin, H., Pol, E., and Myszka, D. G. (2006) Analyzing a kinetic titration series using affinity biosensors. *Analytical biochemistry* **349**, 136-147

27. Myszka, D. G., Jonsen, M. D., and Graves, B. J. (1998) Equilibrium Analysis of High Affinity Interactions Using BIACORE. *Analytical biochemistry* **265**, 326-330

28. Palladino, P., Aura, A., and Spoto, G. (2015) Surface plasmon resonance for the label-free detection of Alzheimer's β-amyloid peptide aggregation. *Analytical and Bioanalytical Chemistry*, 1-6

29. Peterlinz, K., and Georgiadis, R. (1996) Two-color approach for determination of thickness and dielectric constant of thin films using surface plasmon resonance spectroscopy. *Optics Communications* **130**, 260-266

30. Zhou, M., Otomo, A., Yokoyama, S., and Mashiko, S. (2001) Estimation of organic molecular film structures using surface–plasmon resonance spectroscopy. *Thin Solid Films* **393**, 114-118

31. Grassi, J. H., and Georgiadis, R. M. (1999) Temperature-dependent refractive index determination from critical angle measurements: Implications for quantitative SPR sensing. *Analytical chemistry* **71**, 4392-4396

32. Liang, H., Miranto, H., Granqvist, N., Sadowski, J. W., Viitala, T., Wang, B., and Yliperttula, M. (2010) Surface plasmon resonance instrument as a refractometer for liquids and ultrathin films. *Sensors and Actuators B: Chemical* **149**, 212-220

33. Granqvist, N., Liang, H., Laurila, T., Sadowski, J., Yliperttula, M., and Viitala, T. (2013) Characterizing ultrathin and thick organic layers by surface plasmon resonance three-wavelength and waveguide mode analysis. *Langmuir* **29**, 8561-8571

34. Granqvist, N., Yliperttula, M., Välimäki, S., Pulkkinen, P., Tenhu, H., and Viitala, T. (2014) Control of the Morphology of Lipid Layers by Substrate Surface Chemistry. *Langmuir* **30**, 2799-2809

35. Zhang, S., Iwata, K., Lachenmann, M. J., Peng, J. W., Li, S., Stimson, E. R., Lu, Y., Felix, A. M., Maggio, J. E., and Lee, J. P. (2000) The Alzheimer's peptide a beta adopts a collapsed coil structure in water. *J Struct Biol* **130**, 130-141

36. Lim, K. H., Henderson, G. L., Jha, A., and Louhivuori, M. (2007) Structural, dynamic properties of key residues in Abeta amyloidogenesis: implications of an important role of nanosecond timescale dynamics. *Chembiochem* **8**, 1251-1254

37. Yan, Y., and Wang, C. (2006) Abeta42 is more rigid than Abeta40 at the C terminus: implications for Abeta aggregation and toxicity. *J Mol Biol* **364**, 853-862

38. Yan, Y., Liu, J., McCallum, S. A., Yang, D., and Wang, C. (2007) Methyl dynamics of the amyloid-beta peptides Abeta40 and Abeta42. *Biochem Biophys Res Commun* **362**, 410-414

39. Li, J., Liu, R., Lam, K. S., Jin, L. W., and Duan, Y. (2011) Alzheimer's disease drug candidates stabilize A-beta protein native structure by interacting with the hydrophobic core. *Biophys J* **100**, 1076-1082

40. Lesne, S., Koh, M. T., Kotilinek, L., Kayed, R., Glabe, C. G., Yang, A., Gallagher, M., and Ashe, K. H. (2006) A specific amyloid-beta protein assembly in the brain impairs memory. *Nature* **440**, 352-357

41. Kayed, R., and Lasagna-Reeves, C. A. (2013) Molecular mechanisms of amyloid oligomers toxicity. *J Alzheimers Dis* **33 Suppl 1**, S67-78

42. Tiwari, M. K., and Kepp, K. P. (2016) β-Amyloid pathogenesis: Chemical properties versus cellular levels. *Alzheimer's & Dementia* **12**, 184-194

43. Landau, M., Sawaya, M. R., Faull, K. F., Laganowsky, A., Jiang, L., Sievers, S. A., Liu, J., Barrio, J. R., and Eisenberg, D. (2011) Towards a pharmacophore for amyloid. *PLoS Biol* **9**, e1001080

44. Minicozzi, V., Chiaraluce, R., Consalvi, V., Giordano, C., Narcisi, C., Punzi, P., Rossi, G. C., and Morante, S. (2014) Computational and experimental studies on beta-sheet breakers targeting Abeta1-40 fibrils. *The Journal of biological chemistry* **289**, 11242-11252

45. Okuno, H., Mori, K., Okada, T., Yokoyama, Y., and Suzuki, H. (2007) Development of aggregation inhibitors for amyloid-beta peptides and their evaluation by quartz-crystal microbalance. *Chem Biol Drug Des* **69**, 356-361

46. Hilbich, C., Kisters-Woike, B., Reed, J., Masters, C. L., and Beyreuther, K. (1992) Substitutions of hydrophobic amino acids reduce the amyloidogenicity of Alzheimer's disease beta A4 peptides. *J Mol Biol* **228**, 460-473

47. Cerf, E., Sarroukh, R., Tamamizu-Kato, S., Breydo, L., Derclaye, S., Dufrene, Y. F.,

Narayanaswami, V., Goormaghtigh, E., Ruysschaert, J. M., and Raussens, V. (2009) Antiparallel beta-sheet: a signature structure of the oligomeric amyloid beta-peptide. *The Biochemical journal* **421**, 415-423

48. Ahmed, M., Davis, J., Aucoin, D., Sato, T., Ahuja, S., Aimoto, S., Elliott, J. I., Van Nostrand, W. E., and Smith, S. O. (2010) Structural conversion of neurotoxic amyloid-beta(1-42) oligomers to fibrils. *Nat Struct Mol Biol* **17**, 561-567

49. Mitternacht, S., Staneva, I., Hard, T., and Irback, A. (2011) Monte Carlo study of the formation and conformational properties of dimers of Abeta42 variants. *J Mol Biol* **410**, 357-367

50. Larini, L., and Shea, J. E. (2012) Role of beta-hairpin formation in aggregation: the self-assembly of the amyloid-beta(25-35) peptide. *Biophys J* **103**, 576-586

51. Fawzi, N. L., Phillips, A. H., Ruscio, J. Z., Doucleff, M., Wemmer, D. E., and Head-Gordon, T. (2008) Structure and dynamics of the Abeta(21-30) peptide from the interplay of NMR experiments and molecular simulations. *Journal of the American Chemical Society* **130**, 6145-6158

52. Sandberg, A., Luheshi, L. M., Sollvander, S., Pereira de Barros, T., Macao, B., Knowles, T. P., Biverstal, H., Lendel, C., Ekholm-Petterson, F., Dubnovitsky, A., Lannfelt, L., Dobson, C. M., and Hard, T. (2010) Stabilization of neurotoxic Alzheimer amyloid-beta oligomers by protein engineering. *Proceedings of the National Academy of Sciences of the United States of America* **107**, 15595-15600

53. Danielsson, J., Jarvet, J., Damberg, P., and Graslund, A. (2005) The Alzheimer beta-peptide shows temperature-dependent transitions between left-handed 3-helix, beta-strand and random coil secondary structures. *FEBS J* **272**, 3938-3949

54. Qian, R., Mhatre, R., and Krull, I. (1997) Characterization of antigen-antibody complexes by size-exclusion chromatography coupled with low-angle light-scattering photometry and viscometry. *Journal of Chromatography A* **787**, 101-109

55. Ball, V., and Ramsden, J. J. (1998) Buffer dependence of refractive index increments of protein solutions. *Biopolymers* **46**, 489-492

56. Arwin, H. (1986) Optical properties of thin layers of bovine serum albumin, γ-globulin, and hemoglobin. *Applied Spectroscopy* **40**, 313-318

57. Zhao, H., Brown, P. H., and Schuck, P. (2011) On the distribution of protein refractive index increments. *Biophysical journal* **100**, 2309-2317

58. DuBay, K. F., Pawar, A. P., Chiti, F., Zurdo, J., Dobson, C. M., and Vendruscolo, M. (2004) Prediction of the absolute aggregation rates of amyloidogenic polypeptide chains. *J Mol Biol* **341**, 1317-1326

59. Chiti, F., Stefani, M., Taddei, N., Ramponi, G., and Dobson, C. M. (2003) Rationalization of the effects of mutations on peptide and protein aggregation rates. *Nature* **424**, 805-808

60. Fernandez-Escamilla, A. M., Rousseau, F., Schymkowitz, J., and Serrano, L. (2004) Prediction of sequence-dependent and mutational effects on the aggregation of peptides and proteins. *Nat Biotechnol* **22**, 1302-1306

61. Cohen, S. I., Linse, S., Luheshi, L. M., Hellstrand, E., White, D. A., Rajah, L., Otzen, D. E., Vendruscolo, M., Dobson, C. M., and Knowles, T. P. (2013) Proliferation of amyloid-beta42 aggregates occurs through a secondary nucleation mechanism. *Proceedings of the National Academy of Sciences of the United States of America* **110**, 9758-9763

62. Hong, H. S., Maezawa, I., Budamagunta, M., Rana, S., Shi, A., Vassar, R., Liu, R., Lam, K. S., Cheng, R. H., Hua, D. H., Voss, J. C., and Jin, L. W. (2010) Candidate anti-Abeta fluorene compounds selected from analogs of amyloid imaging agents. *Neurobiology of aging* **31**, 1690-1699

63. Karlsson, R., and Fält, A. (1997) Experimental design for kinetic analysis of protein-protein interactions with surface plasmon resonance biosensors. *Journal of immunological methods* **200**, 121-133

64. Albers, W. M., and Vikholm-Lundin, I. (2011) *Surface Plasmon Resonance on Nanoscale Organic Films*, Springer, New York

65. Maier, S. A. (2007) Plasmonics: fundamentals and applications. in *Springer Science & Business Media*.

66. Hayt, W. H., and Buck, J. A. (2001) *Engineering electromagnetics*,

67. Sadowski, J. W., Korhonen, I. K. J., and Peltonen, J. P. K. (1995) Characterization of thin films and their structures in surface plasmon resonance measurements. *OPTICAL ENGINEERING* **34**, 6

68. De Feijter, J., Benjamins, D. J., and Veer, F. (1978) Ellipsometry as a tool to study the adsorption behavior of synthetic and biopolymers at the air–water interface. *Biopolymers* **17**, 1759-1772

69. Trott, O., and Olson, A. J. (2010) AutoDock Vina: improving the speed and accuracy of docking with a new scoring function, efficient optimization and multithreading. *J computational chemistry* **31**, 455-461

70. Vivekanandan, S., Brender, J. R., Lee, S. Y., and Ramamoorthy, A. (2011) A Partially Folded Structure of Amyloid-Beta(1-40) in an Aqueous Environment. *Biochemical and biophysical research communications* **411**, 312-316

71. Pronk, S., Páll, S., Schulz, R., Larsson, P., Bjelkmar, P., Apostolov, R., Shirts, M., Smith, J., Kasson, P., van der Spoel, D., Hess, B., and Lindahl, E. (2013) GROMACS 4.5: a high-throughput and highly parallel open source molecular simulation toolkit. *Bioinformatics* **29**, 845-854

72. Schmid, N., Eichenberger, A. P., Choutko, A., Riniker, S., Winger, M., A.E., M., and W.F., v. G. (2011) Definition and testing of the GROMOS force-field versions 54A7 and 54B7. *Eur Biophys J.* **40**, 843-856

73. Malde, A. K., Zuo, L., Breeze, M., Stroet, M., Poger, D., Nair, P. C., Oostenbrink, C., and Mark, A. E. (2011) An Automated Force Field Topology Builder (ATB) and Repository: Version 1.0. *Journal of Chemical Theory and Computation* **7**, 4026-4037

74. Koziara, K., Stroet, M., Malde, A., and Mark, A. (2014) Testing and validation of the Automated Topology Builder (ATB) version 2.0: prediction of hydration free enthalpies. *J Comput Aided Mol Des.* **28**, 221-233

75. Berendsen, H. J. C., Postma, J. P. M., van Gunsteren, W. F., and Hermans, J. (1981) INTERACTION MODELS FOR WATER IN RELATION TO PROTEIN HYDRATION. in *Intermolecular Forces* (Pullman, B. ed.), D. Reidel Publishing Company. pp 331-342

76. Berendsen, H. J. C., Postma, J. P. M., van Gunsteren, W. F., DiNola, A., and Haak, J. R. Molecular dynamics with coupling to an external bath. *J. Chem. Phys.* **81**, 3684-3690

77. Essmann, U., Perera, L., Berkowitz, M. L., Darden, T., Lee, H., and Pedersen, L. G. (1995) A smooth particle mesh Ewald method. *J. Chem. Phys.* **103**, 8577-8593

78. Hess, B., Bekker, H., Berendsen, H. J. C., and Fraaije, J. G. E. M. (1997) LINCS: A Linear Constraint Solver for Molecular Simulations. *J. Comput. Chem.* **18**, 18-1463

79. Kabsch, W., and Sander, C. (1983) Dictionary of protein secondary structure: pattern recognition of hydrogen-bonded and geometrical features. *Biopolymers* **22**, 2577-2637

80. Humphrey, W., A., D., and Schulten, K. (1996) VMD: visual molecular dynamics. *J Mol Graph.* **14**, 33-38

SUPPLEMENTAL INFORMATION

MP-SPR ADDITIONAL DETAILS

The usefulness of MP-SPR for accurate biosensing measurements is primarily due to two factors. Firstly, for monochromatic (laser) light and a defined prism-metal-dielectric combination, the angle of incidence at which the plasmon resonance occurs, depends on the dielectric constant (i.e. refractive index; dielectric constant and refractive index are related by $\varepsilon=n^2$) of the medium adjacent to the metal surface. This, in turn, is an excellent means to monitor with high sensitivity nano-scale physical and biochemical events occurring at the surface or at the vicinity of the surface. Of importance, the changes caused by the physical and chemical reactions in the medium and at the vicinity of the surface are straightforwardly reflected to the observed resonance angle as a SPR angle dip shift. Secondly, the shape of the SPR curve as a whole is dependent primarily on the thickness and optical properties of the metal layer. In particular, when the full SPR curve data provided by two different wavelength lasers is recorded with the MP-SPR instrument, the thickness and refractive indices of thin (bio) molecule films can be calculated with certain limitations as discussed later in this text. The multi-parametric approach allows us also to exploit the detection of total internal reflection angle (TIR angle) to avoid the unwanted bulk-effect occasionally biasing the interpretation of kinetic measurements in SPR. Furthermore, with this novel approach, we are able to observe the intensity changes of reflectance induced by the different absorption and scattering properties of the biofilm layers to draw conclusions of the compositions of those layers.

Table S1. All the calculated affinity values and parameters for different interaction scenarios of Aβ/SLF binary complexes. Data was processed and fitted using the TraceDrawer™ for MP-SPR Navi™.

	B_{max1} (Signal)	B_{max2} (Signal)	k_{a1} (1/(M*s))	k_{d1} (1/s)	K_{D1} (M)	k_{a2} (1/(M*s))	k_{d2} (1/s)	K_{D2} (M)	χ^2
SLF with biotinylated Aβ monomer	123.73 ($\pm$ 8.07x10^{-1})	119.58 ($\pm$ 4.28x10^{-1})	2.92x10^{2} ($\pm$ 4.95x10^{3})	4.34x10^{-3} ($\pm$ 4.28x10^{-5})	1.49x10^{-5} ($\pm$ 8.81x10^{-7})	1.70x10^{1} ($\pm$ 4.15x10^{3})	6.09x10^{-14} ($\pm$ 1.69x10^{4})	3.58x10^{-15} ($\pm$ 1.67x10^{-2})	34.39
SLF with native Aβ bound to biotinylated Aβ monomer	137.69 ($\pm$ 1.05x10^{0})	947.24 ($\pm$6.40x10^{-1})	4.00x10^{2} ($\pm$ 6.90x10^{3})	1.62x10^{-2} ($\pm$ 1.32x10^{-5})	4.06x10^{-5} ($\pm$ 2.36x10^{-6})	1.69x10^{0} ($\pm$ 5.88x10^{2})	7.78x10^{-13} ($\pm$ 1.70x10^{4})	4.60x10^{-13} ($\pm$ 8.29x10^{-2})	23.30
SLF with AβO	440.06 ($\pm$1.18x10^{0})	1530.53 ($\pm$8.49x10^{-1})	2.20x10^{2} ($\pm$1.63x10^{3})	2.38x10^{-2} ($\pm$1.74x10^{-5})	1.08x10^{-4} ($\pm$-1.48x10^{-5})	1.88x10^{0} ($\pm$1.26x10^{3})	2.28x10^{-4} ($\pm$1.15x10^{-5})	1.21x10^{-4} ($\pm$-1.80x10^{-7})	41.63
SLF with AβO pretreated with SLF	499.48 ($\pm$ 1.25x10^{0})	1169.44 ($\pm$ 1.09x10^{0})	1.78x10^{2} ($\pm$ 1.95x10^{3})	2.05x10^{-2} ($\pm$ 1.17x10^{-5})	1.15x10^{-4} ($\pm$ 1.06x10^{-5})	2.04x10^{0} ($\pm$ 1.82x10^{3})	2.01x10^{-4} ($\pm$ 1.59x10^{-5})	9.84x10^{-5} ($\pm$ 1.11x10^{-7})	44.63

Additional details on relating Aβ self-assembly and aggregation processes in terms of *total surface mass density* generated by the deposition of molecular mass during the interactions. In contrast to the surface mass density changes by SLF deposition alone, our aim was to evaluate how the SLF reduces the total amount of surface-deposited mass by inhibiting Aβ self-association. We chose two time points at which the baseline was considered stable after the injections, and calculated the surface mass densities at those points. In brief review of the experimental arrangement, both of the sample channel surfaces were pre-coated *in situ* in constant buffer flow (10 µL/min) with non-biotinylated Aβ to achieve a biomimetic situation for Aβ aggregation in the consequent Aβ and SLF injections. In the upper sample channel we made an injection of Aβ+SLF mixture (pretreated AβO) with molar ratio 1:2 (10 µM:20 µM) on the basis of our previous experiments and hypothesis that there exists two SLF binding sites in Aβ peptides. Into the lower sample channel we injected only 10 µM of Aβ without any SLF present. We repeated the described injections twice. In the upper flow channel with SLF present, we calculated surface mass densities of ~26 ng/cm² at time point (1), and only ~6 ng/cm² at time point (2), resulting to overall surface mass density increase of ~32 ng/cm². In the lower flow channel without any SLF, the calculated surface mass densities were ~92 ng/cm² at time point (1), and ~45 ng/cm² at time point (2), the overall increase at ~137 ng/cm² after the injections. Hence, the surface mass density evaluations support our previous observations that the SLF is capable of hindering the Aβ self-assembly and aggregation processes.

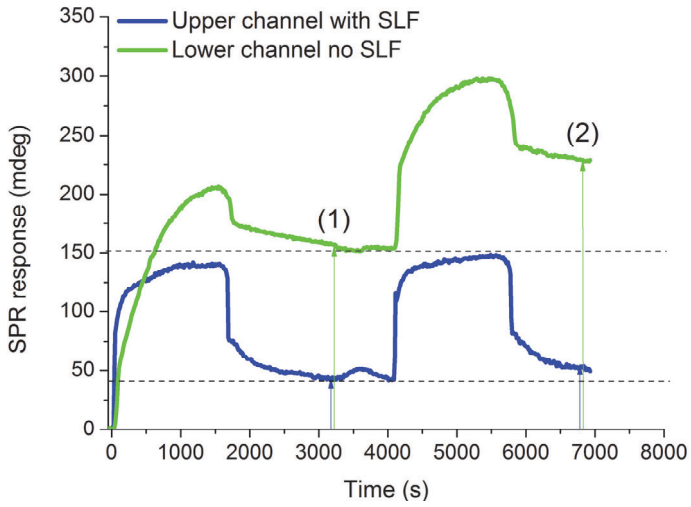

Fig. S1. *Total surface mass densities* on the sensor surface when SLF was shown to prevent Aβ self-association. The green sensorgram trace showing the lower channel deposition, and the blue trace representing the upper channel events. Arrows as guides to the eye to depict the difference in deposited masses. The calculated total surface mass densities are mainly due to the Aβ accumulation onto the surface. In the upper channel with SLF present after the first injection and baseline stabilization at first time point **(1)** surface mass density ~26 ng/cm² was observed. After the second injection at second time point **(2)** surface mass density of only ~6 ng/cm² was detected. In the lower channel without SLF hindering the molecular mass accumulation the detected surface mass densities at corresponding time points were ~92 ng/cm² and ~45 ng/cm², respectively. Finally, the total surface mass densities acquired at the end of the interactions were ~32 ng/cm² in the upper channel, and ~137 ng/cm² in the lower channel.

13 (III) Single Exosome Study Reveals Subpopulations Distributed Among Cell Lines with Variability Related to Membrane Content

‡ Equal contribution

Journal of Extracellular Vesicles

CO-action PUBLISHING

ORIGINAL RESEARCH ARTICLE

Single exosome study reveals subpopulations distributed among cell lines with variability related to membrane content

Zachary J. Smith[1,2], Changwon Lee[1§], Tatu Rojalin[1,3§], Randy P. Carney[4§], Sidhartha Hazari[4], Alisha Knudson[4], Kit Lam[4], Heikki Saari[3], Elisa Lazaro Ibañez[3], Tapani Viitala[3], Timo Laaksonen[3], Marjo Yliperttula[3] and Sebastian Wachsmann-Hogiu[1,5*]

[1]Center for Biophotonics, University of California Davis, Sacramento, CA, USA; [2]Department of Precision Mechanics and Precision Instrumentation, University of Science and Technology of China, Hefei, Anhui, China; [3]Division of Pharmaceutical Biosciences, Centre for Drug Research, University of Helsinki, Helsinki, Finland; [4]Department of Biochemistry and Molecular Medicine, University of California Davis, Sacramento, CA, USA; [5]Department of Pathology and Laboratory Medicine, University of California Davis, Sacramento, CA, USA

Current analysis of exosomes focuses primarily on bulk analysis, where exosome-to-exosome variability cannot be assessed. In this study, we used Raman spectroscopy to study the chemical composition of single exosomes. We measured spectra of individual exosomes from 8 cell lines. Cell-line-averaged spectra varied considerably, reflecting the variation in total exosomal protein, lipid, genetic, and cytosolic content. Unexpectedly, single exosomes isolated from the same cell type also exhibited high spectral variability. Subsequent spectral analysis revealed clustering of single exosomes into 4 distinct groups that were not cell-line specific. Each group contained exosomes from multiple cell lines, and most cell lines had exosomes in multiple groups. The differences between these groups are related to chemical differences primarily due to differing membrane composition. Through a principal components analysis, we identified that the major sources of spectral variation among the exosomes were in cholesterol content, relative expression of phospholipids to cholesterol, and surface protein expression. For example, exosomes derived from cancerous versus non-cancerous cell lines can be largely separated based on their relative expression of cholesterol and phospholipids. We are the first to indicate that exosome subpopulations are shared among cell types, suggesting distributed exosome functionality. The origins of these differences are likely related to the specific role of extracellular vesicle subpopulations in both normal cell function and carcinogenesis, and they may provide diagnostic potential at the single exosome level.

Keywords: *exosomes*; *microvesicles*; *single particle*; *Raman*; *laser trap*; *membrane content*

Responsible Editor: Marca Wauben, Utrecht University, Netherlands.

*Correspondence to: Sebastian Wachsmann-Hogiu, 2700 Stockton Blvd. Suite 1400, Sacramento, CA 95817, Email: swachsmann@ucdavis.edu

To access the supplementary material to this article, please see Supplementary files under 'Article Tools'.

Received: 14 May 2015; Revised: 26 October 2015; Accepted: 6 November 2015; Published: 7 December 2015

Exosomes are nanosized extracellular vesicles (EVs) formed by nearly all types of cells of intracellular multivesicular bodies (MVBs). They are released into the extracellular space when the MVBs fuse with the plasma membrane. Recently, they have been intensely studied due to discoveries that exosomes (a) transport functional mRNA, miRNA, (1,2) and DNA (3); (b) are expressly packaged by cells for highly specific endogenous and exogenous intercellular communication (4); (c) are constitutively integrated in immune cell physiology (5); and (d) are heavily implicated in numerous pathologies, particularly cancer (6,7). Exosome secretion is also now understood to be fundamental in healthy intercellular communication, and exosomes can be isolated from most

[§]These authors contributed equally to this manuscript.

Citation: Journal of Extracellular Vesicles 2015, **4**: 28533 - http://dx.doi.org/10.3402/jev.v4.28533

(page number not for citation purpose)

biological fluids (blood, urine, lymph, etc.) for potential use as biomarkers, since their protein, lipid, genetic, and metabolic content, in addition to frequency of generation, can be altered in diseased cells. Based on the clear evidence that cells actively direct the packing of lipids, protein, RNA, and various cytosolic small metabolites into exosomes, we sought to apply broad chemical spectroscopy to single exosomes for the identification of chemically distinct subpopulations arising from sorting choices during exosome biogenesis or post-translational modification of exosomes after synthesis/release.

Many factors may contribute to perceived chemical dispersity for single exosomes, including exosome isolation techniques (e.g. differential centrifugation vs. commercial precipitation reagents may isolate disparate levels of exosome subpopulations) and also biological mechanisms. For example, exosomal transmembrane proteins exist in various states of post-translational modification [e.g. glycosylation (8)] or lipid/sterol activation (9,10). Finally, while we follow the ISEV characterization guidelines to ensure that the vesicles studied in this paper are exosomes [as opposed to microvesicles (MVs) and other EVs] (11), even this definition is rapidly evolving and may not be soon applicable, hence the continued importance of studies that better define exosomes and their subpopulations.

To explore the chemical content of individual EVs, we utilized Laser tweezers Raman spectroscopy (LTRS). Raman spectroscopy is a well-established, non-destructive, and non-contact method for determining the chemical makeup of a variety of samples (12). Its label-free nature makes it a natural choice for *in vivo* diagnostics and longitudinal studies of cells and tissues over time (13,14). Raman spectroscopy has been successfully applied to a variety of biomedical problems, including cancer detection (15,16), studies of bone health (17,18), response of cells to drugs (19), and quantification of analytes in biofluids (20,21), among many others (22,23).

Among the many forms of Raman spectroscopy, LTRS holds particular promise for study of exosomes. In LTRS, a tightly focused laser beam traps and holds small particles at the laser's focal point. A confocal detection setup collects Raman scattering only from a precise focal volume, allowing cellular and subcellular objects to be studied individually. This method has been used to study, for example, individual cancerous and non-cancerous cells (24,25), the activation response of individual immune cells (26), as well as smaller, nanoscale objects such as lipid droplets in milk (27), latex beads (28), and subcellular organelles (29). These studies highlight the power of Raman spectroscopy to determine the chemical content from individual micro- and nanoparticles, which are well below the limit of detection for conventional "wet chemistry" methods that require a large amount of starting material for analysis. A prior study examined clusters of exosomes, trapped simultaneously in the laser focus, using LTRS, with the disadvantage of obtaining population-averaged information (30). This study found ensemble exosomal chemical differences following cell starvation, highlighting Raman spectroscopy's ability to discriminate between different exosome subpopulations (30). Here, we used LTRS to examine *single* exosomes and MVs isolated from both cancerous and non-cancerous cells to characterize their heterogeneity in chemical content. In this study, exosomes were isolated using both commercial isolation reagents and ultracentrifugation, whereas MVs were separated via ultracentrifugation. Because of the overlapping size distribution of exosomes and MVs when purified with ultracentrifugation, we define *MVs* as those vesicles pelleted at $20{,}000 \times g$, whereas *exosomes* are those vesicles pelleted at $110{,}000 \times g$.

By analysing the Raman spectra of many individual exosomes derived from a multitude of cell lines, we were able to identify several subpopulations of exosomes that appeared to be shared across cell lines, suggesting conserved biological function. Additionally, cancerous and non-cancerous cell types appear to differ in relative production of exosome subpopulations, as identified by principal component analysis (PCA). Furthermore, we compared the spectral differences found by PCA to known membrane constituents as well as to principal components derived from a data set consisting of native and trypsinized EVs. This comparison revealed that the dominant chemical differences between these subpopulations are mostly reflected in the content of the EVs' membranes. These results provide information about exosome variability at the single vesicle level that will further elucidate the role of exosome subtypes with regard to their phenotype and ultimate biological function.

Materials and methods

Raman spectroscopy of single extracellular vesicles

Setup and spectral acquisition

As described below, exosomes were first isolated from cell culture and measured one at a time using our Raman trapping system, as shown schematically in Fig. 1. All measurements were made using the home-built LTRS system described previously (14,19). Briefly, 25 mW of light from a single mode, 785 nm laser (CrystalLaser, Reno, NV), was coupled into an inverted microscope (IX-71, Olympus, Center Valley, PA) outfitted with a $60\times$, 1.2-NA water immersion objective. The light was focused by the objective to a diffraction-limited spot ($\sim 1\,\mu m \times 1\,\mu m \times 3\,\mu m$ in size), capable of trapping cells and other small particles such as lipid droplets and exosomes (14,27). The trapping laser additionally excited Raman scattering from the trapped object, and backscattered light was collected back through the objective. A dichroic beam-splitter and edge filter

Citation: Journal of Extracellular Vesicles 2015, **4**: 28533 - http://dx.doi.org/10.3402/jev.v4.28533

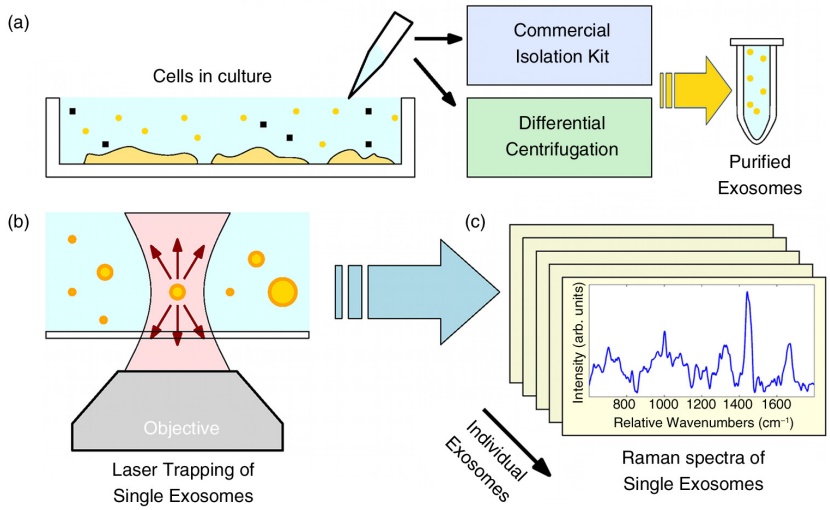

Fig. 1. Schematic diagram of exosome isolation and measurement of single-exosome Raman spectra. (a) Media from cultured cells are purified using a commercial isolation kit or differential centrifugation; (b) purified exosomes are trapped in the laser beam of a home-built microscope system, and Raman spectra are collected, yielding (c) a database of spectra of single exosomes.

(Chroma Technology, Bellows Falls, VT) separated the Raman scattered light from the backscattered excitation light. The filtered Raman signal was focused into a multi-mode optical fibre where it was delivered to a SpectraPro 2300i spectrograph (Princeton Instruments, Trenton, NJ). The dispersed spectrum was measured by a TE-cooled Pixis 100 CCD (Princeton Instruments).

After vesicle preparation, suspensions were diluted 10–100 times in PBS and placed on a quartz coverslip, used to avoid the strong spectral background from glass. The specific dilution factor for each sample was chosen empirically with the goal of having, on average, <1 EV per field of view of the microscope at any 1 time. This step helped to ensure that only single EV particles were measured by our Raman system and to decrease the chance that a second vesicle would wander into the trapping laser beam during spectral acquisition. In order to acquire a spectrum, the stage was manually steered to trap an exosome or MV in solution. The vesicle was levitated away from the quartz coverslip to reduce the signal strength of the substrate. The small volume of the vesicles and the correspondingly small amount of material contained within them necessitated long exposure times to acquire spectra with acceptable signal-to-noise ratios. In our experiments, we recorded ten 30-s spectral frames from each particle.

Following data collection, spectra were imported into MATLAB for all subsequent data processing, described below.

Spectral data processing

All spectra were corrected for cosmic rays using a median threshold filter described previously (31). By comparing spectra pixel-wise across the 10 frames, outlier values caused by cosmic rays can be easily detected and their value replaced by the frame-wise median. Following this correction, the 10 frames from each vesicle were averaged for an equivalent integration time of 5 min per vesicle. The spectra were first smoothed using the Whittaker smoother proposed by Eilers (32) with a Lagrange parameter of 5. Following smoothing, the spectra were background corrected by subtracting off the spectral background from quartz, PBS buffer, total exosome isolation reagent (TEIR), and a fifth order polynomial to account for autofluorescence and other background deviations. Coefficients for each component of the estimated background were determined using an asymmetric least squares (AsLS) model, with a value of the asymmetry parameter of $p=0.001$ (33,34). For exosome samples isolated using the TEIR reagent kit, we found that the reagents remained attached to the exosomes after purification. The TEIR reagents gave an unexpectedly strong signal, whose removal from each exosome spectrum was verified by comparing exosomes isolated using TEIR and those isolated by ultracentrifugation from the same cell culture, as described in the Supplementary File. Following background correction, all spectra were normalized to the area under the curve of the broad peak at 1,450 cm^{-1}, a stand-in for total organic content and a standard normalization region (26,35). The y-axis of the Raman spectra then represents the proportion of individual chemical groups relative to the total organic content within an individual vesicle. This allows PCA to represent differences in chemical *composition*,

rather than differences in chemical *concentration*, as might be encountered, for example, between vesicles of identical content but different size.

Principal components analysis was performed using the built-in MATLAB function princomp. Following principal component decomposition, the first 10 principal component scores for each exosome were submitted to hierarchical clustering analysis using Ward's method for creating linkages based on Euclidean pairwise distances. This analysis was performed using MATLAB's built-in function linkage.

In contrast to the fits of background spectra to the raw spectral data, which were performed with AsLS fitting, fits of principal component spectra shown in the Supplementary File (36) were performed via standard least-squares modelling.

Extracellular vesicle preparation and isolation using the TEIR reagent kit

Cell culture

Human lung carcinoma A549 cell line, human hepatocarcinoma Huh-7 cell line, and mouse embryonic fibroblast 3T3 cell line were cultured in Dulbecco's modified Eagle medium with 10% foetal bovine serum (FBS), 100 units/mL penicillin, and 100 µg/mL streptomycin. Human lung normal fibroblast IMR90 cell line was cultured in Eagle's minimum essential medium with 10% FBS, 100 units/mL penicillin, and 100 µg/mL streptomycin. Human ovarian carcinoma SKOV3 cell line was cultured in McCoy's 5A modified medium with 10% FBS, 100 units/mL penicillin, and 100 µg/mL streptomycin. Human acute T-cell leukaemia Jurkat cell line and human acute myeloblastic leukaemia Kasumi-1 cell line were cultured in RPMI-1640 medium with 10% FBS, 100 units/mL penicillin, and 100 µg/mL streptomycin at 37°C and 5% CO_2. All cell lines were cultured at 37°C and 5% CO_2 and were maintained by splitting upon reaching 80% confluence.

Exosome isolation using commercial precipitation reagent

Exosomes were isolated from cell-conditioned media as previously described (37). Briefly, cells were plated at ~25% confluency in a T-150 flask and incubated in appropriate conditioned medium (CM). CM contained exosome-depleted FBS (bovine-derived exosomes were removed from 30% FBS/media by ultracentrifugation at 100,000 × *g* for 18 h) to ensure that the resulting exosomes in the cell culture medium originated from the plated cells. After 48 h, the cell culture media was collected and centrifuged at 300 × *g* for 10 min, 2,000 × *g* for 20 min, and 10,000 × *g* for 1 h, to remove live cells, dead cells, and cell debris/MVs, respectively.

The exosome-containing CM was incubated with one-half the total volume of TEIR (4478359; Life Technologies®, Grand Island, NY, USA) at 4°C overnight before final centrifugation at 10,000 × *g* for 1 h at 4°C. The supernatant was aspirated to waste and the exosome pellet was resuspended in 1 × phosphate-buffered saline (PBS). These exosomes were used in downstream analysis and were stored at −20°C until thawing just prior to use. Exosomes were stored typically for less than 1 week at −20°C and never for longer than 4 weeks.

Preparation of LNCaP exosomes and MVs via differential centrifugation, treatment with trypsin

Cell culture

LNCaP prostate cancer cell line was used as the source for EVs. The cells were grown at +37°C and 5% CO_2 humidified atmosphere in RPMI-1640 medium supplemented with 10% EV-cleared FBS, 20 units/mL of penicillin, and 20 µg/mL of streptomycin (Gibco Invitrogen, Carlsbad, CA). The EV-cleared FBS was prepared by overnight (20 h) ultracentrifugation at 110,000 × *g* and +4°C of regular FBS using an L-70 ultracentrifuge with rotor type 50.2 Ti (Beckman Coulter, Brea, CA) with approximately 22 mL of supernatant per adaptor tube as described in Ref. (38). The FBS supernatant was then collected and filtered through a 0.22-µm Steritop filter device (Millipore, Billerica, MA). The cells were maintained at 60–90% confluence in T-175 cell culture flasks with 25 mL of medium, and CM was collected after 2–3 days of culture 3 times per week.

Vesicle isolation using differential centrifugation

EVs were isolated from cell-conditioned medium using a differential centrifugation protocol as described previously (3). After collection, any cells and large debris were removed from the CM by centrifugation at 2,500 × *g* and +4°C for 25 min in 50 mL Falcon tubes with an Eppendorf Centrifuge 5810 R with swinging bucket rotor (Hamburg, Germany). The supernatant was then centrifuged at 20,000 × *g* and +4°C for 1 h to pellet MVs using a Sorvall RC 5C centrifuge with SLA-1500 rotor (Thermo Scientific, Waltham, MA) with approximately 125 mL of supernatant per adapter tube. The pellet (MVs) was suspended in 100 µL of Dulbecco's PBS buffer (DPBS, Gibco Invitrogen) and the supernatant was centrifuged at 110,000 × *g* and +4°C for 2 h to pellet exosomes using L-70 ultracentrifuge with Type 50.2 Ti rotor with approximately 22 mL of supernatant per adaptor tube. Because of the overlapping size distributions of the exosomes and MVs, and because of the confusion that still exists about the exact nature of these vesicles' characteristics and defining properties, we adopt the convention in this paper that all vesicles pelleted at 20,000 × *g* are referred to as *MVs*, whereas those pelleted at 110,000 × *g* are referred to as *exosomes*. The clear separation obtained between these 2 populations as probed by Raman spectroscopy confirms that these preparation protocols do isolate distinct EV subpopulations. After the ultracentrifugation, the supernatant was removed and the pellets (EVs) were collected with 100 µL of DPBS. The collected EV samples were then

Citation: Journal of Extracellular Vesicles 2015, **4**: 28533 - http://dx.doi.org/10.3402/jev.v4.28533

stored in −20°C for short-term (maximum 1 week) storage. Three MV and exosome samples collected during 1 week were pooled together, suspended into a total volume of 1 mL with DPBS and concentrated by ultracentrifugation at 170,000 × *g* and +4°C for 3 h using an Optima MAX-XP ultracentrifuge with a TLA-55 rotor (Beckman Coulter). The supernatant was removed from the EV pellets, leaving 30–50 μL to resuspend the pellets, after which they were stored in −80°C.

Cleavage of surface proteins by trypsin treatment

To cleave the membrane protein segments outside of the EVs, the EV samples were incubated in 1 mL of 0.25% (w/v) trypsin (Gibco Invitrogen) in DPBS for 1 h in +37°C. One-half of each sample was treated with trypsin and the other half served as a point of comparison for the effect of the treatment. The effect of trypsin treatment was assessed by western blotting of membrane proteins CD9 and CD63 as described below (39).

Size-exclusion chromatography

The trypsin-treated EVs and their control samples were purified by size-exclusion chromatography to separate the trypsin, cleaved protein segments, and other small molecules from the EVs as described by Boing et al. (40). For each sample, a column was prepared with 10 mL of sepharose CL-2B (GE Healthcare Life Sciences, Little Chalfont, UK) in DPBS running buffer, both degassed under vacuum. The samples were loaded into the column and 11 fractions of 0.5 mL were collected immediately from the start of the run. The presence of small particles in the fractions was confirmed with NTA (see below) from Fractions 7–10, with the highest particle concentrations usually found in Fractions 8 and 9. Fractions 7–10 were then pooled together and concentrated by ultracentrifugation at 170,000 × *g* as described above.

EV characterization

Electron microscopy of exosomes and EVs

TEIR-isolated vesicles were diluted in 1 × PBS and re-pelleted at 100,000 × *g* for direct resuspension in 2% (w/v) paraformaldehyde with 5 μL being deposited on Formvar carbon-coated EM grids. The grids were washed, transferred to 1% glutaraldehyde, contrasted in a solution of uranyl oxalate, and then contrasted and embedded in methyl cellulose–uranyl acetate according to a previously reported methodology (37). The grids were examined in a Philips/FEI BioTwin (Amsterdam, Netherlands) CM120 transmission electron microscope at 80 kV. Representative images from A549 exosomes are shown in Fig. 2a (left), showing the expected cup-shaped morphology.

For LNCaP, MVs both treated with trypsin and untreated were imaged by cryo-electron microscopy. Then, 3 μL of concentrated EV samples was added onto carbon TEM grids purified with a Gatan Solarus (Model 950) plasma cleaning system and frozen with Vitrobot (FEI) in liquid nitrogen. The grids were analysed by a JEOL JEM-3200FSC field emission cryo-TEM with 170 kV. Results are shown in Fig. 2a (middle, right), where the native circular morphology is seen in both treated and untreated MVs.

Immunoblot analysis to confirm exosome isolation

For exosomal western blots, 40 μg exosome aliquots were lysed in SDS sample buffer: 2% (w/v) sodium dodecyl sulphate, 125 mM Tris–HCl, pH 6.8, 12.5% (v/v) glycerol, and 0.02% (w/v) bromophenol blue. They were incubated with 50 mM DTT where necessary (i.e. not for anti-CD9 and anti-CD63 probing), heated for 5 min at 95°C, and spun to precipitate insoluble material (2 min, 14,000 × *g*). Protein was loaded onto gels according to the concentration as measured by BCA assay (Pierce, Rockford, IL), by first assuring no worse than "low" purification according to the ratio of vesicle counts by NTA to protein concentration (41). For whole cell lysates, cells were lysed in RIPA buffer (Thermo Scientific) with protease inhibitor and centrifuged at 18,000 × *g* at 4°C for 30 min to remove cell debris, and protein concentration of the cleared supernatants was determined by BCA assay. Exosomal and whole cell lysate proteins (20 μg per lane) were subjected to electrophoresis on 1-mm 10-well NuPAGE 4–12% (w/v) Bis-Tris Precast gels (ThermoFisher Scientific) performed at 90 V for 30 min and then 120 V until complete in NuPage MOPS buffer using an Xcell Surelock™ gel tank (ThermoScientific). Following electrophoresis, the proteins were transferred onto nitrocellulose membranes (ThermoFisher Scientific) for 2 h at 4°C and subsequently probed with the following antibodies: mouse monoclonal anti-CD63 (ThermoFisher Scientific), mouse monoclonal anti-CD9 (ThermoFisher Scientific), rabbit polyclonal anti-tsg101 (Sigma–Aldrich, St. Louis, MO, USA), and rabbit polyclonal anti-calnexin (Cell Signaling Technology, Danvers, MA, USA). Secondary antibodies (HRP-conjugated) were goat anti-rabbit and goat anti-mouse immunoglobulin (Santa Cruz Biotechnology, Dallas, TX, USA). All antibodies were prepared fresh at 1:1,000 dilutions (except anti-tsg101 at 1:500) in 5% (w/v) non-fat dairy milk in Tris-Buffered Saline with Tween™ (TBST) buffer (also used to block membranes). Immuno-active bands were detected on a (Bio-Rad ChemiDoc™: Hercules, CA, USA) MP Imaging System after 5 min ECL substrate incubation. Blots were re-probed as necessary to conserve exosome protein. The results of the western blot (shown in Fig. 2b) are consistent with exosome properties and thus validate the collection methodology used in this manuscript.

Immunoblot analysis to confirm digestion of surface proteins by trypsin

EV samples and cell lysates were lysed with RIPA buffer in the presence of a protease inhibitor mixture (Sigma–Aldrich) and prepared with 2 × Laemmli buffer (Bio-Rad) in non-reducing conditions. Using SDS–polyacrylamide

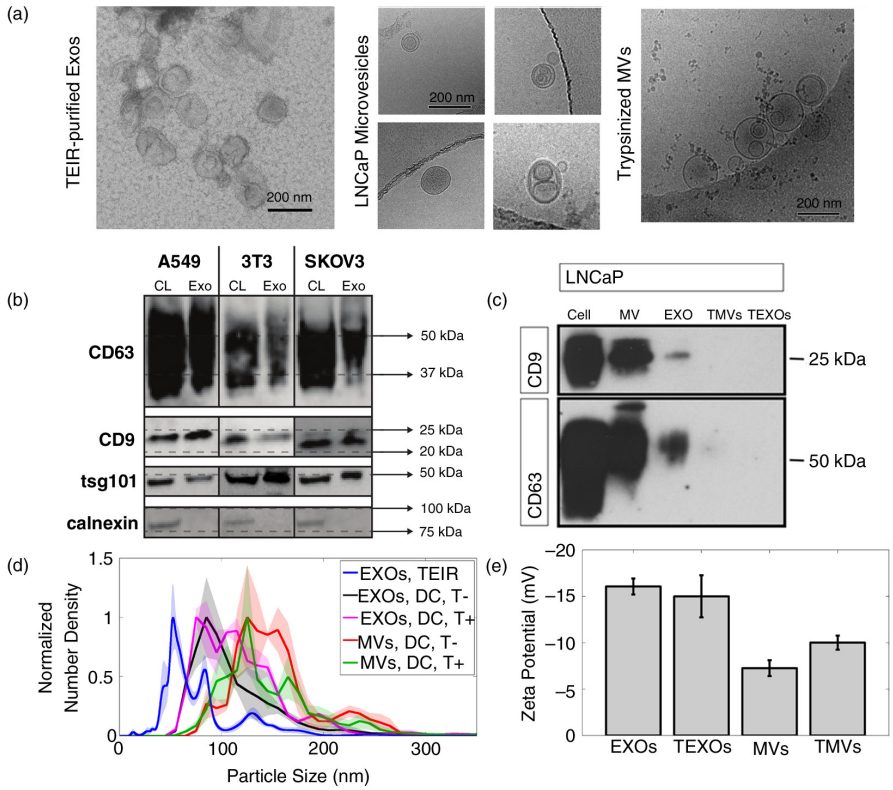

Fig. 2. Characterization of extracellular vesicles by electron microscopy, Western blot, κ-potential, and nanoparticle tracking analysis (NTA). (a) Electron micrographs of exosomes purified by total exosome isolation reagent (TEIR) (left, conventional TEM showing cup-shaped morphology), vesicles purified by differential centrifugation (middle, Cryo-EM showing native circular morphology), and trypsin-treated vesicles (right, cryo-EM). (b) Western blots of CD63, CD9, tsg101, and calnexin from exosomes and cell lysates for 3 representative cell lines (20 µg per lane). (c) Western blot of CD9 and CD63 for LNCaP microvesicles (MVs) and exosomes (EXOs) and trypsinized microvesicles (TMVs) and exosomes (TEXOs) (50 µg per lane). (d) Averaged NTA-determined size distributions for exosomes and microvesicles purified by TEIR and differential centrifugation (DC). Shaded areas represent ±1 standard error. (e) κ-potential for LNCaP extracellular vesicles.

gel electrophoresis (PAGE), 50 µg of proteins was separated into 12% Mini-PROTEAN TGX™ gels (Bio-Rad) and transferred to a Protran nitrocellulose membrane (Whatman International Ltd, Kent, United Kingdom) at 100 V and 30 mA for 1 h. Blots were blocked in 5% (w/v) non-fat dry milk powder (Valio, Helsinki, Finland) in Tris-buffered saline Tween 20 (TBS-T) and then incubated for 1 h at room temperature (RT) with either mouse monoclonal anti-human CD9 (clone ALB 6; Santa Cruz Biotechnology) or anti-CD63 (clone H5C6; BD Pharmingen™, San Jose, CA, USA), both diluted in 5% non-fat dry milk in TBS-T. The membranes were washed 3 × for 10 min and incubated with goat anti-mouse IgG-HRP secondary antibody diluted in 2.5% non-fat dry milk powder in TBS-T for 45 min at RT. The membranes were washed 3 × for 10 min with TBS-T, developed using a Luminata™ Crescendo Western HRP Substrate (Millipore) and visualized with Amersham Hyperfilm™ ECL (GE Healthcare Limited). As shown in Fig. 2c, the LNCaP MVs and exosomes as well as the cell lysates are positive for CD9 and CD63. However, the trypsinization treatment cleaves the cellular surface proteins as shown in the trypsinized microvesicles (TMVs) and exosomes.

Nanoparticle tracking analysis

For the LNCaP cells, purified EV samples were analysed by NTA (36) using Nanosight model LM14 (Malvern, Malvern, UK) equipped with a blue (404 nm) laser and sCMOS camera. The samples were diluted in DPBS to obtain a suitable concentration for the analysis ($3–20 \times 10^8$ particles/mL) and three 90-s videos were recorded from the samples using camera level 13. The data were analysed using NTA 3.0 software with the detection threshold set to 3 and screen gain at 10 to track

Citation: Journal of Extracellular Vesicles 2015, **4**: 28533 - http://dx.doi.org/10.3402/jev.v4.28533

as many particles as possible with little background. These settings have been chosen to closely match prior studies that have used NTA to detect exosomes as small as 30 nm (42–44). Results are shown in Fig. 2d, with the solid lines depicting mean distributions across the replicate measurements and the shaded areas showing the standard error. As expected, MVs have a larger mean size compared to the smaller exosome population. Number densities have been normalized to their maximum value.

We also show a characteristic size NTA result obtained from A549 cells isolated by the commercial TEIR reagent as described above (blue curve in Fig. 2d). These data were recorded by a separate NanoSight LM10 instrument (illumination at 488 nm) equipped with a perfusion pump. The A549 sample was diluted 1000 × in freshly filtered PBS (filtered using a 0.01-μm filter). The filtered PBS was confirmed via NTA to be free of nanoparticle contamination. Diluted exosome samples were passed 3 times through 0.2-μm nylon syringe filters and placed on the NTA instrument at RT. The blue curve in Fig. 2d represents the average and standard error of 6 consecutive measurements. Each repetition recorded 60 s of data, with 30 s of sample flow between replicates.

Zeta potential measurements

For the LNCaP cells, zeta potentials were measured from the purified EV samples with a Zetasizer Nano Z (Malvern), with 3 replicates measured from each sample. The particle concentrations in the samples were prepared at approximately 5×10^8/mL in DPBS using particle size concentrations obtained by paired NTA, such that each sample had similar particle concentrations. The results are shown in Fig. 2e, where it is evident that exosomes and MVs have distinctly different zeta potentials ($p = 8 \times 10^{-4}$), further providing evidence that the differential centrifugation effectively separated exosomes and MVs.

Results and discussion

Raman spectra of exosomes isolated from 7 cancerous and non-cancerous cell lines

LTRS spectra were recorded from exosomes isolated from 7 cell lines divided among cancerous (5) and non-cancerous (2) lines of epithelial and myeloid origin. A schematic diagram of the experiment is shown in Fig. 1. In Fig. 1a, culture media containing exosomes and other contaminating particles are collected, purified, and concentrated to yield a vial with a dense suspension of exosomes. That sample is then diluted and placed on a home-built Raman microscope, where single exosomes are trapped in a laser beam as shown in Fig. 1b. Raman scattered light is collected from each exosome, yielding a database of Raman spectra (Fig. 1c). Between 10 and 20 exosomes from each cell line were measured, with the mean spectra and ±1 standard deviation shown in Fig. 3a. The Raman spectra largely resemble those in the literature acquired from single cells and other biological tissues, and the chemical assignment of the major bands in the exosome spectra can be found in Ref. 30. The mean spectra show striking variability between exosomes derived from different cell lines. Several consistent differences can be observed, including (a) the height of the peak at $\sim 700\,cm^{-1}$, which is significantly elevated in the exosomes derived from non-tumour cell lines 3T3 and IMR90, (b) the shape of the 1,000–1,100 cm^{-1} and 1,200–1,300 cm^{-1} regions, and (c) the 1,600–1,700 cm^{-1} region, which distinguishes the A549, SKOV3, and Jurkat lines from the others. These areas are highlighted in Fig. 3a, d, and e, as a visual aid.

Performing a PCA on the full data set reveals principal component loadings that recapitulate the differences that are apparent by visual inspection, as well as other, subtler differences, as shown in Fig. 3d. The chemical assignments for the major features in the principal components are given in Table I.

The first 3 components represent 33, 18, and 10% of the variance, respectively, in the data set. Thus, cumulatively they represent 61% of the total variance. Scores for the first 3 principal component axes are shown in Fig. 3b and c. To avoid confusion with the principal components analysis performed on measurements of trypsin-treated EVs, described in the next section, we give these principal components the subscript "7c" to reflect that they originate from a data set composed of 7 cell lines. In the data set shown in Fig. 3, distinct clusters of exosomes can be identified using hierarchical clustering analysis, performed as described in the Materials and Methods section, using the first 10 principal component scores for each exosome (see Supplementary File).

Based on this hierarchical clustering analysis, each individual exosome was assigned to 1 of 4 clusters based on its spectrum. The cluster membership of each exosome is indicated in Fig. 3b and c by varying symbols, as shown in the legend. Shaded regions are provided as visual aids to highlight the different cluster regions. For example, Cluster 1 is represented by a star symbol and contains the majority of the Jurkat, SKOV3, and A549 exosomes within the region highlighted by the shaded blue oval. Interestingly, the exosomes derived from the 2 non-tumour cell lines (represented by gold and black colour) fall almost exclusively into Clusters 2 and 3 (represented by circles and triangles, respectively). To identify the specific spectral features of each cluster, we plotted the cluster-averaged spectra in Fig. 3e.

The cluster-averaged spectra reveal clear differences between exosomes from different subgroups. Here, the differences between each group are even more pronounced than in the cell-line-averaged spectra in Fig. 3a, as expected given that many cell lines have exosomes in more than

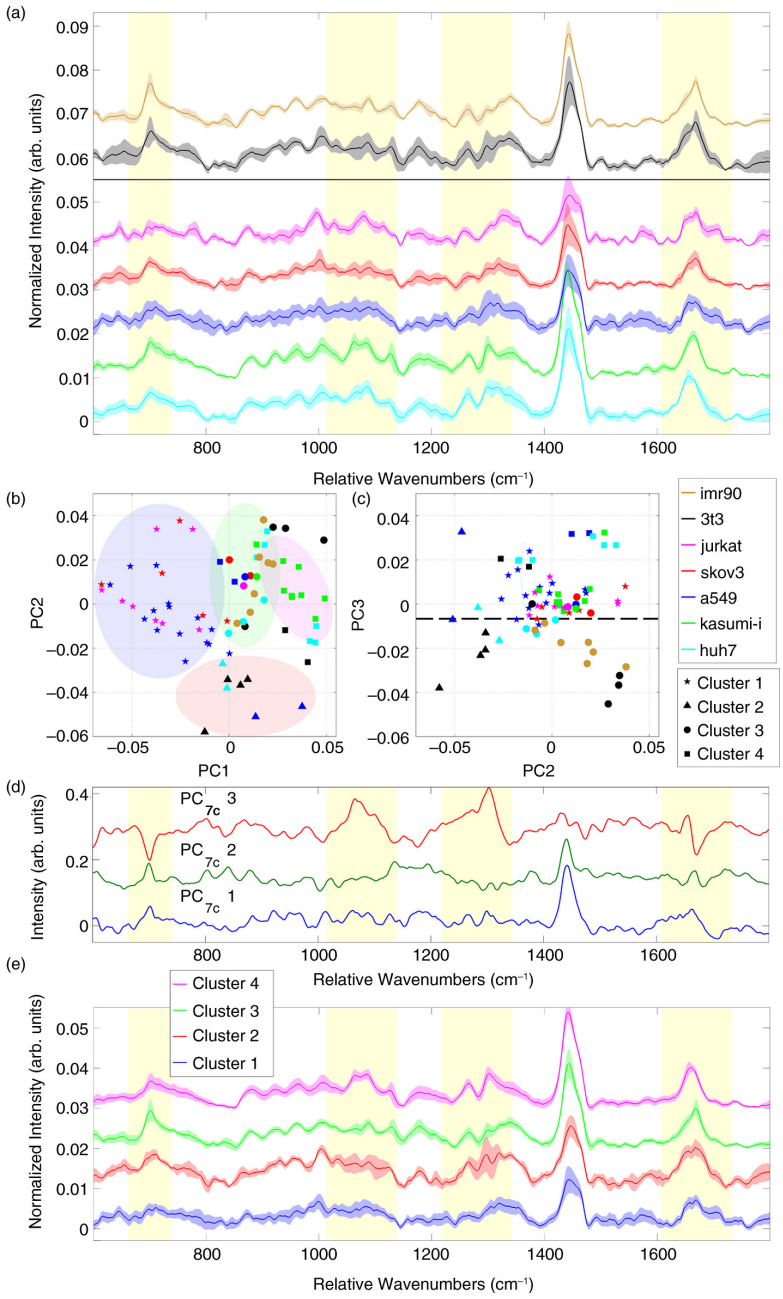

Fig. 3. Analysis of Raman spectra from single exosomes derived from 7 cancerous and non-cancerous cell lines. (a) Average Raman spectra (solid lines) and ±1 standard deviation (shaded areas) of exosomes. Black line separates normal (imr90, 3t3) and cancerous cell–derived exosomes (others). (b) First and second and (c) second and third principal component scores for each cell line. Colours represent cell lines, whereas shapes represent cluster membership, as shown in the legend (right). Clusters are based on a linkage analysis as described in the Supplementary File. Coloured regions throughout figure and dashed line in (c) provided as visual aids. (d) The first 3 principal component loading vectors, calculated from the full exosome spectral data set from all 7 cell lines. (e) Averaged spectra from Clusters 1 through 4. Spectra in panels (a), (d), and (e) offset for clarity.

Citation: Journal of Extracellular Vesicles 2015, **4**: 28533 - http://dx.doi.org/10.3402/jev.v4.28533

Table I. Literature assignments of major spectral features in Fig. 3(d).

Position (cm^{-1})	Peak assignment	Reference
700	Cholesteryl ester	(45)
840	Saccharide/amines	(45,46)
882	Tryptophan side-chain in proteins	(47)
1,066	Chain C–C stretching in lipids	(48)
1,298	CH_2 deformations in lipids	(49)
1,450	CH_2 and CH_3 deformations in proteins and lipids	(49)
1,651	C=C stretching in lipids	(50)
1,668	Amide I vibrations in proteins Cholesteryl ester	(45,51)

1 cluster. Because the differences do not correspond to cell type, we hypothesize that there may be several separate classes of exosomes, varying in content and specific biological directive. The preference of each cell line to create exosomes of a given type is likely to be driven by that cell's role within the organism as a whole and to be heavily influenced by the cellular environment (e.g. tumour microenvironment). The paucity of exosomes from normal cell lines in Clusters 1 and 4 suggests that whatever function these exosomes serve is performed with greater frequency in cancerous versus normal cells. In fact, a close inspection of Fig. 3c reveals that the majority of the exosomes from non-tumour cells (black and gold colour) fall on the low end of the PC_{7c} 3 axis. A dashed line is provided as a visual aid to highlight this discrimination. Identifying the meaning of these principal component axes will allow us to identify what chemical changes are present within each exosome group compared to the others.

Our hypothesis is that the primary spectral differences represented by the first 3 principal component axes are cholesterol content, surface protein expression, and relative expression of phospholipids to cholesterol, respectively. Comparing the major peaks in PC_{7c} 1 to Table I reveals a strong spectral similarity with cholesterol, whereas PC_{7c} 3 shows an inverse relationship between phospholipids and cholesterol [which have been previously shown to have an inverse relationship in exosomal membrane composition (52)]. This hypothesis is further strengthened by comparing these principal components with reference spectra for cholesterol (Sigma–Aldrich, C8667), phosphatidylcholine (Sigma–Aldrich, P3556), and phosphatidylethanolamine (Sigma–Aldrich, P7693), which agree with prior reports in the literature (53), and are provided for visual comparison alongside PC_{7c} 1 and 3 in Fig. 4.

The spectral similarity between the principal components and the spectra of pure chemicals can be quantified through least-squares curve fitting, as described in the Supplementary File. Fitting PC_{7c} 3 with a mixture of cholesterol and phospholipids yields a curve that faithfully reproduces the principal component's major peaks (Pearson's correlation coefficient r = 0.82; see Supplementary Fig. 4). Since Raman spectroscopy is a quantitative technique whose signal is linear with chemical concentration, the fit coefficients can be used to

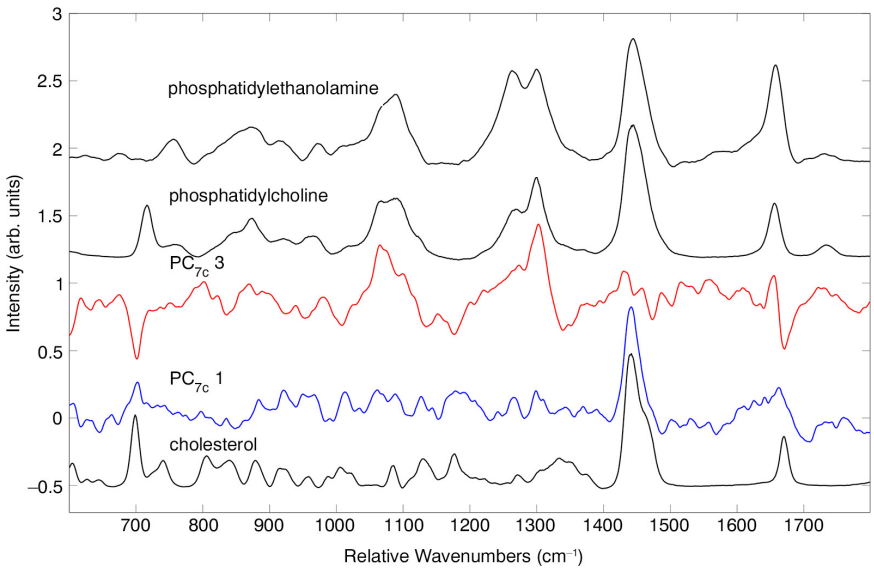

Fig. 4. Comparison of lineshapes of principal components 1 and 3, shown in Fig. 3d, and pure spectra of cholesterol, phosphatidylcholine, and phosphatidylethanolamine (black traces).

determine quantitative relationships between chemicals represented by this principal component. As described in detail in the Supplemental File, the spectral fitting coefficients indicate that PC_{7c} 3 represents a specific exchange ratio between cholesterol and phospholipid, where increasing values on this axis represent phospholipid molecules added to the membrane at the cost of cholesterol, at a 1:1 ratio of cholesterol/phospholipid. Thus, increasing values on the first principal component axis represent increased total cholesterol concentration, while increasing values on the third principal component axis represent an increase in the ratio of phospholipids to cholesterol.

Although this simple comparison of PCs to pure chemical components allows a good understanding of PC_{7c} 1 and PC_{7c} 3, the chemical meaning of the second principal component is not as clear from its overall shape. Comparing its major peaks with those in Table I, we see that the peaks primarily originate from proteins and protein-associated saccharides. Given that cholesterol and phospholipids are membrane components, our hypothesis is that PC_{7c} 2 also represents a membrane component, namely membrane-associated proteins. To confirm our hypothesis that its shape represents surface protein expression, we ran a control experiment where we looked at spectral differences between native and trypsin-treated exosomes, described below.

Raman spectra of extracellular vesicles after treatment with trypsin

Exosomes and MVs were isolated from cultures of LNCaP cells via differential centrifugation of the culture medium as described in the Materials and Methods section. Following isolation, both exosome and MV samples were treated with trypsin, a proteolytic enzyme, to cleave the extracellular portion of most membrane proteins from the surface of the vesicles, leaving them "bald." Trypsin is a digestive enzyme that works by cleaving peptides at certain sites (54), thus breaking large proteins into smaller subunits. Trypsinization is a widely applied technique, used regularly for proteomic sample processing and in cell culture, either to break down cell adhesion proteins or to efficiently strip away surface protein (55). After trypsinization of the EVs isolated in this study [following a previously reported procedure (39)], Western blot analysis (see Materials and Methods section) was used to confirm the removal of tetraspanins CD9 and CD63, transmembrane proteins that are highly expressed at exosomal membranes. Because we found in our previous experiments that purification with the TEIR left a "coating" of the reagent around exosomes (see Ref. (56) and Supplementary File), we used differential centrifugation to purify these vesicles to ensure that the TEIR reagent did not interfere with the digestions of membrane proteins by trypsin.

LTRS spectra were recorded from $\sim$7 to 10 vesicles from each group. Both mean spectra and $\pm$1 standard deviation are shown in Fig. 5a. Subtle spectral differences can be observed between exosomes and MVs, particularly in the region around 1,000 cm^{-1}. Differences between trypsinized and native vesicles can also be seen, particularly in the protein- and lipid-rich 1,200–1,400 cm^{-1} region. To quantify these differences, principal components analysis was performed on the data set. The first 3 principal component loadings are shown in Fig. 5b. Here we labelled each PC with the subscript "Tr" to indicate that they are the principal components from the trypsin-treatment data set and to prevent confusion with the PCs from the 7 cell line experiment, above. These 3 loadings explain 30, 19, and 15% of the variance in the data set, respectively. Thus, the 3 loadings cumulatively explain 64% of the total variance. In Fig. 5c we plotted the first 2 principal component scores for each individual vesicle, revealing the magnitude and consistency of the separation between exosomes and MVs and between trypsin-treated and -untreated vesicles.

Figure 5c reveals consistent differences between native exosomes and native MVs, along both the PC_{Tr} 1 and PC_{Tr} 2 axes, which we hypothesize to be related to the membrane composition, given the different intracellular origin of the different vesicle types. Specifically, as these differences disappear after the trypsin treatment, both PCs are likely to be related to membrane protein content. This suggests that PC_{Tr} 1 and PC_{Tr} 2 report on particular surface proteins that both distinguish exosomes and MVs and are removed by trypsin treatment.

Comparing the principal component loadings from this data set to the previous data set of 7 different cell lines reveals startling similarities, as shown in Fig. 6. Although the first PC axes for the 2 experiments look quite different, this is to be expected, as in one experiment the primary differentiator would be expected to be the difference between exosomes and MVs (likely surface protein content), whereas in the other case the differentiator is hypothesized to be related to cholesterol content. The lineshapes of the second and third component loadings are remarkably similar between the 2 experiments (PC_{7c} 2 and PC_{Tr} 2 have a Pearson's correlation coefficient of $r = 0.74$, whereas PC_{7c} 3 and PC_{Tr} 3 have a correlation coefficient of $r = 0.92$). We have *a priori* knowledge that the difference between the trypsin-treated and -untreated vesicles, which lies primarily along the PC_{Tr} 2 axis, is the surface protein content [see Western blot data, Fig. 2c, Materials and Methods section]. The similarity between the second loadings in both data sets strongly suggests that PC_{7c} 2 reports on surface protein expression. However, PC_{Tr} 1 also reports on surface protein expression, and thus PC_{7c} 2 may be a mixture of PC_{Tr} 1 and 2. As shown in the

Citation: Journal of Extracellular Vesicles 2015, **4**: 28533 - http://dx.doi.org/10.3402/jev.v4.28533

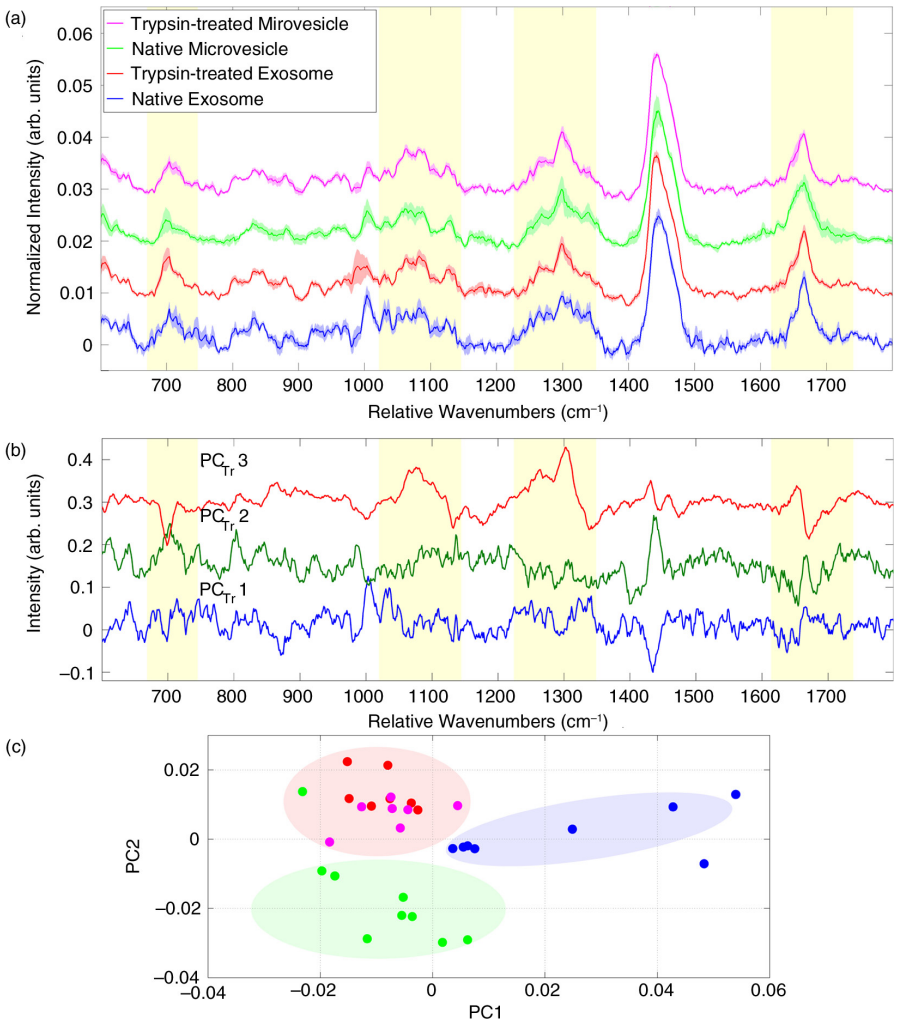

Fig. 5. Analysis of Raman spectra from single LNCaP-derived extracellular vesicles with and without trypsin treatment. (a) Average Raman spectra (solid lines) and ±1 standard deviation (shaded areas). (b) The first 3 principal component loading vectors, calculated from the trypsin-treatment data set. (c) The first 2 principal component scores for individual vesicles, according to the loading vectors shown in (b). Coloured areas in (c) provided as visual aids. Spectra in (a) and (b) offset for clarity.

Supplementary Fig. 5, fitting these curves to PC_{7c} 2 yields a fit that reproduces the major peaks of PC_{7c} 2 (Pearson's correlation coefficient of 0.8). Based on this fit, as well as the position of the trypsinized samples in the PC_{Tr} space (upper left corner, Fig. 5c), we can then hypothesize that increasing values on the PC_{7c} 2 axis corresponds to decreasing surface protein expression.

Conclusions

The current standard practice for exosome analysis relies on bulk isolation and purification from expensive, large-scale *in vitro* cell culture, typically followed by intensive physicochemical analysis, including numerous proteomic, genomic, and sizing techniques. However, it is increasingly clear that conventional analytical tools lack the sensitivity to explore the substantial heterogeneity reported for EVs or are too costly and time-consuming to justify pilot studies. Here, we applied LTRS to truly study the chemical content of exosomes on a vesicle-by-vesicle basis. Additionally, because Raman spectroscopy is a so-called label-free technique, it does not require prior knowledge of, for example, specific surface proteins for fluorophore conjugation and can study EVs in close approximations to their biological milieu.

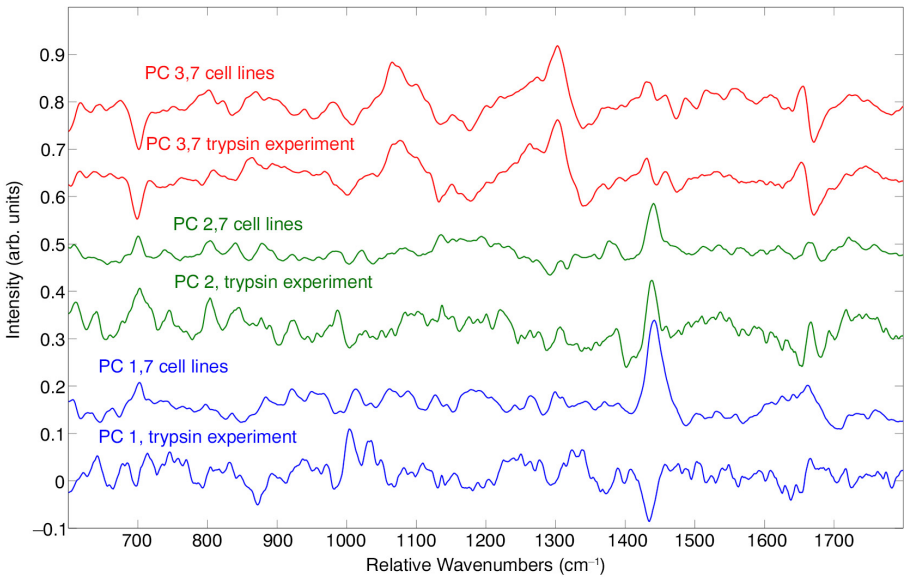

Fig. 6. Comparison of the first 3 principal component loadings from the trypsin and cell line experiments. Spectra are offset for clarity.

However, LTRS does have some limitations. Its primary limitation is signal strength. Raman scattering is a weak process, generally considered to be on the order of 1 million times weaker than fluorescence labelling. This necessitates long integration times (~5 min in our experiments) to measure a spectrum from a single exosome. Furthermore, as discussed in the Supplementary File, because we use bright-field imaging to find and trap exosomes, we are likely biased to looking at exosomes of approximately 100 nm and larger. As signal scales with the cube of the radius, measuring smaller exosomes may require even longer integration times. However, many groups are currently researching methods to speed up measurements by multiplexing measurements (57) or employing "smart" detection strategies (58–61). These advances may make LTRS more approachable as a general analysis technique for exosomes. Another limitation of Raman spectroscopy is that, in complex chemical mixtures such as cells or exosomes, it is difficult for Raman spectroscopy to differentiate between many proteins, especially those at very low concentrations. Therefore, many Raman studies limit themselves to quantifying broad classes of molecules (total protein content, total lipid content, total nucleic acid content, etc.), rather than quantifying the amount of a particular biomolecule (e.g. CD63). We must be careful, then, to limit our conclusions to the information provided by Raman spectroscopy. In the quantitative analysis we present above, we hypothesize that Raman spectroscopy reports on an exosome's surface protein expression level. However, here we must clearly highlight the fact that 2 exosomes may have identical amounts of surface protein, yet be expressing very different types of protein, and Raman spectroscopy may not be able to provide that more detailed information.

Additionally, our experiments also have some limitations. In this study, no density gradient purification steps were performed, and thus protein aggregates or other contaminants may have been present in our sample. However, we would expect such particles to have quite different Raman spectral signatures from exosomes that were not observed in the particles we studied. Nevertheless, we cannot fully eliminate the possibility of these aggregates contaminating our measurements. In performing our experiments, and as detailed in the Supplementary File, we have acquired extensive circumstantial evidence that the measurements we make arise from single exosomes. This evidence comes from confirming our ability to trap and record signals from standard particles in the exosome size range, substantiating via nanoparticle tracking analysis (NTA) that no or few particles exist in our samples outside the exosome size range. This point confirms that we can observe discrete jumps and drops in signal as exosomes enter and leave our laser trap; it shows that our exosome signal for our recorded measurements does not fluctuate over time (as might be expected from multiple exosomes entering the trap). However, we have no direct measurements of the size of the particles measured within the optical trap, and thus the presence of clusters of small numbers of exosomes cannot be rigorously excluded. Despite these limitations, the work described here demonstrates that Raman spectroscopy has

Citation: Journal of Extracellular Vesicles 2015, **4**: 28533 - http://dx.doi.org/10.3402/jev.v4.28533

significant power in quantitatively analysing molecules on a single-to-few-exosome level.

A major finding of this study is the observation of significant variation in the chemical content of EVs reported by Raman spectroscopy. For example, Fig. 5 clearly shows the separation by Raman spectroscopy between exosomes and MVs released from the same cell culture, as prepared by differential centrifugation. Figure 3 also demonstrates that among exosomes from different cell lines, there are strong similarities among the spectra, yet consistent spectral differences that lead to grouping of exosomes into 4 major subpopulations by a hierarchical clustering analysis. These subpopulations are not due to different cell origin, as many cell lines have exosomes in many subpopulations, and all subpopulations contain exosomes from multiple cell lines. Yet, there are some subgroups of exosomes that are preferred by some cell lines versus others. For example, exosomes from non-cancerous cells primarily fall into subgroups 2 and 3. This suggests that each subtype of exosome may play a particular functional role that is common across cell lines.

A principal components analysis of this data set yields insights into the chemical differences between the different EV subpopulations. The second major finding of this study is that these differences are primarily due to membrane content of the EVs. The shapes of the first and third principal components are closely matched with spectra of known membrane constituents. Namely, the first principal component has a spectral shape very similar to that of cholesterol, while the third principal component represents the inverse relationship between cholesterol content and phospholipid content in the membrane, as confirmed by fitting this lineshape to pure chemical spectra. Therefore, increasing values along the PC_{7c} 1 axis corresponds to increasing cholesterol content, while increasing values along the PC_{7c} 3 axis corresponds to increased phospholipid content at the expense of cholesterol, with a 1:1 molecular substitution ratio. Notably, non-cancerous cell-derived exosomes seem to be much more enriched in cholesterol, while being relatively depleted in phospholipid, compared to cancerous cell-derived exosomes. This is the first time the content of EV membranes has been examined at the individual vesicle level, highlighting the fact that achieving this level of quantitative chemical detail at the single vesicle level would be difficult or impossible using conventional methods of exosome chemical analysis. However, it is relatively straightforward with LTRS given its linear relationship to chemical components within the few femtolitre measurement volume.

Treating EVs with trypsin cleaves the external domain of most membrane proteins, leading to an expected alteration in the Raman spectra of these vesicles. Comparing native and treated EVs, native exosomes and MVs are clearly distinguished by their Raman spectra, whereas trypsin-treated ones are not. This difference suggests that these vesicles are distinguished primarily by their membrane components that are altered by trypsinization, such as tetraspanins as shown in the Western blots in Fig. 2c. Furthermore, analysis of trypsin-treated and native EVs leads to the construction of principal components that bear a strong resemblance to those constructed through analysis of exosomes from several different cell lines, discussed above. In particular, the second principal component from the 7 cell line experiment (PC_{7c} 2) can be well-fit by the first and second principal components of the trypsin experiment (PC_{Tr} 1 and 2), lending significant confidence to the conclusion that PC_{7c} 2 reports on surface protein expression, with increasing values along this axis corresponding to decreased surface protein content. Meanwhile, cholesterol content, which PC_{7c} 1 demonstrated to be a key variable among exosomes from different cell lines, was not a significant contributor to the separation between exosomes and MVs from a single cell line.

As mentioned above, Raman spectroscopy has limited speed, meaning that our analysis is necessarily limited to relatively small numbers of exosomes. Measuring a very large number of exosomes could ensure a more robust and accurate representation of the true spectral variation within the data set, compared to noise-induced variations. However, comparing the results of the 7 cell line experiment with the trypsin experiment, we are encouraged by the similarities of the principal components analysis of these 2 independent data sets. Each spectral decomposition was performed using different numbers of measured exosomes, yet the spectral shapes of the first few principal components were largely preserved. This result suggests that these early principal components are quite robust despite the modest number of exosomes studied in total.

Our study highlights the need for the development of new analytical techniques that can study individual vesicles. In light of the observed vesicle-to-vesicle heterogeneity, bulk measurements of EVs may not be enough to fully understand their biological function and variability. Our data demonstrate the existence of multiple populations of exosomes shared among cell lines and suggest further studies aimed at taking vesicles grouped by Raman spectroscopy, or other physical or chemical separation methods, and subjecting them to further analysis to determine the differences in intravesicle cargo and membrane protein content of exosomes produced by even a single cell line. Such studies could help elucidate the various functional relationships between an exosome's construction and the ultimate role it plays in cell function, cellular communication, and, for cancerous cells, carcinogenesis.

Acknowledgements

We would like to thank Dr Matt Mellema of the UC Davis School of Veterinary Medicine for running NTA on the samples and assisting in data analysis/interpretation. We also acknowledge Aalto

University Nanomicroscopy Center (Espoo, Finland) for use of their Cryo-electron microscope.

Conflicts of interest and funding

The authors declare they have no competing interests. ZJS, CL, and SWH acknowledge support from the US National Science Foundation (NSF) through NSF grant 1068109. RPC would like to acknowledge financial support from the T32 HL07013 training grant via the US National Institutes of Health/National Heart, Lung, and Blood Institute Training Program in Comparative Lung Biology and Medicine. TL, TV, and MY gratefully acknowledge funding support from the Academy of Finland. ELI, HS, and MY acknowledge the support of EU-COST, MeHAD, and SalWe Get It Done funding.

References

1. Valadi H, Ekstrom K, Bossios A, Sjostrand M, Lotvall J. Exosomes contain a selective number of mRNA and microRNA. Allergy. 2007;62:S372.
2. Valadi H, Ekstrom K, Bossios A, Sjostrand M, Lee JJ, Lotvall JO. Exosome-mediated transfer of mRNAs and microRNAs is a novel mechanism of genetic exchange between cells. Nat Cell Biol. 2007;9:654–9.
3. Lazaro-Ibanez E, Sanz-Garcia A, Visakorpi T, Escobedo-Lucea C, Siljander P, Ayuso-Sacido A, et al. Different gDNA content in the subpopulations of prostate cancer extracellular vesicles: apoptotic bodies, microvesicles, and exosomes. Prostate. 2014;74:1379–90.
4. Kastelowitz N, Yin H. Exosomes and microvesicles: identification and targeting by particle size and lipid chemical probes. Chembiochem. 2014;15:923–8.
5. Bobrie A, Thery C. Exosomes and communication between tumours and the immune system: are all exosomes equal? Biochem Soc Trans. 2013;41:263–7.
6. Beach A, Zhang HG, Ratajczak MZ, Kakar SS. Exosomes: an overview of biogenesis, composition and role in ovarian cancer. J Ovarian Res. 2014;7:14.
7. Melo SA, Sugimoto H, O'Connell JT, Kato N, Villanueva A, Vidal A, et al. Cancer exosomes perform cell-independent microRNA biogenesis and promote tumorigenesis. Cancer Cell. 2014;26:707–21.
8. Liang Y, Eng WS, Colquhoun DR, Dinglasan RR, Graham DR, Mahal LK. Complex N-linked glycans serve as a determinant for exosome/microvesicle cargo recruitment. J Biol Chem. 2014;289:32526–37.
9. Subra C, Grand D, Laulagnier K, Stella A, Lambeau G, Paillasse M, et al. Exosomes account for vesicle-mediated transcellular transport of activatable phospholipases and prostaglandins. J Lipid Res. 2010;51:2105–20.
10. Laulagnier K, Motta C, Hamdi S, Roy S, Fauvelle F, Pageaux JF, et al. Mast cell- and dendritic cell-derived exosomes display a specific lipid composition and an unusual membrane organization. Biochem J. 2004;380:161–71.
11. Lotvall J, Hill AF, Hochberg F, Buzas EI, Di Vizio D, Gardiner C, et al. Minimal experimental requirements for definition of extracellular vesicles and their functions: a position statement from the International Society for Extracellular Vesicles. J Extracell Vesicles. 2014;3:26913, doi: http://dx.doi.org/10.3402/jev.v3.26913
12. Puppels GJ, Demul FFM, Otto C, Greve J, Robertnicoud M, Arndtjovin DJ, et al. Studying single living cells and chromosomes by confocal Raman microspectroscopy. Nature. 1990; 347:301–3.
13. de Oliveira MAS, Smith ZJ, Knorr F, de Araujo RE, Wachsmann-Hogiu S. Long term Raman spectral study of power-dependent photodamage in red blood cells. Appl Phys Lett. 2014;104:103702.
14. Smith ZJ, Chang CW, Lawson LS, Lane SM, Wachsmann-Hogiu S. Precise monitoring of chemical changes through localization analysis of dynamic spectra (LADS). Appl Spectrosc. 2013;67:187–95.
15. Haka AS, Shafer-Peltier KE, Fitzmaurice M, Crowe J, Dasari RR, Feld MS. Diagnosing breast cancer by using Raman spectroscopy. Proc Natl Acad Sci USA. 2005;102:12371–6.
16. Lieber CA, Majumder SK, Billheimer D, Ellis DL, Mahadevan-Jansen A. Raman microspectroscopy for skin cancer detection in vitro. J Biomed Opt. 2008;13:024013.
17. Schulmerich MV, Cole JH, Kreider JM, Esmonde-White F, Dooley KA, Goldstein SA, et al. Transcutaneous Raman Spectroscopy of Murine Bone In Vivo. Appl Spectrosc. 2009; 63:286–95.
18. Maher JR, Takahata M, Awad HA, Berger AJ. Raman spectroscopy detects deterioration in biomechanical properties of bone in a glucocorticoid-treated mouse model of rheumatoid arthritis. J Biomed Opt. 2011;16:087012.
19. Moritz TJ, Taylor DS, Polage CR, Krol DM, Lane SM, Chan JW. Raman spectroscopic signatures of the metabolic states of *Escherichia coli* cells and their dependence on antibiotics treatment. Biophys J. 2010;98:742A.
20. Berger AJ, Koo TW, Itzkan I, Horowitz G, Feld MS. Multicomponent blood analysis by near-infrared Raman spectroscopy. Appl Optics. 1999;38:2916–26.
21. Qi DH, Berger AJ. Chemical concentration measurement in blood serum and urine samples using liquid-core optical fiber Raman spectroscopy. Appl Optics. 2007;46:1726–34.
22. Wachsmann-Hogiu S, Weeks T, Huser T. Chemical analysis in vivo and in vitro by Raman spectroscopy – from single cells to humans. Curr Opin Biotechnol. 2009;20:63–73.
23. Smith ZJ, Huser TR, Wachsmann-Hogiu S. Raman scattering in pathology. Anal Cell Pathol (Amst). 2012;35:145–63.
24. Chen K, Qin YJ, Zheng F, Sun MH, Shi DR. Diagnosis of colorectal cancer using Raman spectroscopy of laser-trapped single living epithelial cells. Opt Lett. 2006;31:2015–7.
25. Chan JW, Taylor DS, Lane SM, Zwerdling T, Tuscano J, Huser T. Nondestructive identification of individual leukemia cells by laser trapping Raman spectroscopy. Anal Chem. 2008;80: 2180–7.
26. Smith ZJ, Wang JCE, Quataert SA, Berger AJ. Integrated Raman and angular scattering microscopy reveals chemical and morphological differences between activated and nonactivated CD8+T lymphocytes. J Biomed Opt. 2010;15:036021.
27. Argov N, Wachsmann-Hogiu S, Freeman SL, Huser T, Lebrilla CB, German JB. Size-dependent lipid content in human milk fat globules. J Agr Food Chem. 2008;56:7446–50.
28. Ajito K, Torimitsu K. Single nanoparticle trapping using a Raman Tweezers microscope. Appl Spectrosc. 2002;56:541–4.
29. Ajito K, Torimitsu K. Laser trapping and Raman spectroscopy of single cellular organelles in the nanometer range. Lab Chip. 2002;2:11–4.
30. Tatischeff I, Larquet E, Falcon-Perez JM, Turpin PY, Kruglik SG. Fast characterisation of cell-derived extracellular vesicles by nanoparticles tracking analysis, cryo-electron microscopy, and Raman tweezers microspectroscopy. J Extracell Vesicles. 2012;1:19179, doi: http://dx.doi.org/10.3402/jev.v1i0.19179
31. Beier BD. Thesis: confocal Raman microscpectroscopy of oral Streptococci. Institute of Optics. Rochester, NY, USA: University of Rochester; 2011.

32. Eilers PH. A perfect smoother. Anal Chem. 2003;75:3631–6.
33. Boelens HF, Dijkstra RJ, Eilers PH, Fitzpatrick F, Westerhuis JA. New background correction method for liquid chromatography with diode array detection, infrared spectroscopic detection and Raman spectroscopic detection. J Chromatogr A. 2004;1057:21–30.
34. Schie IW, Nolte L, Pedersen TL, Smith Z, Wu J, Yahiatene I, et al. Direct comparison of fatty acid ratios in single cellular lipid droplets as determined by comparative Raman spectroscopy and gas chromatography. Analyst. 2013;138:6662–70.
35. Gniadecka M, Philipsen PA, Sigurdsson S, Wessel S, Nielsen OF, Christensen DH, et al. Melanoma diagnosis by Raman spectroscopy and neural networks: structure alterations in proteins and lipids in intact cancer tissue. J Invest Dermatol. 2004;122:443–9.
36. Tirinato L, Gentile F, Di Mascolo D, Coluccio ML, Das G, Liberale C, et al. SERS analysis on exosomes using superhydrophobic surfaces. Microelectron Eng. 2012;97:337–40.
37. Thery C, Amigorena S, Raposo G, Clayton A. Isolation and characterization of exosomes from cell culture supernatants and biological fluids. Curr Protoc Cell Biol. 2006;Chapter 3:Unit 3 22.
38. Shelke GV, Lasser C, Gho YS, Lotvall J. Importance of exosome depletion protocols to eliminate functional and RNA-containing extracellular vesicles from fetal bovine serum. J Extracell Vesicles. 2014;3:24783, doi: http://dx.doi.org/10.3402/jev.v3.24783
39. Jang SC, Kim OY, Yoon CM, Choi DS, Roh TY, Park J, et al. Bioinspired exosome-mimetic nanovesicles for targeted delivery of chemotherapeutics to malignant tumors. ACS Nano. 2013;7:7698–710.
40. Boing AN, van der Pol E, Grootemaat AE, Coumans FA, Sturk A, Nieuwland R. Single-step isolation of extracellular vesicles by size-exclusion chromatography. J Extracell Vesicles. 2014;3:23430, doi: http://dx.doi.org/10.3402/jev.v3.23430
41. Webber J, Clayton A. How pure are your vesicles? J Extracell Vesicles. 2013;2:19861, doi: http://dx.doi.org/10.3402/jev.v2i0.19861
42. Dragovic RA, Gardiner C, Brooks AS, Tannetta DS, Ferguson DJ, Hole P, et al. Sizing and phenotyping of cellular vesicles using nanoparticle tracking analysis. Nanomed-Nanotechnol. 2011;7:780–8.
43. Filipe V, Hawe A, Jiskoot W. Critical evaluation of nanoparticle tracking analysis (NTA) by NanoSight for the measurement of nanoparticles and protein aggregates. Pharm Res. 2010;27:796–810.
44. Maas SL, de Vrij J, van der Vlist EJ, Geragousian B, van Bloois L, Mastrobattista E, et al. Possibilities and limitations of current technologies for quantification of biological extracellular vesicles and synthetic mimics. J Control Release. 2015;200:87–96.
45. Krafft C, Neudert L, Simat T, Salzer R. Near infrared Raman spectra of human brain lipids. Spectrochim Acta A. 2005;61:1529–35.
46. Naumann D. Infrared and NIR Raman spectroscopy in medical microbiology. Proc Soc Photo-Opt Ins. 1998;3257:245–57.
47. Miura T, Takeuchi H, Harada I. Characterization of individual tryptophan side-chains in proteins using Raman-spectroscopy and hydrogen-deuterium exchange kinetics. Biochemistry. 1988;27:88–94.
48. Edwards HGM, Farwell DW, Williams AC, Barry BW, Rull F. Novel spectroscopic deconvolution procedure for complex biological-systems – vibrational components in the Ft-Raman spectra of ice-man and contemporary skin. J Chem Soc Faraday Trans. 1995;91:3883–7.
49. Notingher I, Verrier S, Haque S, Polak JM, Hench LL. Spectroscopic study of human lung epithelial cells (A549) in culture: living cells versus dead cells. Biopolymers. 2003;72:230–40.
50. Nijssen A, Schut TCB, Heule F, Caspers PJ, Hayes DP, Neumann MHA, et al. Discriminating basal cell carcinoma from its surrounding tissue by Raman spectroscopy. J Invest Dermatol. 2002;119:64–9.
51. Huang ZW, McWilliams A, Lui H, McLean DI, Lam S, Zeng HS. Near-infrared Raman spectroscopy for optical diagnosis of lung cancer. Int J Cancer. 2003;107:1047–52.
52. Raposo G, Stoorvogel W. Extracellular vesicles: exosomes, microvesicles, and friends. J Cell Biol. 2013;200:373–83.
53. Buschman HP, Deinum G, Motz JT, Fitzmaurice M, Kramer JR, van der Laarse A, et al. Raman microspectroscopy of human coronary atherosclerosis: biochemical assessment of cellular and extracellular morphologic structures in situ. Cardiovasc Pathol. 2001;10:69–82.
54. Rodriguez J, Gupta N, Smith RD, Pevzner PA. Does trypsin cut before proline? J Proteome Res. 2008;7:300–5.
55. Huang HL, Hsing HW, Lai TC, Chen YW, Lee TR, Chan HT, et al. Trypsin-induced proteome alteration during cell subculture in mammalian cells. J Biomed Sci. 2010;17:36.
56. Lee C, Carney RP, Hazari S, Smith ZJ, Knudson A, Robertson CS, et al. 3D plasmonic nanobowl platform for the study of exosomes in solution. Nanoscale. 2015;7:9290–7.
57. Kong LB, Chan J. A rapidly modulated multifocal detection scheme for parallel acquisition of Raman spectra from a 2-D focal array. Anal Chem. 2014;86:6604–9.
58. Smith ZJ, Strombom S, Wachsmann-Hogiu S. Multivariate optical computing using a digital micromirror device for fluorescence and Raman spectroscopy. Opt Express. 2011;19:16950–62.
59. Kosmeier S, Zolotovskaya S, De Luca AC, Riches A, Herrington CS, Dholakia K, et al. Nonredundant Raman imaging using optical eigenmodes. Optica. 2014;1:257–63.
60. Wilcox DS, Buzzard GT, Lucier BJ, Wang P, Ben-Amotz D. Photon level chemical classification using digital compressive detection. Anal Chim Acta. 2012;755:17–27.
61. Davis BM, Hemphill AJ, Maltas DC, Zipper MA, Wang P, Ben-Amotz D. Multivariate hyperspectral Raman imaging using compressive detection. Anal Chem. 2011;83:5086–92.

Supplemental Material for: "Single exosome study reveals subpopulations distributed among cell lines with variability related to membrane content"

Zachary J. Smith[1,2], Changwon Lee[1§], Tatu Rojalin[1,3§], Randy P. Carney[4§], Sidhartha Hazari[4] , Alisha Knudson[4] , Kit Lam[4] , Heikki Saari[3] , Elisa Lazaro Ibañez[3] , Tapani Viitala[3] , Timo Laaksonen[3] , Marjo Yliperttula[3] and Sebastian Wachsmann-Hogiu[1,5*]

[1] Center for Biophotonics, University of California Davis, Sacramento, CA, USA;
[2] Department of Precision Mechanics and Precision Instrumentation, University of Science and Technology of China, Hefei, Anhui, China;
[3] Division of Pharmaceutical Biosciences, Centre for Drug Research, University of Helsinki, Helsinki, Finland;
[4] Department of Biochemistry and Molecular Medicine, University of California Davis, Sacramento, CA, USA;
[5] Department of Pathology and Laboratory Medicine, University of California Davis, Sacramento, CA, USA
[§] These authors contributed equally to this manuscript.
[*]Correspondence to: Sebastian Wachsmann-Hogiu, 2700 Stockton Blvd. Suite 1400, Sacramento, CA 95817, Email: swachsmann@ucdavis.edu

Effect of the Total Isolation Reagent on the Exosome Spectrum

Preparation of exosomes is typically performed by ultracentrifugation. However, to alleviate the experimental difficulty of and length of time required for ultracentrifugation, exosome isolation kits are commercially available from several manufacturers. These kits allow exosomes to be pelleted at low centrifuge speeds, as described in the Methods section, above. In this

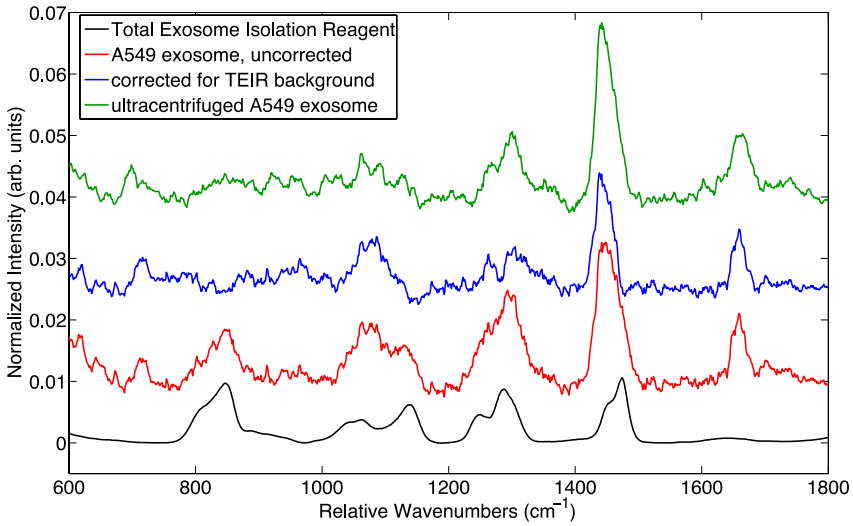

Figure S1. Raman spectra of total exosome isolation reagent (black) and trapped exosomes (colored). Numerical removal of the total isolation reagent by AsLS yields a spectrum (blue) in good agreement with exosomes prepared by ultracentrifugation (green). Spectra offset for clarity.

work we use one standard kit, the Total Exosome Isolation Reagent from Life Technologies (catalog # 4478359).

The spectrum of this reagent is shown as the black trace in Figure S1. Interestingly, although the exosomes are rinsed and resuspended in PBS buffer following separation and pelleting, a strong remnant of the isolation reagent's signal is clearly present in the spectra of individual trapped exosomes. The spectrum of an exosome from an a549 cell culture where the isolation reagent was not included as part of the background model described above is shown in red in Fig. S1. Including the isolation reagent's spectrum in the background model leads to the spectrum shown in blue. Finally, we isolated a549 exosomes by gold-standard ultracentrifugation, leading to the spectrum shown in green. Comparing these curves seems to suggest that the isolation reagent works by coating the exosomes, causing them to precipitate more easily during centrifugation. However, this coating remains even after washing and resuspension. A previous report of Raman measurements of exosomes in the literature (62) did not correct for this effect, and it appears that the majority of the spectral signal they report is due not to the exosomes themselves but to the isolation reagent coating the exosomes. However, by including the isolation kit's spectrum in our background model, AsLS efficiently removes the contaminating peaks, giving rise to a corrected spectrum that agrees well with exosome spectra produced by the more laborious ultracentrifugation. The agreement between our ASLS-corrected spectra from kit-prepared exosomes and ultracentrifuged exosomes is further confirmed by the correspondence between the principal component lineshapes computed from seven cell lines shown in Fig. 3 (prepared with the TEIR reagent), and the principal component lineshapes computed from the trypsin experiment shown in Fig. 5 (computed from ultracentrifuged samples).

Evidence for Measurements of Single Exosomes

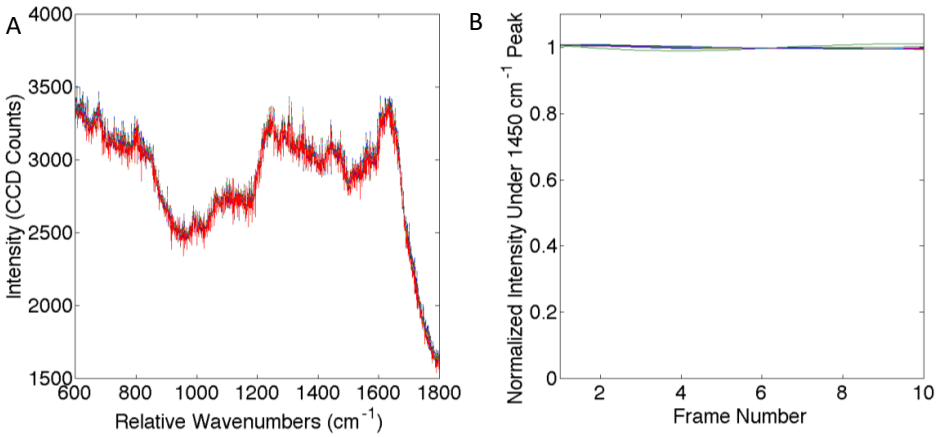

Figure S2. (A) Raw, frame-level data from a single exosome. (B) Integrated area under the 1450 cm^{-1} peak for 10 individual exosomes, showing <1% variation.

In our experiments we purposely choose a large dilution factor to ensure that typically less than one exosome is present, on average, in a field of view of our microscope. Thus, even over the 5 minute duration of our Raman measurements, we do not expect multiple exosomes to wander into our trapping beam. Our 5 minute measurements are broken up into 10 frames of 30 seconds each. We can break the data from a single measurement up into those individual 30 second frames, and see that our signal over time does not change its intensity (as might be expected if a new exosome enters the trap). A representative exosome measurement is shown below (Figure S2 (A)), where the raw data shows no fluctuations over time. Integrating the signal in the 1450 cm^{-1} wavenumber peak and normalizing it to the mean value across the 5 minute measurement (Figure S2 (B)), we see that there is less than a 1% fluctuation in the signal over time.

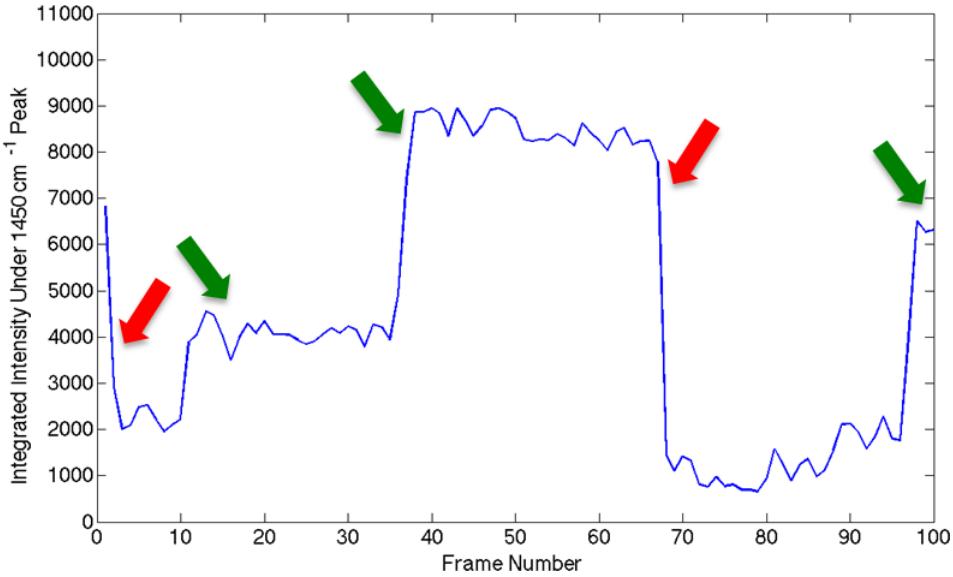

Figure S3 – Integrated Raman signal under 1450 cm^{-1} peak over time. Red arrows mark stage motions to "clear" the optical trap. Green arrows mark stepwise increases in signal due to exosomes appearing in trap. Note the increase at approximately frame number 30, where a second exosome enters the trap causing a distinct rise in signal.

To investigate the case where we expect multiple exosomes to be trapped over time, we prepared a dense suspension of exosomes such that an exosome would wander into the trap without any user intervention on the time scale of 30-60s. We then recorded Raman spectra at 10s intervals, periodically translating the stage to "clear" the laser focus of any trapped exosomes, to examine the change in Raman signal over time. The results of that study are shown in Figure S3, where the integrated area under the 1450 cm^{-1} peak is shown as a function of time and showing the clear, discrete decreases when the trap is cleared, and increases when individual exosomes enter the trap.

This is strong evidence that we can observe signals from individual exosomes, and can trap and release them with our laser tweezers setup. We can also see discrete changes in intensity when

new exosomes enter the trapping beam. Given that we are sensitive to individual exosomes, that our signal undergoes no changes during the 5 minute measurements we perform, and based on our NTA data where the dominant particles in each sample fall within the size range of exosomes, we believe that our signal originate from single particles in the exosome size range.

However, one caveat to this must be acknowledged. In our experiments we use bright field imaging to identify particles. One remaining question is whether we see the smallest exosomes, or only those above a certain size. To address the question of whether bright field imaging can observe particles in the exosome size range, we selected several synthetic particles with known size distributions:

1. NIST-traceable 50 nm polystyrene beads,
2. 100 nm silver nanoparticles,
3. 130 nm PEG micelles,
4. 160nm core-shell gold-glass nanoparticles (60nm gold core, 50nm-thick glass shell), and
5. NIST-traceable 220 nm polystyrene beads.

We present in Figure S4 example data from NIST-traceable 220 nm polystyrene beads (Duke Scientific, 5022A). Figure S4 (A) shows three representative, unprocessed bright field images of the polystyrene beads taken by our system showing the high contrast for these larger particles. Figure S4 (B) shows a time-course similar to Figure S3, where we can see individual polystyrene beads trapped and released by our system. The advantage of the stronger Raman signal from polystyrene is that we have much faster time resolution, confirming that beads enter and exit the trap causing step-wise changes in the Raman signal. Finally, by integrating the time-course in Figure S4 (B) we get a high-quality Raman spectrum as shown in Figure S4 (C), confirming our ability to record Raman spectra from individual nanoparticles. This data confirms our ability to observe individual nanoparticles and record Raman spectra from them using bright-field imaging as a feedback mechanism. However the smallest particles, the 50 nm polystyrene beads, were not observable under bright field illumination, while all other particles were. Due to the apparent similarity in optical contrast between polystyrene and extracellular vesicles, we believe that when we use bright-field to identify single particles, we very likely are biased towards selecting particles that are ~100 nm and larger. In the future it may be more advantageous to use light scattering (such as that used in NTA) rather than imaging as a feedback mechanism to detect a trapped particle. We emphasize here that it was possible to record Raman spectra from trapped 50 nm polystyrene beads, even though it was impossible to deterministically trap them using bright-field imaging. Therefore, given an appropriate feedback

mechanism (such as light scattering or dark-field imaging) to know when a particle is trapped, the LTRS method can still be used to acquire spectra of single exosomes in this size range.

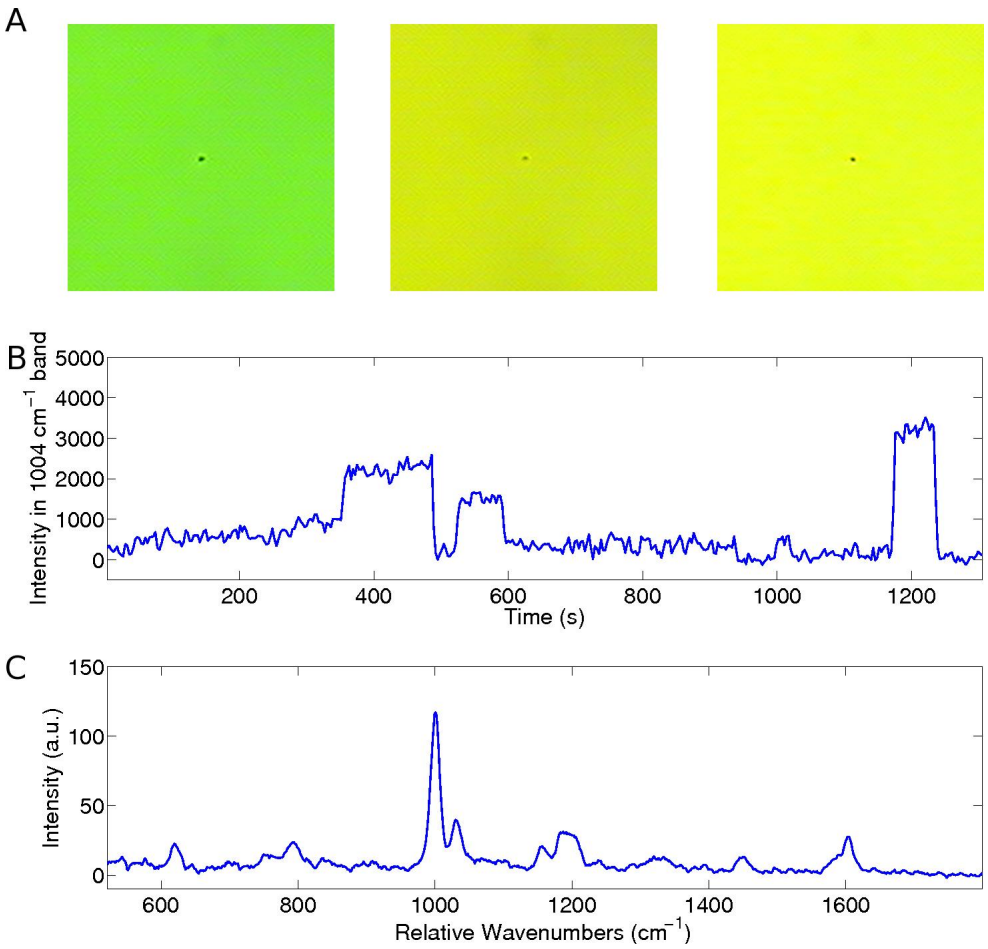

Figure S4 – Raman trap measurements of individual NIST-traceable nanoparticles. (A) Bright field images of 3 separate 220nm polystyrene beads. (B) Integrated intensity under the 1004 cm^{-1} peak over time as individual nanoparticles enter and are released from the trap. (C) Raman spectrum of polystyrene nanoparticles obtained by integrating the entire timecourse shown in (B).

Hierarchical Clustering of Cell Line Spectra

Figure S5. The first ten principal component loading vectors, calculated from the full exosome spectral dataset from all seven cell lines.

Following principal components decomposition, we plot the first 10 principal component loadings, shown in Figure S5 (first three curves identical to Fig. 3 (D)). Projecting the Raman spectra onto these 10 principal component axes yields 10 scores. A hierarchical clustering analysis, performed as described in the Methods section, above, using these scores, yields a dendrogram as shown in Figure S6. The dendrogram describes spectral distance, where branches of the dendrogram tree are connected based on the similarity of one spectrum to another. This similarity is assessed by computing pairwise distances between each spectrum in the 10-space described by first 10 principal components. Spectra with small pairwise distances are more similar to each other (have more similar PC scores). The dendrogram tree has been extended to the level of individual exosomes, with each terminus label color-coded as in Fig. 3 in the main text. The dendrogram reveals four major clusters, with clusters 2 and 3 having a heavy representation from exosomes of non-tumor cell lines. Spectra from each cluster can be averaged to yield cluster-averaged spectra as shown in Figure 3 (E) from the main text.

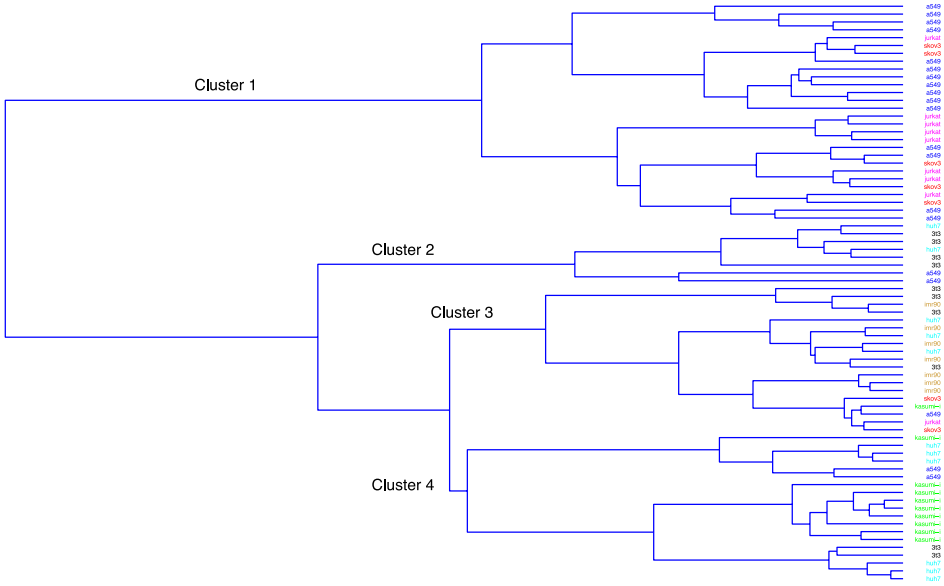

Figure S6. Dendrogram showing the clustering result using the first 10 principal components. Labels are color coded as in Figure 2.

Fitting Principal Component Axes from Seven Cell Lines to Pure Components and Principal Components of Control Experiments

Pure component spectra of membrane lipid components were fit to the shape of the 3rd principal component axis from the seven cell lines experiments using standard least-squares fitting, with the result shown in Figure S7. Note that the pure spectra in Figure S7 are scaled by their fit coefficient, so cholesterol, for example, has a negative fit coefficient and therefore is the negative of the lineshape shown in Fig. 4 from the main text, above. A 5th order polynomial was also included in the model to account for baseline fluctuations between the two experiments. The fit has a high correlation (r=0.82) with the PC_{7c} 3. The fitting coefficients can be used to quantitatively determine the molecular relationship between cholesterol and phospholipid represented by the principal component. The pure components were measured from solid forms of the chemicals that fully filled the confocal measurement volume of the LTRS system. Thus, the focal volume was filled with a certain number of molecules related to the density and molecular weight of the chemical being measured. Given this, the total number of molecules measured per focal volume can be calculated following Equation S1, below, where N_A is Avogadro's number:

$$\frac{molecules}{Vmeas} = density\left(\frac{g}{mL}\right) \times \frac{1}{Mol.Wt.}\left(\frac{mol}{g}\right) \times N_A\left(\frac{molecules}{mol}\right) \quad \text{(Equation S1)}$$

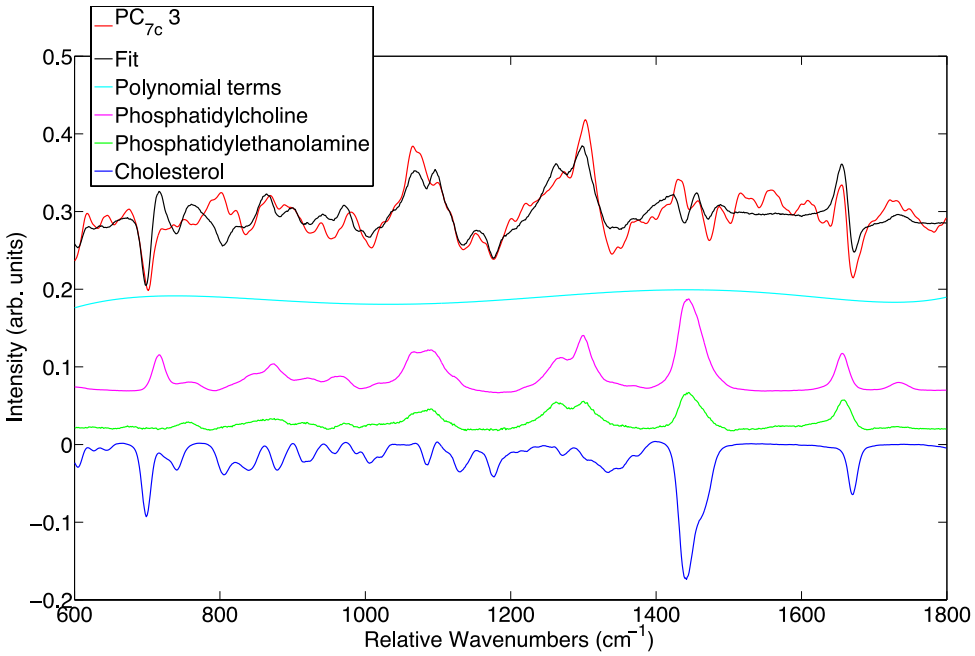

Figure S7. Least squares fit of the 3rd principal component from Figure 3 (D) to the pure spectra of cholesterol, phosphatidylcholine, and phosphatidylethanolamine shown in Figure 4. Spectra offset for clarity.

Cholesterol, phosphatidylcholine, and phosphatidylethanolamine have similar densities (1.067, 1.019, and 1.0, respectively). Thus, the primary determinant in the number of molecules per measurement volume is the molecular weight of each component (386.95 for cholesterol, 768 for phosphatidylcholine, and 744 for phosphatidylethanolamine). Thus, each pure component spectrum represents the signal from a certain number of molecules of that pure chemical, which could be determined by multiplying Eq. S1 by a highly accurate measure of the measurement volume V_{meas}. However, even in the absence of that information, because V_{meas} is constant between experiments, ratios of fit coefficients can be used to quantitatively determine the ratios of different molecules represented by PC_{7c} 3. The coefficients of the fit are:

$$-0.42 \times chol. + 0.28 \times phosphatidylcholine \; + \; 0.6 \times phosphatidylethanolamine$$

where "chol," "phosphatidylcholine" and "phosphatidylethanolamine" represent one unit spectrum of pure crystals of these compounds. Taking the ratio of the fit values for cholesterol and phospholipids, where each fit value is scaled by the number of molecules represented by each unit spectrum using Eq. S1, we can determine the ratio of cholesterol to phospholipid represented by PC_{7c} 3, as shown in Eq. S2, below:

$$\frac{-0.42}{386.95} \div \left(\frac{.28}{768} + \frac{.6}{744}\right) \approx 1 \qquad \text{(Equation S2)}$$

Therefore, PC_{Tr} 3 represents an exchange of cholesterol for phospholipids, with an exchange ratio of 1 cholesterol molecule for 1 phospholipid.

A similar fitting can be carried out for the 2nd principal component from the 7 cell lines experiment (PC_{7c} 2), which is hypothesized to report on membrane protein. In this case, we have *a priori* knowledge that PC_{Tr} 1 and PC_{Tr} 2 from the trypsin experiment are related to membrane protein (as they are the dominant sources of spectral difference between native and trypsinized exosomes and microvesicles). Therefore, we can attempt to fit PC_{7c} 2 with PC_{Tr} 1 and PC_{Tr} 2 of the trypsin experiment. The results of this fit are shown below, in Figure S8 (fit coefficients = -0.22*PC_{Tr} 1 + 0.43*PC_{Tr} 2). Similar to above, note that PC_{Tr} 1 in this case has a negative fit coefficient and is therefore the inverse lineshape compared to its presentation in Fig. 4(B). The fit has a high correlation with PC_{7c} 2 (r = 0.8), and provides strong support for the hypothesis that PC_{7c} 2 and PC_{Tr} 1 and 2 report on the same quantity: surface protein expression.

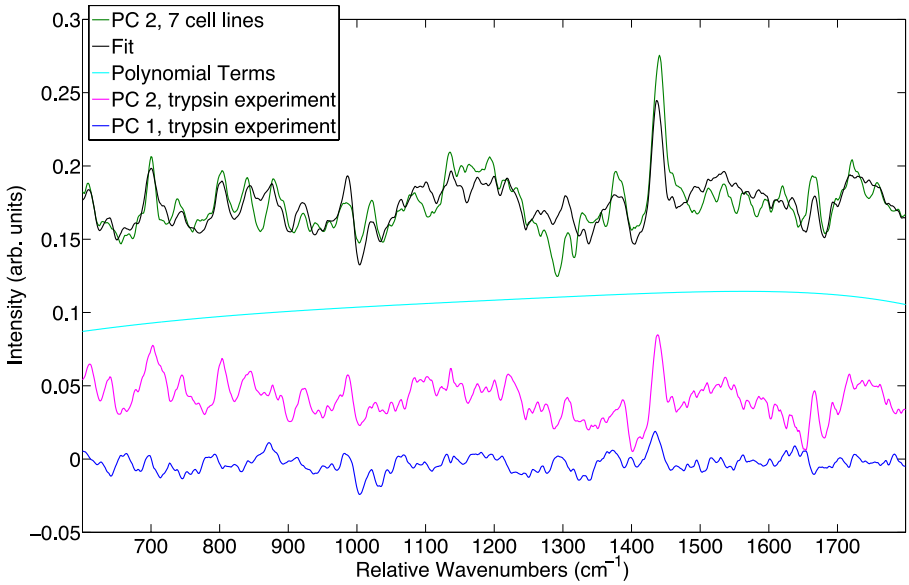

Figure S8. Least squares fit of the 2nd principal component from Figure 3 (D) by the 1st and 2nd principal components from the trypsin control experiment shown in Figure 5 (B). Spectra offset for clarity.

14 (IV) Multi-Parametric Surface Plasmon Resonance Platform for Studying Liposome-Serum Interactions and Protein Corona Formation

Reprinted with the permission of Controlled Release Society: Rojalin T‡, Kari OK‡, Salmaso S, Barattin M, Jarva H, Meri S, Yliperttula M, Viitala T, Urtti A. Multi-Parametric Surface Plasmon Resonance Platform for Studying Liposome-Serum Interactions and Protein Corona Formation. Drug Delivery and Translational Research 1-13, 2016. Copyright © Controlled Release Society 2016. http://dx.doi.org/10.1007/s13346-016-0320-0

‡ Equal contribution

Drug Deliv. and Transl. Res.
DOI 10.1007/s13346-016-0320-0

METHODS ARTICLE

Multi-parametric surface plasmon resonance platform for studying liposome-serum interactions and protein corona formation

Otto K. Kari[1] · Tatu Rojalin[1] · Stefano Salmaso[2] · Michela Barattin[2] · Hanna Jarva[3] · Seppo Meri[3] · Marjo Yliperttula[1,2] · Tapani Viitala[1] · Arto Urtti[1,4]

Abstract When nanocarriers are administered into the blood circulation, a complex biomolecular layer known as the "protein corona" associates with their surface. Although the drivers of corona formation are not known, it is widely accepted that this layer mediates biological interactions of the nanocarrier with its surroundings. Label-free optical methods can be used to study protein corona formation without interfering with its dynamics. We demonstrate the proof-of-concept for a multi-parametric surface plasmon resonance (MP-SPR) technique in monitoring the formation of a protein corona on surface-immobilized liposomes subjected to flowing 100 % human serum. We observed the formation of formulation-dependent "hard" and "soft" coronas with distinct refractive indices, layer thicknesses, and surface mass densities. MP-SPR was also employed to determine the affinity (K_D) of a complement system molecule (C3b) with cationic liposomes with and without polyethylene glycol. Tendency to create a thick corona correlated with a higher affinity of opsonin C3b for the surface. The label-free platform provides a fast and robust preclinical tool for tuning nanocarrier surface architecture and composition to control protein corona formation.

Keywords Multi-parametric surface plasmon resonance (MP-SPR) · Protein corona · Soft corona · Liposome · Complement system · Opsonin

Otto K. Kari and Tatu Rojalin contributed equally to this work

Electronic supplementary material The online version of this article (doi:10.1007/s13346-016-0320-0) contains supplementary material, which is available to authorized users.

✉ Tapani Viitala
tapani.viitala@helsinki.fi

[1] Centre for Drug Research and Division of Pharmaceutical Biosciences, Faculty of Pharmacy, University of Helsinki, Viikinkaari 5, P.O. Box 56, FI-00014 Helsinki, Finland

[2] Department of Pharmaceutical and Pharmacological Sciences, University of Padova, Via F. Marzolo 5, 35131 Padova, Italy

[3] Department of Bacteriology and Immunology, Immunobiology Research Program, Faculty of Medicine, and HUSLAB, Division of Clinical Microbiology, Haartmaninkatu 3, P.O. Box 21, FI-00014 Helsinki, Finland

[4] School of Pharmacy, University of Eastern Finland, Yliopistonranta 1, FI-70211 Kuopio, Finland

Introduction

Nanomedicine has advanced several research fields (e.g., cancer and gene therapy, medical imaging) by enabling the targeted delivery of therapeutic and diagnostic molecules while protecting the sensitive cargo [1, 2]. Hydrophilic molecules, such as polyethylene glycol (PEG), are used to shield nanocarriers from unspecific protein binding that may change biodistribution, decrease cellular uptake, and lead to premature nanocarrier clearance by the mononuclear phagocyte system (MPS) [3]. In fact, PEG can increase the average circulation time of liposomal drugs from minutes to up to days [3]. However, it is widely accepted that the steric hindrance provided by PEG and other hydrophilic coatings does not abrogate unspecific protein binding, and these coatings can act as immune activators [4–7]. Since severe hypersensitivity reactions to nanocarriers have been reported in clinical use, improved preclinical methods to assess the safety of nanocarriers are needed [2, 4, 5, 8–10]. In particular, label-free methods to predict biological interactions of nanocarriers are warranted, as labels may lead to biased results [2, 11]. The safety of

Published online: 04 August 2016

nanocarriers can be improved by decreasing the immunogenicity of nanocarriers, or by increasing their cellular targeting, both of which are affected by the proteins adsorbed on the nanocarrier surface.

After nanocarrier introduction into the blood circulation, their surface is rapidly covered with a complex and dynamic layer of biomolecules such as proteins, lipids, and other plasma components [3, 12–14]. This layer is often referred to as the "protein corona" and it is further divided into a stable "hard corona" and a diffuse secondary layer of proteins, the "soft corona" [3, 12–14]. Following the pioneering work of Cedervall et al. [14] to characterize the kinetics of protein corona formation on nanoparticle surfaces, protein-nanocarrier interactions have received increasing attention [15, 16]. At present, the influence of the protein corona on the fate of the nanocarriers in the body has been clearly demonstrated [3, 11, 13, 17]. Proteomic characterization of the protein corona has helped to identify nanocarrier-specific protein fingerprints—not a simple task considering the highly dynamic nature of the protein corona [15, 17–20]. More recently, the focus has shifted towards exploiting protein corona formation for extracellular and intracellular targeting, understanding its evolution, and its role in mediating physiological responses to nanocarriers [8, 15, 17, 20]. However, there is still a need to increase our understanding of the protein corona phenomenon and its dynamics due to its biological significance.

The prevailing hypothesis on the dynamics of corona formation assumes the formation of a highly dynamic but slowly-developing hard corona with a limited number of proteins [11, 14, 18]. This paradigm was challenged by Tenzer et al. [17], who reported the formation of a highly complex and particle-specific protein corona on all nanoparticles tested in 30 s. The rapid formation and composition of the protein coronas could not be explained merely by the physicochemical properties of the nanoparticles, and at longer incubation times, the protein composition changed only quantitatively but not qualitatively [17]. According to the authors, the rapid formation of a protein fingerprint is sensible considering the highly dynamic nature of physiological systems, which have evolved to "react instantly" to preserve homeostasis. The effect of dynamic incubation on protein corona formation was recently demonstrated with PEG-modified liposomes when static incubation was compared to flow conditions mimicking blood flow dynamics [12]. Over 200 corona proteins were identified, with 108 proteins common to both incubation conditions, whereas 10 and 99 proteins were observed only after incubation in static or dynamic conditions, respectively [12]. For increased in vivo relevance, the protein corona formation should therefore be tested in flow conditions.

The studies by Palchetti et al. [12] and Tenzer et al. [17] indicate the presence of complement system proteins in the corona. This is not surprising considering the nature of these proteins as the probes of the immune system, and the non-allergic hypersensitivity reactions that have been reported following the administration of PEGylated liposomes (e.g., Doxil©) that has been linked to complement system activation [5, 9]. For instance, covalent depositions of C3b on the surface of nanocarriers lead to an increased MPS clearance rate and a tendency to activate an innate immune response [3, 21, 22]. C3b is an activated opsonin formed from the central complement protein C3, at which all three activation pathways converge for amplification [21]. Complement proteins can carry out their functions by binding both to the native nanocarrier surface and through attachment to surface-bound proteins such as albumin [23]. Therefore, for reduced immunogenicity, nanocarrier surfaces should not favor the binding of C3b or other complement components [5, 9, 21].

Most analytical techniques are not suitable to study the soft corona on nanocarriers [12, 16, 17, 20]. Biophysical analytical approaches to monitor the soft corona could provide important information, and there is a growing interest in Raman spectroscopy, quartz crystal microbalance (QCM), and surface plasmon resonance (SPR) to study the evolution of corona formation in real time [16, 20]. The SPR phenomenon has been widely used for biosensing applications, including the interaction kinetics of individual proteins and complement system components on biomaterial surfaces [24]. Previous SPR studies on the interactions of nanocarriers with blood proteins have employed diluted plasma [13, 23, 25]. The surface of biosensors can be functionalized with specific chemistries of interest, proteins, or a hydrogel and lipid matrix that can be used to capture nanocarriers on the sensor surface—an approach we utilize in this work among others [14, 25–27].

SPR permits the sensitive label-free monitoring of molecular interactions [28, 29]. It is based on propagating waves of surface plasmons produced on a metal surface upon excitation with light. The conditions for exciting the surface plasmons are dependent on the refractive index of the medium in contact with the metal surface, and the molecular mass changes on the metal surface. In essence, the binding of molecules such as proteins to the metal surface can be detected as a change in the SPR peak angular position, θ_{SPR}. Figure 1 illustrates a set of idealized full SPR angular spectra; the solid red and blue traces representing measured spectra and the black and orange dotted lines showing calculated counterparts for the red and blue spectra, respectively. The main components of spectra are marked as ① the angular position of total internal reflection (TIR) event and ② the angular position of SPR peak minimum, referred to as θ_{SPR} in this manuscript. As the analytes are deposited onto the sensor surface, a shift towards larger angular values takes place in the θ_{SPR} (Fig. 1②). However, the angular position of TIR may also undergo a change towards larger values if the refractive properties of running buffer and injected analyte differ significantly (Fig. 1①). This bulk effect, in turn, can be compensated for in the

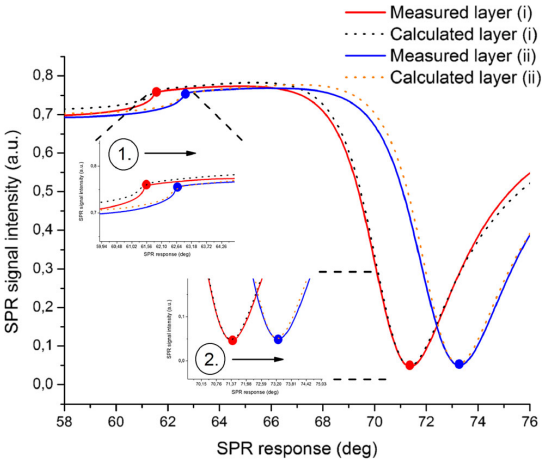

Fig. 1 An idealized example of two measured full SPR angular spectra (*red* and *blue solid curves*) and the fitted spectra (*black* and *orange dotted curves*, respectively). The shape and quantities associated with the SPR curve are used to fit the measured data and, consequently, solve for surface-deposited layer thicknesses (*d*) and refractive indices (*n*). The calculation is carried out in a stepwise numerical iteration routine whereby the parameters (*d* and *n*) for each layer are calculated utilizing the information provided by two independent excitation wavelengths (670 and 785 nm). For clarity, instead of displaying four measured curves, spectra recorded from one wavelength are depicted in the figure. The shift in angular position of total internal reflection (TIR) is used to compensate for bulk effect caused by the differences between the running buffer and injected sample; e.g., serum injection into the flow system consisting of a running buffer induces a significant change in the TIR angle (①). In order to estimate the signal for the binding event to the surface, the TIR shift contribution can be compensated by a subtraction from the overall signal. In general, binding events are detected as a shift in θ_{SPR} (②)

$\theta_{SPR,}$ and thus, the remaining part of the angular change mainly represents the binding event at the surface. In general, the full SPR angular spectra contain all the physical information to solve for the layer thicknesses and refractive indices; the shape and quantities associated with the SPR curve are utilized. A more profound mathematical description of solving for the layer thickness and refractive index is given in Materials and Methods section. Lastly, it is worthwhile pointing out, that the *full SPR angular spectra* are used to solve for deposited layer thicknesses and refractive indices, whereas the *sensorgrams* are utilized for determining the interaction kinetics parameters. Importantly, in the sensorgrams, the θ_{SPR} (displayed in Fig. 1 as red and blue dots) is followed in real time which allows for calculating the kinetic parameters if the injected analyte concentrations are known.

Multi-parametric surface plasmon resonance (MP-SPR) refers to an adaptation of the SPR technology that can be used to optically characterize biomolecular layers in more detail and with thicknesses of up to several micrometers [28] (Fig. 1). Traditionally, the incident angle of minimum reflectance has been monitored over a narrow angular area near the θ_{SPR}. With the MP-SPR technique, the full SPR angular spectrum is recorded by scanning over a wide angular range (~40–78°) and multiple parameters can be acquired simultaneously; for example, the angular position of the TIR angle, the angular position of θ_{SPR}, the half-width of the main SPR peak, and the change in the main SPR peak intensity at θ_{SPR} can be monitored in real time. The combination of two or more wavelengths and a scanning angle feature makes it possible to record the entire SPR angular spectrum as a function of time. Unlike with other SPR instruments that employ only one wavelength, the MP-SPR adaptation allows for determination of layer thicknesses, refractive indices, and surface mass densities in addition to traditional kinetic association and dissociation events [28, 30, 31]. These features provide new opportunities for a more detailed surface characterization of protein coronas, which we have explored in this work. In this paper, we describe the proof-of-concept for an MP-SPR method to monitor the formation of protein coronas on nanocarriers in real-time at the interface of flowing undiluted serum. We also demonstrate the use of MP-SPR to determine the affinity of a complement system probe molecule C3b interaction with the sensor-immobilized liposome surface.

Materials and methods

Serum preparation Blood drawn from seven healthy and fasted donors using Vacutainer glass tubes without clot activator (BD, Franklin Lakes, NJ, USA) was left to clot for 30 min at 22 °C, followed by centrifugation at 2500 × *g* for 5 min and 3500 × *g* for 5 min. The serum fractions were collected manually and pooled together with serum from other donors in aseptic conditions, and stored in aliquots at −80 °C. Before SPR measurements, aliquots were thawed rapidly in a 37 °C water bath until 90 % thawed. Heat homogeneity was checked with a FLIR TG165 imaging IR thermometer (FLIR Systems, Inc., OR, USA) to avoid bubble formation inside the SPR flow channel due to temperature changes.

Liposome samples The film re-hydration method followed by extrusion through a polycarbonate membrane was used to prepare liposome samples [32]. Control liposomes were replicas of the Doxil© (Johnson and Johnson, NJ, USA; marketed in Europe under the name Caelyx© by Janssen-Cilag International NV, Beerse, Belgium) formulation with and without PEG (referred to as DOX + PEG and DOX, respectively) but without doxorubicin [32]. The molar ratio of fully hydrogenated soy phosphatidylcholine (HSPC), cholesterol and *N*-(carbonyl-methoxypolyethylene glycol 2000)-1,2-distearoyl-sn-glycero-3-phosphoethanolamine sodium

salt (DSPE-PEG_{2000}) or 1,2-distearoyl-sn-glycero-3-phosphoethanolamine (DSPE) was 55:40:5, respectively [32]. After preparation the DOX and DOX + PEG liposome stock suspensions were stored at 4 °C until use. For SPR measurements, the DOX and DOX + PEG liposome samples were adjusted to a 3 mM total lipid concentration.

Positively charged liposomes with oligo-guanidyl lipid derivative (OGD) with a 0.2 mg/ml total lipid concentration in HEPES 10 mM and NaCl 150 mM (pH 7.4) buffer solution were freeze dried after preparation and stored at −20 °C until use [33]. For SPR measurements, the OGD liposomes samples were quickly thawed and vortexed. The OGD liposomes adsorbed on the sensor surface were then coated in situ according to a charge-to-charge association process with a polyanionic-PEG block-copolymer (PEG) with a concentration of 0.1085 mg/ml in HEPES 10 mM and NaCl 150 mM (pH 7.4) buffer solution (OGD + PEG).

Endotoxin detection The presence of endotoxins was tested using Limulus Amoebocyte Lysate (LAL) assays: Pierce LAL chromogenic endotoxin quantitation kit (Thermo Fisher Scientific, Waltham, MA, USA) and Pyrogent Plus Gel Clot LAL at 0.06 EU/ml sensitivity (Lonza, Basel, Switzerland). Assays were performed according to manufacturers' instructions using endotoxin-free consumables. Test samples were incubated using a Thermomixer C heating block (Eppendorf AG, Hamburg, Germany). Absorbance (405 nm) was measured using a Spectrostar Nano plate reader (BMG Labtech, Ortenberg, Germany) and calculated using the accompanying MARS software. Inhibition and enhancement controls and transmissivity measurements of the liposome solution at assay wavelength were performed to rule out liposome interference with the LAL assays.

Physicochemical characterization of liposome samples Hydrodynamic diameter measurements were performed at 25 °C with a Zetasizer APS DLS automated plate sampler (Malvern Instruments, Malvern, United Kingdom). Results are reported as size distributions (average hydrodynamic diameter ± S.D.) derived from relative signal intensities and in the form of a polydispersity index (PDI). Surface charge of the liposomes was determined by measuring the ζ-potential in DTS 1070 folded capillary cells (Malvern Instruments) by using a Zetasizer Nano ZS instrument (Malvern Instruments).

MP-SPR measurements Measurements were performed with a SPR Navi™ 200 (BioNavis Ltd., Ylöjärvi, Finland) instrument. The setup was equipped with two incident laser wavelengths, 670 nm and 785 nm, two independent flow channels, inlet tubing and outlet (waste) tubing. Both of the flow channels were measured in parallel with 670 nm and 785 nm incident light. The measurement temperature was kept constant at 20 °C, and the flow rates used for liposome immobilization and for serum interactions were 50 and 100 μL/min, respectively. Liposomes were captured and immobilized on SPR sensors consisting of a thin 6-kD carboxymethyl dextran hydrogel layer functionalized with dodecyl lipid anchors [26, 34]. The SPR sensors were used repeatedly after rejuvenation with an injection series of Hellmanex II 2 % (Hellma Analytics, Müllheim, Germany) or CHAPS 20 mM (Sigma-Aldrich), ethanol 80 % (Altia Oyj, Rajamäki, Finland) and deionized water from a Milli-Q water purification system (Merck KGaA, Darmstadt, Germany). In between measurements, the sensors were stored immersed in CHAPS at 4 °C. During the SPR measurements, the functionalized gold sensor slides were first subjected to the running buffer for respective liposome for approximately 5–10 min until a stable baseline was achieved. In the second phase, the liposomes were injected into both flow channels for 10 min, and lastly, sensor surfaces containing the immobilized liposome species were subjected to 100 % serum. The PEGylation step for the OGD liposomes was performed in situ with a polyanionic-PEG block-copolymer after liposome immobilization to create a surface with OGD + PEG, whereas DOX + PEG liposomes contained PEG prior to immobilization.

MP-SPR data analysis The shape and quantities associated with the SPR curve are utilized for the layer thickness and refractive index calculations. The SPR spectrum can be described with Fresnel's equations as the reflectivity of a multilayered system for *p-polarized* light [28, 30]. In essence, the layers are assumed linear, homogenous, and isotropic. The calculation is based on a 2 × 2 scattering matrix that is derived from Fresnel's complex-amplitude reflection and transmission coefficients. The matrix represents the summarized optical properties of the system; the properties are expressed as a product of the interface and layer matrices of the entire structure. Furthermore, the intermediate zones between different layers are introduced into Fresnel's equations as new layers. Thus, the thickness of the intermediate layer describes the average roughness of the surface, whereas its complex refractive index corresponds to the light losses via scattering and plasmon decoupling into radiative modes (essentially the imaginary part of the complex refractive index). The benefit of this approach is that only Fresnel's equations can be used without the need to apply, e.g., scattering theories. In practice, the modeling and solving for the matrix formalism is performed by mathematical fitting tools or dedicated software. To solve for the layer thicknesses and refractive indices of the thin biomolecular layers, a two-wavelength method combined with angular scanning over a wide range of incident light angles is particularly efficient [35–37]. The measured full angular SPR spectrum and matrix formalism are utilized to model the layers. Even though the overall mathematics behind the calculations is relatively complicated, the solving process can be simplified to a level that the

modeling still produces accurate results for most of the situations that deal with common materials and biological molecules. Additionally, the sources for error are feasible to track due to the known limitations of these evaluations. It is worth emphasizing that the multi-wavelength approach for surface characterization has been successfully implemented in previous studies [26, 31, 38, 39].

The general solution for a multilayered, optically active system that is connected with measurable and controllable quantities, can be derived using the aforementioned transfer matrix formalism of 2 X 2 matrices. In the complex refractive index $n = n + ik$ the real part n corresponds to the refraction of light, and the complex coefficient k to the extinction or absorption of light by the material. Furthermore, the relationship $n = \sqrt{\varepsilon}$ connects the refractive index and dielectric constant. Finally, in practical experiments, the surface plasmon wave vector (k_{sp}) is considered to contain all the information and constants that affect the measured SPR spectra and lead to differences in SPR spectra measured at multiple wavelengths. Therefore, the continuum solution for surface plasmon wave vector (k_{sp}) in one set of conditions can be deducted to describe the mathematical relationship between (k_{sp}), the material layer thickness d, and the refractive index n:

$$k_{sp} \propto n*d$$

However, the definition above describes only *one continuum solution* for the (k_{sp}). The unique solution for the apparently interconnected thickness d and refractive index n of the sample layer build in the given experimental conditions can be found from the intersection of *two continuum solutions*. Therefore, a measurement in two different media or multiple wavelengths is needed [28, 31]. In the mathematical treatment of the two-wavelength method, the refractive index n has also a wavelength dependency, dn/dλ. The unique solution for layer thickness d and refractive index n can be found by solving for the equations:

$$k_{sp1} = n_{\lambda 1}*d$$

$$k_{sp2} = n_{\lambda 2}*d$$

where k_{sp1} denotes the surface plasmon vector for wavelength 1, $n_{\lambda 1}$ the refractive index for wavelength 1, k_{sp2} the surface plasmon vector for wavelength 2, and $n_{\lambda 2}$ the refractive index for wavelength 2, and:

$$n_{\lambda 2} = n_{\lambda 1} + \frac{dn}{d\lambda} * (\lambda_2 - \lambda_{1.})$$

and:

$$k_{sp1} = n_{\lambda 1}*d$$

$$k_{sp2} = \left(n_{\lambda 1} + \frac{dn}{d\lambda} * (\lambda_2 - \lambda_1) \right) * d$$

The statements above hold true for sample layers that do not absorb light at the wavelengths used in the SPR spectrum measurement. In practice, it means that the imaginary component k for the refractive index = 0, which is the case for the majority of organic sample layers. However, if the layer absorbs light, $k \neq 0$, and there is a unique solution for the sample layer in the $k_{sp} = (n + ik) * d$ space, one can utilize laser wavelengths 670 and 785 nm that are aligned to irradiate simultaneously the same spot in each sample channel. The thicknesses of modeled layers can be linked as common for both wavelengths in the modeling step, i.e., the layer thickness is expected to be the same for both wavelengths since the SPR angular spectra are measured from the same spot. The complex refractive index can be inputted as an independent variable for background (e.g., pure metal layer) modeling, or as a linearly dependent variable between the two used wavelengths for reasons described above.

The SPR Navi LayerSolver v. 1.2.1 (BioNavis Ltd., Ylöjärvi, Finland) software was used for the layer thickness (d) and refractive index (n) modeling and calculations. In essence, the modeling and calculation of layer thickness and refractive index were carried out using the two-wavelength method. The LayerSolver allows for multiple SPR spectra processing, and a stepwise approach for calculations where the biophysical properties of the molecular layers are determined by numerical iteration one layer at a time. The software was used to simultaneously solve the thickness and refractive index based on full SPR angular spectra measured with two different wavelength lasers (670 and 785 nm) at the same time point [28, 30]. The numerical iteration is performed by the embedded algorithms in LayerSolver software. The equations described in section "MP-SPR data analysis" constitute the physical cornerstone for the calculation routines in LayerSolver. As input variables, the following layer thickness and refractive index values were used: for OGD, d = 45–70 nm and n = 1.357–1.355; for DOX, d = 80–120 nm and n = 1.357–1.352; for OGD and DOX soft corona, d = 20–70 nm and n = 1.37–1.38; for OGD and DOX hard corona d = 5–10 nm and n = 1.38–1.39. In the optical modeling performed in this work, the thickness values were defined as global variables for the two wavelengths used and the refractive indices were defined as independent variables for the iteration cycles.

Interaction kinetics were modeled with TraceDrawer v. 1.6 (Ridgeview Instruments AB, Vänge, Sweden) software. The calculation of interaction parameters is based on well-established kinetic models [40]. Herein, a one binding site model was used for determining the affinity of the human native complement component C3b (diluted in Dulbecco's phosphate-buffered saline, obtained from Merck KGaA, Darmstadt, Germany) interacting with immobilized OGD or OGD + PEG liposomes. According

to the supplier, the C3b protein used should display at least 60 % of its physiological activity. A concentration series 0.00833, 0.0833, and 0.833 mol (determined with a MW of 180 kDa from 0.0015, 0.015, and 0.15 mg/ml) fitting with negligible dissociation phases was performed for the measured C3b sensorgrams in order to calculate the kinetic parameters for C3b. In general, molecular mass that binds onto the SPR sensor surface has a well-defined correlation with the observed SPR angular spectrum and the SPR resonance angle shift in particular. Hence, the surface mass densities of C3b can be calculated by using the de Feijter equation that is derived from the definition of refractive index increment of adsorbing biomolecules, with some limitations [41, 42]. For the used SPR Navi™ 200 instrument and 670-nm laser wavelength, the actual surface mass density conversion coefficient can be defined using a value of $^{dn}/_{dc}$ = 0.182 cm^3/g. In this study, to convert the observed SPR signal responses to surface mass densities (Γ), we used the conversion factor Δ 1 mdeg = Δ (Γ)~0.6 ng/cm^2 for the lower limit of deposited surface mass density. To estimate the error in the calculation, we also defined the higher limit using the conversion factor Δ 1 mdeg = Δ (Γ)~1.0 ng/cm^2.

Results and discussion

Liposome immobilization and serum interaction with the immobilized liposomes Figure 2 illustrates the measurement scheme for serum interaction studies with the liposomes. Undiluted serum was used instead of anticoagulated plasma since it contains a functioning complement system. Roman numerals are used consistently to refer to the modeled physical events. Figures 3 and 4 (a, b), and Figs. 5 and 6 (a, b) display the MP-SPR sensorgrams and full SPR angular spectra, respectively, with: (I) the liposome layer after immobilization onto the sensor surface, (II) serum interaction with liposomes and ensuing soft corona formation, and (III) the hard corona after restoration of buffer flow. In this work, the term soft corona is used to refer to the combination of a denser corona layer accompanied by a more diffuse layer of weakly interacting proteins. The averages of the modeled and calculated layer thicknesses (d) and refractive index (n) values of three independently repeated measurements are found in Table 1 for OGD and OGD + PEG liposomes and in Table 2 for DOX and DOX + PEG liposomes. In order to emphasize the highly dynamic behavior of the modeled systems, to take into account the possible sensitivity of differential equations to initial conditions provided as inputs in LayerSolver, and to estimate the uncertainties in experimental procedures and calculations, we chose to define a range for the calculated (d) and (n) values. Thus, instead of representing one set of (d) and (n)

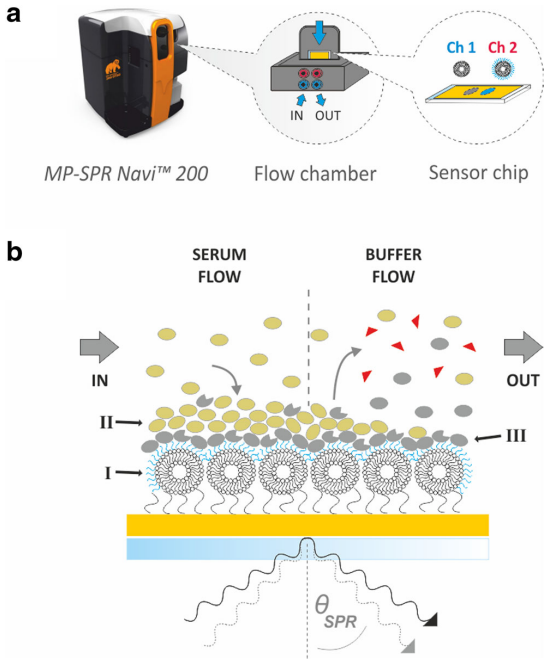

Fig. 2 Schematic representation of the experimental setup using an MP-SPR Navi™ 200 instrument (instrument image courtesy of BioNavis Ltd., Ylöjärvi, Finland). **a** Liposomes were captured from inflow and immobilized onto functionalized sensors. Measurements were run in parallel with the same serum source to compare the effect of hydrophilic coating molecules on protein corona formation. **b** Simplified representation of the sensor surface to demonstrate the distinct layers of interest in the modeling step. *Roman numerals* indicate (*I*) the OGD liposome layer after immobilization onto the sensor and in situ functionalization with the polyanionic-PEG block-copolymer (*blue*), (*II*) serum interaction with liposomes and following soft corona formation, and (*III*) the hard corona after restoration of buffer flow

values, our intention was to determine the d_{low} and n_{low} as well as d_{high} and n_{high}, between which the calculated values could potentially vary. The d_{low}, n_{low}, d_{high}, and n_{high} values were calculated by using a consistent set of initial values throughout the layer modeling. Table S1 presents the results of physicochemical characterization (size, PDI, and ζ-potential) and endotoxin determination. The results for each individual experiment are found in Table S2 for OGD and OGD + PEG liposomes and Table S3 for DOX and DOX + PEG liposomes. In order to show that the observed events are not dependent on the flow channel used, the immobilized liposome species were interchanged between the flow channels from experiment to experiment.

OGD and OGD + PEG liposome interaction with 100 % serum Figure 3a shows the real-time sensorgrams from one measurement demonstrating OGD liposome immobilization onto the SPR sensor in both channels, followed by the

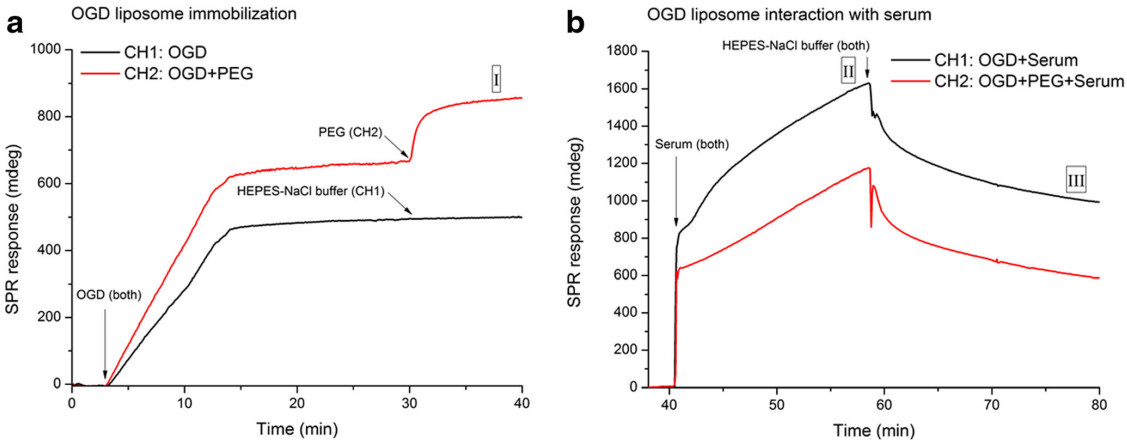

Fig. 3 MP-SPR sensorgrams for immobilization of OGD liposomes and their interaction with serum. **a** Liposome immobilization to both channels with PEG modification in situ at *t*~30 min for CH2. Thickness (*d*) and refractive index (*n*) of liposome layers have been modeled and calculated at time point I. **b** Serum interaction (from 40 to 60 min) with the immobilized OGD (CH1) or OGD + PEG (CH2) liposomes at a flow speed of 100 μL/min. Thickness (*d*) and refractive index (*n*) were modeled and calculated at *II* for soft corona, and at *III* for hard corona after restoration of buffer flow

PEGylation step in channel 2 (CH2) at t ~ 30 min to form OGD + PEG. In channel 1 (CH1) with plain OGD liposomes, the signal remains at a constant level during running buffer injection. Figure 3b and Table 1 present the serum interaction results.

Figure 4 **a, b** present the full SPR spectra from real-time experiments for OGD and OGD + PEG liposomes at time points when the upper and lower boundaries for layer thicknesses and refractive indices were determined. First, the functionalized gold sensor surface with a 6-kDa carboxymethyl dextran hydrogel matrix with dodecyl lipid anchors was measured and modeled (*black line*), followed by the (*I*) immobilized liposome layer, (*II*) soft corona and (*III*) hard corona. For clarity, the measured metal layer and OGD or OGD + PEG liposome layers are displayed without the fitted curves, whereas the soft and hard corona layers are depicted with both measured and fitted curves. Based on the stepwise numerical iteration procedure in LayerSolver, where the previous layer acts as a background to solve for the thickness and refractive index of the consequent layer, the modeling yields fairly good alignment between the calculated and measured SPR spectra throughout the procedure. Typically, the SPR angular peak minimum tends to shift towards larger angles as molecules (mass) adsorbing onto the surface and consequently change the refractive index in close vicinity to the surface. Thus, the

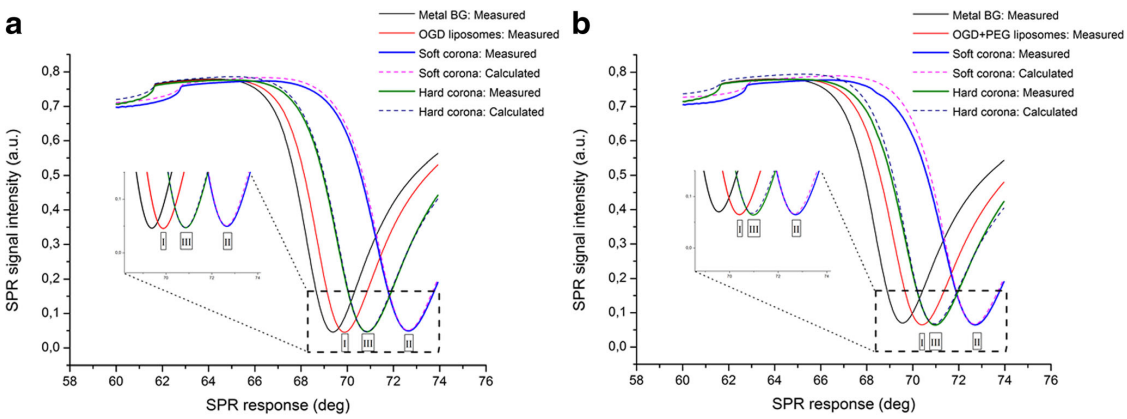

Fig. 4 Layer modeling for OGD and OGD + PEG liposomes using the measured full SPR angular spectra. **a** SPR peak minimum shifts for the measured and modeled phases from the metal sensor surface (*black line*) to plain OGD (*I*) liposome immobilization, (*II*) soft corona, and (*III*) hard corona. **b** Corresponding events for OGD + PEG

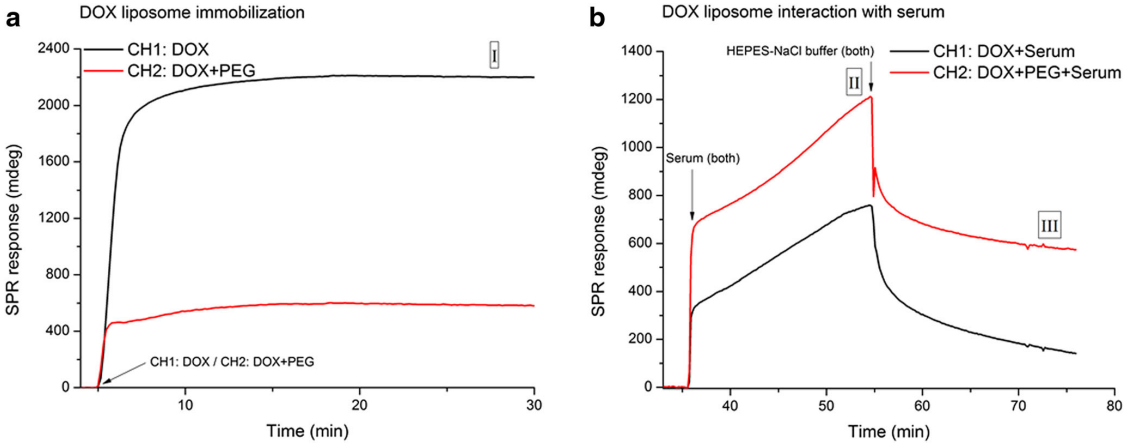

Fig. 5 MP-SPR sensorgram for DOX and DOX + PEG liposome immobilization and interaction with serum. **a** Liposome immobilization onto the sensor surface with DOX in CH1 and DOX + PEG in CH2. The liposome layer thickness has been modeled and calculated at time point I. **b** Serum interaction (from 35 to 55 min) with DOX (CH1) or DOX + PEG (CH2) liposomes at a flow speed of 100 μL/min. Thickness (*d*) and refractive index (*n*) were modeled and calculated for soft corona (*II*) and hard corona (*III*) after restoration of buffer flow

surface plasmon coupling condition undergoes a change that can be observed as a shift in the peak minimum angular position [27, 43, 44]. The biomolecular layer build-up is clearly seen in Fig. 4 (insets in **a** and **b**) where the SPR peak minimum shifts from the value observed for the metal (*black traces*) to the right when liposomes are associating with the surface (*red traces*) and both the total internal reflection (TIR) angle and the SPR peak minimum shifts further to the right when a soft corona forms (*blue solid trace* and the corresponding *fitted purple dashed line*). Interestingly, when the hard corona layer is revealed after restoration of buffer flow, the peak minimum value shifts back to the left (*green solid traces* and the *navy blue dashed fitted lines*)—which is an expected phenomenon when serum with a much higher refractive index is replaced by a buffer solution with lower refractive index (affects mainly TIR angular position) and when components of the looser soft corona layer dissociate, leaving a denser layer on the surface of immobilized liposomes.

As shown in Table 1, the immobilized OGD liposomes form on average a slightly thinner layer on the sensor surface (40.4–55.5 nm) compared to the PEGylated OGD layer (44.4–60.9 nm), with basically the same refractive index for both systems. The slightly larger thickness for the ODG + PEG layer can be attributed to the additional PEG layer deposited on the adsorbed OGD liposome layer, whereas the additional PEG layer will not significantly affect the refractive index due to the high water content in the PEG layer. Although MP-SPR signal response levels exceeding ~500 mdeg suggest that

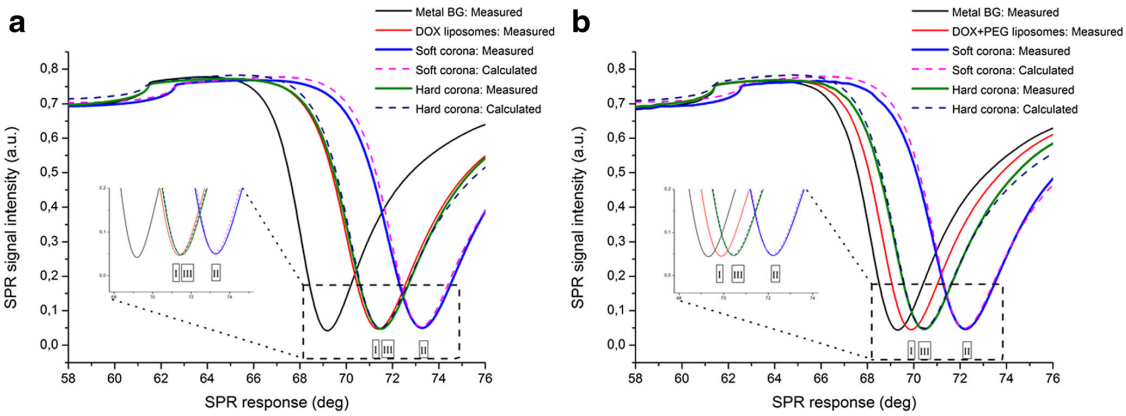

Fig. 6 Layer modeling for DOX and DOX + PEG liposomes using the measured full SPR angular spectra. **a** SPR peak minimum shifts for the measured and modeled phases from the metal sensor surface (*black line*) to plain DOX (*I*) liposome immobilization, (*II*) soft corona, and (*III*) hard corona. **b** Corresponding events for DOX + PEG

Table 1 OGD and OGD + PEG liposomes and serum interaction results. The calculated values are low and high limits for layer thickness (*d*) with corresponding refractive index (*n*) values as averages (±standard deviation) of three independent measurements for: (I) immobilized OGD liposomes with and without PEG modification; (II) soft protein corona formation following serum interaction; and (III) the residual hard corona after buffer flow restoration when a stable baseline is observed

		(I) Liposome		(II) Soft corona		(III) Hard corona	
OGD		Low	High	Low	High	Low	High
	d	40.4 ± 9.3	55.5 ± 16.0	34.2 ± 2.1	106.0 ± 17.4	9.6 ± 1.0	16.4 ± 0.9
	n	1.35302 ± 0.0021	1.34996 ± 0.00151	1.39701 ± 0.0080	1.37742 ± 0.0016	1.44627 ± 0.0072	1.41121 ± 0.0035
OGD + PEG		Low	High	Low	High	Low	High
	d	44.4 ± 4.2	60.9 ± 8.1	22.2 ± 14.5	63.2 ± 57.2	4.6 ± 2.7	8.6 ± 6.4
	n	1.35679 ± 0.00292	1.35263 ± 0.00215	1.37931 ± 0.0178	1.38013 ± 0.0071	1.39524 ± 0.0393	1.37531 ± 0.0227

Refractive indices extracted during fitting procedure: serum 1.34960, buffer 1.33535

saturation of the sensor was achieved by both OGD and OGD + PEG, it is noteworthy that the SPR curve produced by MP-SPR is an average of the entire sensor surface; factors such as the non-homogeneous placement of liposomes, gaps in the layers, or the formation of multilayers can also influence the layer thicknesses and refractive indices observed [45]. Morphological changes in the shape of the liposome due to the interactions with the functionalized sensor surface and the shear stress from buffer flow are also expected, and they account for the differences to hydrodynamic diameters measured in bulk (Table S1).

Following serum injection, a thicker soft corona layer (34.2–106.0 nm) forms on the plain OGD liposome layer compared to the OGD + PEG liposome layer (22.2–63.2 nm). The plain OGD liposome layer presents surface charges that favor the association of passing serum components. Moving beyond the presumption that steric PEG protection decreases protein adsorption to liposome surfaces, we hypothesize that this observation can be explained by higher opsonisation and possible surface-induced activation of the complement system by the OGD liposome bearing oligoguanidyl moieties and traces of endotoxin (Table S1) [12, 21, 24]. Complement activation leads to the recruitment of other complement components and formation of enzyme convertases that amplify the activation process by catalyzing opsonin production and their surface deposition in high quantities, thereby producing more molecular mass on the surface [21, 24]. The tendency to activate the complement system is influenced by the amount and orientation of PEG molecules on the surface of liposomes [5, 46, 47]. However, the standard deviation of soft corona layer thickness in the case of OGD + PEG is relatively large (±57.2 at upper boundary) and a more definitive conclusion warrants further studies. Despite the difference in soft corona layer thicknesses, refractive indices in the same range for OGD and OGD + PEG suggest a similar consistency, presumably related to the more diffuse and rapidly exchanging nature of the soft corona layer at the vicinity of the surface. Finally, when a buffer rinse is performed after serum injection, a significantly thicker and denser hard corona layer remains on the surface of the plain OGD liposomes compared to OGD + PEG, which may report of complement activation and deposition of covalently bound complement end products onto the surface. To our knowledge, this is the first time when MP-SPR is used to optically characterize

Table 2 DOX and DOX + PEG liposomes and serum interaction results. The calculated values are low and high limits for layer thickness (*d*) with corresponding refractive index (*n*) values as averages (±standard deviation) of three independent measurements for: (I) the immobilized DOX and DOX + PEG liposome layer; (II) soft protein corona formation following serum interaction; and (III) the residual hard corona after buffer flow restoration when a stable baseline is observed

		(I) Liposome		(II) Soft corona		(III) Hard corona	
DOX		Low	High	Low	High	Low	High
	d	99.1 ± 5.0	153.2 ± 8.2	37.5 ± 1.7	86.8 ± 19.6	3.4 ± 1.2	6.6 ± 1.9
	n	1.36237 ± 0.0010	1.35680 ± 0.0009	1.41742 ± 0.0046	1.42930 ± 0.0175	1.39440 ± 0.0034	1.38614 ± 0.0063
DOX + PEG		Low	High	Low	High	Low	High
	d	37.3 ± 4.7	49.1 ± 2.9	25.8 ± 4.8	60.0 ± 18.0	7.6 ± 0.9	13.0 ± 0.8
	n	1.34971 ± 0.0017	1.34722 ± 0.0002	1.39711 ± 0.0069	1.37730 ± 0.0026	1.42353 ± 0.0075	1.39187 ± 0.0085

Refractive indices extracted during fitting procedure: serum 1.34960, buffer 1.33535

properties of protein corona layers. These results provide clear support for the existence of a distinct, more diffuse soft corona layer on top of the hard corona [13, 17, 20].

DOX and DOX + PEG liposome interaction with 100 % serum Figures 5 and 6 show the real-time sensorgrams and the full angular SPR spectra, respectively, for DOX and DOX + PEG liposomes. The layer thicknesses and refractive indices are shown in Table 2**.** In Fig. 4a, DOX liposomes without PEG were immobilized to CH1 and DOX + PEG to CH2. Since DOX + PEG liposomes were already PEGylated ex situ, a separate functionalization step on the sensor was not needed. The clearly larger signal response for the DOX liposome layer compared to the DOX + PEG liposome layer can be explained by the different penetration properties of the liposomes into the carboxymethyl dextran hydrogel matrix and interactions with the dodecyl lipid anchors depending on liposome properties. Lundquist and her colleagues have demonstrated that the hydrophilic PEG coating on liposomes decreases interactions with lipid anchors, preventing deep penetration into the carboxymethyl hydrogel matrix on the Biacore L1 chip [48]. The lower layer thickness for DOX + PEG liposomes could therefore be a result of smaller penetration PEGylated liposomes into the hydrogel, and stronger interaction of the plain DOX liposomes with the dodecyl moieties. It is important to note, however, that layer thicknesses and refractive indices cannot be interpreted solely by visual inspection of the sensorgrams. For example, the sensorgram in Fig. 5 (b, II) shows a higher signal for DOX + PEG liposomes during soft corona formation, but in Table 2 (II) the average calculated soft corona layer thickness is slightly smaller for DOX + PEG liposomes. To explain these occasional abnormalities in signal behavior in brief, the modeled layer thickness (*d*) and refractive index (*n*) are dependent on the relative SPR peak minimum shift compared to the previous (lower) layer and its SPR peak minimum position, as well as the intensity fluctuations and SPR minimum peak width observed in the SPR angular spectra. Our modeling approach is a layer-by-layer evaluation procedure where the next layer is built by using the previous layer as a starting point for subsequent steps, in particular, the protein corona determinations at II and III. Since the initial signal levels of DOX liposome immobilization compared to DOX + PEG are significantly higher (Fig. 5a), this difference can be expected to have a distorting effect on the subsequent protein corona modeling steps. Therefore, in addition to performing accurate modeling and calculations based on the full angular SPR curves and using data from several reproducible experiments, careful inspection of the signal levels at these different phases is needed in order to correctly interpret the phenomena taking place at the surface or in its near vicinity. Layer thicknesses and refractive indices for subsequent serum interactions were calculated as described previously. As previously perceived in the layer modeling process for OGD and OGD + PEG, hereby a similar observation can be made on the relatively good alignment between the measured and calculated SPR spectra.

Table 2 represents the modeled and calculated values of DOX liposomes forming on average a 99.1–153.2 nm layer on the sensor surface with an average refractive index of 1.35680–1.36237. The immobilized DOX + PEG liposomes form a significantly thinner layer with an average of 37.3–49.1 and with a lower refractive index range of 1.34722–1.34971. We speculate that the exceedingly high signal produced by plain DOX liposomes is a consequence of its lipophilic interactions with the lipid anchors, promoted by the smaller size and absence of oligo-guanidyl moieties comparing to plain OGD liposomes, which are likely to lead to the formation of liposome multilayers instead of monolayers on the sensor surface [45, 48]. After serum injection, a soft corona of 37.5–86.8 nm forms on DOX liposomes with a refractive index of 1.41742–1.42930, whereas the layer thickness on DOX + PEG is slightly thinner 25.8–60.0 ± 18.0 nm. As with the liposome layer, the refractive index range of the DOX + PEG soft corona layer is lower 1.37730–1.39711. After restoration of buffer flow, a significantly thinner hard corona remains on DOX compared to DOX + PEG (3.4–6.6 vs. 7.6–13.0 nm). Interestingly, the refractive index of DOX hard corona is lower than the soft corona for the same liposome, or the hard corona observed on DOX + PEG (1.38614–1.39440 vs. 1.39187–1.42353, respectively). We hypothesize that these could be explained by a higher amount of light refracting species remaining at the vicinity of the surface, but may also be caused by events such as restructuring and phase transformations taking place in the biomolecular layers [49]. Based on the observations on the possible distorting effect of the significantly higher signal response in the DOX liposome immobilization step, contrasting DOX liposome results reliably with the three other liposome types would require further optimization of sensor saturation levels. Therefore, for proof-of-concept, we limit our discussion to compare protein corona formation on OGD and OGD + PEG to DOX + PEG as a "benchmark" liposome formulation.

Comparison of OGD and OGD + PEG with DOX + PEG serum interaction events When the serum interaction events described in Tables 1 and 2 are compared, some important observations can be made. Firstly, refractive indices of soft corona layers on OGD and OGD + PEG liposomes are clearly smaller than the refractive indices of soft corona layers on DOX + PEG liposomes. This disparity is not dependent on the liposomes having PEG or not. This may be in relation to the differences in the properties of these liposome species, for example surface lipophilicity or hydrophilicity, surface charge and rheological properties, which translate into different compositions for the protein corona [17, 26]. Secondly, OGD

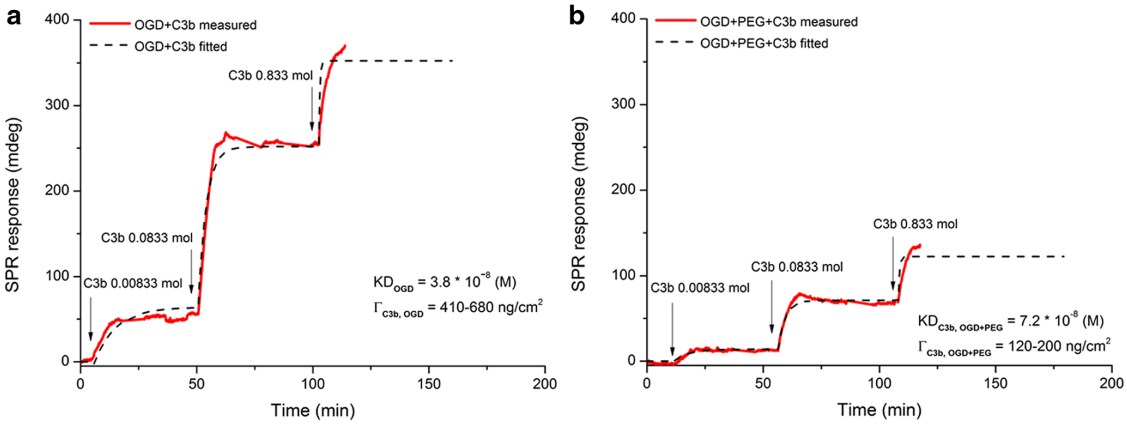

Fig. 7 C3b binding affinity and surface mass density onto OGD and OGD + PEG liposomes

liposomes favor a soft corona layer formation that is slightly thicker and denser than in the case of OGD + PEG or DOX + PEG liposomes (34.2–106.0 vs. 22.2–63.2 and 25.8–60.0 nm, respectively). Absence of PEG increases the lipophilicity of the surface, and increased protein binding is expected [49]. Dynamic conditions may also contribute to this effect, as protein coronas formed on PEG-modified liposomes under dynamic conditions tends to be thicker than those resulting from static incubations, i.e. around ~20–25 nm thicker [12]. For OGD and in a lesser extent for OGD + PEG, the presence of OGD oligo-guanidyl moieties and traces of endotoxin on the surface might also attract specific serum components, as we discussed earlier [15]. Thirdly and most interestingly, the plain OGD liposomes induce the formation of a thicker (9.6–16.4 nm) and denser (1.41121–1.44627) hard corona layer as a result of interaction with serum components compared to the other liposome samples. This is in line with the results of Walczyk et al. [13], who presented a range of 11–12 nm for "protein shell thickness" prior to extensive washing and around 10.5 nm after washing using differential centrifugal sedimentation of polystyrene model nanoparticles incubated for up to 6 h with diluted plasma.

C3b interaction with immobilized OGD and OGD + PEG liposomes Using MP-SPR, we determined the affinity and surface density mass of the opsonin C3b on the OGD and OGD + PEG liposome surfaces. This was done in order to gain insight whether the observed differences in the serum interaction studies could be explained at least in part by immunogenic properties of the nanocarriers—the increased tendency to recruit opsonins from the serum and, possibly, activate the complement system. C3b is a 180-kDa fragment that results from the cleavage of anaphylatoxin C3a from complement component C3 [21, 24]. C3b is able to covalently bind to amino or hydroxyl groups on artificial surfaces through its exposed thioester [21, 24]. After immobilization of OGD or OGD + PEG liposomes to sensor surfaces in parallel channels, a series of C3b concentrations was injected into both channels: 0.00833, 0.0833, and 0.833 mol. As shown in Fig. 7, a clearly larger stepwise SPR response signal is achieved in terms of C3b interacting with OGD surface without PEG (**a**) in comparison to OGD liposome surface with PEG (**b**). The calculated results for deposited C3b surface mass densities were Γ(total) ~410–680 ng/cm^2 for OGD liposomes without PEG, and Γ(total) ~120–200 ng/cm^2 for OGD liposomes with PEG. These results are consistent with the findings of the serum interaction measurements. The calculated equilibrium dissociation constants for C3b match up reasonably well between the different liposome interaction schemes: for C3b interacting with OGD and OGD + PEG, $K_{D,OGD} = 3.8 \times 10^{-8}$ M and $K_{D,OGD+PEG} = 7.2 \times 10^{-8}$ M were obtained, respectively. To the best of our knowledge, this is the first time the C3b affinities have been determined on biomaterial surfaces and on intact surface-immobilized liposomes.

Based on these results, we demonstrate a connection between the tendency of the surface to adsorb serum components and a preference of C3b for the surface. Hence, the observed differences in interaction experiments of OGD liposomes with undiluted serum, as discussed above, may be in relation to complement system activation. In particular, the observed significant difference in the hard corona composition formed onto the OGD liposome layer without PEG may report that the OGD liposomes without PEG are capable of inducing more drastic opsonisation-related responses than the OGD liposomes with PEG. Unfortunately, since the OGD liposomes (but not the PEG added to functionalize these liposomes in situ to form OGD + PEG) used were shown to contain traces of endotoxins, it is not possible to reliably link increased opsonisation to PEG conformation or liposome properties at this stage. However, these observations merit further studies using other complement trigger molecules, as well as assays to confirm complement activation taking place

at the surface, such as using antibodies specific to C3b degradation products such as C3c [25].

In summary, we have demonstrated a convenient way to bind clinically relevant samples of nanocarriers to sensor surfaces and to study their interactions with full serum. Our focus was on intact liposomes that we modified with hydrophilic coating molecules before and after immobilization to sensor, which has not been reported previously. This method can be applied with relative ease to assess the effect of different surface modifications on unspecific protein binding with different types of nanocarriers. The main limitation in the present work was the use of serum instead of plasma; for instance, fibrinogen that is not present in the serum is known to bind to PEG-coated liposomes [12]. This is explained in part by our interest in the complement activating properties of surface-immobilized liposomes, which cannot be studied in EDTA-anticoagulated plasma. We demonstrated that undiluted serum can be successfully used in the interaction studies, but we suggest that any blood product without cells—such as plasma or serum that has been depleted of some component or associated to a certain disease state—is equally suited for this experimental setup. In regard to the safety of nanocarriers, the possibility to link the production of secondary inflammatory mediators to surface events would provide complementary evidence of the immunogenic properties of nanocarriers. Even though it is difficult to replicate the in vivo conditions in blood circulation in vitro, the dynamic flow and temperature-controlled conditions improve the in vivo relevance of the presented method. Using MP-SPR and layer-by-layer modeling, we were able to separately identify distinct soft and hard coronas. The possibility to identify and elute these biomolecular layers from the surface of nanocarriers might provide interesting opportunities: for example, coupling MP-SPR technology to other analysis instruments such as LC-MS could permit dissecting subclasses of the protein corona, and producing snapshots of the protein corona at different times [16, 17, 20].

Conclusions

In this study, we have developed a flexible, highly modifiable, and sensitive one-instrument MP-SPR technology platform that can be used for interaction studies using undiluted serum with nanocarriers in controlled dynamic settings. We explored its essential capabilities with four different liposomes and conclude that MP-SPR is suitable for optical characterization of the formation and evolution of protein coronas on nanocarrier surfaces. Our reproducible measurements clearly demonstrated the formation of a distinct soft corona. In addition, we were able to determine binding affinity (K_D) for an essential opsonin, C3b, directly on a biomaterial surface. Therefore, the described label-free platform provides a powerful preclinical tool for tuning nanocarrier surface architecture and composition to control protein corona formation.

Acknowledgments We are grateful to M.Sc. Tatu Lajunen, B.Sc. Riikka Nurmi, and M.Sc. Antti Louna for the help in preparing and characterizing the control liposome formulations, and to Leena Pietilä and Dr. Mari Palviainen for the help with serum collection and pooling. Liposomes coated with a lipidated oligo-guanidyl derivative were kindly supplied by Professor Stefano Salmaso, University of Padova. Financial support by the Academy of Finland (grants: #137053, #263861, #263567), Tekes—the Finnish Funding Agency for Innovation EV-Extra-Tox project and the Professor Pool—Orion Research Foundation are gratefully acknowledged.

Compliance with ethical standards All the reported experiments are in compliance with current Finnish law.

Conflict of interest The authors declare that they have no conflicts of interest. T.R. is affiliated with BioNavis Ltd., Ylöjärvi, Finland.

References

1. Shi J, Votruba AR, Farokhzad OC, Langer R. Nanotechnology in drug delivery and tissue engineering: from discovery to applications. Nano Lett. 2010;10:3223–30.
2. Nyström AM, Fadeel B. Safety assessment of nanomaterials: implications for nanomedicine. J Control Release. 2012;161:403–8.
3. Bertrand N, Leroux J-C. The journey of a drug-carrier in the body: an anatomo-physiological perspective. J Control Release. 2012;161:152–63.
4. Knop K, Hoogenboom R, Fischer D, Schubert US. Poly(ethylene glycol) in drug delivery: pros and cons as well as potential alternatives. Angew Chemie - Int Ed. 2010;49:6288–308.
5. Hamad I, Al-hanbali ŔO, Hunter AC, Rutt KJ, Andresen TL, Moghimi SM. Switching of complement activation pathways at the Nanosphere serum Interface : implications for stealth nanoparticle engineering. ACS Nano. 2010;4:6629–38.
6. Arima Y, Toda M, Iwata H. Complement activation on surfaces modified with ethylene glycol units. Biomaterials. 2008;29:551–60.
7. Salmaso S, Caliceti P. Stealth properties to improve therapeutic efficacy of drug nanocarriers. J Drug Deliv. 2013;2013:1–19.
8. Mahon E, Salvati A, Baldelli Bombelli F, Lynch I, Dawson KA. Designing the nanoparticle–biomolecule interface for "targeting and therapeutic delivery.". J Control Release. Elsevier B.V2012;161:164–74.
9. Szebeni J, Muggia F, Gabizon A, Barenholz Y. Activation of complement by therapeutic liposomes and other lipid excipient-based therapeutic products: prediction and prevention. Adv Drug Deliv Rev. Elsevier B.V2011;63:1020–30.
10. Chanan-Khan A. Complement activation following first exposure to pegylated liposomal doxorubicin (Doxil(R)): possible role in hypersensitivity reactions. Ann Oncol. 2003;14:1430–7.
11. Lynch I, Cedervall T, Lundqvist M, Cabaleiro-Lago C, Linse S, Dawson KA. The nanoparticle-protein complex as a biological entity; a complex fluids and surface science challenge for the twenty-first century. Adv Colloid Interf Sci. 2007;134-135:167–74.
12. Palchetti S, Colapicchioni V, Digiacomo L, Caracciolo G, Pozzi D, Capriotti AL, et al. The protein corona of circulating PEGylated liposomes. Biochim Biophys Acta - Biomembr. Elsevier B.V2016;1858:189–96.
13. Walczyk D, Bombelli FB, Monopoli MP, Lynch I. Dawson K a. What the cell "sees" in bionanoscience. J AmChem Soc. 2010;132:5761–8.

14. Cedervall T, Lynch I, Lindman S, Berggård T, Thulin E, Nilsson H, et al. Understanding the nanoparticle-protein corona using methods to quantify exchange rates and affinities of proteins for nanoparticles. Proc Natl Acad Sci U S A. 2007;104:2050–5.
15. Corbo C, Molinaro R, Parodi A, Furman NET, Salvatore F, Tasciotti E. The impact of nanoparticle protein corona on cytotoxicity, immunotoxicity and target drug delivery. Nanomedicine. 2016;11: 81–100.
16. Docter D, Westmeier D, Markiewicz M, Stolte S, Knauer SK, Stauber RH. The nanoparticle biomolecule corona: lessons learned—challenge accepted? Chem Soc Rev Royal Society of Chemistry. 2015;44:6094–121.
17. Tenzer S, Docter D, Kuharev J, Musyanovych A, Fetz V, Hecht R, et al. Rapid formation of plasma protein corona critically affects nanoparticle pathophysiology. Nat Nanotechnol. 2013;8:772–81.
18. Lundqvist M, Stigler J, Elia G, Lynch I, Cedervall T, Dawson KA. Nanoparticle size and surface properties determine the protein corona with possible implications for biological impacts. Proc Natl Acad Sci U S A. 2008;105:14265–70.
19. Lundqvist M. Nanoparticles: tracking protein corona over time. Nat Publ Gr. 2013;8:1–2.
20. Monopoli MP, Åberg C, Salvati A, Dawson KA, Åberg C, Salvati A, et al. Biomolecular coronas provide the biological identity of nanosized materials. Nat Nanotechnol. Nature Publishing Group2012;7:779–86.
21. Carroll MV, Sim RB. Complement in health and disease. Adv Drug Deliv Rev. 2011;1–11. Elsevier B.V.
22. Pangburn MK, Schreiber RD, Müller-Eberhard HJ. C3b deposition during activation of the alternative complement pathway and the effect of deposition on the activating surface. J Immunol. 1983;131:1930–5.
23. Andersson J, Ekdahl KN, Lambris JD, Nilsson B. Binding of C3 fragments on top of adsorbed plasma proteins during complement activation on a model biomaterial surface. Biomaterials. 2005;26: 1477–85.
24. Nilsson B, Ekdahl KN, Mollnes TE, Lambris JD. The role of complement in biomaterial-induced inflammation. Mol Immunol. 2007;44: 82–94.
25. Arima Y, Toda M, Iwata H. Surface plasmon resonance in monitoring of complement activation on biomaterials. Adv Drug Deliv Rev. Elsevier B.V2011;63:988–99.
26. Granqvist N, Yliperttula M, Välimäki S, Pulkkinen P, Tenhu H, Viitala T. Control of the morphology of lipid layers by substrate surface chemistry. Langmuir. 2014;30:2799–809.
27. Kretschmann E. Determination of optical constants of metals by excitation of surface plasmons. Zeitschrift Fur Phys. 1971;241:313–24.
28. Granqvist N, Liang H, Laurila T, Sadowski J, Yliperttula M, Viitala T. Characterizing ultrathin and thick organic layers by surface plasmon resonance three-wavelength and waveguide mode analysis. Langmuir. 2013;29:8561–71.
29. Bakhtiar R. Surface plasmon resonance spectroscopy: a versatile technique in a biochemist ' s toolbox. 2013.
30. Albers WM, Vikholm-lundin I. Surface plasmon resonance on nanoscale organic films. 1988;83–125.
31. Liang H, Miranto H, Granqvist N, Sadowski JW, Viitala T, Wang B, et al. Surface plasmon resonance instrument as a refractometer for liquids and ultrathin films. Sensors Actuators B Chem. Elsevier B.V2010;149:212–20.
32. Abraham SA, Waterhouse DN, Mayer LD, Cullis PR, Madden TD, Bally MB. The liposomal formulation of doxorubicin. Methods Enzymol. 2005;391:71–97.
33. Bersani S, Salmaso S, Mastrotto F, Ravazzolo E, Semenzato A, Caliceti P. Star-like oligo-arginyl-maltotriosyl derivatives as novel cell-penetrating enhancers for the intracellular delivery of colloidal therapeutic systems. Bioconjug Chem. 2012;23:1415–25.
34. Löfås S, Johnsson B. A novel hydrogel matrix on gold surfaces in surface plasmon resonance sensors for fast and efficient covalent immobilization of ligands. J Chem Soc Chem Commun. 1990;1526.
35. Peterlinz KA, Georgiadis R. Two-color approach for determination of thickness and dielectric constant of thin films using surface plasmon resonance spectroscopy. Opt Commun North-Holland. 1996;130:260–6.
36. Grassi JH, Georgiadis RM. Temperature-dependent refractive index determination from critical angle measurements: implications for quantitative SPR sensing. Am Chem Soc. 1999.
37. Zhou M, Otomo A, Yokoyama S, Mashiko S. Estimation of organic molecular film structures using surface–plasmon resonance spectroscopy. Thin Solid Films. 2001;393:114–8.
38. Viitala T, Granqvist N, Hallila S, Raviña M, Yliperttula M. Elucidating the signal responses of multi-parametric surface plasmon resonance living cell sensing: a comparison between optical modeling and drug-MDCKII cell interaction measurements. PLoS One. Public Library of Science2013;8:e72192.
39. Granqvist N, Hanning A, Eng L, Tuppurainen J, Viitala T. Label-enhanced surface plasmon resonance: a new concept for improved performance in optical biosensor analysis. Sensors (Basel). Multidisciplinary Digital Publishing Institute (MDPI)2013;13: 15348–63.
40. Karlsson R, Fält A. Experimental design for kinetic analysis of protein-protein interactions with surface plasmon resonance biosensors. J Immunol Methods. 1997;200:121–33.
41. Zhao H, Brown PH, Schuck P. On the distribution of protein refractive index increments. Biophys J Biophysical Society. 2011;100:2309–17.
42. Ball V, Ramsden JJ. Buffer dependence of refractive index increments of protein solutions. Biopolymers. 1998;46:489–92.
43. Sadowski JW, Korhonen IKJ, Peltonen JPK. Characterization of thin films and their structures in surface plasmon resonance measurements. Opt Eng. 1995;34:2581–6.
44. Kretschmann E, Raether H. Radiative decay of non-radiative surface plasmons excited by light. Z Naturforsch. 1968;23:2135–6.
45. Hall D. Kinetic models describing biomolecular interactions at surfaces. Handb Surf Plasmon Reson. 2008;81–122.
46. Hamad I, Hunter AC, Szebeni J, Moghimi SM. Poly(ethylene glycol)s generate complement activation products in human serum through increased alternative pathway turnover and a MASP-2-dependent process. Mol Immunol. 2008;46:225–32.
47. Gref R, Lück M, Quellec P, Marchand M, Dellacherie E, Harnisch S, et al. "Stealth" corona-core nanoparticles surface modified by polyethylene glycol (PEG): influences of the corona (PEG chain length and surface density) and of the core composition on phagocytic uptake and plasma protein adsorption. Colloids Surfaces B Biointerfaces. 2000;18:301–13.
48. Lundquist A, Hansen SB, Nordström H, Danielson UH, Edwards K. Biotinylated lipid bilayer disks as model membranes for biosensor analyses. Anal Biochem. Elsevier Inc.2010;405:153–9.
49. Nel AE, Mädler L, Velegol D, Xia T, Hoek EMV, Somasundaran P, et al. Understanding biophysicochemical interactions at the nano-bio interface. Nat Mater Nature Publishing Group. 2009;8: 543–57.

Supplementary Material for Revised Manuscript:

Multi-Parametric Surface Plasmon Resonance Platform for Studying Liposome-Serum Interactions and Protein Corona Formation

Otto K. Kari (equal contribution), Tatu Rojalin (equal contribution), Stefano Salmaso, Michela Barattin, Hanna Jarva, Seppo Meri, Marjo Yliperttula, Tapani Viitala (corresponding author), Arto Urtti

Table S1. Physicochemical characterization and endotoxin determination results for DOX, DOX+PEG, OGD and OGD+PEG liposomes. Results are presented as average (± standard deviation) for hydrodynamic diameter and ζ-potential. Results for endotoxins are reported in EU/ml and described as positive (+) and negative (-) based on two complementary assays.

	Hydrodynamic diameter	Polydispersity index	ζ-potential	Endotoxin
DOX	98.12 ± 14.80 nm	0.324	-1.42 ± 0.16 mV	<0.1 EU/ml (-)
DOX +PEG	105.07 ± 2.64 nm	0.017	-1.90 ± 0.17 mV	<0.1 EU/ml (-)
OGD	227.03 ± 19.28 nm	0.254	+20.10 ± 0.40 mV	>1.0 EU/ml (+)
OGD +PEG	248.43 ± 30.40 nm	0.328	-1.84 ± 0.41 mV	>1.0 EU/ml (+)[a]

[a] OGD+PEG liposome tested after the charge-to-charge association process tested positive for endotoxin, but the polyanionic-PEG block-copolymer solution alone contained <0.1 EU/ml of endotoxin.

Table S2. The compiled modeling results of separate experiments for OGD and OGD+PEG liposomes and serum interactions. The calculated values are low and high limits for layer thickness (*d*) with corresponding refractive index (*n*) values from all three independent measurements and their average (± standard deviation). Refractive indices extracted during fitting procedure: serum 1.34960, buffer 1.33535.

		(I) Liposome		(II) Soft corona		(III) Hard corona	
OGD		**Low**	**High**	**Low**	**High**	**Low**	**High**
	1	39.97	51.08	32.7	94.28	9.73	16.0
	2	31.31	42.15	33.37	97.72	10.5	17.45
	3	49.88	73.27	36.61	126.05	8.59	15.79
	d	40.3867 ± 9.29201	55.5 ± 16.0239	34.2267 ± 2.09104	106.017 ± 17.4344	9.60667 ± 0.96095	16.4133 ± 0.9039
	1	39.97	1.35166	1.40034	1.37681	1.44632	1.41075
	2	31.31	1.34876	1.40279	1.37927	1.45346	1.41491
	3	49.88	1.34947	1.38789	1.37619	1.43904	1.40797
	n	1.35302 ± 0.0021	1.34996 ± 0.00151	1.39701 ± 0.00799	1.37742 ± 0.00163	1.44627 ± 0.0072	1.41121 ± 0.0035
OGD+PEG		**Low**	**High**	**Low**	**High**	**Low**	**High**
	1	48.0	61.94	22.63	54.75	3.2	4.99
	2	45.44	68.51	36.53	124.19	7.73	15.99
	3	39.72	52.35	7.5	10.64	2.99	4.8
	d	44.3867 ± 4.23931	60.9333 ±8.1269	22.22 ± 14.5193	63.1933 ± 57.2439	4.64 ± 2.67808	8.6 ± 6.4

	1	1.35643	1.35295	1.38403	1.37284	1.3802	1.36849
	2	1.35987	1.35461	1.39426	1.38047	1.43979	1.40062
	3	1.35406	1.35034	1.35963	1.38709	1.36573	1.35681
	n	1.35679 ± 0.00292	1.35263 ± 0.00215	1.37931 ± 0.01779	1.38013 ± 0.00713	1.39524 ± 0.03925	1.37531 ± 0.02269

Table S3. The compiled modeling results of separate experiments for DOX and DOX+PEG liposomes and serum interactions. The calculated values are low and high limits for layer thickness (*d*) with corresponding refractive index (*n*) values from all three independent measurements and their average (± standard deviation). Refractive indices extracted during fitting procedure: serum 1.34960, buffer 1.33535.

		(I) Liposome		**(II) Soft corona**		**(III) Hard corona**	
DOX		**Low**	**High**	**Low**	**High**	**Low**	**High**
	1	104.01	161.5	39.48	88.5	3.85	7.45
	2	93.98	145.02	36.32	105.39	1.98	4.39
	3	99.16	153.05	36.63	66.41	4.26	7.81
	d	99.05 ± 5.015905	153.19 ± 8.240892	37.47667 ± 1.741848	86.76667 ± 19.54772	3.363333 ± 1.215415	6.55 ± 1.879255
	1	1.36309	1.35754	1.42127	1.4351	1.39668	1.39222
	2	1.36128	1.35579	1.42137	1.40966	1.39603	1.37973
	3	1.36275	1.35706	1.41862	1.44315	1.39048	1.38648
	n	1.362373 ± 0.000962	1.356797 ± 0.0009	1.41742 ± 0.00457	1.429303 ± 0.017481	1.39440 ± 0.00341	1.38614 ± 0.00625
DOX+PEG		**Low**	**High**	**Low**	**High**	**Low**	**High**
	1	40.8	50.64	20.27	51.26	6.65	12.17
	2	31.98	45.78	27.62	48.07	8.25	13.57
	3	39.2	50.87	29.36	80.68	7.96	13.36
	d	37.3267 ± 4.69895	49.0967 ± 2.87462	25.75 ± 4.8249	60.0033 ± 17.9774	7.62 ± 0.85247	13.0333 ± 0.75501
	1	1.34788	1.34742	1.40478	1.38021	1.41521	1.38219
	2	1.35118	1.34706	1.39126	1.37628	1.42977	1.39814
	3	1.35008	1.34719	1.39528	1.3754	1.42562	1.39527
	n	1.34971 ± 0.00168	1.34722 ± 0.00018	1.39711 ± 0.00694	1.37730 ± 0.00256	1.42353 ± 0.0075	1.39187 ± 0.0085

Supplementary Material for Revised Manuscript:

Multi-Parametric Surface Plasmon Resonance Platform for Studying Liposome-Serum Interactions and Protein Corona Formation

Otto K. Kari (equal contribution), Tatu Rojalin (equal contribution), Stefano Salmaso, Michela Barattin, Hanna Jarva, Seppo Meri, Marjo Yliperttula, Tapani Viitala (corresponding author), Arto Urtti

15 GENERAL DISCUSSION AND FUTURE OUTLOOK

15.1 RAMAN SPECTROSCOPY OFFERS OPPORTUNITIES FOR CREATIVE SOLUTIONS IN BIOPHARMACEUTICS

Due to its high specificity for vibrational modes of various chemical bonds, Raman spectroscopy is a practical tool for characterization of new NMEs or for monitoring the solid state behavior of drugs – for instance in the pharmaceutical research and development [277, 278]. Major obstacles in the widespread use of Raman spectroscopy have been the weak Raman scattering signals and strong photoluminescence signals swamping the Raman lines in spectra [265, 279]. In order to overcome these limitations, a number of technical and spectral post-processing improvements have been introduced with the intention to separate the photoluminescence, and recover the Raman signal [280, 282, 339]. In particular, the realization of the benefits of a streak camera, i.e. an intensified charge-coupled device (ICCD), and an optical Kerr gate brought about significant advancements to the problem [340, 341]. Those techniques are called time-resolved methods, and are based on the idea of exploiting the time difference between photoluminescence and Raman phenomena. Hence, the "slow" photoluminescence and "fast" Raman signals can be distinguished by using a sequenced detecting technique whereby the almost instantaneously scattered Raman photons are mainly detected whereas most of the photoluminescence-originating photons are not detected. However, all of the aforementioned systems have suffered from inherent complexity, bulkiness, and/or cost – and the photoluminescence suppression was still inadequate. In these studies, a robust, compact, and affordable time-gated Raman spectrometer with <100 ps time resolution was used (I). Its advantages over the existing Raman instrumentation are based on a fast, picosecond pulsed 532 nm laser excitation coupled with a fast and sensitive complementary metal-oxide semiconductor single-photon avalanche diode (CMOS SPAD) detector. In the time-gated instrument, the time-resolved detection is carried out by synchronizing the detector and pulsed laser excitation. While detecting during a narrow time window, the 128 × 8 CMOS SPAD matrix detector accumulates single-photon events in an internal time histogram consisting of bins. That allows for efficient separation of Raman and photoluminescence signals. From the technical standpoint, the CMOS SPAD detector does not require excessive cooling unlike conventional scientific charge-coupled device (CCD) detectors, and the used laser technology is compact.

Raman is a prominent technology for analysis in life sciences, including biomedical and pharmaceutical settings offering detailed chemical information on the samples. In the best sequence of events, such analysis can be performed label-free, without

labor intensive sample preparation steps. However, as with many other Raman-based applications, the disadvantage is the strong photoluminescence background signals. The features of the new instrument gave rise to a question whether the favorable properties of the time-gated system could be effectively used for such analysis. Hence, four different pharmaceutical compounds – of which some were highly photoluminescent – were investigated with the new system (I). In comparison with continuous wave (CW) 532 nm and 785 nm Raman instruments, unparalleled improvement was accomplished by demonstrating effective photoluminescence suppression and capability to record highly accurate Raman spectra. Additionally, time-resolved fluorescence spectra can be acquired by the sequential sampling of the fluorescence emission at various temporal phases. This opens a new window to Raman spectroscopy; time-resolved fluorescence information can be collected to monitor e.g. molecular interactions while molecular structures are revealed by the Raman emission. The findings indicate that the new Raman spectrometer could be used in several applications in the field of life sciences. For instance, phase transition processes in the pharmaceutical industry or cellular nanoparticle uptake studies in the biomedical settings.

The results encouraged for envisaging whether the new Raman technology could be also exploited for nanomedical investigations such as EVs. Indeed, a couple of favorable properties stand out. First, the Raman phenomenon is an inelastic scattering process occurring at all excitation wavelengths (λ_E), and the intensity of Raman scattering is approximately proportional to ($1/ \lambda^4_E$). Hence, the shorter excitation wavelengths give rise to stronger Raman signal intensities. On the other hand, surface enhanced Raman spectroscopy (SERS) is known to amplify the weak Raman signals by orders of magnitude [342]. The physics of enhancement is based on triggering localized surface plasmons on the irregular or patterned noble metallic surfaces, e.g. gold or silver. Different shaped and sized metal substrates or metal nanocolloids have been used for Raman signal enhancement [342-344]. Taken all these into account, (i) relatively high Raman scattering could be accomplished with the 532 nm excitation wavelength, (ii) effective photoluminescence suppression could be achieved, and (iii) the use of SERS could improve further the acquired Raman signal. Thereby the time-gated system could provide a prospective tool for EV characterization.

In order to take an initial step towards Raman-based EV characterization, another type of Raman instrument was employed; the Laser Tweezers Raman Spectroscopy (LTRS) (III). An ambitious goal was set to characterize a broad number of different EV types on a *single-vesicle* basis. The underlying motivation was to circumvent the limitations of measuring a pool of or clusters of vesicles [300]. In general, the downside of measuring several particles simultaneously is that it provides an average over a multimodal sample having different subpopulations [345, 346]. Thus, it can potentially underestimate the roles of subpopulations. The same applies to

EV samples that typically embody distributions in characteristics such as vesicle size or overall biochemical content. For the first time, single EVs originating from non-cancerous (2 different) and cancerous (5 different) cell lines were investigated (III) with the aim of distinguishing them on the basis of their biochemical contents. By visual inspection, the collected Raman data was not easily sorted out. Therefore advanced data analysis methods, PCA and hierarchical clustering analysis were employed, and the analysis was complemented with rigorous and established EV characterization methods; electron microscopy, western blotting, NTA, and ζ-potential measurements. The observed differences between different types of EVs were evidently related to their membrane contents. To peel off the membrane protein segments outside of one type of cancerous vesicles, LNCaP, a trypsin treatment was carried out. This in turn further facilitated the data interpretation generated by the multivariate analysis. Eventually significant variation in the biochemical content between different EV types was observed. The spectral differences led to grouping of EVs into 4 major subpopulations of vesicles by hierarchical clustering analysis. The subpopulations were not due to different cell origin. Instead, several cell lines had EVs in several subpopulations. Additionally, all subpopulations had EVs from multiple cell lines. In essence, some subgroups of exosomes were preferred by some cell lines versus the others. This indicated that each subpopulation of EV may play a particular functional role that is common across certain cell lines. The perceived chemical differences were primarily due to variation in cholesterol, phospholipid, and protein content of the membranes of EVs.

15.2 THE POTENTIAL OF MULTI-PARAMETRIC SPR FOR THE BIOPHARMACEUTICAL FIELD

SPR has gained a strong foothold in the life sciences – including the biopharmaceutical field. It is a feasible technique for a broad range of affinity studies and interaction kinetics evaluations [50, 105, 163, 315, 316, 320, 347]. Although a versatile technology, more could be accomplished with regard to the applications. New inventions are continuously needed to develop *in vitro* assays that would provide not only statistically orchestrated data but also biologically relevant results. In this Thesis such assays are called *bio-functional assays*. In the context of SPR it means designing methodologies that can provide – in addition to the conventional parameters that are expected from SPR measurements, i.e. affinities, association and dissociation constants – simultaneously data and perceptions that have not been traditionally available when using SPR. In an ideal situation, the methodologies can be brought into general use for a group of assays that deal with similar types of physicochemical scenarios. Examples of this orientation are highlighted in the next chapters where the studies (II and IV) are described; the emphasis is to introduce

methodologies that could be implemented in the future to a broad range of studies having potentially similar dilemmas. In order to develop such assays, essentially some instrument-related novelties are needed with sophisticated data analysis and a flicker of courage to analyze the acquired data thoroughly. The technical advances can be achieved with the use of a next-generation MP-SPR technology. The MP-SPR enables scanning and recording the full angular SPR spectra over a broad range of incident light angles, and measurements can be performed with multiple excitation wavelengths. These features allow for obtaining more data than with the conventional SPR instruments. Thus, by implementing biophysical modeling in the data analysis phase, for example the thin films adsorbed onto the sensor surface can be analyzed. Consequently, new opportunities are opened as the assays can be designed with these new standpoints in mind. The studies (II and IV) highlight some of the opportunities found and developed for the analysis of small drug molecules and liposomes.

Alzheimer's disease (AD) is a difficult neurodegenerative disease affecting millions of people worldwide. Approximations state that the incidence of AD only in the US may triple by 2050 [348]. The disruptions in biochemical pathways of amyloid peptide (Aβ) have been recognized as the principal factors in the pathophysiology of AD [239]. Although adequate models for the pathophysiology of AD have been identified, the complex nature of the pathogenesis hinders the development of drug preparations against it [322, 323, 349]. A novel molecule, spin-labeled fluorene (SLF), has been previously developed, and its capability to block Aβ toxicity and oligomer growth has been demonstrated [350, 351]. However, the oligomeric Aβs express highly dynamic nature [352], which encumbers the endeavors to obtain fundamental mechanistic insights of small molecule modulators of Aβ toxicity and aggregation. In order to address these challenges, a *bio-functional* label-free assay platform was developed to mimic the Aβ self-assembly and aggregation at the vicinity of the sensor surface (II). Two distinctive aims were set; (i) to measure the SLF binding affinities to different states of the Aβ peptide, including a virtually monomeric Aβ peptide scheme and a scenario where further oligomerized Aβ peptides were employed. Additionally, the intention was to (ii) demonstrate, how the Aβ self-assembly and aggregation can be interfered by the SLF. By utilizing the technical advances provided by the MP-SPR instrument and molecular layer characterization in the data analysis, we were able to model and calculate the interaction kinetics for the SLF in 4 different biomimetic situations (II). The calculations suggested for strong Aβ binding of SLF, and existence of 2 binding sites for SLF in the structures of Aβ peptides. The aggregating Aβ layer was demonstrated to build ~ 30 times thinner in the scenario where the SLF was present compared with the events where the Aβ peptides were let to interact and aggregate freely without the disrupting effect of the SLF. The data analysis and conclusions were coherent with the results obtained by the complementary methods;

DLS, molecular docking and molecular dynamics simulations. These findings could be expanded further to probe for similar diseases manifesting pathogenic behavior where protein aggregation plays a role. Such pathogenic phenomena could be mimicked accordingly to develop and optimize therapeutic agents against them; a descriptive example is the plaque formation in cardiovascular diseases.

As a continuation to the small drug analytics, DDCs, in particular liposomal nanocarriers, were taken under investigation. As of today, liposomal drug delivery systems (LDSs) are the only FDA approved nanocarriers for human medication. Upon nanocarrier entering the blood circulation, the most essential question is how it interacts with the complex biochemical surroundings formed by the proteins, peptides and cellular apparatus found in biological fluids. A formation of a layer known as the protein corona is of utmost importance when evaluating the ultimate properties of the nanocarriers and their pathophysiological effects [329, 353-357]. The structure of the protein corona can be highly dynamic and complex. Furthermore, it can vary between nanoparticles having the same composition but different surface chemistries and size in the same solution. An array of technologies has been employed to examine the corona, including mass spectrometry [358], DLS and differential centrifugal sedimentation [329, 359], circular dichroism [360], and fluorescence quenching [361]. Isothermal calorimetry and SPR have been used to measure the affinities of protein coronas [362]. Additionally, the zeta potential is a frequently used value to characterize the coronas [354, 356]. In general, when nanoparticles are introduced to biological fluids such as serum, the protein corona is generated in a series of layers called the "soft" and "hard" corona [359, 363]. The composition of a protein corona can be defined by 5 distinct components: thickness and density, identity and quantity, orientation, conformation and affinities [364]. Regardless the rather rigorous approval requisites for LDSs with regard to *in vivo* usage, severe hypersensitivity reactions to existing LDSs have been reported in clinical use [332, 365, 366]. The prevailing consensus is to use PEGylation as the primary shielding agent for LDSs in order to enhance their bioavailability but it has been demonstrated to pose occasional problems as well [143, 144]. The biological significance of the liposome-serum interactions and particularly the protein corona formation has provoked a need for new and complementing label-free *bio-functional in vitro* assays to probe the interactions and corona characteristics at the early stages of LDS development. A deeper motivation for performing such studies is to develop generalized methodology for designing safe and effective LDSs.

Physicochemical interactions at the nano-bio interface between LDSs and serum components were probed by using 4 different model liposomes immobilized onto the SPR sensor surface, one liposome type at a time (IV). The goal was to characterize the hypothesized "soft" and "hard" protein corona formation when the serum components – particularly immune system – was responding to the presence of the model liposomes. Since the interactions in real biological environment take

place in dynamic flow conditions, such conditions were established in order to accomplish resemblance with the natural biological milieu of administered LDSs. An important complement system peptide C3b was chosen for the purpose of collecting experimental proof that the observed phenomena could be related to immune responses. The "soft" and "hard" protein corona thicknesses (d) and refractive indices (n) were calculated on the basis of the acquired MP-SPR data using biophysical modeling for each liposome type (IV). The physicochemical characterization of liposomes was performed by the NTA, zeta potential measurements, and endotoxin detection. Interestingly, clearly distinguishable "soft" protein corona and "hard" protein corona phases were observed during the interactions, and the thicknesses and refractive indices of the coronas were quantitatively evaluated. The perceived differences in the protein corona compositions between various liposome types may be in relation to immune system activation induced by the different surface chemistries of the used model liposomes. The developed *bionanophotonic* platform is a versatile and sensitive tool to investigate nanocarrier surface chemistries and physicochemical events induced by the different nanocarrier compositions. It can provide an additional preclinical *in vitro* method for the purposes of rational and efficient design of DDCs.

An ultimate step in developing *bionanophotonic* methodologies for larger scale analytes would be to make a transition to EV analytics. By taking advantage of the previously learned lessons from the LTRS studies (II) and LDS investigations (IV), a comprehensive sequence of methods for the analysis of EVs could be developed. To date, all cells that have been tested, are known to secrete EVs, and their molecular compositions reflect their specific functions [367]. The tumor-associated EVs could act as biomarkers for cancer diagnostics [104, 337], or they could be harnessed as biomimetic DDCs [250, 251]. However, regardless the serious efforts the application of tumor-originating EVs as biomarkers is still difficult. The most pertinent problem appears the lack of compounds or other means that could provide *specific* targeting to EVs. In order to acquire valid and accurate data on the structures and interactions of EVs, a diverse scheme of biophysical measurements is often needed. The introduced Raman and MP-SPR techniques are both extremely sensitive, label-free optical measurement methods suitable for *bionanophotonic* studies of EVs.

As an example, the cancerous SKOV-3 ovarian tumor cells are known to express the $\alpha_3\beta_1$ integrin [368]. Thus based on the biogenesis of the EVs [369], it is exceedingly likely that the EVs derived from the SKOV-3 cells express the $\alpha_3\beta_1$ integrin on their membrane structures. A unique ligand capable of binding specifically to the $\alpha_3\beta_1$ integrin could be developed with the use of combinatorial chemistry, for example the one-bead, one-compound (OBOC) combinatorial library approach [370, 371]. By utilizing such targeting ligand a sequence of bulk and single EV measurements could be implemented. For instance, flow cytometry and MP-SPR as representatives of bulk techniques and LTRS as the single EV measurement method. In essence, a

biotinylated targeting ligand could be pre-immobilized onto the SPR sensor surface using the well-established biotin-avidin immobilization techniques. In the case of LTRS analysis, the ligand could be tagged with a highly Raman-active moiety (e.g. alkyne group or groups) in order to produce discernible Raman signal denoting of successful $\alpha_3\beta_1$ integrin-ligand binding. Furthermore, this scheme of various approaches could be complemented with the time-gated SERS measurements in bulk conditions. The time-gated Raman system would allow circumventing the conceivably interfering photoluminescence signals. The developed versatile scheme of measurements could be later applied to the measurements of EV compositions and interactions across a large number of different EV types. The findings could be applied for cancer diagnostics or development of biomimetic DDCs. Overall, these studies would further elucidate, how the EVs interact at various interfaces in their microenvironments, and valuable structural information on distinct EVs could be obtained.

15.3 CONCLUSIONS

In these studies, a new Raman technique was employed and its capabilities demonstrated (I). Innovative applications exploiting biophotonics were introduced (I-IV), and versatile data analysis methods were used to new applications in unconventional ways (I-IV). From the standpoint of the aims set for the studies, following conclusions can be made:

I The time-gated Raman technology accomplished effective *fluorescence suppression* in solid state small drug studies. An additional benefit in comparison with conventional Raman technology is achieved since time-resolved fluorescence information can be collected simultaneously with the Raman emission. The system holds potential for SERS and biopharmaceutical applications in general.

II A *bio-functional* MP-SPR *in vitro* assay platform was developed to investigate prospective small drug candidates against AD. The Aβ peptide aggregation and its prevention with a new molecule (SLF) was mimicked; computational simulations strengthened the perceptions made. Aβ peptide layer thickness and refractive index evaluations provided quantitative information on the peptide aggregation which has not been previously available within SPR studies.

III *Single extracellular vesicles* from 7 different cell lines were measured with LTRS technology, and Raman data analyzed by using multivariate data analysis methods. Observed variations were in relation to the biochemical compounds on the vesicle membranes, in particular cholesterol, phospholipid and protein contents. The data analysis revealed the existence of 4 vesicle subpopulations. However, the subgrouping was not due to different cell origin but potentially due to a particular functional role that is common across certain cell lines.

IV An *in vitro bionanophotonic* MP-SPR methodology was designed for liposomal DDC development. Interactions of 4 model liposomes with serum were examined in dynamic flow conditions. For the first time, the composition of distinct "soft" and "hard" protein corona onto the immobilized liposomes was quantitatively characterized with respect to thickness and refractive index. The variations in corona structures between liposomes may implicate that different liposomal surface chemistries induce the immune system activation divergently. These perceptions can assist in the development of safe and effective liposomal DDCs.

Taken together the results represented and discussed here, when complemented with conventional techniques and assays, Raman and MP-SPR are effective biophotonic tools for a range of applications in the biopharmaceutical research. In the future, these results and findings hold potential to be refined further in order to accomplish transformation into validated or widely-used methodologies.

16 REFERENCES

1. Nel, A.E., L. Mädler, D. Velegol, T. Xia, E.M. Hoek, P. Somasundaran, F. Klaessig, V. Castranova, and M. Thompson, *Understanding biophysicochemical interactions at the nano–bio interface*. Nature Materials, 2009. **8**(7): p. 543-557.

2. Wang, L.V. and H.-i. Wu, *Biomedical Optics: Principles and Imaging*. 2012: John Wiley & Sons.

3. Lee, G., K. Chu, L. Conroy, L. Fix, G. Lui, C. Truesdell, R. Dorf, D. Matthews, and J. Walter, *A Study of Biophotonics*. Optik & Photonik, 2007. **2**(2): p. 30-35.

4. Shcherbo, D., C.S. Murphy, G.V. Ermakova, E.A. Solovieva, T.V. Chepurnykh, A.S. Shcheglov, V.V. Verkhusha, V.Z. Pletnev, K.L. Hazelwood, and P.M. Roche, *Far-red fluorescent tags for protein imaging in living tissues*. Biochemical Journal, 2009. **418**(3): p. 567-574.

5. Cao, Y.C., R. Jin, J.-M. Nam, C.S. Thaxton, and C.A. Mirkin, *Raman dye-labeled nanoparticle probes for proteins*. Journal of the American Chemical Society, 2003. **125**(48): p. 14676-14677.

6. Inglese, J., R.L. Johnson, A. Simeonov, M. Xia, W. Zheng, C.P. Austin, and D.S. Auld, *High-throughput screening assays for the identification of chemical probes*. Nature Chemical Biology, 2007. **3**(8): p. 466-479.

7. Gao, F., J. Lei, and H. Ju, *Label-free surface-enhanced Raman spectroscopy for sensitive DNA detection by DNA-mediated silver nanoparticle growth*. Analytical Chemistry, 2013. **85**(24): p. 11788-93.

8. Han, X. and E.S. Boyden, *Multiple-color optical activation, silencing, and desynchronization of neural activity, with single-spike temporal resolution*. PLOS ONE, 2007. **2**(3): p. e299.

9. Lozier, R.H., R.A. Bogomolni, and W. Stoeckenius, *Bacteriorhodopsin: a light-driven proton pump in Halobacterium Halobium*. Biophysical Journal, 1975. **15**(9): p. 955.

10. Adronov, A. and J.M. Fréchet, *Light-harvesting dendrimers*. Chemical Communications, 2000(18): p. 1701-1710.

11. Huang, B., W. Wang, M. Bates, and X. Zhuang, *Three-dimensional super-resolution imaging by stochastic optical reconstruction microscopy*. Science, 2008. **319**(5864): p. 810-813.

12. Liedberg, B., I. Lundström, and E. Stenberg, *Principles of biosensing with an extended coupling matrix and surface plasmon resonance*. Sensors and Actuators B: Chemical, 1993. **11**(1): p. 63-72.

13. Deniz, A.A., S. Mukhopadhyay, and E.A. Lemke, *Single-molecule biophysics: at the interface of biology, physics and chemistry*. Journal of the Royal Society Interface, 2008. **5**(18): p. 15-45.

14. Kneipp, K., Y. Wang, H. Kneipp, L.T. Perelman, I. Itzkan, R.R. Dasari, and M.S. Feld, *Single molecule detection using surface-enhanced Raman scattering (SERS)*. Physical Review Letters, 1997. **78**(9): p. 1667.

15. Boyd, R.W., *Nonlinear Optics*. 2003: Academic press.

16. Coldren, L.A., S.W. Corzine, and M.L. Mashanovitch, *Diode Lasers and Photonic Integrated Circuits*. Vol. 218. 2012: John Wiley & Sons.

17. Korkin, A., S. Goodnick, and R. Nemanich, *Nanoscale Materials and Devices for Electronics, Photonics and Solar Energy*. 2015: Springer.

18. McNally, K., J. Dawes, A. Parker, A. Lauto, J. Piper, and E. Owen, *Laser-activated solid protein solder for nerve repair: In vitro studies of tensile strength and Solder/Tissue temperature*. Lasers in Medical Science, 1999. **14**(3): p. 228-237.

19. Abramczyk, H., B. Brozek-Pluska, J. Surmacki, J. Jablonska-Gajewicz, and R. Kordek, *Raman 'optical biopsy'of human breast cancer*. Progress in Biophysics and Molecular Biology, 2012. **108**(1): p. 74-81.

20. Jain, M., N. Narula, A. Aggarwal, B. Stiles, M.M. Shevchuk, J. Sterling, B. Salamoon, V. Chandel, W.W. Webb, and N.K. Altorki, *Multiphoton microscopy: a potential "optical biopsy" tool for real-time evaluation of lung tumors without the need for exogenous contrast agents*. Archives of Pathology and Laboratory Medicine, 2013. **138**(8): p. 1037-1047.

21. Nuxoll, E., *BioMEMS in drug delivery*. Advanced Drug Delivery Reviews, 2013. **65**(11): p. 1611-1625.

22. Rusciano, G., P. Capriglione, G. Pesce, P. Abete, V. Carnovale, and A. Sasso, *Raman spectroscopy as a new tool for early detection of bacteria in patients with cystic fibrosis*. Laser Physics Letters, 2013. **10**(7): p. 075603.

23. Duraipandian, S., W. Zheng, J. Ng, J.J. Low, A. Ilancheran, and Z. Huang, *Simultaneous fingerprint and high-wavenumber confocal Raman spectroscopy enhances early detection of cervical precancer in vivo*. Analytical Chemistry, 2012. **84**(14): p. 5913-5919.

24. Aaron, J., K. Travis, N. Harrison, and K. Sokolov, *Dynamic imaging of molecular assemblies in live cells based on nanoparticle plasmon resonance coupling*. Nano Letters, 2009. **9**(10): p. 3612-3618.

25. Oh, P., P. Borgström, H. Witkiewicz, Y. Li, B.J. Borgström, A. Chrastina, K. Iwata, K.R. Zinn, R. Baldwin, and J.E. Testa, *Live dynamic imaging of caveolae pumping targeted antibody rapidly and specifically across endothelium in the lung*. Nature Biotechnology, 2007. **25**(3): p. 327-337.

26. Shamah, S.M. and B.T. Cunningham, *Label-free cell-based assays using photonic crystal optical biosensors*. Analyst, 2011. **136**(6): p. 1090-1102.

27. Nel, A., T. Xia, L. Mädler, and N. Li, *Toxic potential of materials at the nanolevel*. Science, 2006. **311**(5761): p. 622-627.

28. Peppas, N.A. and R. Langer, *New challenges in biomaterials*. Science, 1994. **263**(5154): p. 1715-1719.

29. Wojtkowski, M., R. Leitgeb, A. Kowalczyk, T. Bajraszewski, and A.F. Fercher, *In vivo human retinal imaging by Fourier domain optical coherence tomography*. Journal of Biomedical Optics, 2002. **7**(3): p. 457-463.

30. Nassif, N., B. Cense, B.H. Park, S.H. Yun, T.C. Chen, B.E. Bouma, G.J. Tearney, and J.F. de Boer, *In vivo human retinal imaging by ultrahigh-speed spectral domain optical coherence tomography*. Optics Letters, 2004. **29**(5): p. 480-482.

31. Zhang, H.F., K. Maslov, G. Stoica, and L.V. Wang, *Functional photoacoustic microscopy for high-resolution and noninvasive in vivo imaging*. Nature Biotechnology, 2006. **24**(7): p. 848-851.

32. Wachsmann-Hogiu, S., T. Weeks, and T. Huser, *Chemical analysis in vivo and in vitro by Raman spectroscopy-from single cells to humans*. Current Opinion on Biotechnology, 2009. **20**(1): p. 63-73.

33. Schober, R., F. Ulrich, T. Sander, H. Durselen, and S. Hessel, *Laser-induced alteration of collagen substructure allows microsurgical tissue welding*. Science, 1986. **232**(4756): p. 1421-1422.

34. Yager, P., G.J. Domingo, and J. Gerdes, *Point-of-care diagnostics for global health*. Annual Review on Biomedical Engineering, 2008. **10**: p. 107-144.

35. Myers, F.B. and L.P. Lee, *Innovations in optical microfluidic technologies for point-of-care diagnostics*. Lab on a Chip, 2008. **8**(12): p. 2015-2031.

36. Cooper, M.A., *Optical biosensors in drug discovery*. Nature Reviews Drug Discovery, 2002. **1**(7): p. 515-528.

37. Rudin, M. and R. Weissleder, *Molecular imaging in drug discovery and development*. Nature Reviews Drug Discovery, 2003. **2**(2): p. 123-131.

38. Dittrich, P.S. and A. Manz, *Lab-on-a-chip: microfluidics in drug discovery*. Nature Reviews Drug Discovery, 2006. **5**(3): p. 210-218.

39. Fang, Y., *Label-free cell-based assays with optical biosensors in drug discovery*. Assay and Drug Development Technologies, 2006. **4**(5): p. 583-595.

40. Licha, K. and C. Olbrich, *Optical imaging in drug discovery and diagnostic applications*. Advanced Drug Delivery Reviews, 2005. **57**(8): p. 1087-1108.

41. Intes, X., J. Ripoll, Y. Chen, S. Nioka, A. Yodh, and B. Chance, *In vivo continuous-wave optical breast imaging enhanced with Indocyanine Green*. Medical Physics, 2003. **30**(6): p. 1039-1047.

42. Alacam, B., B. Yazici, X. Intes, and B. Chance, *Extended Kalman filtering for the modeling and analysis of ICG pharmacokinetics in cancerous tumors using NIR optical methods*. IEEE Transactions on Biomedical Engineering, 2006. **53**(10): p. 1861-1871.

43. König, K., A. Ehlers, F. Stracke, and I. Riemann, *In vivo drug screening in human skin using femtosecond laser multiphoton tomography*. Skin Pharmacology and Physiology, 2006. **19**(2): p. 78-88.

44. Workman, P., *How much gets there and what does it do? The need for better pharmacokinetic and pharmacodynamic endpoints in contemporary drug discovery and development*. Current Pharmaceutical Design, 2003. **9**(11): p. 891-902.

45. Kadurugamuwa, J.L., L.V. Sin, J. Yu, K.P. Francis, T.F. Purchio, and P.R. Contag, *Noninvasive optical imaging method to evaluate postantibiotic effects on biofilm infection in vivo*. Antimicrobial Agents and Chemotherapy, 2004. **48**(6): p. 2283-2287.

46. Hertzberg, R.P. and A.J. Pope, *High-throughput screening: new technology for the 21st century*. Current Opinion in Chemical Biology, 2000. **4**(4): p. 445-451.

47. Rathore, A., R. Bhambure, and V. Ghare, *Process analytical technology (PAT) for biopharmaceutical products*. Analytical and Bioanalytical Chemistry, 2010. **398**(1): p. 137-154.

48. Keiser, G., *Biophotonics: Concepts to Applications*. 2016: Springer.

49. Bugay, D.E., *Characterization of the solid-state: spectroscopic techniques*. Advanced Drug Delivery Reviews, 2001. **48**(1): p. 43-65.

50. Homola, J., *Surface plasmon resonance sensors for detection of chemical and biological species*. Chemical Reviews, 2008. **108**(2): p. 462-493.

51. Jepsen, P.U., D.G. Cooke, and M. Koch, *Terahertz spectroscopy and imaging–Modern techniques and applications*. Laser & Photonics Reviews, 2011. **5**(1): p. 124-166.

52. Ishikawa-Ankerhold, H.C., R. Ankerhold, and G.P. Drummen, *Advanced fluorescence microscopy techniques—Frap, Flip, Flap, Fret and Flim*. Molecules, 2012. **17**(4): p. 4047-4132.

53. Murphy, D.B., *Fundamentals of Light Microscopy and Electronic Imaging*. 2002: John Wiley & Sons.

54. Rust, M.J., M. Bates, and X. Zhuang, *Sub-diffraction-limit imaging by stochastic optical reconstruction microscopy (STORM)*. Nature Methods, 2006. **3**(10): p. 793-796.

55. Freudiger, C.W., W. Min, B.G. Saar, S. Lu, G.R. Holtom, C. He, J.C. Tsai, J.X. Kang, and X.S. Xie, *Label-free biomedical imaging with high sensitivity by stimulated Raman scattering microscopy*. Science, 2008. **322**(5909): p. 1857-1861.

56. Hell, S.W., *Microscopy and its focal switch*. Nature Methods, 2009. **6**(1): p. 24-32.

57. Gubala, V., L.F. Harris, A.J. Ricco, M.X. Tan, and D.E. Williams, *Point of care diagnostics: status and future*. Analytical Chemistry, 2011. **84**(2): p. 487-515.

58. Moan, J. and Q. Peng, *An outline of the hundred-year history of PDT*. Anticancer Research, 2002. **23**(5A): p. 3591-3600.

59. Hawkins, D., N. Houreld, and H. Abrahamse, *Low level laser therapy (LLLT) as an effective therapeutic modality for delayed wound healing*. Annals of the New York Academy of Sciences, 2005. **1056**(1): p. 486-493.

60. Solomon, K.D., L.E.F. de Castro, H.P. Sandoval, J.M. Biber, B. Groat, K.D. Neff, M.S. Ying, J.W. French, E.D. Donnenfeld, and R.L. Lindstrom, *LASIK world literature review: quality of life and patient satisfaction*. Ophthalmology, 2009. **116**(4): p. 691-701.

61. Ashkin, A. and J. Dziedzic, *Observation of radiation-pressure trapping of particles by alternating light beams*. Physical Review Letters, 1985. **54**(12): p. 1245.

62. Guck, J., R. Ananthakrishnan, H. Mahmood, T.J. Moon, C.C. Cunningham, and J. Käs, *The optical stretcher: a novel laser tool to micromanipulate cells*. Biophysical Journal, 2001. **81**(2): p. 767-784.

63. Sun, Z., T. Hasan, F. Torrisi, D. Popa, G. Privitera, F. Wang, F. Bonaccorso, D.M. Basko, and A.C. Ferrari, *Graphene mode-locked ultrafast laser*. ACS Nano, 2010. **4**(2): p. 803-810.

64. Tyson, R.K., *Principles of Adaptive Optics*. 2015: CRC press.

65. Fischler, M.A. and R.C. Bolles, *Random sample consensus: a paradigm for model fitting with applications to image analysis and automated cartography*. Communications of the ACM, 1981. **24**(6): p. 381-395.

66. Wold, S., M. Sjöström, and L. Eriksson, *PLS-regression: a basic tool of chemometrics*. Chemometrics and Intelligent Laboratory Systems, 2001. **58**(2): p. 109-130.

67. Tegenfeldt, J.O., C. Prinz, H. Cao, R.L. Huang, R.H. Austin, S.Y. Chou, E.C. Cox, and J.C. Sturm, *Micro-and nanofluidics for DNA analysis*. Analytical and Bioanalytical Chemistry, 2004. **378**(7): p. 1678-1692.

68. Li, K.-C., H. Jiang, L.T. Yang, and A. Cuzzocrea, *Big Data: Algorithms, Analytics, and Applications*. 2015: CRC Press.

69. Turner, A., I. Karube, and G.S. Wilson, *Biosensors: Fundamentals and Applications*. 1987: Oxford University Press

70. Bunker, A., A. Magarkar, and T. Viitala, *Rational design of liposomal drug delivery systems, a review: Combined experimental and computational studies of lipid membranes, liposomes and their PEGylation*. Biochimica et Biophysica Acta (BBA)-Biomembranes, 2016.

71. Granqvist, N., M. Yliperttula, S. Välimäki, P. Pulkkinen, H. Tenhu, and T. Viitala, *Control of the Morphology of Lipid Layers by Substrate Surface Chemistry*. Langmuir, 2014. **30**(10): p. 2799-2809.

72. Maier, S.A., *Plasmonics: Fundamentals and Applications*. 2007: Springer Science & Business Media.

73. Thévenot, D.R., K. Toth, R.A. Durst, and G.S. Wilson, *Electrochemical biosensors: recommended definitions and classification*. Biosensors and Bioelectronics, 2001. **16**(1): p. 121-131.

74. Scheller, F.W., U. Wollenberger, A. Warsinke, and F. Lisdat, *Research and development in biosensors*. Current Opinion in Biotechnology, 2001. **12**(1): p. 35-40.

75. Day, Y.S., C.L. Baird, R.L. Rich, and D.G. Myszka, *Direct comparison of binding equilibrium, thermodynamic, and rate constants determined by surface- and solution-based biophysical methods*. Protein Science, 2002. **11**(5): p. 1017-1025.

76. Myszka, D., Y. Abdiche, F. Arisaka, O. Byron, E. Eisenstein, P. Hensley, J. Thomson, C. Lombardo, F. Schwarz, and W. Stafford, *The ABRF-MIRG'02 study: assembly state, thermodynamic, and kinetic analysis of an enzyme/inhibitor interaction*. Journal of Biomolecular Techniques, 2003. **14**(4): p. 247.

77. Cannon, M.J., G.A. Papalia, I. Navratilova, R.J. Fisher, L.R. Roberts, K.M. Worthy, A.G. Stephen, G.R. Marchesini, E.J. Collins, and D. Casper, *Comparative analyses of a small molecule/enzyme interaction by multiple users of Biacore technology*. Analytical Biochemistry, 2004. **330**(1): p. 98-113.

78. Myszka, D.G., *Analysis of small-molecule interactions using Biacore S51 technology*. Analytical Biochemistry, 2004. **329**(2): p. 316-323.

79. Bravman, T., V. Bronner, K. Lavie, A. Notcovich, G.A. Papalia, and D.G. Myszka, *Exploring "one-shot" kinetics and small molecule analysis using the ProteOn XPR36 array biosensor*. Analytical Biochemistry, 2006. **358**(2): p. 281-288.

80. Papalia, G.A., S. Leavitt, M.A. Bynum, P.S. Katsamba, R. Wilton, H. Qiu, M. Steukers, S. Wang, L. Bindu, and S. Phogat, *Comparative analysis of 10 small molecules binding to carbonic anhydrase II by different investigators using Biacore technology*. Analytical Biochemistry, 2006. **359**(1): p. 94-105.

81. Navratilova, I., G.A. Papalia, R.L. Rich, D. Bedinger, S. Brophy, B. Condon, T. Deng, A.W. Emerick, H.-W. Guan, and T. Hayden, *Thermodynamic benchmark study using Biacore technology*. Analytical Biochemistry, 2007. **364**(1): p. 67-77.

82. Rich, R.L., G.A. Papalia, P.J. Flynn, J. Furneisen, J. Quinn, J.S. Klein, P.S. Katsamba, M.B. Waddell, M. Scott, and J. Thompson, *A global benchmark study using affinity-based biosensors*. Analytical Biochemistry, 2009. **386**(2): p. 194-216.

83. Homola, J., S.S. Yee, and G. Gauglitz, *Surface plasmon resonance sensors: review*. Sensors and Actuators B: Chemical, 1999. **54**(1): p. 3-15.

84. Wolfbeis, O.S., *Fiber-optic chemical sensors and biosensors*. Analytical Chemistry, 2000. **72**(12): p. 81-90.

85. Homola, J., *Present and future of surface plasmon resonance biosensors*. Analytical and Bioanalytical Chemistry, 2003. **377**(3): p. 528-539.

86. Lambeck, P.V., *Integrated optical sensors for the chemical domain*. Measurement Science and Technology, 2006. **17**(8): p. R93.

87. Wolfbeis, O.S., *Fiber-optic chemical sensors and biosensors*. Analytical Chemistry, 2006. **78**(12): p. 3859-3874.

88. Wolfbeis, O.S., *Fiber-optic chemical sensors and biosensors*. Analytical Chemistry, 2008. **80**(12): p. 4269-4283.

89. Clark, L.C. and C. Lyons, *Electrode systems for continuous monitoring in cardiovascular surgery*. Annals of the New York Academy of Sciences, 1962. **102**(1): p. 29-45.

90. Nico, J., M.J. Fischer, N.J. Mol, and M.J. Fischer, *Surface Plasmon Resonance: Methods and Protocols*. 2010: Humana Press.

91. Albers, W.M. and I. Vikholm-Lundin, *Surface Plasmon Resonance on Nanoscale Organic Films*, in *Nano-Bio-Sensing*. 2011, Springer. p. 83-125.

92. Boozer, C., G. Kim, S. Cong, H. Guan, and T. Londergan, *Looking towards label-free biomolecular interaction analysis in a high-throughput format: a review of new surface plasmon resonance technologies.* Current Opinion in Biotechnology, 2006. **17**(4): p. 400-405.

93. Sang, S., Y. Wang, Q. Feng, Y. Wei, J. Ji, and W. Zhang, *Progress of new label-free techniques for biosensors: a review.* Critical Reviews in Biotechnology, 2016. **36**(3): p. 465-481.

94. Cooper, M.A., *Label-free screening of bio-molecular interactions.* Analytical and Bioanalytical Chemistry, 2003. **377**(5): p. 834-842.

95. Rader, R.A., *(Re) defining biopharmaceutical.* Nature Biotechnology, 2008. **26**(7): p. 743-751.

96. Hendrix, M., E.S. Priestley, G.F. Joyce, and C.-H. Wong, *Direct observation of aminoglycoside-RNA interactions by surface plasmon resonance.* Journal of the American Chemical Society, 1997. **119**(16): p. 3641-3648.

97. Smith, E.A., W.D. Thomas, L.L. Kiessling, and R.M. Corn, *Surface plasmon resonance imaging studies of protein-carbohydrate interactions.* Journal of the American Chemical Society, 2003. **125**(20): p. 6140-6148.

98. Ramakrishnan, M., K.K. Kandimalla, T.M. Wengenack, K.G. Howell, and J.F. Poduslo, *Surface plasmon resonance binding kinetics of Alzheimer's disease amyloid β peptide-capturing and plaque-binding monoclonal antibodies.* Biochemistry, 2009. **48**(43): p. 10405-10415.

99. Hearty, S., P.J. Conroy, B.V. Ayyar, B. Byrne, and R. O'Kennedy, *Surface plasmon resonance for vaccine design and efficacy studies: recent applications and future trends.* Expert Review of Vaccines, 2010. **9**(6): p. 645-664.

100. Wagner, V., A. Dullaart, A.-K. Bock, and A. Zweck, *The emerging nanomedicine landscape.* Nature Biotechnology, 2006. **24**(10): p. 1211-1217.

101. Venditto, V.J. and F.C. Szoka, *Cancer nanomedicines: so many papers and so few drugs!* Advanced Drug Delivery Reviews, 2013. **65**(1): p. 80-88.

102. Hafner, A., J. Lovrić, G.P. Lakoš, and I. Pepić, *Nanotherapeutics in the EU: an overview on current state and future directions.* International Journal of Nanomedicine, 2014. **9**: p. 1005-1023.

103. Zocco, D., P. Ferruzzi, F. Cappello, W.P. Kuo, and S. Fais, *Extracellular vesicles as shuttles of tumor biomarkers and anti-tumor drugs.* Frontiers in Oncology, 2014. **4**.

104. Fais, S., L. O'Driscoll, F.E. Borras, E. Buzas, G. Camussi, F. Cappello, J. Carvalho, A. Cordeiro da Silva, H. Del Portillo, and S. El Andaloussi, *Evidence-Based Clinical Use of Nanoscale Extracellular Vesicles in Nanomedicine.* ACS Nano, 2016. **10**(4): p. 3886-3899.

105. Thillaivinayagalingam, P., J. Gommeaux, M. McLoughlin, D. Collins, and A.R. Newcombe, *Biopharmaceutical production: Applications of surface plasmon resonance biosensors*. Journal of Chromatography B, 2010. **878**(2): p. 149-153.

106. Bakhtiar, R., *Surface plasmon resonance spectroscopy: a versatile technique in a biochemist's toolbox*. Journal of Chemical Education, 2012. **90**(2): p. 203-209.

107. Kell, D.B. and R. Goodacre, *Metabolomics and systems pharmacology: why and how to model the human metabolic network for drug discovery*. Drug Discovery Today, 2014. **19**(2): p. 171-182.

108. Chung, T.D., D.B. Terry, and L.H. Smith, *Assay Guidance Manual*, S. Sittampalam, Editor. 2015, NIH: National Center for Advancing Translational Sciences.

109. Zhou, W., Y. Wang, A. Lu, and G. Zhang, *Systems Pharmacology in Small Molecular Drug Discovery*. International Journal of Molecular Sciences, 2016. **17**(2): p. 246.

110. Caldwell, G.W., *Compound optimization in early-and late-phase drug discovery: acceptable pharmacokinetic properties utilizing combined physicochemical, in vitro and in vivo screens*. Current Opinion in Drug Discovery and Development, 2000. **3**(1): p. 30-41.

111. Lipinski, C.A., *Drug-like properties and the causes of poor solubility and poor permeability*. Journal of Pharmacological and Toxicological Methods, 2000. **44**(1): p. 235-249.

112. Lipinski, C.A., *Lead- and drug-like compounds: the rule-of-five revolution*. Drug Discovery Today Technologies, 2004. **1**(4): p. 337-41.

113. Lipinski, C.A., F. Lombardo, B.W. Dominy, and P.J. Feeney, *Experimental and computational approaches to estimate solubility and permeability in drug discovery and development settings*. Advanced Drug Delivery Reviews, 2012. **64**: p. 4-17.

114. Ghose, A.K., V.N. Viswanadhan, and J.J. Wendoloski, *A knowledge-based approach in designing combinatorial or medicinal chemistry libraries for drug discovery. 1. A qualitative and quantitative characterization of known drug databases*. Journal of Combinatorial Chemistry, 1999. **1**(1): p. 55-68.

115. Declerck, P., *Biologicals and biosimilars: a review of the science and its implications*. Generics and Biosimilars Initiative Journal, 2012. **1**(1): p. 13-16.

116. Kinch, M.S., *2015 in review: FDA approval of new drugs*. Drug Discovery Today, 2016.

117. Kinch, M.S., J. Merkel, and S. Umlauf, *Trends in pharmaceutical targeting of clinical indications: 1930–2013*. Drug Discovery Today, 2014. **19**(11): p. 1682-1685.

118. Duncan, R., *Nanomedicines in action*. The Pharmaceutical Journal, 2004. **273**: p. 485-488.

119. Dowling, A., R. Clift, N. Grobert, D. Hutton, R. Oliver, O. O'neill, J. Pethica, N. Pidgeon, J. Porritt, and J. Ryan, *Nanoscience and nanotechnologies: opportunities and uncertainties*. The Royal Society & The Royal Academy of Engineering Report, 2004. **61**: p. e64.

120. Ramezanpour, M., S. Leung, K. Delgado-Magnero, B. Bashe, J. Thewalt, and D. Tieleman, *Computational and experimental approaches for investigating nanoparticle-based drug delivery systems*. Biochimica et Biophysica Acta (BBA)-Biomembranes, 2016.

121. Suk, J.S., Q. Xu, N. Kim, J. Hanes, and L.M. Ensign, *PEGylation as a strategy for improving nanoparticle-based drug and gene delivery*. Advanced Drug Delivery Reviews, 2015.

122. Shen, Y., C.S. Friend, Y. Jiang, D. Jakubczyk, J. Swiatkiewicz, and P.N. Prasad, *Nanophotonics: interactions, materials, and applications*. The Journal of Physical Chemistry B, 2000. **104**(32): p. 7577-7587.

123. Xin, H., Y. Li, and B. Li, *Bacteria-based branched structures for bionano-photonics*. Laser & Photonics Reviews, 2015. **9**(5): p. 554-563.

124. M Rabanel, J., V. Aoun, I. Elkin, M. Mokhtar, and P. Hildgen, *Drug-loaded nanocarriers: passive targeting and crossing of biological barriers*. Current Medicinal Chemistry, 2012. **19**(19): p. 3070-3102.

125. Owens, D.E. and N.A. Peppas, *Opsonization, biodistribution, and pharmacokinetics of polymeric nanoparticles*. International Journal of Pharmaceutics, 2006. **307**(1): p. 93-102.

126. Moghimi, S.M. and S.S. Davis, *Innovations in avoiding particle clearance from blood by Kupffer cells: cause for reflection*. Critical Reviews in Therapeutic Drug Carrier Systems, 1993. **11**(1): p. 31-59.

127. Ricklin, D., G. Hajishengallis, K. Yang, and J.D. Lambris, *Complement: a key system for immune surveillance and homeostasis*. Nature Immunology, 2010. **11**(9): p. 785-797.

128. Yan, X., G.L. Scherphof, and J.A. Kamps, *Liposome opsonization*. Journal of Liposome Research, 2005. **15**(1-2): p. 109-139.

129. Pattni, B.S., V.V. Chupin, and V.P. Torchilin, *New developments in liposomal drug delivery*. Chemical Reviews, 2015. **115**(19): p. 10938-10966.

130. Gillies, E.R. and J.M. Frechet, *Dendrimers and dendritic polymers in drug delivery*. Drug Discovery Today, 2005. **10**(1): p. 35-43.

131. Bianco, A., K. Kostarelos, and M. Prato, *Applications of carbon nanotubes in drug delivery*. Current Opinion in Chemical Biology, 2005. **9**(6): p. 674-679.

132. Ghosh, P., G. Han, M. De, C.K. Kim, and V.M. Rotello, *Gold nanoparticles in delivery applications*. Advanced Drug Delivery Reviews, 2008. **60**(11): p. 1307-1315.

133. Kim, C.S., G.Y. Tonga, D. Solfiell, and V.M. Rotello, *Inorganic nanosystems for therapeutic delivery: status and prospects*. Advanced Drug Delivery Reviews, 2013. **65**(1): p. 93-99.

134. Duncan, R., *The dawning era of polymer therapeutics*. Nature Reviews Drug Discovery, 2003. **2**(5): p. 347-360.

135. Moghimi, S.M., A.C. Hunter, and J.C. Murray, *Long-circulating and target-specific nanoparticles: theory to practice*. Pharmacological Reviews, 2001. **53**(2): p. 283-318.

136. Allen, T.M. and P.R. Cullis, *Drug delivery systems: entering the mainstream*. Science, 2004. **303**(5665): p. 1818-1822.

137. Allen, T.M. and P.R. Cullis, *Liposomal drug delivery systems: from concept to clinical applications*. Advanced Drug Delivery Reviews, 2013. **65**(1): p. 36-48.

138. Blanco, E., H. Shen, and M. Ferrari, *Principles of nanoparticle design for overcoming biological barriers to drug delivery*. Nature Biotechnology, 2015. **33**(9): p. 941-951.

139. Ogawara, K.-i., Y. Yoshizawa, K. Un, T. Araki, T. Kimura, and K. Higaki, *Nanoparticle-based passive drug targeting to tumors: considerations and implications for optimization*. Biological and Pharmaceutical Bulletin, 2013. **36**(5): p. 698-702.

140. Bazak, R., M. Houri, S. El Achy, S. Kamel, and T. Refaat, *Cancer active targeting by nanoparticles: a comprehensive review of literature*. Journal of Cancer Research and Clinical Oncology, 2015. **141**(5): p. 769-784.

141. Mayer, L.D., M.B. Bally, and P.R. Cullis, *Strategies for optimizing liposomal doxorubicin*. Journal of Liposome Research, 1990. **1**(4): p. 463-480.

142. Zelphati, O., C. Nguyen, M. Ferrari, J. Felgner, Y. Tsai, and P. Felgner, *Stable and monodisperse lipoplex formulations for gene delivery*. Gene Therapy, 1998. **5**(9): p. 1272-1282.

143. Chanan-Khan, A., J. Szebeni, S. Savay, L. Liebes, N. Rafique, C. Alving, and F. Muggia, *Complement activation following first exposure to pegylated liposomal doxorubicin (Doxil®): possible role in hypersensitivity reactions*. Annals of Oncology, 2003. **14**(9): p. 1430-1437.

144. Knop, K., R. Hoogenboom, D. Fischer, and U.S. Schubert, *Poly (ethylene glycol) in drug delivery: pros and cons as well as potential alternatives*. Angewandte Chemie International Edition, 2010. **49**(36): p. 6288-6308.

145. Hamad, I., O. Al-Hanbali, A.C. Hunter, K.J. Rutt, T.L. Andresen, and S.M. Moghimi, *Distinct polymer architecture mediates switching of complement activation pathways at the nanosphere– serum interface: implications for stealth nanoparticle engineering*. ACS Nano, 2010. **4**(11): p. 6629-6638.

146. Hu, C.-M.J., L. Zhang, S. Aryal, C. Cheung, R.H. Fang, and L. Zhang, *Erythrocyte membrane-camouflaged polymeric nanoparticles as a biomimetic delivery platform*. Proceedings of the National Academy of Sciences, 2011. **108**(27): p. 10980-10985.

147. Pelegri-O'Day, E.M., E.-W. Lin, and H.D. Maynard, *Therapeutic protein–polymer conjugates: advancing beyond PEGylation*. Journal of the American Chemical Society, 2014. **136**(41): p. 14323-14332.

148. Engler, A.C., X. Ke, S. Gao, J.M. Chan, D.J. Coady, R.J. Ono, R. Lubbers, A. Nelson, Y.Y. Yang, and J.L. Hedrick, *Hydrophilic polycarbonates: Promising degradable alternatives to poly (ethylene glycol)-based stealth materials*. Macromolecules, 2015. **48**(6): p. 1673-1678.

149. Sprague, B.L., R.L. Pego, D.A. Stavreva, and J.G. McNally, *Analysis of binding reactions by fluorescence recovery after photobleaching*. Biophysical Journal, 2004. **86**(6): p. 3473-3495.

150. Madeira, C., L.M. Loura, M.R. Aires-Barros, and M. Prieto, *Fluorescence methods for lipoplex characterization*. Biochimica et Biophysica Acta (BBA)-Biomembranes, 2011. **1808**(11): p. 2694-2705.

151. Hassan, P.A., S. Rana, and G. Verma, *Making sense of brownian motion: colloid characterization by dynamic light scattering*. Langmuir, 2014. **31**(1): p. 3-12.

152. Filipe, V., A. Hawe, and W. Jiskoot, *Critical evaluation of Nanoparticle Tracking Analysis (NTA) by NanoSight for the measurement of nanoparticles and protein aggregates*. Pharmaceutical Research, 2010. **27**(5): p. 796-810.

153. Bangham, A., D.H. Heard, R. Flemans, and G. Seaman, *An apparatus for microelectrophoresis of small particles*. Nature, 1958. **182**(4636): p. 642-644.

154. Almgren, M., K. Edwards, and G. Karlsson, *Cryo transmission electron microscopy of liposomes and related structures*. Colloids and Surfaces A: Physicochemical and Engineering Aspects, 2000. **174**(1): p. 3-21.

155. Warschawski, D.E., A.A. Arnold, M. Beaugrand, A. Gravel, É. Chartrand, and I. Marcotte, *Choosing membrane mimetics for NMR structural studies of transmembrane proteins*. Biochimica et Biophysica Acta (BBA)-Biomembranes, 2011. **1808**(8): p. 1957-1974.

156. Chiu, M.H. and E.J. Prenner, *Differential scanning calorimetry: an invaluable tool for a detailed thermodynamic characterization of macromolecules and their interactions*. Journal of Pharmacy and Bioallied Sciences, 2011. **3**(1): p. 39.

157. Tellinghuisen, J., *Optimizing experimental parameters in isothermal titration calorimetry: variable volume procedures*. The Journal of Physical Chemistry B, 2007. **111**(39): p. 11531-11537.

158. Langmuir, I., *THE CONSTITUTION AND FUNDAMENTAL PROPERTIES OF SOLIDS AND LIQUIDS. PART I. SOLIDS*. Journal of the American Chemical Society, 1916. **38**(11): p. 2221-2295.

159. Hoenig, D. and D. Moebius, *Direct visualization of monolayers at the air-water interface by Brewster angle microscopy*. The Journal of Physical Chemistry, 1991. **95**(12): p. 4590-4592.

160. Pérez-Morales, M., J.M. Pedrosa, E. Muñoz, M.T. Martín-Romero, D. Möbius, and L. Camacho, *Ellipsometric study of a phospholipid monolayer at the air–water interface in presence of large organic counter ions*. Thin Solid Films, 2005. **488**(1): p. 247-253.

161. Bandey, H.L., S.J. Martin, R.W. Cernosek, and A.R. Hillman, *Modeling the responses of thickness-shear mode resonators under various loading conditions*. Analytical Chemistry, 1999. **71**(11): p. 2205-2214.

162. Reviakine, I., D. Johannsmann, and R.P. Richter, *Hearing what you cannot see and visualizing what you hear: interpreting quartz crystal microbalance data from solvated interfaces*. Analytical Chemistry, 2011. **83**(23): p. 8838-8848.

163. Nguyen, H.H., J. Park, S. Kang, and M. Kim, *Surface plasmon resonance: a versatile technique for biosensor applications*. Sensors, 2015. **15**(5): p. 10481-10510.

164. Escorihuela, J., M.Á. González-Martínez, J.L. López-Paz, R. Puchades, Á. Maquieira, and D. Gimenez-Romero, *Dual-polarization interferometry: A novel technique to light up the nanomolecular world*. Chemical Reviews, 2014. **115**(1): p. 265-294.

165. Jiang, C., A. Gamarnik, and C.P. Tripp, *Identification of lipid aggregate structures on TiO2 surface using headgroup IR bands*. The Journal of Physical Chemistry B, 2005. **109**(10): p. 4539-4544.

166. Walker, R.A., J.C. Conboy, and G.L. Richmond, *Molecular structure and ordering of phospholipids at a liquid-liquid interface*. Langmuir, 1997. **13**(12): p. 3070-3073.

167. Chen, X., W. Hua, Z. Huang, and H.C. Allen, *Interfacial water structure associated with phospholipid membranes studied by phase-sensitive vibrational sum frequency generation spectroscopy*. Journal of the American Chemical Society, 2010. **132**(32): p. 11336-11342.

168. Varga, Z., S. Berényi, B. Szokol, L.s. Őrfi, G.r. Kéri, I. Peták, A. Hoell, and A. Bóta, *A closer look at the structure of sterically stabilized liposomes: a small-angle X-ray scattering study*. The Journal of Physical Chemistry B, 2010. **114**(20): p. 6850-6854.

169. Yaghmur, A., L. Paasonen, M. Yliperttula, A. Urtti, and M. Rappolt, *Structural elucidation of light activated vesicles*. The Journal of Physical Chemistry Letters, 2010. **1**(6): p. 962-966.

170. Miller, C., J. Majewski, and T. Kuhl, *Characterization of single biological membranes at the solid–liquid interface by X-ray reflectivity*. Colloids and Surfaces A: Physicochemical and Engineering Aspects, 2006. **284**: p. 434-439.

171. Vacklin, H.P., F. Tiberg, G. Fragneto, and R.K. Thomas, *Composition of supported model membranes determined by neutron reflection*. Langmuir, 2005. **21**(7): p. 2827-2837.

172. Yáñez-Mó, M., P.R.-M. Siljander, Z. Andreu, A.B. Zavec, F.E. Borràs, E.I. Buzas, K. Buzas, E. Casal, F. Cappello, and J. Carvalho, *Biological properties of extracellular vesicles and their physiological functions*. Journal of Extracellular Vesicles, 2015. **4**.

173. Heijnen, H.F., A.E. Schiel, R. Fijnheer, H.J. Geuze, and J.J. Sixma, *Activated Platelets Release Two Types of Membrane Vesicles: Microvesicles by Surface Shedding and Exosomes Derived From Exocytosis of Multivesicular Bodies and α-Granules*. Blood, 1999. **94**(11): p. 3791-3799.

174. Deregibus, M.C., V. Cantaluppi, R. Calogero, M.L. Iacono, C. Tetta, L. Biancone, S. Bruno, B. Bussolati, and G. Camussi, *Endothelial progenitor cell–derived microvesicles activate an angiogenic program in endothelial cells by a horizontal transfer of mRNA*. Blood, 2007. **110**(7): p. 2440-2448.

175. Théry, C., S. Amigorena, G. Raposo, and A. Clayton, *Isolation and characterization of exosomes from cell culture supernatants and biological fluids*. Current Protocols in Cell Biology, 2006: p. 3.22. 1-3.22. 29.

176. Bobrie, A., M. Colombo, G. Raposo, and C. Théry, *Exosome secretion: molecular mechanisms and roles in immune responses*. Traffic, 2011. **12**(12): p. 1659-1668.

177. Raposo, G. and W. Stoorvogel, *Extracellular vesicles: exosomes, microvesicles, and friends*. The Journal of Cell Biology, 2013. **200**(4): p. 373-83.

178. Palanisamy, V., S. Sharma, A. Deshpande, H. Zhou, J. Gimzewski, and D.T. Wong, *Nanostructural and transcriptomic analyses of human saliva derived exosomes*. PLOS ONE, 2010. **5**(1): p. e8577.

179. Admyre, C., S.M. Johansson, K.R. Qazi, J.-J. Filén, R. Lahesmaa, M. Norman, E.P. Neve, A. Scheynius, and S. Gabrielsson, *Exosomes with immune modulatory features are present in human breast milk*. The Journal of Immunology, 2007. **179**(3): p. 1969-1978.

180. Caby, M.-P., D. Lankar, C. Vincendeau-Scherrer, G. Raposo, and C. Bonnerot, *Exosomal-like vesicles are present in human blood plasma*. International Immunology, 2005. **17**(7): p. 879-887.

181. Pisitkun, T., R.-F. Shen, and M.A. Knepper, *Identification and proteomic profiling of exosomes in human urine*. Proceedings of the National Academy of Sciences, 2004. **101**(36): p. 13368-13373.

182. Masyuk, A.I., B.Q. Huang, C.J. Ward, S.A. Gradilone, J.M. Banales, T.V. Masyuk, B. Radtke, P.L. Splinter, and N.F. LaRusso, *Biliary exosomes influence cholangiocyte regulatory mechanisms and proliferation through interaction with primary cilia*. American Journal of Physiology-Gastrointestinal and Liver Physiology, 2010. **299**(4): p. G990-G999.

183. Vella, L., R. Sharples, V. Lawson, C. Masters, R. Cappai, and A. Hill, *Packaging of prions into exosomes is associated with a novel pathway of PrP processing*. The Journal of Pathology, 2007. **211**(5): p. 582-590.

184. Huotari, J. and A. Helenius, *Endosome maturation*. The EMBO Journal, 2011. **30**(17): p. 3481-3500.

185. Zöller, M., *Tetraspanins: push and pull in suppressing and promoting metastasis*. Nature Reviews Cancer, 2009. **9**(1): p. 40-55.

186. Simpson, R.J., S.S. Jensen, and J.W. Lim, *Proteomic profiling of exosomes: current perspectives*. Proteomics, 2008. **8**(19): p. 4083-4099.

187. Wubbolts, R., R.S. Leckie, P.T. Veenhuizen, G. Schwarzmann, W. Möbius, J. Hoernschemeyer, J.-W. Slot, H.J. Geuze, and W. Stoorvogel, *Proteomic and biochemical analyses of human B cell-derived exosomes Potential implications for their function and multivesicular body formation*. Journal of Biological Chemistry, 2003. **278**(13): p. 10963-10972.

188. Subra, C., K. Laulagnier, B. Perret, and M. Record, *Exosome lipidomics unravels lipid sorting at the level of multivesicular bodies*. Biochimie, 2007. **89**(2): p. 205-212.

189. Brouwers, J.F., M. Aalberts, J.W. Jansen, G. van Niel, M.H. Wauben, T.A. Stout, J.B. Helms, and W. Stoorvogel, *Distinct lipid compositions of two types of human prostasomes*. Proteomics, 2013. **13**(10-11): p. 1660-1666.

190. Colombo, M., G. Raposo, and C. Théry, *Biogenesis, secretion, and intercellular interactions of exosomes and other extracellular vesicles*. Annual Review of Cell and Developmental Biology, 2014. **30**: p. 255-289.

191. Valadi, H., K. Ekström, A. Bossios, M. Sjöstrand, J.J. Lee, and J.O. Lötvall, *Exosome-mediated transfer of mRNAs and microRNAs is a novel mechanism of genetic exchange between cells*. Nature Cell Biology, 2007. **9**(6): p. 654-659.

192. Lazaro-Ibanez, E., A. Sanz-Garcia, T. Visakorpi, C. Escobedo-Lucea, P. Siljander, A. Ayuso-Sacido, and M. Yliperttula, *Different gDNA content in the subpopulations of prostate cancer extracellular vesicles: apoptotic bodies, microvesicles, and exosomes*. Prostate, 2014. **74**(14): p. 1379-90.

193. Cantin, R., J. Diou, D. Bélanger, A.M. Tremblay, and C. Gilbert, *Discrimination between exosomes and HIV-1: purification of both vesicles from cell-free supernatants*. Journal of Immunological Methods, 2008. **338**(1): p. 21-30.

194. Lässer, C., M. Eldh, and J. Lötvall, *Isolation and characterization of RNA-containing exosomes*. Journal of Visualized Experiments, 2012(59): p. e3037-e3037.

195. Witwer, K.W., E.I. Buzas, L.T. Bemis, A. Bora, C. Lässer, J. Lötvall, E.N. Nolte, M.G. Piper, S. Sivaraman, and J. Skog, *Standardization of sample collection, isolation and analysis methods in extracellular vesicle research*. Journal of Extracellular Vesicles, 2013. **2**.

196. Johnstone, R.M., M. Adam, J. Hammond, L. Orr, and C. Turbide, *Vesicle formation during reticulocyte maturation. Association of plasma membrane activities with released vesicles (exosomes)*. Journal of Biological Chemistry, 1987. **262**(19): p. 9412-9420.

197. Raposo, G., H.W. Nijman, W. Stoorvogel, R. Liejendekker, C.V. Harding, C. Melief, and H.J. Geuze, *B lymphocytes secrete antigen-presenting vesicles*. The Journal of Experimental Medicine, 1996. **183**(3): p. 1161-1172.

198. Zitvogel, L., A. Regnault, A. Lozier, J. Wolfers, C. Flament, D. Tenza, P. Ricciardi-Castagnoli, G. Raposo, and S. Amigorena, *Eradication of established murine tumors using a novel cell-free vaccine: dendritic cell derived exosomes*. Nature Medicine, 1998. **4**(5): p. 594-600.

199. Baietti, M.F., Z. Zhang, E. Mortier, A. Melchior, G. Degeest, A. Geeraerts, Y. Ivarsson, F. Depoortere, C. Coomans, and E. Vermeiren, *Syndecan-syntenin-ALIX regulates the biogenesis of exosomes*. Nature Cell Biology, 2012. **14**(7): p. 677-685.

200. Taylor, D.D., I.-N. Chou, and P.H. Black, *Isolation of plasma membrane fragments from cultured murine melanoma cells*. Biochemical and Biophysical Research Communications, 1983. **113**(2): p. 470-476.

201. Baj-Krzyworzeka, M., R. Szatanek, K. Węglarczyk, J. Baran, B. Urbanowicz, P. Brański, M.Z. Ratajczak, and M. Zembala, *Tumour-derived microvesicles carry several surface determinants and mRNA of tumour cells and transfer some of these determinants to monocytes*. Cancer Immunology, Immunotherapy, 2006. **55**(7): p. 808-818.

202. Muralidharan-Chari, V., J. Clancy, C. Plou, M. Romao, P. Chavrier, G. Raposo, and C. D'Souza-Schorey, *ARF6-regulated shedding of tumor cell-derived plasma membrane microvesicles.* Current Biology, 2009. **19**(22): p. 1875-1885.

203. Kleijmeer, M.J., W. Stoorvogel, J.M. Griffith, O. Yoshie, and H.J. Geuze, *Selective enrichment of tetraspan proteins on the internal vesicles of multivesicular endosomes and on exosomes secreted by human B-lymphocytes.* Journal of Biological Chemistry, 1998. **273**(32): p. 20121-20127.

204. Lamparski, H.G., A. Metha-Damani, J.-Y. Yao, S. Patel, D.-H. Hsu, C. Ruegg, and J.-B. Le Pecq, *Production and characterization of clinical grade exosomes derived from dendritic cells.* Journal of Immunological Methods, 2002. **270**(2): p. 211-226.

205. Yoshioka, Y., Y. Konishi, N. Kosaka, T. Katsuda, T. Kato, and T. Ochiya, *Comparative marker analysis of extracellular vesicles in different human cancer types.* Journal of Extracellular Vesicles, 2013. **2**.

206. Llorente, A., T. Skotland, T. Sylvänne, D. Kauhanen, T. Róg, A. Orłowski, I. Vattulainen, K. Ekroos, and K. Sandvig, *Molecular lipidomics of exosomes released by PC-3 prostate cancer cells.* Biochimica et Biophysica Acta (BBA)-Molecular and Cell Biology of Lipids, 2013. **1831**(7): p. 1302-1309.

207. Nolte, E.N., H.P. Buermans, M. Waasdorp, W. Stoorvogel, M.H. Wauben, and P. AC't Hoen, *Deep sequencing of RNA from immune cell-derived vesicles uncovers the selective incorporation of small non-coding RNA biotypes with potential regulatory functions.* Nucleic Acids Research, 2012. **40**(18): p. 9272-9285.

208. Rodrigues, M.L., E.S. Nakayasu, D.L. Oliveira, L. Nimrichter, J.D. Nosanchuk, I.C. Almeida, and A. Casadevall, *Extracellular vesicles produced by Cryptococcus neoformans contain protein components associated with virulence.* Eukaryotic Cell, 2008. **7**(1): p. 58-67.

209. Hergenreider, E., S. Heydt, K. Tréguer, T. Boettger, A.J. Horrevoets, A.M. Zeiher, M.P. Scheffer, A.S. Frangakis, X. Yin, and M. Mayr, *Atheroprotective communication between endothelial cells and smooth muscle cells through miRNAs.* Nature Cell Biology, 2012. **14**(3): p. 249-256.

210. Conde-Vancells, J., E. Rodriguez-Suarez, N. Embade, D. Gil, R. Matthiesen, M. Valle, F. Elortza, S.C. Lu, J.M. Mato, and J.M. Falcon-Perez, *Characterization and comprehensive proteome profiling of exosomes secreted by hepatocytes.* Journal of Proteome Research, 2008. **7**(12): p. 5157-5166.

211. Sharma, S., B.M. Gillespie, V. Palanisamy, and J.K. Gimzewski, *Quantitative nanostructural and single-molecule force spectroscopy biomolecular analysis of human-saliva-derived exosomes.* Langmuir, 2011. **27**(23): p. 14394-14400.

212. Cossetti, C., N. Iraci, T.R. Mercer, T. Leonardi, E. Alpi, D. Drago, C. Alfaro-Cervello, H.K. Saini, M.P. Davis, and J. Schaeffer, *Extracellular vesicles from neural stem cells transfer IFN-γ via Ifngr1 to activate Stat1 signaling in target cells*. Molecular Cell, 2014. **56**(2): p. 193-204.

213. Soo, C.Y., Y. Song, Y. Zheng, E.C. Campbell, A.C. Riches, F. Gunn-Moore, and S.J. Powis, *Nanoparticle tracking analysis monitors microvesicle and exosome secretion from immune cells*. Immunology, 2012. **136**(2): p. 192-197.

214. Gardiner, C., Y.J. Ferreira, R.A. Dragovic, C.W. Redman, and I.L. Sargent, *Extracellular vesicle sizing and enumeration by nanoparticle tracking analysis*. Journal of Extracellular Vesicles, 2013. **2**.

215. Nolte, E.N., E.J. van der Vlist, M. Aalberts, H.C. Mertens, B.J. Bosch, W. Bartelink, E. Mastrobattista, E.V. van Gaal, W. Stoorvogel, and G.J. Arkesteijn, *Quantitative and qualitative flow cytometric analysis of nanosized cell-derived membrane vesicles*. Nanomedicine: Nanotechnology, Biology and Medicine, 2012. **8**(5): p. 712-720.

216. van der Vlist, E.J., E.N. Nolte, W. Stoorvogel, G.J. Arkesteijn, and M.H. Wauben, *Fluorescent labeling of nano-sized vesicles released by cells and subsequent quantitative and qualitative analysis by high-resolution flow cytometry*. Nature Protocols, 2012. **7**(7): p. 1311-1326.

217. Tirinato, L., F. Gentile, D. Di Mascolo, M. Coluccio, G. Das, C. Liberale, S. Pullano, G. Perozziello, M. Francardi, and A. Accardo, *SERS analysis on exosomes using super-hydrophobic surfaces*. Microelectronic Engineering, 2012. **97**: p. 337-340.

218. Lee, C., R.P. Carney, S. Hazari, Z.J. Smith, A. Knudson, C.S. Robertson, K.S. Lam, and S. Wachsmann-Hogiu, *3D plasmonic nanobowl platform for the study of exosomes in solution*. Nanoscale, 2015. **7**(20): p. 9290-9297.

219. Grasso, L., R. Wyss, L. Weidenauer, A. Thampi, D. Demurtas, M. Prudent, N. Lion, and H. Vogel, *Molecular screening of cancer-derived exosomes by surface plasmon resonance spectroscopy*. Analytical and Bioanalytical Chemistry, 2015. **407**(18): p. 5425-5432.

220. Gámez-Valero, A., S.I. Lozano-Ramos, I. Bancu, R. Lauzurica-Valdemoros, and F.E. Borràs, *Urinary extracellular vesicles as source of biomarkers in kidney diseases*. Frontiers in Immunology, 2015. **6**.

221. Azmi, A.S., B. Bao, and F.H. Sarkar, *Exosomes in cancer development, metastasis, and drug resistance: a comprehensive review*. Cancer and Metastasis Reviews, 2013. **32**(3-4): p. 623-642.

222. Admyre, C., E. Telemo, N. Almqvist, J. Lötvall, R. Lahesmaa, A. Scheynius, and S. Gabrielsson, *Exosomes–nanovesicles with possible roles in allergic inflammation*. Allergy, 2008. **63**(4): p. 404-408.

223. Schneider, A. and M. Simons, *Exosomes: vesicular carriers for intercellular communication in neurodegenerative disorders*. Cell and Tissue Research, 2013. **352**(1): p. 33-47.

224. Beyer, C. and D.S. Pisetsky, *The role of microparticles in the pathogenesis of rheumatic diseases*. Nature Reviews Rheumatology, 2010. **6**(1): p. 21-29.

225. Lener, T., M. Gioma, L. Aigner, V. Börger, E. Buzas, G. Camussi, N. Chaput, D. Chatterjee, H.A. Del Portillo, and L. O'Driscoll, *Applying extracellular vesicles based therapeutics in clinical trials-an ISEV position paper*. Journal of Extracellular Vesicles, 2015. **4**.

226. Logozzi, M., A. De Milito, L. Lugini, M. Borghi, L. Calabro, M. Spada, M. Perdicchio, M.L. Marino, C. Federici, and E. Iessi, *High levels of exosomes expressing CD63 and caveolin-1 in plasma of melanoma patients*. PLOS ONE, 2009. **4**(4): p. e5219.

227. Melo, S.A., L.B. Luecke, C. Kahlert, A.F. Fernandez, S.T. Gammon, J. Kaye, V.S. LeBleu, E.A. Mittendorf, J. Weitz, and N. Rahbari, *Glypican-1 identifies cancer exosomes and detects early pancreatic cancer*. Nature, 2015.

228. Ogorevc, E., V. Kralj-Iglic, and P. Veranic, *The role of extracellular vesicles in phenotypic cancer transformation*. Radiology and Oncology, 2013. **47**(3): p. 197-205.

229. Campanella, C., F. Rappa, C. Sciumè, A. Marino Gammazza, R. Barone, F. Bucchieri, S. David, G. Curcurù, C. Caruso Bavisotto, and A. Pitruzzella, *Heat shock protein 60 levels in tissue and circulating exosomes in human large bowel cancer before and after ablative surgery*. Cancer, 2015. **121**(18): p. 3230-3239.

230. Skog, J., T. Würdinger, S. van Rijn, D.H. Meijer, L. Gainche, W.T. Curry, B.S. Carter, A.M. Krichevsky, and X.O. Breakefield, *Glioblastoma microvesicles transport RNA and proteins that promote tumour growth and provide diagnostic biomarkers*. Nature Cell Biology, 2008. **10**(12): p. 1470-1476.

231. Manterola, L., E. Guruceaga, J.G. Pérez-Larraya, M. González-Huarriz, P. Jauregui, S. Tejada, R. Diez-Valle, V. Segura, N. Samprón, and C. Barrena, *A small noncoding RNA signature found in exosomes of GBM patient serum as a diagnostic tool*. Neuro-Oncology, 2014: p. not218.

232. Tokuhisa, M., Y. Ichikawa, N. Kosaka, T. Ochiya, M. Yashiro, K. Hirakawa, T. Kosaka, H. Makino, H. Akiyama, and C. Kunisaki, *Exosomal miRNAs from peritoneum lavage fluid as potential prognostic biomarkers of peritoneal metastasis in gastric cancer*. PLOS ONE, 2015. **10**(7): p. e0130472.

233. Szajnik, M., M. Derbis, M. Lach, P. Patalas, M. Michalak, H. Drzewiecka, D. Szpurek, A. Nowakowski, M. Spaczynski, and W. Baranowski, *Exosomes in plasma of patients with ovarian carcinoma: potential biomarkers of tumor progression and response to therapy*. Gynecology & Obstetrics, 2013: p. 003.

234. Chen, C.-L., Y.-F. Lai, P. Tang, K.-Y. Chien, J.-S. Yu, C.-H. Tsai, H.-W. Chen, C.-C. Wu, T. Chung, and C.-W. Hsu, *Comparative and targeted proteomic analyses of urinary microparticles from bladder cancer and hernia patients.* Journal of Proteome Research, 2012. **11**(12): p. 5611-5629.

235. Admyre, C., J. Grunewald, J. Thyberg, S. Gripenbäck, G. Tornling, A. Eklund, A. Scheynius, and S. Gabrielsson, *Exosomes with major histocompatibility complex class II and co-stimulatory molecules are present in human BAL fluid.* European Respiratory Journal, 2003. **22**(4): p. 578-583.

236. Lässer, C., S.E. O'Neil, L. Ekerljung, K. Ekström, M. Sjöstrand, and J. Lötvall, *RNA-containing exosomes in human nasal secretions.* American Journal of Rhinology & Allergy, 2011. **25**(2): p. 89-93.

237. Pocsfalvi, G., C. Stanly, A. Vilasi, I. Fiume, R. Tatè, and G. Capasso, *Employing Extracellular Vesicles for Non-Invasive Renal Monitoring: A Captivating Prospect.* World Journal of Clinical Urology, 2014. **3**(2): p. 66-80.

238. Budnik, V., C. Ruiz-Cañada, and F. Wendler, *Extracellular vesicles round off communication in the nervous system.* Nature Reviews Neuroscience, 2016. **17**(3): p. 160-172.

239. Viola, K.L. and W.L. Klein, *Amyloid β oligomers in Alzheimer's disease pathogenesis, treatment, and diagnosis.* Acta Neuropathologica, 2015. **129**(2): p. 183-206.

240. Walsh, D., I. Klyubin, J. Fadeeva, M. Rowan, and D. Selkoe, *Amyloid-β oligomers: their production, toxicity and therapeutic inhibition.* Biochemical Society Transactions, 2002. **30**(4): p. 552-557.

241. Rajendran, L., M. Honsho, T.R. Zahn, P. Keller, K.D. Geiger, P. Verkade, and K. Simons, *Alzheimer's disease β-amyloid peptides are released in association with exosomes.* Proceedings of the National Academy of Sciences, 2006. **103**(30): p. 11172-11177.

242. Yuyama, K., H. Sun, S. Mitsutake, and Y. Igarashi, *Sphingolipid-modulated exosome secretion promotes clearance of amyloid-β by microglia.* Journal of Biological Chemistry, 2012. **287**(14): p. 10977-10989.

243. Yuyama, K., H. Sun, S. Sakai, S. Mitsutake, M. Okada, H. Tahara, J.-i. Furukawa, N. Fujitani, Y. Shinohara, and Y. Igarashi, *Decreased amyloid-β pathologies by intracerebral loading of glycosphingolipid-enriched exosomes in Alzheimer model mice.* Journal of Biological Chemistry, 2014. **289**(35): p. 24488-24498.

244. Marcilla, A., L. Martin-Jaular, M. Trelis, A. de Menezes-Neto, A. Osuna, D. Bernal, C. Fernandez-Becerra, I.C. Almeida, and H.A. del Portillo, *Extracellular vesicles in parasitic diseases.* Journal of Extracellular Vesicles, 2014. **3**.

245. Schwab, A., S.S. Meyering, B. Lepene, S. Iordanskiy, M.L. Van Hoek, R.M. Hakami, and F. Kashanchi, *Extracellular vesicles from infected cells: potential for direct pathogenesis*. Frontiers in Microbiology, 2015. **6**.

246. Delabranche, X., A. Berger, J. Boisrame-Helms, and F. Meziani, *Microparticles and infectious diseases*. Médecine et Maladies Infectieuses, 2012. **42**(8): p. 335-343.

247. Direskeneli, H., *Autoimmunity vs autoinflammation in Behcet's disease: do we oversimplify a complex disorder?* Rheumatology, 2006. **45**(12): p. 1461-1465.

248. Staubach, S., P. Schadewaldt, U. Wendel, K. Nohroudi, and F.-G. Hanisch, *Differential glycomics of epithelial membrane glycoproteins from urinary exovesicles reveals shifts toward complex-type N-glycosylation in classical galactosemia*. Journal of Proteome Research, 2011. **11**(2): p. 906-916.

249. Lakhal, S. and M.J. Wood, *Exosome nanotechnology: an emerging paradigm shift in drug delivery*. Bioessays, 2011. **33**(10): p. 737-741.

250. Kooijmans, S., P. Vader, S.M. van Dommelen, W.W. van Solinge, and R.M. Schiffelers, *Exosome mimetics: a novel class of drug delivery systems*. International Journal of Nanomedicine, 2012. **7**(1525): p. e41.

251. Jang, S.C., O.Y. Kim, C.M. Yoon, D.-S. Choi, T.-Y. Roh, J. Park, J. Nilsson, J. Lötvall, Y.-K. Kim, and Y.S. Gho, *Bioinspired exosome-mimetic nanovesicles for targeted delivery of chemotherapeutics to malignant tumors*. ACS Nano, 2013. **7**(9): p. 7698-7710.

252. Dai, S., D. Wei, Z. Wu, X. Zhou, X. Wei, H. Huang, and G. Li, *Phase I clinical trial of autologous ascites-derived exosomes combined with GM-CSF for colorectal cancer*. Molecular Therapy, 2008. **16**(4): p. 782-790.

253. Aline, F., D. Bout, S. Amigorena, P. Roingeard, and I. Dimier-Poisson, *Toxoplasma gondii antigen-pulsed-dendritic cell-derived exosomes induce a protective immune response against T. gondii infection*. Infection and Immunity, 2004. **72**(7): p. 4127-4137.

254. Corbin, I.R. and G. Zheng, *Mimicking nature's nanocarrier: synthetic low-density lipoprotein-like nanoparticles for cancer-drug delivery*. International Journal of Pharmaceutics, 2007.

255. Nikanjam, M., E.A. Blakely, K.A. Bjornstad, X. Shu, T.F. Budinger, and T.M. Forte, *Synthetic nano-low density lipoprotein as targeted drug delivery vehicle for glioblastoma multiforme*. International Journal of Pharmaceutics, 2007. **328**(1): p. 86-94.

256. Bertrand, N. and J.-C. Leroux, *The journey of a drug-carrier in the body: an anatomo-physiological perspective*. Journal of Controlled Release, 2012. **161**(2): p. 152-163.

257. O'Brien, K., M.C. Lowry, C. Corcoran, V.G. Martinez, M. Daly, S. Rani, W.M. Gallagher, M.W. Radomski, R.A. MacLeod, and L. O'Driscoll, *miR-134 in extracellular vesicles reduces triple-negative breast cancer aggression and increases drug sensitivity*. Oncotarget, 2015. **6**(32): p. 32774-32789.

258. Haney, M.J., N.L. Klyachko, Y. Zhao, R. Gupta, E.G. Plotnikova, Z. He, T. Patel, A. Piroyan, M. Sokolsky, and A.V. Kabanov, *Exosomes as drug delivery vehicles for Parkinson's disease therapy*. Journal of Controlled Release, 2015. **207**: p. 18-30.

259. Fang, R.H., C.-M.J. Hu, B.T. Luk, W. Gao, J.A. Copp, Y. Tai, D.E. O'Connor, and L. Zhang, *Cancer cell membrane-coated nanoparticles for anticancer vaccination and drug delivery*. Nano Letters, 2014. **14**(4): p. 2181-2188.

260. Parodi, A., N. Quattrocchi, A.L. Van De Ven, C. Chiappini, M. Evangelopoulos, J.O. Martinez, B.S. Brown, S.Z. Khaled, I.K. Yazdi, and M.V. Enzo, *Synthetic nanoparticles functionalized with biomimetic leukocyte membranes possess cell-like functions*. Nature Nanotechnology, 2013. **8**(1): p. 61-68.

261. Almutairi, A., W.J. Akers, M.Y. Berezin, S. Achilefu, and J.M. Fréchet, *Monitoring the biodegradation of dendritic near-infrared nanoprobes by in vivo fluorescence imaging*. Molecular Pharmaceutics, 2008. **5**(6): p. 1103-1110.

262. Viger, M.L., W. Sheng, C.L. McFearin, M.Y. Berezin, and A. Almutairi, *Application of time-resolved fluorescence for direct and continuous probing of release from polymeric delivery vehicles*. Journal of Controlled Release, 2013. **171**(3): p. 308-314.

263. Raman, C.V. and K.S. Krishnan, *A new type of secondary radiation*. Nature, 1928. **121**: p. 501-502.

264. Kettering, C., L. Shutts, and D.H. Andrews, *A representation of the dynamic properties of molecules by mechanical models*. Physical Review, 1930. **36**(3): p. 531.

265. Colthup, N., *Introduction to Infrared and Raman Spectroscopy*. 2012: Elsevier.

266. Ferraro, J.R., *Introductory Raman Spectroscopy*. 2003: Academic Press.

267. Larkin, P., *Infrared and Raman Spectroscopy; Principles and Spectral Interpretation*. 2011: Elsevier.

268. Pitt, G.D., D.N. Batchelder, K.P.J. Williams, S. Webster, K.J. Baldwin, I.P. Hayward, R. Bennett, Y.Y. Yang, B.J.E. Smith, and R.W. Bormett, *Engineering aspects and applications of the new Raman instrumentation*. IEE Proceedings - Science, Measurement and Technology, 2005. **152**(6): p. 241-318.

269. Mehta, A.D., K.A. Pullen, and J.A. Spudich, *Single molecule biochemistry using optical tweezers*. FEBS letters, 1998. **430**(1-2): p. 23-27.

270. Strick, T., J.-F. Allemand, V. Croquette, and D. Bensimon, *The manipulation of single biomolecules*. Physics Today, 2001. **54**(10): p. 46-51.

271. Lieber, C.A. and A. Mahadevan-Jansen, *Automated method for subtraction of fluorescence from biological Raman spectra*. Applied Spectroscopy, 2003. **57**(11): p. 1363-1367.

272. Bell, S.J. and E.O. Bourguignon, *Analysis of luminescent samples using subtracted shifted Raman spectroscopy*. Analyst, 1998. **123**(8): p. 1729-1734.

273. Krzanowski, W., *Principles of Multivariate Analysis*. 2000: OUP Oxford.

274. Chalmers, J.M., *Handbook of Vibrational Spectroscopy*. 2002: Wiley.

275. Meier, R.J., *Calculating the vibrational spectra of molecules: An introduction for experimentalists with contemporary examples*. Vibrational Spectroscopy, 2007. **43**(1): p. 26-37.

276. Beebe, K.R., R.J. Pell, and M.B. Seasholtz, *Chemometrics: A Practical Guide*. Vol. 4. 1998: Wiley-Interscience.

277. Wartewig, S. and R.H. Neubert, *Pharmaceutical applications of Mid-IR and Raman spectroscopy*. Advanced Drug Delivery Reviews, 2005. **57**(8): p. 1144-70.

278. Vankeirsbilck, T., A. Vercauteren, W. Baeyens, G. Van der Weken, F. Verpoort, G. Vergote, and J.P. Remon, *Applications of Raman spectroscopy in pharmaceutical analysis*. TrAC Trends in Analytical Chemistry, 2002. **21**(12): p. 869-877.

279. Cialla, D., A. Marz, R. Bohme, F. Theil, K. Weber, M. Schmitt, and J. Popp, *Surface-enhanced Raman spectroscopy (SERS): progress and trends*. Analytical and Bioanalytical Chemistry, 2012. **403**(1): p. 27-54.

280. Denson, S.C., C.J. Pommier, and M.B. Denton, *The impact of array detectors on Raman spectroscopy*. Journal of Chemical Education, 2007. **84**(1): p. 67.

281. Funfschilling, J. and D.F. Williams, *CW Laser Wavelength Modulation in Raman and Site Selection Fluorescence Spectroscopy*. Applied Spectroscopy, 1976. **30**(4): p. 443-446 UR - http://as.osa.org/abstract.cfm?URI=as-30-4-443.

282. Shreve, A.P., N.J. Cherepy, and R.A. Mathies, *Effective rejection of fluorescence interference in Raman spectroscopy using a shifted excitation difference technique*. Applied Spectroscopy, 1992. **46**(4): p. 707-711.

283. Kneipp, K., A.S. Haka, H. Kneipp, K. Badizadegan, N. Yoshizawa, C. Boone, K.E. Shafer-Peltier, J.T. Motz, R.R. Dasari, and M.S. Feld, *Surface-enhanced Raman spectroscopy in single living cells using gold nanoparticles*. Applied Spectroscopy, 2002. **56**(2): p. 150-154.

284. Théry, C., M. Boussac, P. Véron, P. Ricciardi-Castagnoli, G. Raposo, J. Garin, and S. Amigorena, *Proteomic analysis of dendritic cell-derived exosomes: a secreted subcellular compartment distinct from apoptotic vesicles*. The Journal of Immunology, 2001. **166**(12): p. 7309-7318.

285. Théry, C., M. Ostrowski, and E. Segura, *Membrane vesicles as conveyors of immune responses*. Nature Reviews Immunology, 2009. **9**(8): p. 581-593.

286. Chaput, N. and C. Théry. *Exosomes: immune properties and potential clinical implementations*. in *Seminars in Immunopathology*. 2011. Springer.

287. Bobrie, A., M. Colombo, S. Krumeich, G. Raposo, and C. Thery, *Diverse subpopulations of vesicles secreted by different intracellular mechanisms are present in exosome preparations obtained by differential ultracentrifugation*. Journal of Extracellular Vesicles, 2012. **1**.

288. Colombo, M., C. Moita, G. van Niel, J. Kowal, J. Vigneron, P. Benaroch, N. Manel, L.F. Moita, C. Théry, and G. Raposo, *Analysis of ESCRT functions in exosome biogenesis, composition and secretion highlights the heterogeneity of extracellular vesicles*. Journal of Cell Science, 2013. **126**(24): p. 5553-5565.

289. Laulagnier, K., C. Motta, S. Hamdi, R. Sébastien, F. Fauvelle, J.-F. Pageaux, T. Kobayashi, J.-P. Salles, B. Perret, and C. Bonnerot, *Mast cell-and dendritic cell-derived exosomes display a specific lipid composition and an unusual membrane organization*. Biochemical Journal, 2004. **380**(1): p. 161-171.

290. Subra, C., D. Grand, K. Laulagnier, A. Stella, G. Lambeau, M. Paillasse, P. De Medina, B. Monsarrat, B. Perret, and S. Silvente-Poirot, *Exosomes account for vesicle-mediated transcellular transport of activatable phospholipases and prostaglandins*. Journal of Lipid Research, 2010. **51**(8): p. 2105-2120.

291. Liang, Y., W.S. Eng, D.R. Colquhoun, R.R. Dinglasan, D.R. Graham, and L.K. Mahal, *Complex N-linked glycans serve as a determinant for exosome/ microvesicle cargo recruitment*. Journal of Biological Chemistry, 2014. **289**(47): p. 32526-32537.

292. Chen, K., Y. Qin, F. Zheng, M. Sun, and D. Shi, *Diagnosis of colorectal cancer using Raman spectroscopy of laser-trapped single living epithelial cells*. Optics Letters, 2006. **31**(13): p. 2015-2017.

293. Chan, J.W., D.S. Taylor, S.M. Lane, T. Zwerdling, J. Tuscano, and T. Huser, *Nondestructive identification of individual leukemia cells by laser trapping Raman spectroscopy*. Analytical Chemistry, 2008. **80**(6): p. 2180-2187.

294. Smith, Z.J., J.-C.E. Wang, S.A. Quataert, and A.J. Berger, *Integrated Raman and angular scattering microscopy reveals chemical and morphological differences between activated and nonactivated CD8+ T lymphocytes*. Journal of Biomedical Optics, 2010. **15**(3): p. 036021-036021-11.

295. Moritz, T.J., C.R. Polage, D.S. Taylor, D.M. Krol, S.M. Lane, and J.W. Chan, *Evaluation of Escherichia coli cell response to antibiotic treatment by use of Raman spectroscopy with laser tweezers*. Journal of Clinical Microbiology, 2010. **48**(11): p. 4287-4290.

296. Chan, J., A. Esposito, C. Talley, C. Hollars, S. Lane, and T. Huser, *Reagentless identification of single bacterial spores in aqueous solution by confocal laser tweezers Raman spectroscopy*. Analytical Chemistry, 2004. **76**(3): p. 599-603.

297. Argov, N., S. Wachsmann-Hogiu, S.L. Freeman, T. Huser, C.B. Lebrilla, and J.B. German, *Size-dependent lipid content in human milk fat globules*. Journal of Agricultural and Food Chemistry, 2008. **56**(16): p. 7446-7450.

298. Ajito, K. and K. Torimitsu, *Laser trapping and Raman spectroscopy of single cellular organelles in the nanometer range*. Lab on a Chip, 2002. **2**(1): p. 11-14.

299. Van Der Pol, E., A. Hoekstra, A. Sturk, C. Otto, T. Van Leeuwen, and R. Nieuwland, *Optical and non-optical methods for detection and characterization of microparticles and exosomes*. Journal of Thrombosis and Haemostasis, 2010. **8**(12): p. 2596-2607.

300. Tatischeff, I., E. Larquet, J.M. Falcon-Perez, P.Y. Turpin, and S.G. Kruglik, *Fast characterisation of cell-derived extracellular vesicles by nanoparticles tracking analysis, cryo-electron microscopy, and Raman tweezers microspectroscopy*. Journal of Extracellular Vesicles, 2012. **1**.

301. Kretschmann, E. and H. Raether, *Notizen: radiative decay of non radiative surface plasmons excited by light*. Zeitschrift für Naturforschung A, 1968. **23**(12): p. 2135-2136.

302. E, K., *Determination of optical constants of metals by excitation of surface plasmons*. Zeitschrift Fur Physik, 1971. **241**(4): p. 313-&.

303. J. W. Sadowski, I.K.J.K., J. P. K. Peltonen, *Characterization of thin films and their structures in surface plasmon resonance measurements*. Optical Engineering, 1995. **34**(9): p. 6.

304. Hayt, W.H. and J.A. Buck, *Engineering Electromagnetics*. Vol. 7. 2001: McGraw-Hill New York.

305. De Feijter, J., d.J. Benjamins, and F. Veer, *Ellipsometry as a tool to study the adsorption behavior of synthetic and biopolymers at the air–water interface*. Biopolymers, 1978. **17**(7): p. 1759-1772.

306. Schasfoort, R.B. and A.J. Tudos, *Handbook of Surface Plasmon Resonance*. 2008: Royal Society of Chemistry.

307. Ekgasit, S., C. Thammacharoen, and W. Knoll, *Surface plasmon resonance spectroscopy based on evanescent field treatment*. Analytical Chemistry, 2004. **76**(3): p. 561-568.

308. Liang, H., H. Miranto, N. Granqvist, J.W. Sadowski, T. Viitala, B. Wang, and M. Yliperttula, *Surface plasmon resonance instrument as a refractometer for liquids and ultrathin films*. Sensors and Actuators B: Chemical, 2010. **149**(1): p. 212-220.

309. Granqvist, N., H. Liang, T. Laurila, J. Sadowski, M. Yliperttula, and T. Viitala, *Characterizing ultrathin and thick organic layers by surface plasmon resonance three-wavelength and waveguide mode analysis*. Langmuir, 2013. **29**(27): p. 8561-8571.

310. Peterlinz, K. and R. Georgiadis, *Two-color approach for determination of thickness and dielectric constant of thin films using surface plasmon resonance spectroscopy*. Optics Communications, 1996. **130**(4): p. 260-266.

311. Karlsson, R. and A. Fält, *Experimental design for kinetic analysis of protein-protein interactions with surface plasmon resonance biosensors*. Journal of Immunological Methods, 1997. **200**(1): p. 121-133.

312. Grassi, J.H. and R.M. Georgiadis, *Temperature-dependent refractive index determination from critical angle measurements: Implications for quantitative SPR sensing*. Analytical Chemistry, 1999. **71**(19): p. 4392-4396.

313. Zhou, M., A. Otomo, S. Yokoyama, and S. Mashiko, *Estimation of organic molecular film structures using surface–plasmon resonance spectroscopy*. Thin Solid Films, 2001. **393**(1): p. 114-118.

314. Zhao, H., P.H. Brown, and P. Schuck, *On the distribution of protein refractive index increments*. Biophysical Journal, 2011. **100**(9): p. 2309-2317.

315. Liedberg, B., C. Nylander, and I. Lundström, *Biosensing with surface plasmon resonance—how it all started*. Biosensors and Bioelectronics, 1995. **10**(8): p. i-ix.

316. Schuck, P., *Use of surface plasmon resonance to probe the equilibrium and dynamic aspects of interactions between biological macromolecules 1*. Annual Review of Biophysics and Biomolecular Structure, 1997. **26**(1): p. 541-566.

317. Jussila, H., H. Yang, N. Granqvist, and Z. Sun, *Surface plasmon resonance for characterization of large-area atomic-layer graphene film*. Optica, 2016. **3**(2): p. 151-158.

318. Viitala, T., N. Granqvist, S. Hallila, M. Raviña, and M. Yliperttula, *Elucidating the Signal Responses of Multi-Parametric Surface Plasmon Resonance Living Cell Sensing: A Comparison between Optical Modeling and Drug–MDCKII Cell Interaction Measurements*. PLOS ONE, 2013. **8**(8): p. e72192.

319. Rich, R.L. and D.G. Myszka, *Advances in surface plasmon resonance biosensor analysis*. Current Opinion in Biotechnology, 2000. **11**(1): p. 54-61.

320. Shankaran, D.R., K.V. Gobi, and N. Miura, *Recent advancements in surface plasmon resonance immunosensors for detection of small molecules of biomedical, food and environmental interest*. Sensors and Actuators B: Chemical, 2007. **121**(1): p. 158-177.

321. Löfås, S. and B. Johnsson, *A novel hydrogel matrix on gold surfaces in surface plasmon resonance sensors for fast and efficient covalent immobilization of ligands*. Journal of the Chemical Society, Chemical Communications, 1990(21): p. 1526-1528.

322. Bartolini, M., C. Bertucci, M.L. Bolognesi, A. Cavalli, C. Melchiorre, and V. Andrisano, *Insight Into the Kinetic of Amyloid β (1–42) Peptide Self-Aggregation: Elucidation of Inhibitors' Mechanism of Action*. ChemBioChem, 2007. **8**(17): p. 2152-2161.

323. Sgarbossa, A., *Natural biomolecules and protein aggregation: emerging strategies against amyloidogenesis*. International Journal of Molecular Sciences, 2012. **13**(12): p. 17121-17137.

324. Kayed, R., E. Head, J.L. Thompson, T.M. McIntire, S.C. Milton, C.W. Cotman, and C.G. Glabe, *Common structure of soluble amyloid oligomers implies common mechanism of pathogenesis*. Science, 2003. **300**(5618): p. 486-489.

325. Klein, W., W. Stine, and D. Teplow, *Small assemblies of unmodified amyloid β-protein are the proximate neurotoxin in Alzheimer's disease*. Neurobiology of Aging, 2004. **25**(5): p. 569-580.

326. Baird, C.L., E.S. Courtenay, and D.G. Myszka, *Surface plasmon resonance characterization of drug/liposome interactions*. Analytical Biochemistry, 2002. **310**(1): p. 93-99.

327. Brändén, M., S.R. Tabaei, G. Fischer, R. Neutze, and F. Höök, *Refractive-index-based screening of membrane-protein-mediated transfer across biological membranes*. Biophysical Journal, 2010. **99**(1): p. 124-133.

328. Liang, H., J.-P. Tuppurainen, J. Lehtinen, T. Viitala, and M. Yliperttula, *Non-labeled monitoring of targeted liposome interactions with a model receptor surface: Effect of flow rate and water content*. European Journal of Pharmaceutical Sciences, 2013. **50**(3): p. 492-501.

329. Cedervall, T., I. Lynch, S. Lindman, T. Berggård, E. Thulin, H. Nilsson, K.A. Dawson, and S. Linse, *Understanding the nanoparticle–protein corona using methods to quantify exchange rates and affinities of proteins for nanoparticles*. Proceedings of the National Academy of Sciences, 2007. **104**(7): p. 2050-2055.

330. Corbo, C., R. Molinaro, A. Parodi, N.E.T. Furman, F. Salvatore, and E. Tasciotti, *The impact of nanoparticle protein corona on cytotoxicity, immunotoxicity and target drug delivery*. Nanomedicine, 2016. **11**(1): p. 81-100.

331. Arima, Y., M. Toda, and H. Iwata, *Complement activation on surfaces modified with ethylene glycol units*. Biomaterials, 2008. **29**(5): p. 551-560.

332. Szebeni, J., F. Muggia, A. Gabizon, and Y. Barenholz, *Activation of complement by therapeutic liposomes and other lipid excipient-based therapeutic products: prediction and prevention*. Advanced Drug Delivery Reviews, 2011. **63**(12): p. 1020-1030.

333. Crielaard, B., A. Yousefi, J. Schillemans, C. Vermehren, K. Buyens, K. Braeckmans, T. Lammers, and G. Storm, *An in vitro assay based on surface plasmon resonance to predict the in vivo circulation kinetics of liposomes*. Journal of Controlled Release, 2011. **156**(3): p. 307-314.

334. Im, H., H. Shao, Y.I. Park, V.M. Peterson, C.M. Castro, R. Weissleder, and H. Lee, *Label-free detection and molecular profiling of exosomes with a nano-plasmonic sensor*. Nature Biotechnology, 2014. **32**(5): p. 490-5.

335. Rupert, D.L., C. Lässer, M. Eldh, S. Block, V.P. Zhdanov, J.O. Lotvall, M. Bally, and F. Höök, *Determination of exosome concentration in solution using surface plasmon resonance spectroscopy*. Analytical Chemistry, 2014. **86**(12): p. 5929-5936.

336. Roden, L.D. and D.G. Myszka, *Global analysis of a macromolecular interaction measured on BIAcore*. Biochemical and Biophysical Research Communications, 1996. **225**(3): p. 1073-1077.

337. Melo, S.A., H. Sugimoto, J.T. O'Connell, N. Kato, A. Villanueva, A. Vidal, L. Qiu, E. Vitkin, L.T. Perelman, and C.A. Melo, *Cancer exosomes perform cell-independent microRNA biogenesis and promote tumorigenesis*. Cancer Cell, 2014. **26**(5): p. 707-721.

338. Smith, Z., C. Lee, T. Rojalin, and S. Wachsmann-Hogiu, *Comment on "Label-Free Single Exosome Detection Using Frequency Locked Microtoroid Optical Resonators"*. ACS Photonics, 2016. **3**(4): p. 716-717.

339. S. M. Angel, M.K.D., K. W. Hanck, and D.W. Wertz, *Computer-Controlled Instrument for the Recovery of a Resonance Raman Spectrum in the Presence of Strong Luminescence*. Analytical Chemistry, 1984.

340. Matousek, P., M. Towrie, and A.W. Parker, *Fluorescence background suppression in Raman spectroscopy using combined Kerr gated and shifted excitation Raman difference techniques*. Journal of Raman Spectroscopy, 2002. **33**(4): p. 238-242.

341. Efremov, E.V., J.B. Buijs, C. Gooijer, and F. Ariese, *Fluorescence rejection in resonance Raman spectroscopy using a picosecond-gated intensified charge-coupled device camera*. Applied Spectroscopy, 2007. **61**(6): p. 571-578.

342. Anker, J.N., W.P. Hall, O. Lyandres, N.C. Shah, J. Zhao, and R.P. Van Duyne, *Biosensing with plasmonic nanosensors*. Nature Materials, 2008. **7**(6): p. 442-453.

343. Nie, S., *Probing Single Molecules and Single Nanoparticles by Surface-Enhanced Raman Scattering*. Science, 1997. **275**(5303): p. 1102-1106.

344. Bantz, K.C., A.F. Meyer, N.J. Wittenberg, H. Im, Ö. Kurtuluş, S.H. Lee, N.C. Lindquist, S.-H. Oh, and C.L. Haynes, *Recent progress in SERS biosensing*. Physical Chemistry Chemical Physics, 2011. **13**(24): p. 11551-11567.

345. Hupfeld, S., A.M. Holsæter, M. Skar, C.B. Frantzen, and M. Brandl, *Liposome size analysis by dynamic/static light scattering upon size exclusion-/field flow-fractionation*. Journal of Nanoscience and Nanotechnology, 2006. **6**(9-1): p. 3025-3031.

346. Murdock, R.C., L. Braydich-Stolle, A.M. Schrand, J.J. Schlager, and S.M. Hussain, *Characterization of nanomaterial dispersion in solution prior to in vitro exposure using dynamic light scattering technique*. Toxicological Sciences, 2008. **101**(2): p. 239-253.

347. Myszka, D.G. and R.L. Rich, *Implementing surface plasmon resonance biosensors in drug discovery*. Pharmaceutical Science & Technology Today, 2000. **3**(9): p. 310-317.

348. Hebert, L.E., J. Weuve, P.A. Scherr, and D.A. Evans, *Alzheimer disease in the United States (2010–2050) estimated using the 2010 census*. Neurology, 2013. **80**(19): p. 1778-1783.

349. Wang, Q., X. Yu, L. Li, and J. Zheng, *Inhibition of amyloid-β aggregation in Alzheimer's disease*. Current Pharmaceutical Design, 2014. **20**(8): p. 1223-1243.

350. Petrlova, J., T. Kálai, I. Maezawa, R. Altman, G. Harishchandra, H.-S. Hong, D.A. Bricarello, A.N. Parikh, G.A. Lorigan, and L.-W. Jin, *The influence of spin-labeled fluorene compounds on the assembly and toxicity of the Aβ peptide*. PLOS ONE, 2012. **7**(4): p. e35443.

351. Altman, R., S. Ly, S. Hilt, J. Petrlova, I. Maezawa, T. Kálai, K. Hideg, L.-W. Jin, T.A. Laurence, and J.C. Voss, *Protective spin-labeled fluorenes maintain amyloid beta peptide in small oligomers and limit transitions in secondary structure*. Biochimica et Biophysica Acta (BBA)-Proteins and Proteomics, 2015. **1854**(12): p. 1860-1870.

352. Hubin, E., N. Van Nuland, K. Broersen, and K. Pauwels, *Transient dynamics of Aβ contribute to toxicity in Alzheimer's disease*. Cellular and Molecular Life Sciences, 2014. **71**(18): p. 3507-3521.

353. Lundqvist, M., J. Stigler, T. Cedervall, T. Berggård, M.B. Flanagan, I. Lynch, G. Elia, and K. Dawson, *The evolution of the protein corona around nanoparticles: a test study*. ACS Nano, 2011. **5**(9): p. 7503-7509.

354. Monopoli, M.P., D. Walczyk, A. Campbell, G. Elia, I. Lynch, F. Baldelli Bombelli, and K.A. Dawson, *Physical– chemical aspects of protein corona: relevance to in vitro and in vivo biological impacts of nanoparticles*. Journal of the American Chemical Society, 2011. **133**(8): p. 2525-2534.

355. Tenzer, S., D. Docter, J. Kuharev, A. Musyanovych, V. Fetz, R. Hecht, F. Schlenk, D. Fischer, K. Kiouptsi, and C. Reinhardt, *Rapid formation of plasma protein corona critically affects nanoparticle pathophysiology*. Nature Nanotechnology, 2013. **8**(10): p. 772-781.

356. Pozzi, D., G. Caracciolo, L. Digiacomo, V. Colapicchioni, S. Palchetti, A.L. Capriotti, C. Cavaliere, R.Z. Chiozzi, A. Puglisi, and A. Laganà, *The biomolecular corona of nanoparticles in circulating biological media*. Nanoscale, 2015. **7**(33): p. 13958-13966.

357. Ritz, S., S. Schöttler, N. Kotman, G. Baier, A. Musyanovych, J.r. Kuharev, K. Landfester, H.r. Schild, O. Jahn, and S. Tenzer, *Protein corona of nanoparticles: distinct proteins regulate the cellular uptake*. Biomacromolecules, 2015. **16**(4): p. 1311-1321.

358. Cedervall, T., I. Lynch, M. Foy, T. Berggård, S.C. Donnelly, G. Cagney, S. Linse, and K.A. Dawson, *Detailed identification of plasma proteins adsorbed on copolymer nanoparticles*. Angewandte Chemie International Edition, 2007. **46**(30): p. 5754-5756.

359. Walczyk, D., F.B. Bombelli, M.P. Monopoli, I. Lynch, and K.A. Dawson, *What the cell "sees" in bionanoscience*. Journal of the American Chemical Society, 2010. **132**(16): p. 5761-5768.

360. Lacerda, S.H.D.P., J.J. Park, C. Meuse, D. Pristinski, M.L. Becker, A. Karim, and J.F. Douglas, *Interaction of gold nanoparticles with common human blood proteins*. ACS Nano, 2009. **4**(1): p. 365-379.

361. Deng, Z.J., M. Liang, M. Monteiro, I. Toth, and R.F. Minchin, *Nanoparticle-induced unfolding of fibrinogen promotes Mac-1 receptor activation and inflammation*. Nature Nanotechnology, 2011. **6**(1): p. 39-44.

362. Lindman, S., I. Lynch, E. Thulin, H. Nilsson, K.A. Dawson, and S. Linse, *Systematic investigation of the thermodynamics of HSA adsorption to N-iso-propylacrylamide/N-tert-butylacrylamide copolymer nanoparticles. Effects of particle size and hydrophobicity*. Nano Letters, 2007. **7**(4): p. 914-920.

363. Lynch, I., T. Cedervall, M. Lundqvist, C. Cabaleiro-Lago, S. Linse, and K.A. Dawson, *The nanoparticle–protein complex as a biological entity; a complex fluids and surface science challenge for the 21st century*. Advances in Colloid and Interface Science, 2007. **134**: p. 167-174.

364. Walkey, C.D. and W.C. Chan, *Understanding and controlling the interaction of nanomaterials with proteins in a physiological environment*. Chemical Society Reviews, 2012. **41**(7): p. 2780-2799.

365. Mahon, E., A. Salvati, F.B. Bombelli, I. Lynch, and K.A. Dawson, *Designing the nanoparticle–biomolecule interface for "targeting and therapeutic delivery"*. Journal of Controlled Release, 2012. **161**(2): p. 164-174.

366. Nyström, A.M. and B. Fadeel, *Safety assessment of nanomaterials: implications for nanomedicine*. Journal of Controlled Release, 2012. **161**(2): p. 403-408.

367. Harding, C.V., J.E. Heuser, and P.D. Stahl, *Exosomes: looking back three decades and into the future*. The Journal of Cell Biology, 2013. **200**(4): p. 367-371.

368. Nishiuchi, R., O. Murayama, H. Fujiwara, J. Gu, T. Kawakami, S. Aimoto, Y. Wada, and K. Sekiguchi, *Characterization of the ligand-binding specificities of integrin α3β1 and α6β1 using a panel of purified laminin isoforms containing distinct α chains*. Journal of Biochemistry, 2003. **134**(4): p. 497-504.

369. Fuhrmann, G., I.K. Herrmann, and M.M. Stevens, *Cell-derived vesicles for drug therapy and diagnostics: opportunities and challenges*. Nano Today, 2015. **10**(3): p. 397-409.

370. Lam, K.S., M. Lebl, and V. Krchnák, *The "one-bead-one-compound" combinatorial library method*. Chemical Reviews, 1997. **97**(2): p. 411-448.

371. Aina, O.H., J. Marik, R. Liu, D.H. Lau, and K.S. Lam, *Identification of novel targeting peptides for human ovarian cancer cells using "one-bead one-compound" combinatorial libraries*. Molecular Cancer Therapeutics, 2005. **4**(5): p. 806-813.